Conference Proceedings of the Society for Experimental Mechanics Series

Christopher Niezrecki · Javad Baqersad
Dario Di Maio *Editors*

Rotating Machinery, Optical Methods & Scanning LDV Methods, Volume 6

Proceedings of the 37th IMAC, A Conference and Exposition on Structural Dynamics 2019

SEM

Springer

Conference Proceedings of the Society for Experimental Mechanics Series

Series Editor

Kristin B. Zimmerman, Ph.D.
Society for Experimental Mechanics, Inc.,
Bethel, CT, USA

More information about this series at http://www.springer.com/series/8922

Christopher Niezrecki • Javad Baqersad • Dario Di Maio
Editors

Rotating Machinery, Optical Methods & Scanning LDV Methods, Volume 6

Proceedings of the 37th IMAC, A Conference and Exposition on Structural Dynamics 2019

Springer

Editors
Christopher Niezrecki
Department Mechanical Engineering
University of Massachusetts Lowell
Lowell, MA, USA

Javad Baqersad
Kettering University
Flint, MI, USA

Dario Di Maio
Department of Mechanical Engineering
University of Bristol, Queens Building
Bristol, UK

ISSN 2191-5644 ISSN 2191-5652 (electronic)
Conference Proceedings of the Society for Experimental Mechanics Series
ISBN 978-3-030-12934-7 ISBN 978-3-030-12935-4 (eBook)
https://doi.org/10.1007/978-3-030-12935-4

Library of Congress Control Number: 2019936301

© Society for Experimental Mechanics, Inc. 2019
This work is subject to copyright. All rights are reserved by the Publisher, whether the whole or part of the material is concerned, specifically the rights of translation, reprinting, reuse of illustrations, recitation, broadcasting, reproduction on microfilms or in any other physical way, and transmission or information storage and retrieval, electronic adaptation, computer software, or by similar or dissimilar methodology now known or hereafter developed.
The use of general descriptive names, registered names, trademarks, service marks, etc. in this publication does not imply, even in the absence of a specific statement, that such names are exempt from the relevant protective laws and regulations and therefore free for general use.
The publisher, the authors, and the editors are safe to assume that the advice and information in this book are believed to be true and accurate at the date of publication. Neither the publisher nor the authors or the editors give a warranty, express or implied, with respect to the material contained herein or for any errors or omissions that may have been made. The publisher remains neutral with regard to jurisdictional claims in published maps and institutional affiliations.

This Springer imprint is published by the registered company Springer Nature Switzerland AG.
The registered company address is: Gewerbestrasse 11, 6330 Cham, Switzerland

Preface

Rotating Machinery, Optical Methods & Scanning LDV Methods represents one of the eight volumes of technical papers presented at the 37th IMAC, A Conference and Exposition on Structural Dynamics, organized by the Society for Experimental Mechanics, and held in Orlando, Florida, January 28–31, 2019. The full proceedings also include volumes on Nonlinear Structures and Systems; Dynamics of Civil Structures; Model Validation and Uncertainty Quantification; Dynamics of Coupled Structures; Special Topics in Structural Dynamics & Experimental Techniques; Sensors and Instrumentation, Aircraft/Aerospace, Energy Harvesting & Dynamic Environments Testing; and Topics in Modal Analysis & Testing.

Each collection presents early findings from experimental and computational investigations on an important area within structural dynamics.

The organizers would like to thank the authors, presenters, session organizers, and session chairs for their participation in this track.

Lowell, MA, USA — Christopher Niezrecki
Flint, MI, USA — Javad Baqersad
Bristol, UK — Dario Di Maio

Contents

Chapter 1
Detection of Sources of Nonlinearity in Multiple Bolted Joints by Use of Laser Vibrometer

Arnaldo delli Carri, Sante Campanelli, and Dario Di Maio

Abstract The use of non-contact measurement methods for detecting and locating sources of nonlinearities can be potentially a break-through in the nowadays experimental modal analysis. The primary goal is to define more effective test strategies, whereby contact sensors will measure the nonlinear vibration responses at the best location possible. Jointed structures are a typical example where a large number of the joint can pose the question of where what and how to measure the nonlinear response. Upon the identification of one, or more, nonlinear response mode the objective is to determine where is the source of such nonlinear vibration. Nonlinearity can be characterised when its source is well defined and can be adequately tested. This paper will attempt to detect and locate the source of nonlinearity from a multi-beam jointed assembly. The approach will be carried out by using both contact and non-contact measurement methods, the results of which will be compared and evaluated. The operator to detect the source of nonlinearity will be the coherence function applied to random response data.

Keywords SLDV · Bolted joints · Nonlinear vibration testing

1.1 Introduction

This paper attempts to exploit the potential of the scanning LDV system to measure vibration nonlinear response at a much greater number of locations, than it can be done by using setup based on contact sensors. The objective is to use such denser measurement grid to identify one, or more, sources of nonlinearity. It is not intended to replace the accelerometer for the characterization and quantification of a source of nonlinearity. The localization of nonlinearities is fundamental when such sources are discrete as for bolted structures. It is notorious that structures with a high number of interfaces will exhibit nonlinear responses when subjected to high amplitude of excitation forces. From a model validation viewpoint, the accurate localization, characterization and quantification of the nonlinearity can make the modelling work more effective and time efficient. Resources can be dedicated to improving the model where it is needed by inclusion of the nonlinear physics.

The localization of nonlinearities was usefully carried out in [1]. It was demonstrated that by setting up a good number of accelerometers on a structure the localization can be done with a good level of accuracy. However, it looked clear that such a method of localization depends on the setup of the contact sensors, and when an engineering judgment is not based on the identification of nonlinearity it might be possible that nonlinearities stay hidden to the sensors. Following the methodology applied to locate the source of nonlinearity (explained in the following sections), it become interesting to use a different technology which would enable much denser measurement grind than offered by contact sensors. Three research works addressed the topic of localization by using the scanning laser vibrometer. One research was focussed on bolted flanges and the use of continuous scanning methods to identify the source of nonlinearity. That approach showed that by mapping the response phase of the deflection shape measured at constant frequency and several level of amplitudes one could determine the level of nonlinearity exhibited by a vibration mode [2]. The scanning laser vibrometer was used in its step-scanning mode in two attempts, where high resolution mode shapes were measured to determine which mode would exert more nonlinear

---

A. delli Carri
School of Mechanical, Aerospace and Automotive Engineering, Coventry University, Coventry, UK

S. Campanelli
Department of Mechanical Engineering, Universita' Politecnica delle Marche, Ancona, Italy

D. Di Maio (✉)
Department of Mechanical Engineering, University of Bristol, Queens Building, Bristol, UK
e-mail: aeddm@bristol.ac.uk

C. Niezrecki et al. (eds.), *Rotating Machinery, Optical Methods & Scanning LDV Methods, Volume 6*, Conference Proceedings of the Society for Experimental Mechanics Series, https://doi.org/10.1007/978-3-030-12935-4_1

response [3]. The outcome of that research showed that some mode shapes create high strain distribution at the flanges' region and thus enabling interface nonlinear conditions. A more recently publication was focussed on use the stepped scanning method to measure the response phase of the deflection shapes of an aero-engine casing assembly onto which accessories were mounted to generate sources of nonlinearities [4]. The research showed that response phase of the deflection shape was a good indicator of the source of nonlinearity.

The present paper aims (i) at starting from those earlier success to detect the nonlinearities of a structure, and (ii) at combining the method of localization based on accelerometers with the use of a scanning laser vibrometer. A novel structure will be used to explore these new developments. The structure is made of ten blocks each of which bolted by two bolts to form a single prismatic beam. The source of nonlinearity can be moved by opening one or more pairs of bolts. The next section will explain in more details the tests structure and setup. The paper will proceed by attempting the same localization method using a set of four reference accelerometers and the measurement made by a scanning laser vibrometer over a grid of 30 points.

1.2 Test Structure, Setup and Experimental Method

The test structure was designed with the idea to repeat the same basic unit ten times. Figure 1.1 shows the basic unit which can be bolted by two pairs of M8 bolts. Figure 1.2 shows both the solid mode and the real unit made of mild steel. The full assembly of the ten units is presented in Fig. 1.3. The 18 bolts were tightened up to 20 Nm to assure full clamping conditions.

The beam was suspended by strings from a frame and a shaker was installed at the bottom of the assembly, as showed in Fig. 1.4a. Thirty measurement points were marked on the beam where the laser beam would measure the vibrations. Four reference accelerometers were also included in the measurement setup, one of which at the drive point location. Figure 1.4b shows the measurement setup.

A custom-made control LabView panel was used to drive the laser beam onto the measurement points and to acquire the vibration response. It was decided to avoid the use the Polytec control panel to give full accessibility to the generation of the excitation signal. Four random noise signals, with 1M samples at 10 kHz sampling frequency, were generated at four different amplitudes. These four signals were stored and used for measuring the 30 LDV measurement points and the four accelerometers. This approach was decided to allow the excitation signal from the generator to be always the same, avoiding

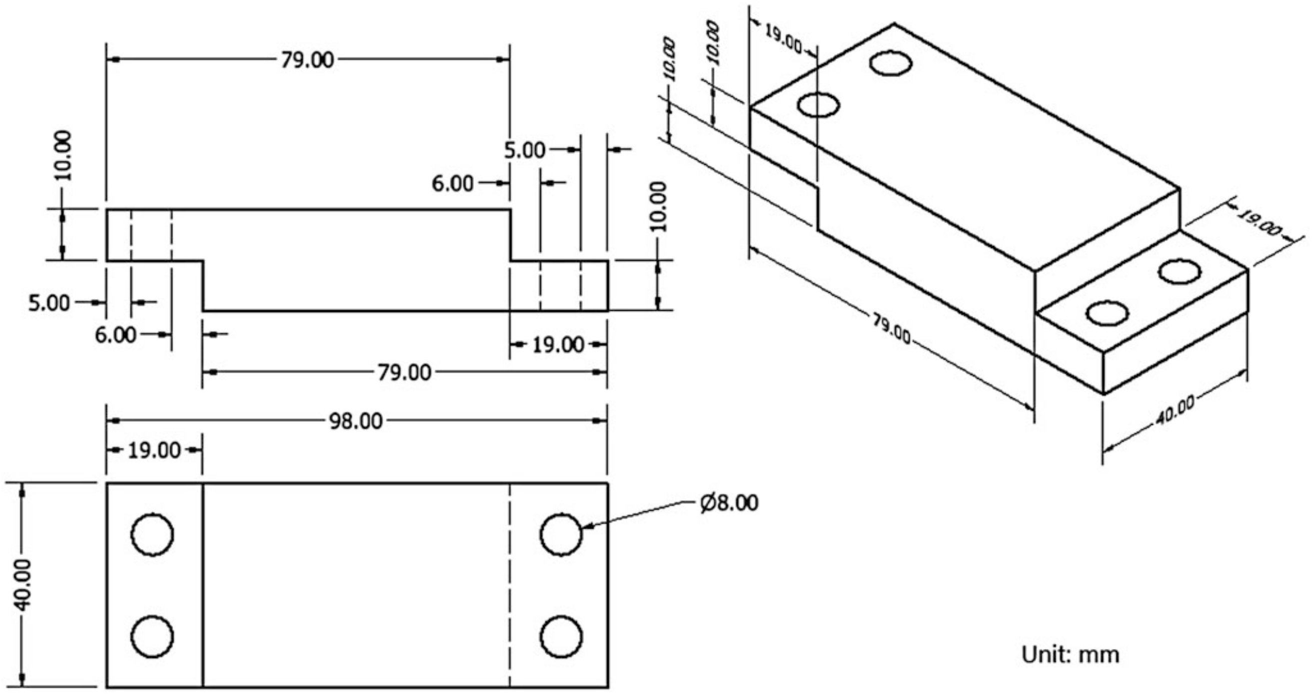

Fig. 1.1 CAD drawing of the basic unit

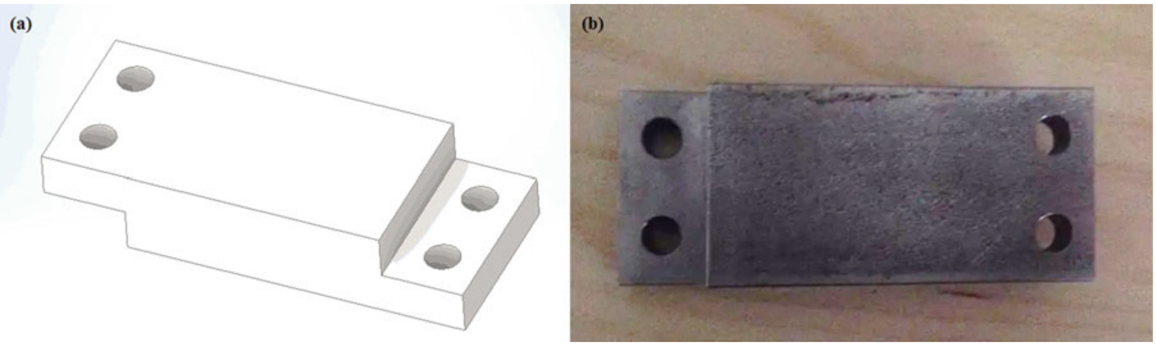

Fig. 1.2 Solid model in (**a**) and real unit in (**b**)

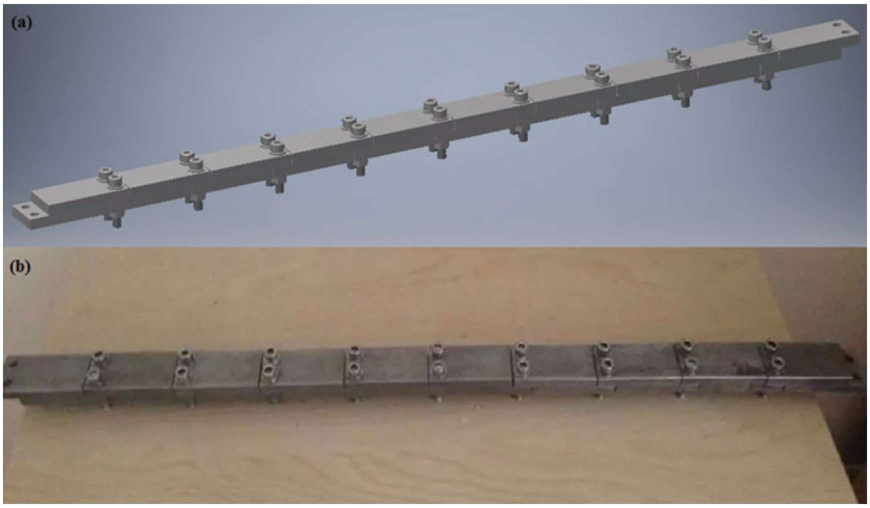

Fig. 1.3 Solid model in (**a**) and real assembly in (**b**)

variations if it were to be generated every time. The four amplitudes were identified as follows, 18 mV, 180 mV, 1080 mV and 1800 mV, respectively. The gain of the amplifier was fixed at one level and never changed.

The test programme was designed as such. The first trial was focussed on assuring the complete linearity of the structure for the 20 Nm torque applied to the 18 bolts. Hence, levels 18 mV, 180 mV and 1800 mV were attempted. The second trial, labelled as configuration A, was carried out by reducing the torque from 20 Nm, to 13 Nm and 8 Nm of the pair of bolts, the fifth from the top. The third trial, labelled configuration B, was carried out using the same torque levels reducing the pair of bolts, the third from the top, and by resetting the fifth pair to 20 Nm. A total of three configuration were tried.

1.3 Theoretical Method

The analysis was performed using conditioned spectral techniques from [5–8] and already applied in an earlier form in [1, 9]. The general equation of motion for a n-DOFs nonlinear system is

$$\boldsymbol{M}\ddot{x}(t) + \boldsymbol{C}\dot{x}(t) + \boldsymbol{K}x(t) + \sum_{i=1}^{M}\left[q_i \cdot g_i\Big(w_i x(t), w_i \dot{x}(t)\Big)\right] = f(t)$$

Where $\boldsymbol{M}$, $\boldsymbol{K}$, $\boldsymbol{C}$ are the $n \times n$ mass, stiffness and damping matrices, $x(t)$ and its derivatives are the $nx1$ displacements, velocities and accelerations vectors, $f(t)$ is the $nx1$ forcing vector.

In addition to the usual linear terms, there are M nonlinear (vectorial) terms that contribute to the system: under the summation operator one can discriminate the scaling factor q_i that quantifies the strength of the nonlinearity with respect

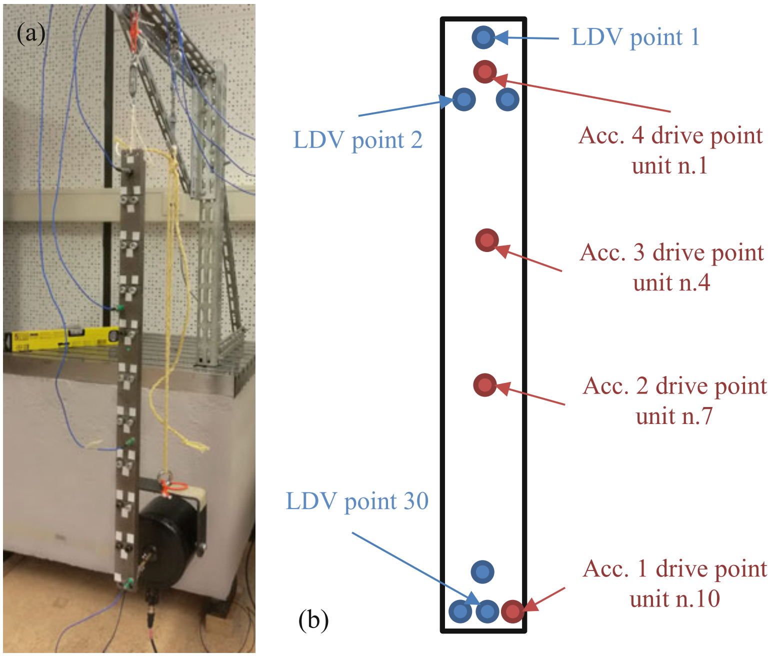

Fig. 1.4 Test setup in (**a**) and measurement points in (**b**)

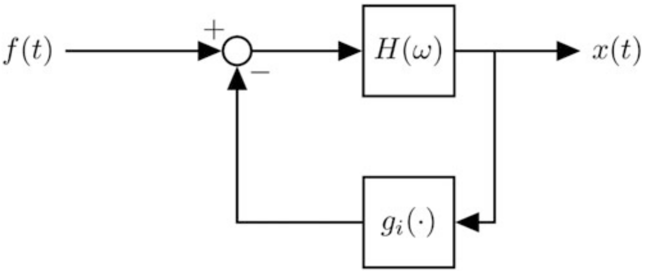

Fig. 1.5 Block diagram

to the other linear terms, the nonlinear function $g_i(\cdot,\cdot)$ that characterises the shape of the nonlinearity and the boolean-like vector w_i used to describe the location of the nonlinear term.

Using the Fourier Transform $\mathcal{F}[\cdot]$ to pass from the time domain to the frequency domain:

$$\left[\boldsymbol{K}-\omega^2\boldsymbol{M}+j\omega\boldsymbol{C}\right]X(\omega)=F(\omega)-\sum_{i=1}^{M}\mathcal{F}\left[q_i\cdot g_i\left(w_i x(t),\, w_i\dot{x}(t)\right)\right]$$

$$\boldsymbol{A}(\omega)\,X(\omega)=F(\omega)-G(\omega)$$

$$X(\omega)=\boldsymbol{H}(\omega)\cdot\left(F(\omega)-G(\omega)\right)$$

This can be viewed as a set of nonlinear feedback forces acting on an underlying linear system and can be represented as a block diagram in Fig. 1.5.

For the case of a 4-DOFs system with a grounded nonlinearity at DOF#1 and a non-grounded nonlinearity between DOF#3 and DOF#4 and excited at DOF#2

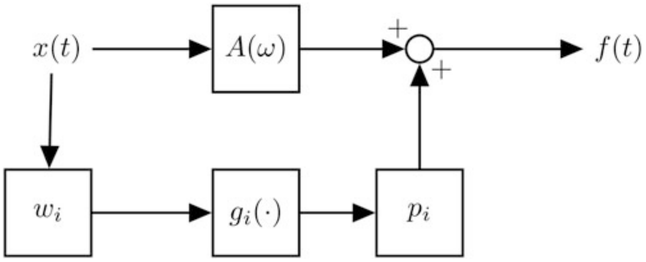

Fig. 1.6 MISO system

$$\begin{bmatrix} X_1 \\ X_2 \\ X_3 \\ X_4 \end{bmatrix} = \begin{bmatrix} H_{11} & \cdots & H_{14} \\ \vdots & \ddots & \vdots \\ H_{41} & \cdots & H_{44} \end{bmatrix} \cdot \begin{bmatrix} -\mathcal{F}\left[q_1 \cdot g_1\left(x_1\right)\right] \\ F_2 \\ -\mathcal{F}\left[q_2 \cdot g_2\left(x_3 - x_4\right)\right] \\ \mathcal{F}\left[q_2 \cdot g_2\left(x_3 - x_4\right)\right] \end{bmatrix}$$

$$\begin{cases} X_1 = -H_{11}G_1 + H_{12}F_2 - H_{13}G_2 + H_{14}G_2 \\ X_2 = -H_{21}G_1 + H_{22}F_2 - H_{23}G_2 + H_{24}G_2 \\ X_3 = -H_{31}G_1 + H_{32}F_2 - H_{33}G_2 + H_{34}G_2 \\ X_4 = -H_{41}G_1 + H_{42}F_2 - H_{43}G_2 + H_{44}G_2 \end{cases}$$

Rewriting the equations in terms of the input force, one decomposes a single SIMO system with nonlinear feedback into a set of reverse MISO systems like in Fig. 1.6.

$$\begin{cases} F_2 = H_{12}^{-1}X_1 + H_{12}^{-1}H_{11}G_1 + H_{12}^{-1}\left(H_{13} - H_{14}\right)G_2 \\ F_2 = H_{22}^{-1}X_2 + H_{22}^{-1}H_{21}G_1 + H_{22}^{-1}\left(H_{13} - H_{14}\right)G_2 \\ F_2 = H_{32}^{-1}X_3 + H_{32}^{-1}H_{31}G_1 + H_{32}^{-1}\left(H_{13} - H_{14}\right)G_2 \\ F_2 = H_{42}^{-1}X_4 + H_{42}^{-1}H_{41}G_1 + H_{42}^{-1}\left(H_{13} - H_{14}\right)G_2 \end{cases}$$

By feeding in any combination of location vectors w_i, nonlinear operators $g_i(\cdot,\cdot)$ and scaling factors q_i, it is possible to assess the quality of the system by making use of standard spectral techniques. One of the best suitable metrics of causality is the multiple coherence between the one output and all the inputs, defined as

$$\gamma^2(\omega) = \frac{S_{FX}(\omega) \cdot S_{XX}^{-1}(\omega) \cdot S_{FX}^{H}(\omega)}{S_{FF}(\omega)}$$

Where S are the frequency-dependent averaged auto and cross-spectral density matrices. Finally, this can be turned into a *coherence index* by normalising its integral over the considered bandwidth:

$$\kappa = \frac{1}{\omega_2 - \omega_1} \cdot \int_{\omega_1}^{\omega_2} \gamma^2(\omega)\ d\omega$$

1.4 Preliminary Analysis

As stated in the previous section, accelerometers and laser data have different structure: the former consists of 30 different tests of 4 acceleration response channels acquired at the same time while the latter is a single collection of 30 velocity response channels acquired at different times. It is thus necessary to perform some preliminary data analysis to check the sanity of the data, in form of linearity and stationarity checks.

Linearity checks are performed by super-imposing FRFs and coherences of the systems at different force levels. The plots in Figure 1.7 show severe curve degradations in the tests at 8 Nm torque.

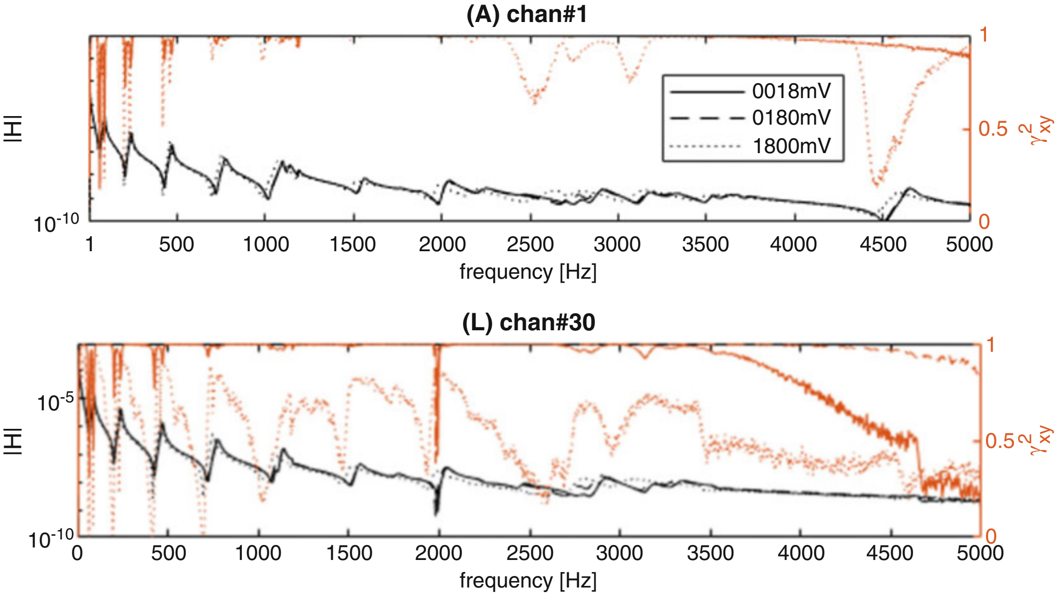

Fig. 1.7 FRFs and Coherences of LDV point 1 and LDV point 30

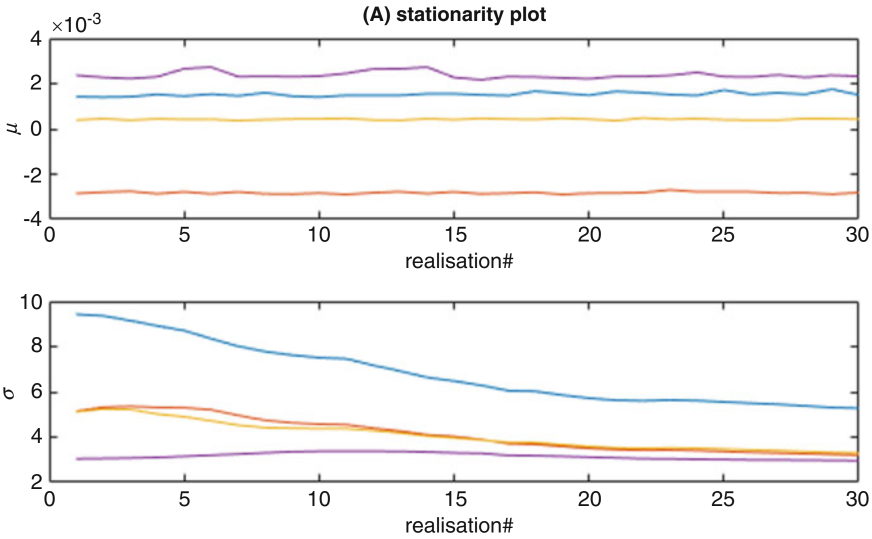

Fig. 1.8 Accelerometers stationarity plots

If gaussian input voltage is provided, a gaussian output force is expected from the shaker. This is not generally the case due to shaker-structure interactions. A gaussian time history passing through a non-linear system always generates a non-gaussian output [1]. Stationarity checks are performed to assess the quality of the data and determine if the system is changing over time (the structure might be settling on supports or getting to the operating temperature). The stationarity plots for both accelerometers and lasers are found in Figs. 1.8 and 1.9.

By inspecting the mean and standard deviation of the channels, it can be observed that the accelerometric channels are quite stationary in mean, but the structure had to settle at around the 15th realisation for a stable standard deviation. The laser means and standard deviations are more scattered around an average. Since the laser channels were not captured at the same time it is complicated to discern if the ensemble data is ergodic or even stationary, as some channels might have been captured before the structure had any time to settle.

Since the quality metric chosen is the multiple coherence, the data was sanitised by detrending. This operation has no impact on coherence, that only measures the input-output causality, but will hinder any calculation and retrieval of frequency response functions.

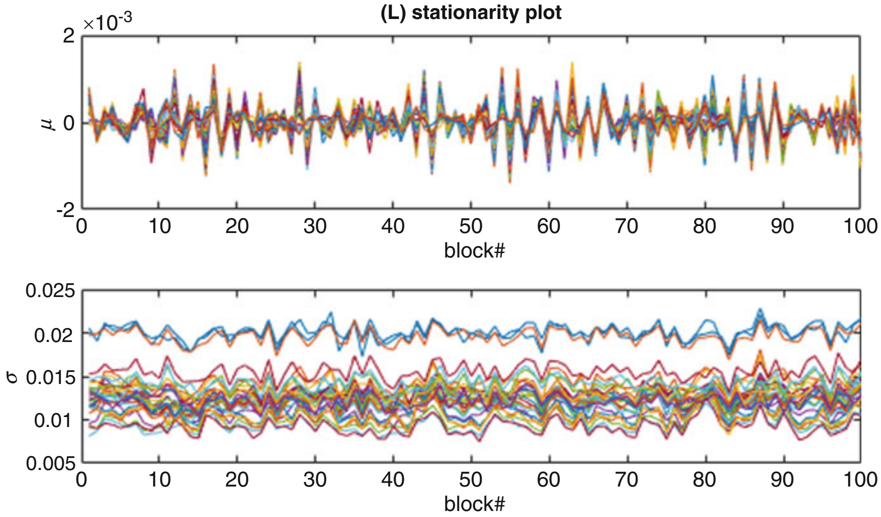

Fig. 1.9 LDV stationarity plots

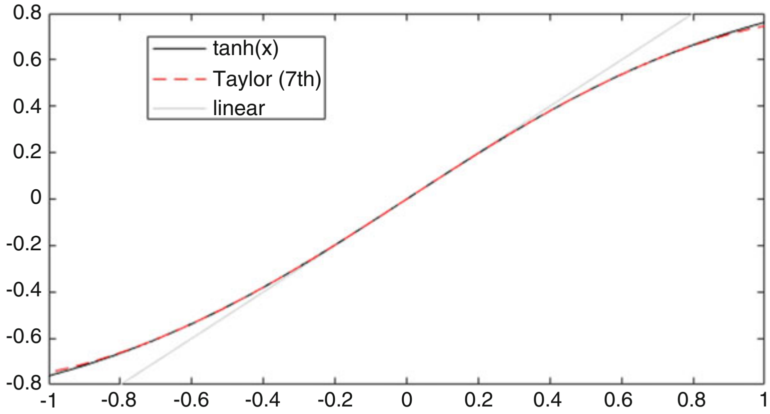

Fig. 1.10 Hyperbolic tangent function

1.5 Characterisation of the Nonlinearity

The frequency response functions (Fig. 1.7) show a left-shift in natural frequencies over the force range, thus indicating a softening stiffness nonlinearity in play. This is to be expected, as loose joints have some degree of play and the prestress of the bolt is small enough that fails to provide stiffness after a given threshold.

After feeding in several softening nonlinear operators into the system the most responsive (i.e. the one that gives the greatest improvement in multiple coherence) is a combination of alternating softening/hardening monomials and a tapering-saturation effect. This unfortunately makes the numerical analysis extremely cumbersome. The best approximation of this behaviour is the hyperbolic tangent function in Fig. 1.10.

Its Taylor expansion being

$$\tanh(x) = \sum_{n=0}^{\infty} \frac{2^{2n}\left(2^{2n}-1\right)B_{2n}}{(2n)!}x^{2n-1} = x - \frac{1}{3}x^3 + \frac{2}{15}x^5 - \frac{17}{345}x^7 + \dots$$

By using this nonlinear operator, it was possible to cut the processing time without incurring in any sensible loss of accuracy.

Given a suitable nonlinear operator, the location of the nonlinearity is performed by reverse MISO analysis of every nonlinear term by rotating the location vectors. These can also be filtered to include or exclude locations based on any prior information available to the engineer. In this case it is known that the nonlinearity locations will always be between two consecutive channels, thus only three locations were tested for the accelerometric channels (i.e. between 1–2, 2–3,

Table 1.1 Results

Location		Coherence index					
		Test3		Test4		Test5	
LASER	ACCEL	LASER	ACCEL	LASER	ACCEL	LASER	ACCEL
1–2	3–4	0.5622	0.9452	0.5228	0.9522	0.7747	**0.9818**
2–3		0.5575		0.5110		0.7957	
3–4		0.5555		0.5113		**0.8243**	
4–5		0.5556		0.5093		0.7912	
5–6	2–3	0.5555	0.9603	0.5082	0.9716	0.7875	0.9592
6–7		0.5585		0.5151		0.7945	
7–8		0.5634		0.5076		0.7962	
8–9		**0.5950**		0.5132		0.7919	
9–10	1–2	0.5783	**0.9851**	**0.5243**	**0.9746**	0.7858	0.9436

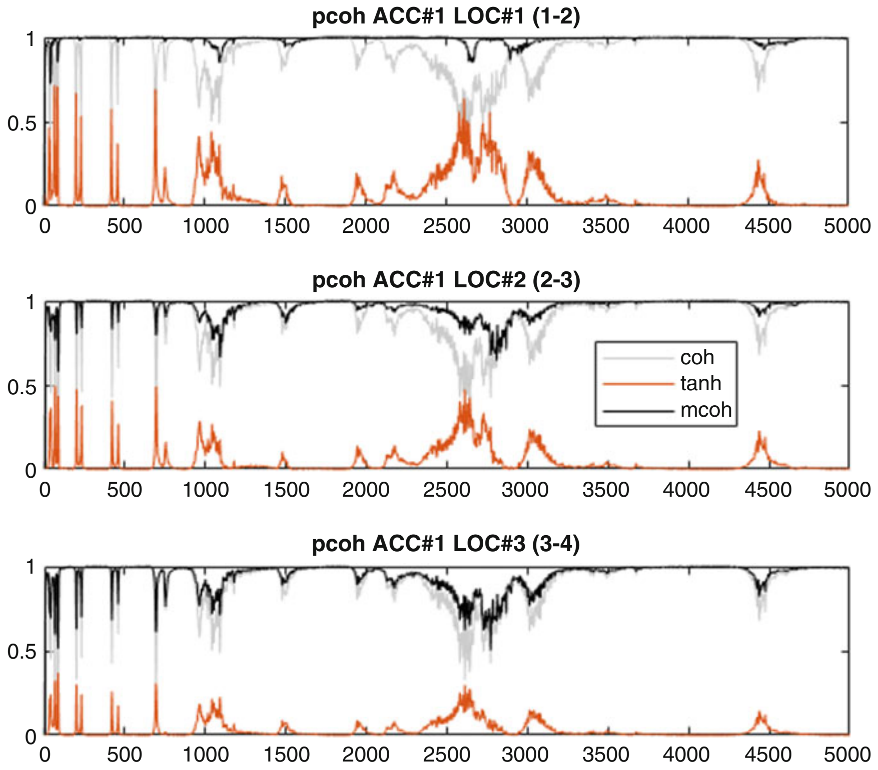

Fig. 1.11 Test3 - accelerometers

3–4) and nine for the laser channels (i.e. 1–2, 2–3, 3–4, 4–5, 5–6, 6–7, 7–8, 8–9, 9–10). The multiple coherence index was then calculated for all these combinations. The highest multiple coherence index should indicate the correct location of the nonlinearity. Results can be found in Table 1.1 and all the relevant plots in Figs. 1.11 and 1.12.

Accelerometric data features a much higher coherence index. This is expected, all channels being acquired at the same time and thus having direct causality relationship with the excitation. Test3 and Test5 are correctly identified while Test4 is not, with some degree of ambiguity. This might be due to the low spatial resolution of accelerometers, but it is more likely an issue with the test, as it is observed that laser data share the same degree of uncertainty. Laser data is more spatially dense and so more precise with respect to location. The main issue is the possible lack of causality due to the channels not being acquired at the same time (non-ergodicity or non-stationarity). Although the voltage excitation is the same, the force output from the shaker is different for every channel due to shaker-structure interactions and settling of the joints. This leads to generally poorer coherence and lack of causality that renders the method incapable of giving correct results in a consistent way, especially in non-lab conditions. As a result, laser results are much harder to interpret using the coherence index alone and reading the coherence plots (Figs. 1.11, 1.12, 1.13, 1.14, 1.15, and 1.16) proves challenging as well, as some locations perform better in certain frequency ranges than others, unlike what happens with accelerometric data.

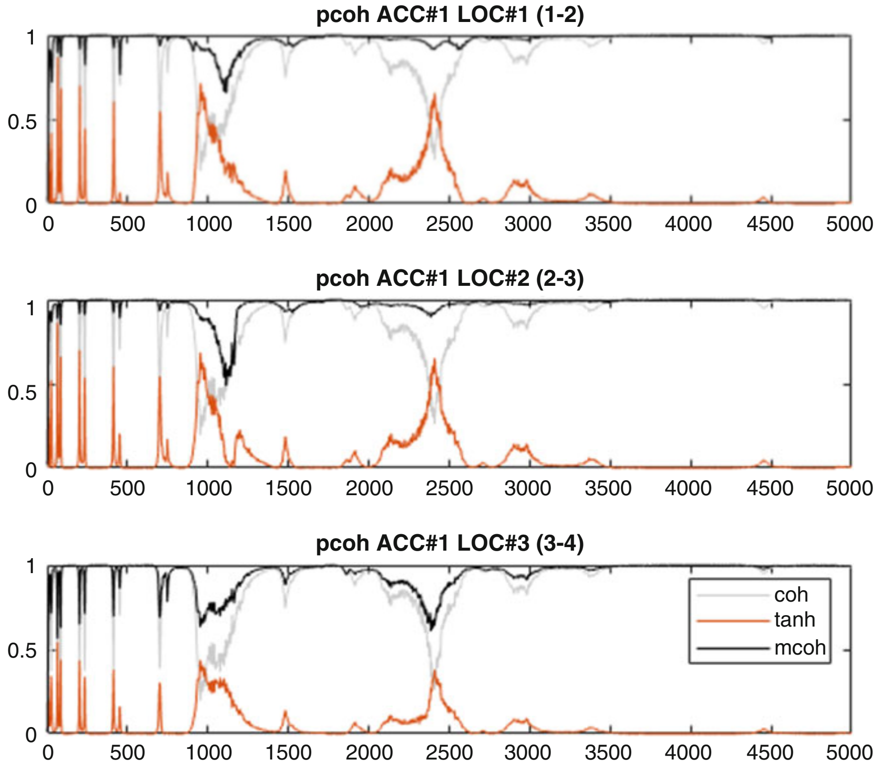

Fig. 1.12 Test4 – accelerometers

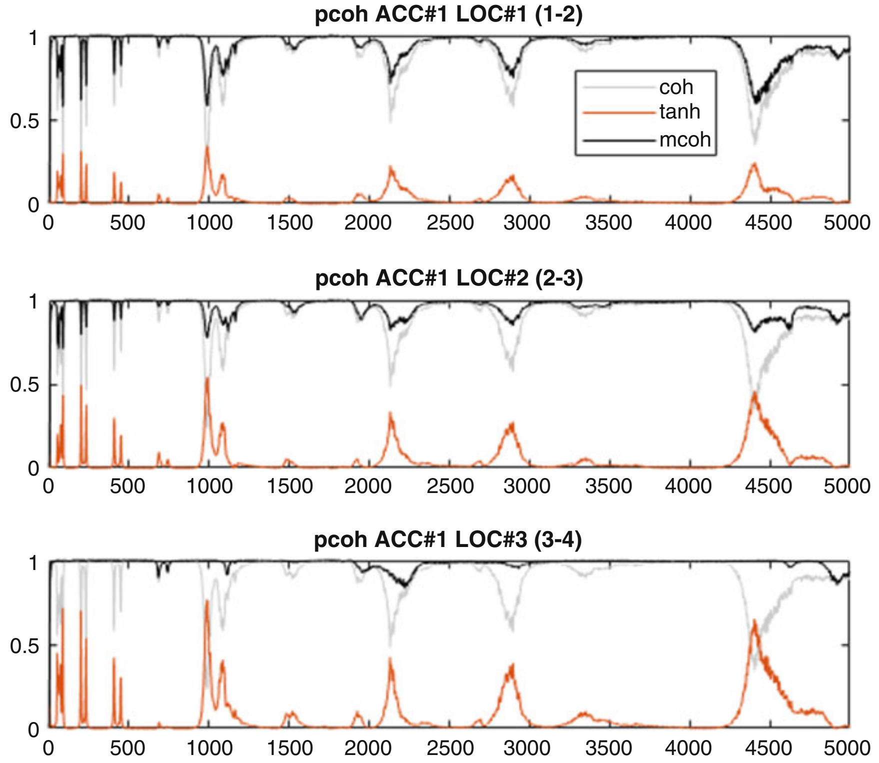

Fig. 1.13 Test 5 – accelerometers

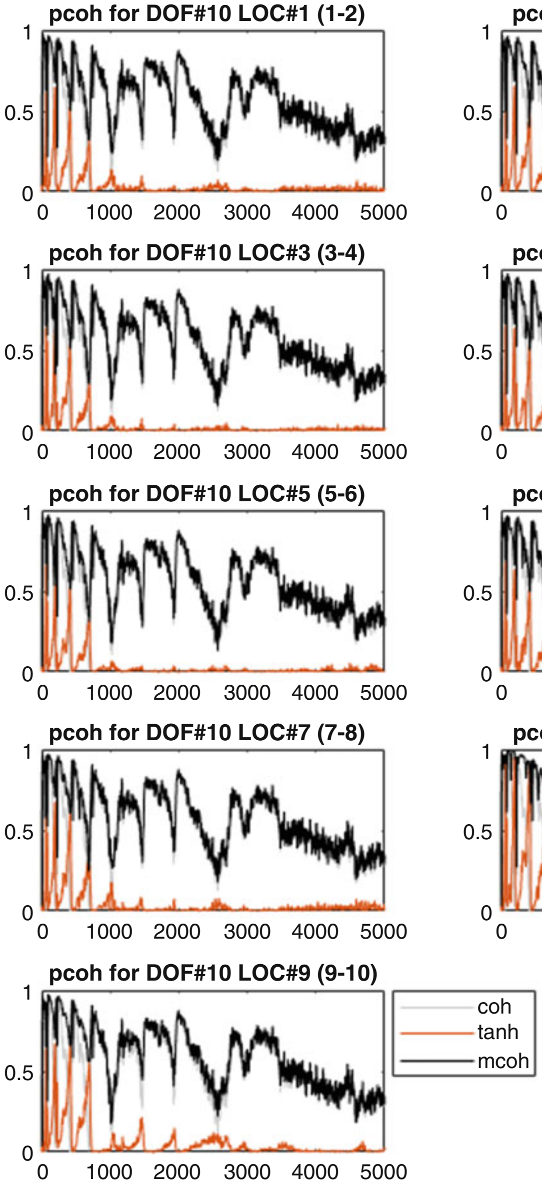

Fig. 1.14 Test3 - LDV

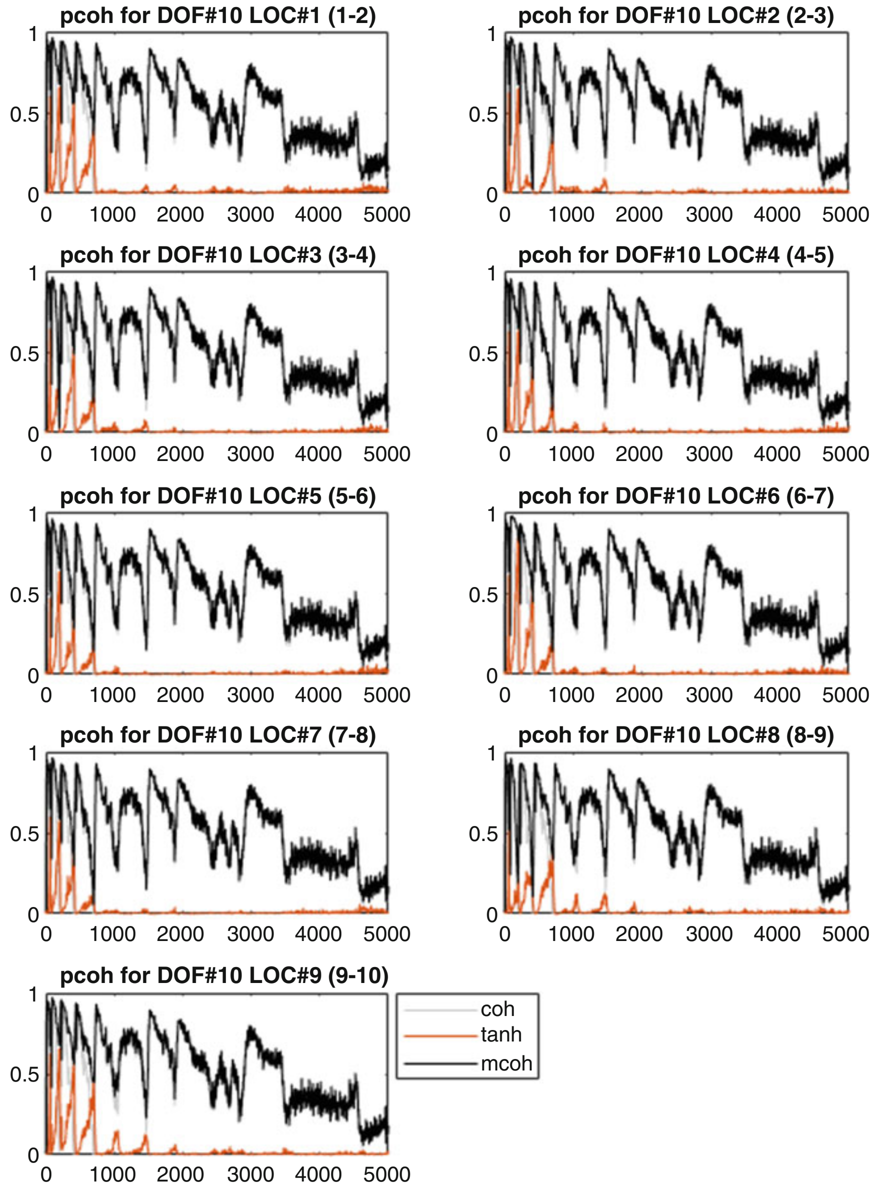

Fig. 1.15 Test4 - LDV

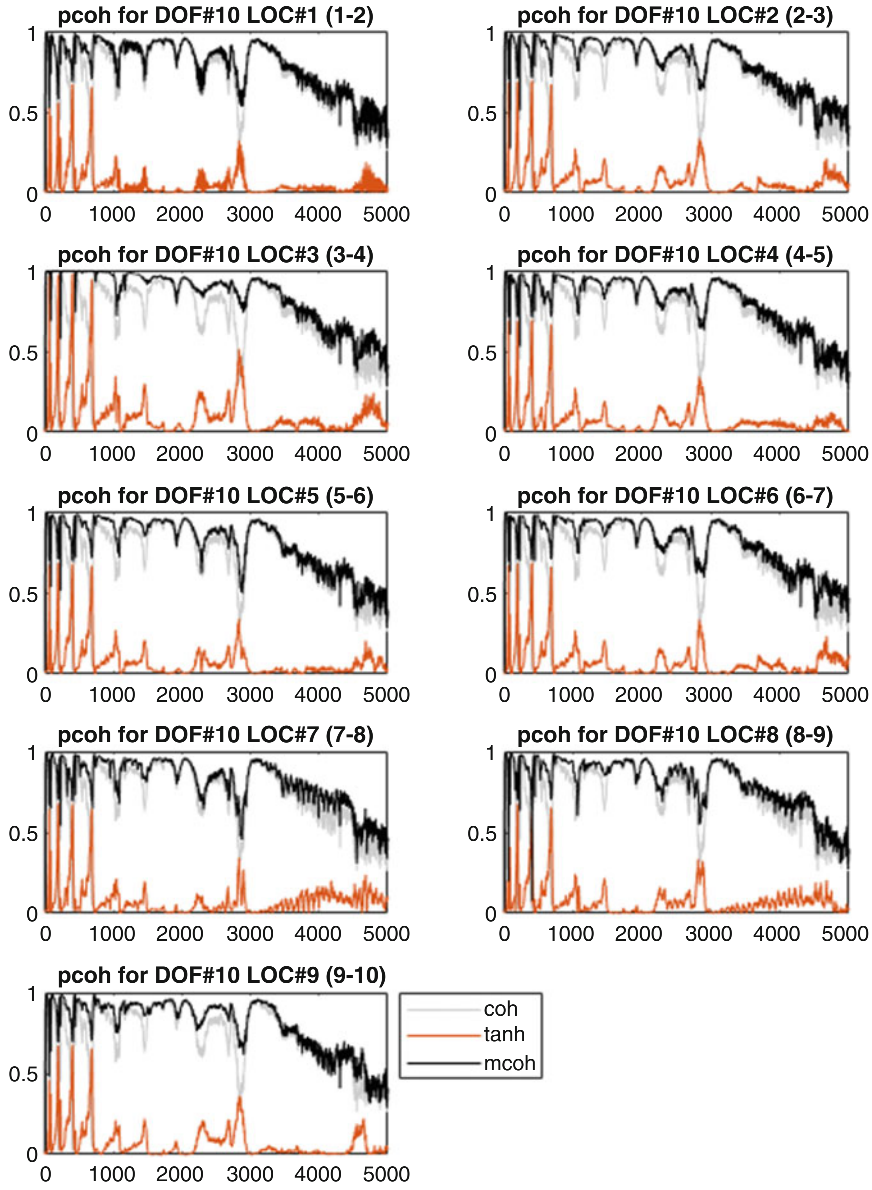

Fig. 1.16 Test5 - LDV

1.6 Conclusions

Random accelerometric data has successfully been used to locate the source of nonlinear effects. The main issue with accelerometers are the highly complex setup procedures, coupled with some inevitable mass loading effects. One of the clear advantages of LDV measurements is the possibility to easily acquire many more points than accelerometers can achieve, without any mass loading drawbacks. Having a finer point-mesh makes the location procedure ideally more accurate, albeit at the cost of much more expensive processing power. However, the biggest drawback of LDV measurements lies in the fact that the points are not excited and acquired all at the same time - unlike with accelerometers – but over the span of several minutes. This means that any settling of the structure, small relaxation in boundary conditions or any time-variant properties of the environment like temperature or exogenous inputs causes the random process to become non-stationary and therefore non-ergodic, resulting in a loss of causality between excitations and responses. All these drawbacks make the application of random LDV measurements for location of nonlinearities yet unsuitable for unexperienced operators and industrial settings but confined to extremely well-equipped laboratory environments with trained personnel.

References

1. delli Carri, A., Weekes, B., Di Maio, D., Ewins, D.J.: Extending modal testing technology for model validation of engineering structures with sparse nonlinearities: a first case study. Mech. Syst. Signal Process. **84**, 97–115 (2017)
2. Di Maio, D., Bozzo, A., Peyret, N.: Response phase mapping of nonlinear joint dynamics using continuous scanning LDV measurement method. In: AIP Conference Proceedings, vol. 1740, (2016)
3. Di Maio, D., Bennett, P., Schwingshackl, C., Ewins, D.: Experimental non-linear modal testing of an aircraft engine casing assembly. In: Kerschen, G., Adams, D., Carrella, A. (eds.) Topics in Nonlinear Dynamics, Volume 1 SE - 2, vol. 35, pp. 15–36. Springer, New York (2013)
4. Di Maio, D., Ramakrishnan, G., Pascalis, S., Rajasagaran, Y., Ghambir, S.: A study on detection of nonlinearity using an aero-engine casing assembly. In: ISMA (2016)
5. Bendat, J.S., Piersol, A.G.: Random Data: Analysis and Measurement Procedures, vol. 729. John Wiley & Sons (2011)
6. Muhamad, P., Sims, N.D., Worden, K.: On the orthogonalised reverse path method for nonlinear system identification. J. Sound Vib. **331**(20), 4488–4503 (2012)
7. Richards, C.M., Singh, R.: Identification of multi-degree-of-freedom non-linear systems under random excitations by the ‘reverse path’ spectral method. J. Sound Vib. **213**(4), 673–708 (1998)
8. Bendat, J.S.: New techniques for nonlinear system analysis and identification from random data. ASA. **102**, 3075 (1997)
9. Ewins, D.J., Weekes, B., Carri, A.D.: Modal testing for model validation of structures with discrete nonlinearities. Philos. Trans. R. Soc. A Math. Phys. Eng. Sci. **373**(2051), 20140410 (2015)

Chapter 2
Single High-Speed Camera Based 3D Deflection Reconstruction in Frequency Domain

Janko Slavič, Domen Gorjup, and Miha Boltežar

Abstract High-speed camera systems are a well-established alternative to traditional vibration measurement techniques, particularly in cases when the region of interest on the observed object is near-planar. With the introduction of 3D digital image correlation some of the traditional limitations of 2D imaging systems are eliminated, but the limited field of view of stereo camera pairs remain problematic in some applications.

In this paper the possibility of extending the use of high-speed camera systems to vibration measurement of arbitrarily shaped structures by applying methods, commonly used in multi-view computer vision is explored. A single high speed camera is used to record the vibrating structure from multiple points of view. By utilizing properties of linear, time-invariant mechanical systems, multi-view triangulation is then performed in frequency domain on displacement data, extracted from these image sequences using optical flow or digital image correlation. The acquired 3D spectra are finally used in full-field deflection reconstruction.

Keywords High-speed camera · Vibration measurement · Frequency domain · Multiview geometry · Optical flow

2.1 Introduction

The use of high-speed cameras in vibration measurement is best suited to near-planar structures due to an inherent limitation of 2D imaging systems. Depth information, lost in the imaging process, can be recovered by using the well-established 3D DIC technique [1]. Its field of view is, however, usually limited to a single face of the object, observed by the stereo pair.

In recent years, various methods have been proposed that extend the use of digital cameras for displacement measurements to objects of arbitrary shapes and dimensions. These methods employ the principles of multiview geometry and triangulation [2] to extract spatial information from simultaneously acquired image sequences of the observed mechanical process [3–5]. Multiple digital cameras used in the measurement process can be arranged in various configurations around [6]. Data acquired by a moving stereo-pair of high-speed cameras can also be used to extend the field of view of 3D DIC in a process called surface stitching [7, 8].

2.2 Measurement Setup

A concave steel object, composed of three 1 mm thick 200 × 200 mm sheet metal planes, bent and welded at one seam (Fig. 2.1) was placed on a LDS V555 electrodynamic shaker and excited with a constant profile of 3 g in the 25 Hz–2000 Hz frequency range. The object was mounted to the shaker in such a way that the excitation force vector formed an equal angle with all of its three planes. Six separate video sequences were acquired using a single Photron Fastcam SA-Z monochrome high-speed camera operating at 20,000 fps and a resolution of 640 × 640 pixels. Each video contained a sequence of 20,000 images for a sampling period of 1 s. The camera was stationary during the measurement process, but the object was rotated by 60 degrees around the vertical axis between each consecutive video acquisition session. The multiview system was calibrated using the Perspective n-point algorithm [2] and a set of markers with known positions on the surface of the observed object.

J. Slavič (✉) · D. Gorjup · M. Boltežar
Faculty of Mechanical Engineering, University of Ljubljana, Ljubljana, Slovenia
e-mail: janko.slavic@fs.uni-lj.si

C. Niezrecki et al. (eds.), *Rotating Machinery, Optical Methods & Scanning LDV Methods, Volume 6*, Conference Proceedings of the Society for Experimental Mechanics Series, https://doi.org/10.1007/978-3-030-12935-4_2

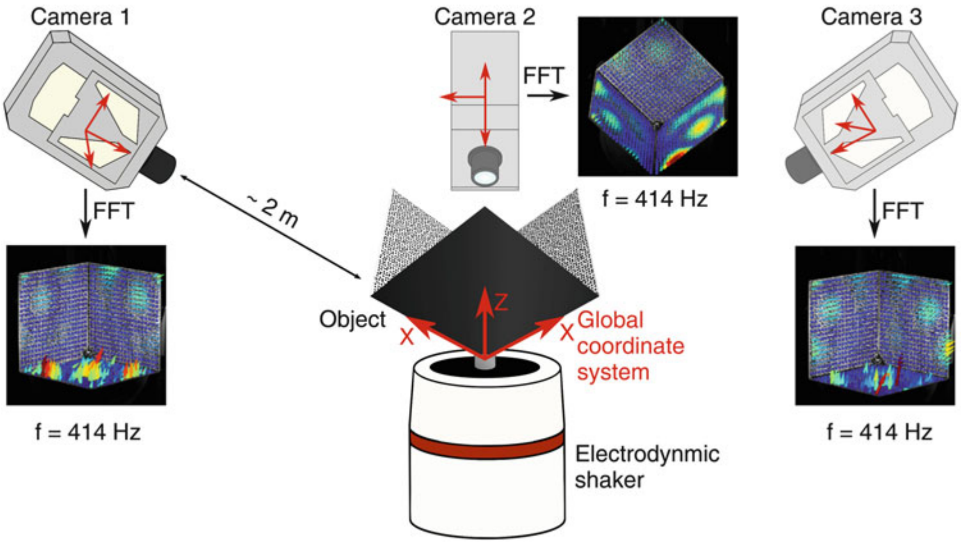

Fig. 2.1 Multiview measurement setup

2.3 Image Based 2D Displacement Measurement

Acquired images were processes by the Simplified gradient-based optical flow method [9] to identify the 2D displacements for each video sequence. The points to be analyzed in each image were selected by projecting a rectangular grid of 30 × 30 points onto each of the three object planes, totaling 2700 points per image. A rectangular region of interest of 11 × 11 pixels with the grid node in the middle was analyzed for each of the selected points.

2.4 Multiview Geometry and Triangulation

Each camera position in a multiview imaging setup (Fig. 2.1) can be defined by a transformation matrix that projects the coordinates of a point $\boldsymbol{X}$ in space into the image plane:

$$\boldsymbol{x} = \mathbf{P}\boldsymbol{X} \tag{2.1}$$

where $\boldsymbol{x}$ denotes the coordinates of a point in an image and $\mathbf{P} = \mathbf{K}[\mathbf{R}|\,\mathbf{t}]$ is a projective transform matrix, composed of a 3×3 matrix of intrinsic camera parameters $\mathbf{K}$, 3×3 rotation matrix $\mathbf{R}$ and a 3×1 translation vector $\mathbf{t}$ [2].

By matching the position of a point in an image $\boldsymbol{x}$ to the position of the same real-world point in another image, $\boldsymbol{x}'$, the 3D position of the original point in a chosen global coordinate frame is triangulated by solving the following system of equations for three unknown coordinates in $\boldsymbol{X}$ [10]:

$$\boldsymbol{x} = \mathbf{P}_1\boldsymbol{X}$$

$$\boldsymbol{x}' = \mathbf{P}_2\boldsymbol{X} \tag{2.2}$$

Each camera view adds another matrix equation to the already overdetermined system of algebraic equations, which was solved in a least-squares sense using singular value decomposition in our case.

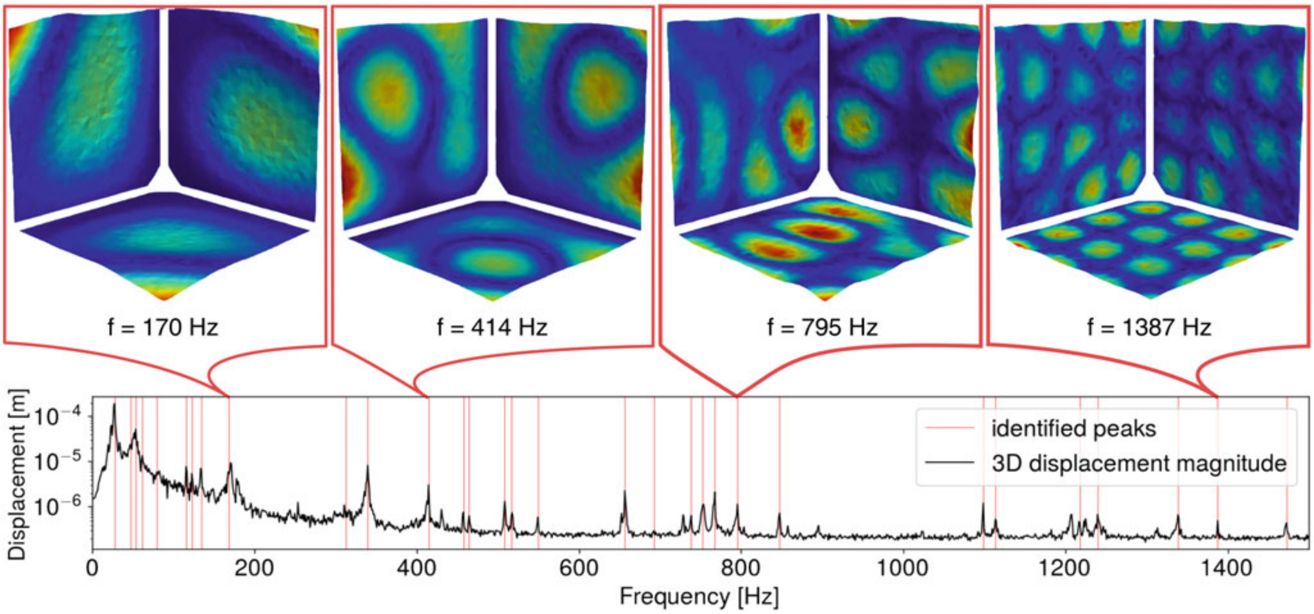

Fig. 2.2 Examples of measured spatial deflection shapes

2.5 Results

The measured displacements were first transformed into frequency domain using Fast Fourier transform (Fig. 2.1). Deflection magnitude peaks were identified in the resulting amplitude spectra (Fig. 2.2). Multiview triangulation was then performed for the deflection shapes at selected frequencies in each of the 6 video sequences, assuming linearity of the observed response. Examples of resulting 3D deflection shapes are visualized in Fig. 2.2. In this experiment, spatial deflection shapes of a vibrating 3D object at frequencies up to 1500 Hz were successfully reconstructed using a single moving high-speed camera.

References

1. Chu, T.C., Ranson, W.F., Sutton, M.A.: Applications of digital-image-correlation techniques to experimental mechanics. Exp. Mech. **25**(3), 232–244 (1985)
2. Hartley, R., Zisserman, A.: Multiple View Geometry in Computer Vision, 2nd edn. Cambridge University Press, New York (2003)
3. Harvent, J., Bugarin, F., Orteu, J.-J., Devy, M., Barbeau, P., Marin, G. Inspection of aeronautics parts for shape defect detection using a multi-camera system. In: Proc. SEM XI Int. Congr. Exp. Appl. Mech. Orlando, FL, USA, pp. 2–5, 2008
4. Orteu, J.-J., Bugarin, F., Harvent, J., Robert, L., Velay, V.: Multiple-camera instrumentation of a single point incremental forming process pilot for shape and 3D displacement measurements: methodology and results. Exp. Mech. **51**(4), 625–639 (2011)
5. Wang, Y., Lava, P., Coppieters, S., Houtte, P.V., Debruyne, D.: Application of a multi-camera stereo DIC set-up to assess strain fields in an Erichsen test: methodology and validation. Strain. **49**(2), 190–198 (2013)
6. Pan, B.: Digital image correlation for surface deformation measurement: historical developments, recent advances and future goals. Meas. Sci. Technol. **29**(8), 82001 (2018)
7. LeBlanc, B., Niezrecki, C., Avitabile, P., Sherwood, J., Chen, J.: Surface stitching of a wind turbine blade using digital image correlation. In: Topics in Modal Analysis II, vol. 6, pp. 277–284. Springer, New York (2012)
8. Patil, K., Baqersad, J., Sheidaei, A.: A multi-view digital image correlation for extracting mode shapes of a tire. In: Shock & Vibration, Aircraft/Aerospace, Energy Harvesting, Acoustics & Optics, vol. 9, pp. 211–217. Springer, Cham (2017)
9. Javh, J., Slavič, J., Boltežar, M.: The subpixel resolution of optical-flow-based modal analysis. Mech. Syst. Signal Process. **88**, 89–99 (2017)
10. Hartley, R.I., Sturm, P.: Triangulation. Comput. Vis. Image Underst. **68**(2), 146–157 (1997)

Chapter 3
Operational Modal Analysis of a Thin-Walled Rocket Nozzle Using Phase-Based Image Processing and Complexity Pursuit

Marc A. Eitner, Benjamin G. Miller, Jayant Sirohi, and Charles E. Tinney

Abstract In this work, the modal parameters of a reduced scale, thin-walled, metallic rocket nozzle are extracted through Operational Modal Analysis (OMA). The specimen is excited using pressurized gas from a rocket nozzle test stand. Deformation of the nozzle lip is measured using a non-contact optical technique consisting of two-dimensional marker tracking in conjunction with phase-based motion amplification. OMA methods that use digital image data suffer from low signal to noise ratios (SNR), especially in higher modes with small amplitude vibrations. The structural displacements are often on a subpixel scale and therefore difficult to analyze without additional image processing. Phase-based motion amplification (PMA) offers a possible solution to this problem by magnifying subpixel motion. This work focuses on the implementation of the technique in a marker-tracking algorithm, which serves to extract the time-history of high-contrast markers placed on a large area ratio nozzle with a 5.3 inch exit diameter. Grayscale images taken with a high-speed camera are first processed with the phase-based algorithm to increase the marker motion in a certain broad frequency band. This results in a set of modified images, which are then analyzed with a tracking algorithm that identifies centroid positions of fluorescent markers. The time-history of these markers is then used as input for an OMA algorithm, namely the Complexity Pursuit algorithm, which leads to estimates of eigenfrequencies, damping ratios and mode shapes. A quantitative comparison between the modal parameters obtained with and without additional motion magnification is provided. Results of a numerical simulation are provided that demonstrate the improvement of estimated modal parameters. The modal parameters of the first six modes of the nozzle are found using this method. The motion was amplified in the range of 0–1400 Hz which includes the six eigenfrequencies. Without application of the broad band PMA, the highest mode cannot clearly be identified and the quality of the other modes decreases.

Keywords Operational modal analysis · Phase based motion estimation · Complexity pursuit · Blind source separation · Optical vibration measurement

3.1 Introduction

This study was motivated by the problem of unsteady side loads in large area-ratio rocket nozzles. Unsteady flow phenomena consisting of oscillating compression shocks occurring in the supersonic part of a converging-diverging rocket nozzle can lead to large pressure fluctuations [1, 2]. The resulting forces acting on the nozzle induce structural deformation and potentially large bending moments acting in the support structure of the nozzle [3]. If the nozzle is sufficiently compliant, the unsteady pressure fluctuations induce vibrations of the nozzle wall which are large enough to be measured using optical techniques [4]. In this study, a metallic large area-ratio nozzle with a thin wall (0.03 inches) was excited by these unsteady flow phenomena. The vibration of the structure was captured using a digital camera in combination with 2-dimensional point tracking.

In theory, knowledge of the displacement history of discrete points of the nozzle in combination with an adequate reduced order model of the nozzle, should allow reconstruction of the aerodynamic forces. The solution of such an inverse problem depends on the order and quality of the model. For the construction of such a model, knowledge of the modal parameters (eigenfrequencies, damping ratios, mode shapes) is crucial.

The quality of the modal parameters extracted from experimental data depends, among other things, on the algorithm used and on the signal to noise ratio (SNR) in the data. In this study the Complexity Pursuit (CP) algorithm [5] was used to

---

M. A. Eitner (✉) · B. G. Miller · J. Sirohi
The University of Texas at Austin, Department of Aerospace Engineering and Engineering Mechanics, Austin, TX, USA
e-mail: marceitner@utexas.edu

C. E. Tinney
The University of Texas at Austin, Applied Research Laboratories, Austin, TX, USA

C. Niezrecki et al. (eds.), *Rotating Machinery, Optical Methods & Scanning LDV Methods, Volume 6*, Conference Proceedings of the Society for Experimental Mechanics Series, https://doi.org/10.1007/978-3-030-12935-4_3

estimate modal parameters from output only (camera images) data. The goal of this process is to find as many vibrational modes as possible. Finding accurate modal parameters becomes more and more difficult as the eigenfrequency increases. This is generally due to the reduction in SNR, meaning that for higher modes, the low amplitude and high frequency oscillations of the test specimen eventually fall below the level of noise present in any given measurement. Therefore it is necessary to utilize signal processing techniques to increase the SNR of the higher modes. A potentially promising algorithm that preprocesses the set of high-speed images is the Phase-based Motion Amplification algorithm (PMA).

PMA, or motion microscope was developed by Wadhwa et al. [6]. This image processing technique utilizes complex-steerable pyramids to decompose, filter and reconstruct a set of images in order to amplify motion in a certain frequency range. Since this algorithm is fairly new, few studies have been published on its application to structural dynamics and modal parameter identification. Poozesh et al. [7] demonstrated experimentally that by amplifying the motion in the frequency range of a noisy mode, the SNR of that mode can be significantly improved. Using OMA and comparing modal parameters before and after motion amplification it was shown that a clear improvement could be observed in terms of the modal assurance criterion (MAC). In this paper, motion is amplified in a broad frequency range that includes all known eigenfrequencies. The earlier work of Yang et al. [8] used PMA in combination with Complexity Pursuit to extract and visualize full-field mode shapes of a scaled multi-story building. PMA was used after the CP algorithm, like a post-processing step. This is significantly different from the approach in this study, where PMA is used in a preprocessing step.

The current study uses PMA as a preprocessing step to increase the SNR of images from high-speed video from vibration tests. The images contain several discrete markers that are painted on the surface of a structure. Using PMA, the motion of the markers is amplified within a certain broad frequency band. The images are then analyzed by a two-dimensional point tracking (2DPT) algorithm that extracts the marker positions in each image frame, which results in the displacement history of each marker. These amplified displacements are used to estimate the modal parameters of the structure using the CP algorithm. By also estimating the modal parameters of the unprocessed images directly, the effect of motion amplification can be quantified.

This paper is structured in the following way. The first section covers a summary of the algorithms and methods used in this study. The 2DPT, PMA, and CP algorithms are briefly described. The entire process is summarized and outlined. In the second part of this paper, two experiments were performed. First, the vibration of an eight degree of freedom system (8DOF) was simulated in a numerical study. Images showing oscillating markers were artificially created and processed using PMA, 2DPT, and CP to obtain estimates of the system's modal parameters. Since the true modal parameters were known, a detailed error analysis was performed. Then, in a laboratory experiment, vibration tests were performed on a large area-ratio nozzle with a 5 inch exit diameter. Actual images from high-speed video taken of the vibrating nozzle were used to obtain the nozzle's modal parameters. As in the numerical experiment, the modal parameters are estimated from the original images as well as from the motion amplified images. The last chapter contains the discussion and evaluation of the test results.

3.2 Methods

The broad-band PMA methodology for modal parameter estimation described in this paper is based on a two-dimensional point tracking method, the Phase-based Motion Amplification algorithm, and the Complexity Pursuit algorithm. These three methods are outlined in this section.

3.2.1 2-Dimensional Point Tracking (2DPT)

When performing vibration measurements, the goal is to obtain the displacement history of discrete points on the structure. A common way of doing this is to use accelerometers. Attaching these to the surface of a structure allows the measurement of acceleration at these points, which can then be numerically integrated to obtain the displacement history. Numerical errors such as drift and errors resulting from the added mass of the sensor are disadvantages of this method. By using cameras to detect the vibration of the structure, non-contact measurements can be performed. The 2DPT method consist of painting a number of discrete markers on the surface of a structure and tracking their locations using a high-speed camera and an image processing algorithm. The markers are painted on the structure using fluorescent paint. High contrast between the markers and the surface of the structure is obtained. A marker tracking algorithm then detects the position of each marker in each camera image. The algorithm used in this paper first converts each greyscale camera image into a binary image (pixels either pure black or pure white) based on a user-defined pixel intensity threshold. The algorithm then looks for accumulations of

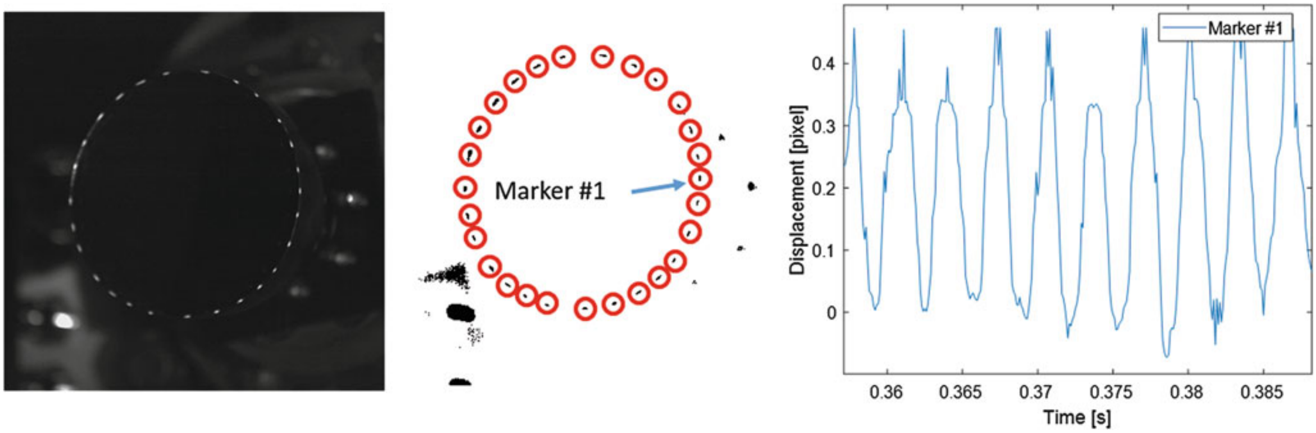

Fig. 3.1 Outline of point tracking method. Grayscale image taken with high-speed camera (left); identified markers (center); displacement history of centroid of single marker (right)

high intensity pixels to find all pixels that make up a marker. In a final step, the centroid of each marker is calculated. This is done by weighing the location of each pixel that is part of the marker with the pixel intensity and then dividing by the number of pixels in the marker. This process is performed independently for each image, leading to the displacement history of all markers throughout the entire measurement. An example of this process is shown in Fig. 3.1, where the position of markers on the lip of a nozzle are extracted from grayscale test images.

3.2.2 *Phase-Based Motion Amplification (PMA)*

The original PMA algorithm by Wadhwa et al. [6] reads an input video, amplifies motions in a certain frequency band, and outputs a reconstructed video. Motions are processed by first breaking the video into a set of images, and then breaking each image into constitutive layers through spatial filtering.

Spatial filtering is performed through the Complex Steerable Pyramid Decomposition (CSPD) process developed by Simoncelli et al. [9, 10]. In CSPD, a 2D transfer function library is constructed using a set of Gabor filters. These are linear filters that have a direction, position, and frequency. Convolving an image by this library decomposes the original image into several layers or levels containing filtered images differing in spatial resolution. Summing these back together results in the reconstructed image, whereby lower-ordered levels of the decomposition (containing low-resolution decompositions) contribute more to the overall behavior – a structure similar to a Taylor expansion. The total number of levels is dictated by the image size and number of filter orientations.

Localized phase changes in CSPD are proportionally related to displacements through Fourier transformation [6]. The local motion in an image can therefore be computed by subtracting the phase angles of each frame from the phase angles of the first frame. A band-pass filter is then applied to these motions and they are multiplied by an amplification factor ($\alpha + 1$). When the pyramid is ‘collapsed’, meaning the decomposition into different layers is reversed, a reconstructed video is obtained that contains the amplified motion.

3.2.3 *Modal Parameter Estimation Using Complexity Pursuit*

The Blind Source Separation algorithm called Complexity Pursuit (CP) is used to extract modal parameters from the displacement history of the markers, identified by the previously described 2DPT algorithm. CP was proposed by Stone [5] and uses a temporal predictability function that acts as a measure of complexity of an observed signal. Stone’s theorem states that source signals making up any measured signal have higher predictability than the measured signal itself. The algorithm assumes that measured observations are made up of a linear mixture of source signals according to:

$$\overrightarrow{x} = [A]\,\overrightarrow{s} \tag{3.1}$$

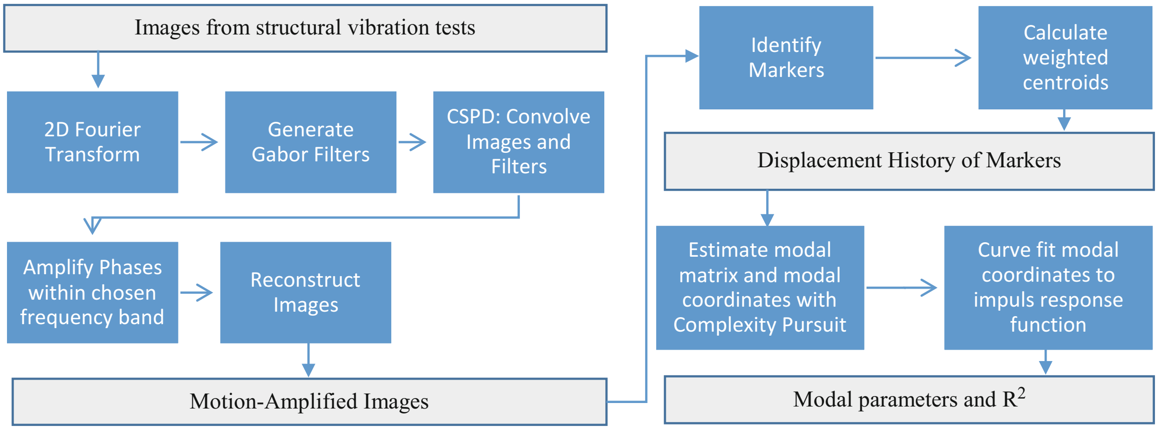

Fig. 3.2 Outline of the modal parameter identification process

Here $[A]$ is the $N \times N$ mixing matrix, $\overrightarrow{s}$ is the $N \times 1$ vector of source signals with maximum predictability and $\overrightarrow{x}$ is the $N \times 1$ vector of measurements. The CP algorithm estimates the mixing matrix in such a way that the resulting source signals exhibit maximum temporal predictability. When applied to structural dynamics the matrix $[A]$ is the modal matrix containing the mode shapes, $\overrightarrow{x}$ is the vector of instantaneous displacement measurements at N locations and $\overrightarrow{s}$ is the vector of modal coordinates. If the structure was excited with an impulsive force, the extracted modal coordinates will be impulse response functions of damped single degree of freedom oscillators. The modal coordinates are therefore fit to an impulse response function of the form

$$s_i = Ce^{-\zeta 2\pi f_i t} \sin\left(2\pi f_i \sqrt{1-\zeta_i^2}\, t - \phi\right), \qquad (3.2)$$

where f_i and ζ_i are the eigenfrequency and damping ratio of the i^{th} mode respectively and C and ϕ are constants. The curve fit results in values for the eigenfrequency and damping ratio associated with that mode. If the system was excited with random force the response of the modal coordinates will also be random. Computing their autocorrelation function recovers the impulse response function [11] and the modal parameters can be estimated once again via curve fitting. Using a goodness of fit value (e.g. R^2) gives an indication of the quality of the separated modal coordinates.

A summary of the entire process is shown in Fig. 3.2.

3.3 Experiments

Two sets of experiments were performed to test and quantify the effect of PMA on modal parameter estimation. First the structural vibration of an 8DOF system was numerically simulated. Images of markers placed on the simulated system were artificially generated, as if they had been taken during a real vibration test. These images were used in conjunction with PMA, 2DPT and CP to obtain estimates of the system's modal parameters. Since the true modal parameters of the simulated system were known, errors in modal parameters could be computed.

Next, two vibration tests of a small, thin-walled, large area-ratio nozzle were performed. The nozzle was attached to a test rig and excited by pressurized air from a plenum. The induced vibration was captured using a high-speed camera. The test was performed twice, once with the camera placed close to the nozzle and once with the camera placed further away to decrease the SNR. The resulting images were then used to estimate the modal parameters of the nozzle, using the previously discussed process of PMA, 2DPT and CP.

3.3.1 Numerical Simulation

A simulation was performed to compare the modal parameters estimated from motion amplified images to true values, thus allowing detailed error analysis. The simulated structure consisted of four point masses arranged in a square connected to

Table 3.1 Modal parameters of simulated system

Mode	Eigenfrequency f [Hz]	Damping ratio ζ	Mode shape Φ
1	5	0.005	$(1\ 1\ -1\ 1\ -1\ -1\ 1\ -1)^{\mathrm{T}}$
2	7	0.005	$(1\ 1\ 1\ -1\ -1\ -1\ -1\ 1)^{\mathrm{T}}$
3	10	0.005	$(1\ 1\ 1\ 1\ 1\ 1\ 1\ 1)^{\mathrm{T}}$
4	15	0.005	$(-1\ 1\ -1\ 1\ -1\ 1\ -1\ 1)^{\mathrm{T}}$

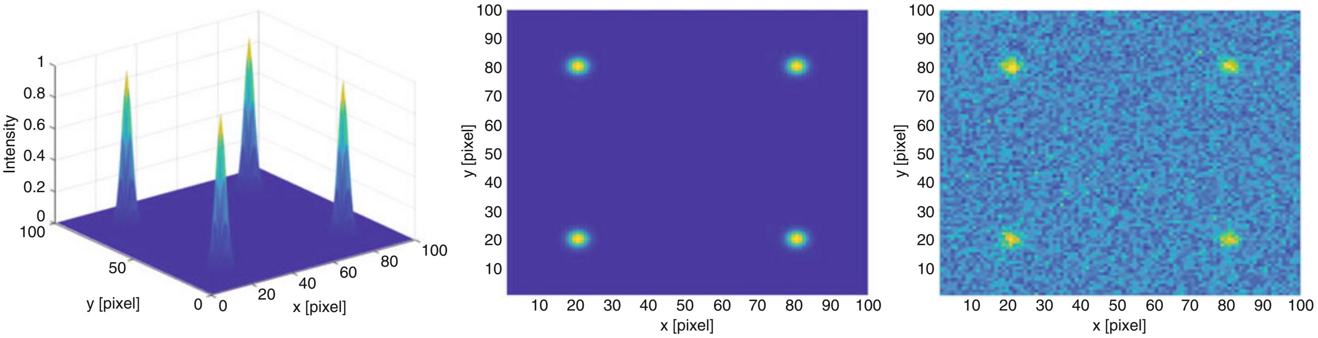

Fig. 3.3 Images with oscillating markers; (left) Gaussian distribution; (center) top view; (right) with added noise

linear springs. Since each mass was allowed to move in the $x - y$ plane, the system had eight degrees of freedom. The modal parameters of the system's first four modes are listed in Table 3.1.

The structural response of the system to an initial excitation was generated by superimposing the first four modal coordinates of the system according to the linear relation

$$\overrightarrow{x} = [\Phi]\overrightarrow{s} \tag{3.3}$$

Here $[\Phi]$ is the 8×4 modal matrix, $\overrightarrow{x}$ is the $8 \times N$ displacement vector and $\overrightarrow{s}$ is the $4 \times N$ vector of modal coordinates with

$$s_i = A_i e^{-\zeta 2\pi f_i t} \sin\left(2\pi f_i \sqrt{1 - \zeta_i^2 t}\right);\ i = 1, \ldots, 4 \tag{3.4}$$

The amplitudes of the motion in each mode was adjusted so that the low frequency modes exhibited larger movement. The amplitudes were set to $A = (0.2, 0.15, 0.1, 0.05)$ pixels respectively. In real vibration tests, high contrast markers are painted on the structure and their oscillation is captured with a high-speed camera. In order to simulate this, a set of images was artificially created showing the planar motion of the structure. The painted markers of a real test are simulated using two-dimensional Gaussian distributions centered at the position of the point masses. The Gaussian distribution for each marker had a standard deviation of two pixels and a maximum pixel intensity of one. The images had a size of 100×100 pixels. The simulated images are shown in Fig. 3.3. Random noise of varying intensity was added to the generated images to closer resemble real images from experimental measurements.

A series of $N = 5000$ images was created with a sampling frequency of $f_s = 100\ Hz$. The previously described marker tracking algorithm was then used to extract the position of each marker from the generated images. Limitations of the algorithm resulted in low errors, even in the case of no noise. An average centroid position error lower than 0.001 pixels and a maximum error of less than 0.08 pixels remained in the centroid motion extracted from noise-free images. The marker positions were extracted for each image separately, resulting in the displacement history of all markers. These displacements were then used as input for the CP algorithm to yield estimates of the modal parameters. The motion of the markers was then amplified and the process was repeated, leading to a second set of modal parameters. Comparison of these two sets with the true known values allowed quantification of the effect of PMA on the modal parameter estimation. The process was performed for different amplification factors as well as for different amplified frequency bands. The results are discussed in the last section of this paper.

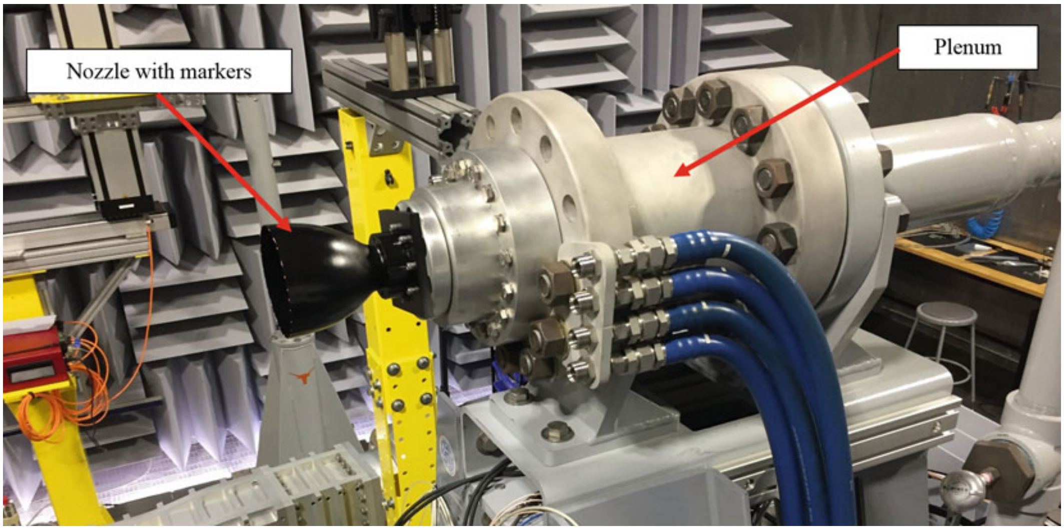

Fig. 3.4 Illustration of the setup at the Applied Research Laboratories at Austin used to measure aerodynamically induced nozzle vibration. Diameter of the nozzle exit is 5.3 inches

3.3.2 Nozzle Experiment

An experiment was performed to test how well the PMA preprocessing method works when applied to real high-speed video images taken of an oscillating structure. A reduced scale, metallic, large area-ratio nozzle was used as the test specimen. The nozzle diameter was 2 inches at the throat and 5.3 inches at the exit. Its wall thickness was constant at 0.03 inches. The nozzle was attached to a test rig, which was connected to a pressure controlled plenum containing unheated air. A description of this facility is provided in References [2, 12]. By increasing the pressure in the plenum the flow conditions in the nozzle could be modified. While the exact flow phenomena in the nozzle were unknown, the pressure in the plenum (before entering the nozzle) was large enough to ensure that a supersonic flow had formed just downstream of the nozzle throat. Given the large area-ratio of the nozzle, an unsteady separation shock formed in the diverging part of the nozzle. This unsteady flow resulted in pressure oscillations on the inside of the nozzle and acted as a random force on the structure. The induced vibration of the nozzle was measured using 2DPT. For this purpose, a number of markers were painted on the lip of the nozzle with fluorescent paint. A high speed camera[1] took greyscale images of the nozzle at a frame rate of 10 kHz. Each image consisted of 1098 × 1512 pixels, with a spatial resolution of 0.2 mm/pixel. The camera was placed at a slight angle to the centerline of the nozzle, to avoid potential damage to the camera from the nozzle jet. Fig. 3.4 shows the nozzle attached to the test rig.

The images taken with the high-speed camera exhibited sufficient contrast between the markers and the nozzle so that each marker could be clearly identified. Using the same 2DPT technique as in the numerical study, the centroid motion of each marker on the nozzle lip was identified; see Fig. 3.1. The camera was then placed further away from the nozzle and the test was repeated, yielding a second set of measurements. This was done to lower the pixel resolution in the acquired images (to 0.4 mm/pixel), leading to lower SNR of the marker displacements. The displacement history of all markers was used as input for the Complexity Pursuit algorithm to determine the modal parameters of the nozzle.

3.4 Results and Discussion

3.4.1 Results of the Numerical Study

For the evaluation of the results a set of scalar errors is first defined in Eq. 3.5. Eigenfrequency error e_f and damping error e_ζ are averages of the relative errors in extracted eigenfrequency and damping ratio respectively. The motion error e_m is simply the Euclidian norm of the absolute error in centroid motion. The mode shape error e_Φ computes the Frobenius norm

---

[1] i-SPEED 726 monochromatic camera manufactured by ix Cameras™.

of the error in the modal assurance criterion (MAC). The reference values ζ_i and f_i for the damping and eigenfrequency errors are listed in Table 3.1. The reference value $MAC(\Phi_{CP})$ is a 4 × 4 unit matrix and the reference motion $\overrightarrow{x}_i$ is defined by Eq. 3.1.

$$\begin{gathered}
e_\zeta = \sum\nolimits_{i=1}^{4} \frac{\left|\zeta_i - \zeta_{i,CP}\right|}{\zeta_i} \\
e_f = \sum\nolimits_{i=1}^{4} \frac{\left|f_i - f_{i,CP}\right|}{f_i} \\
\mathrm{e_m} = \left|\,\left|\overrightarrow{\mathrm{x}}_{\mathrm{PT}}\left(\mathrm{t_i}\right) - \overrightarrow{\mathrm{x}}\left(\mathrm{t_i}\right)\right|\,\right| \\
e_\Phi = \left|\,\left|MAC\left(\Phi\right) - MAC\left(\Phi_{CP}\right)\right|\,\right|
\end{gathered} \tag{3.5}$$

The magnification factor α defines the amount of motion magnification in the reconstructed video. The factor cannot be arbitrarily large because the cluster of high intensity pixels that make up the markers becomes distorted at higher values of α. An optimal value is therefore sought. First the level of image noise was kept constant (random white noise with standard deviation of 0.17) as well as the amplified frequency band, which was set at 3–20 Hz to include all eigenfrequencies. The motion was amplified with amplification factors of $\alpha = 0, 1, 2, 3, 4, 5, 6, 7$ and the 2DPT algorithm extracted the motion of the centroids. The modal parameters estimated from the centroid motion were compared to the true values (listed in Table 3.1) and errors were computed. All runs were repeated 20 times and the errors were averaged. The results are shown in Table 3.2.

The main result is that the errors of the modal parameters (column 2, 3 and 4 in Table 3.2) are all lower than those computed from the unprocessed images (highlighted row in Table 3.2). This is true for all investigated values of the magnification factor. However, it does not seem to matter what the value of the magnification factor is. No clear relation between α and the modal parameter errors could be observed. Interestingly, even when using PMA without any actual amplification ($\alpha = 0$), the modal parameter estimation improves. The pure application of the spatial decomposition and reconstruction of the images already suffices to reduce the modal parameter errors significantly. This is also true for the error in the extracted marker motion e_m. Further increase of α decreases the motion error even more, without affecting the modal parameter estimates significantly.

Next, the effect of the choice of amplified frequency spectrum was investigated. Modal parameters were estimated from images in which motion was amplified in different frequency bands. The noise level was kept constant and the frequency spectrum to be amplified was chosen arbitrarily. The images were first processed using PMA with an amplification factor of $\alpha = 1$, then the centroid motion was extracted and finally the modal parameters were estimated. All runs were performed 20 times and the resulting errors were averaged; Table 3.3 shows the results. Amplifying the bandwidth 3–20 Hz lead to the

Table 3.2 Effect of magnification factor on modal parameters

Magnification factor α	Mode shape error e_Φ	Frequency error e_f[*100]	Damping error e_ξ[*100]	Motion error e_m
Unprocessed	0.596	0.182	27.058	142.766
0	0.354	0.087	16.877	118.775
1	0.418	0.084	12.873	81.911
3	0.393	0.127	15.650	71.130
5	0.347	0.092	18.387	70.662
7	0.433	0.095	20.691	69.952

Table 3.3 Effect of amplified bandwidth on modal parameter estimation

Amplified frequency bandwidth [Hz]	Mode shape error e_Φ	Frequency error e_f [*100]	Damping error e_ξ [*100]	Motion error e_m
1–49	0.443	0.084	17.485	87.683
1–30	0.4912	0.091	19.256	84.343
3–20	0.418	0.084	12.873	81.911
8–20	0.497	0.088	18.403	65.364
4–16	0.444	0.098	20.657	81.109

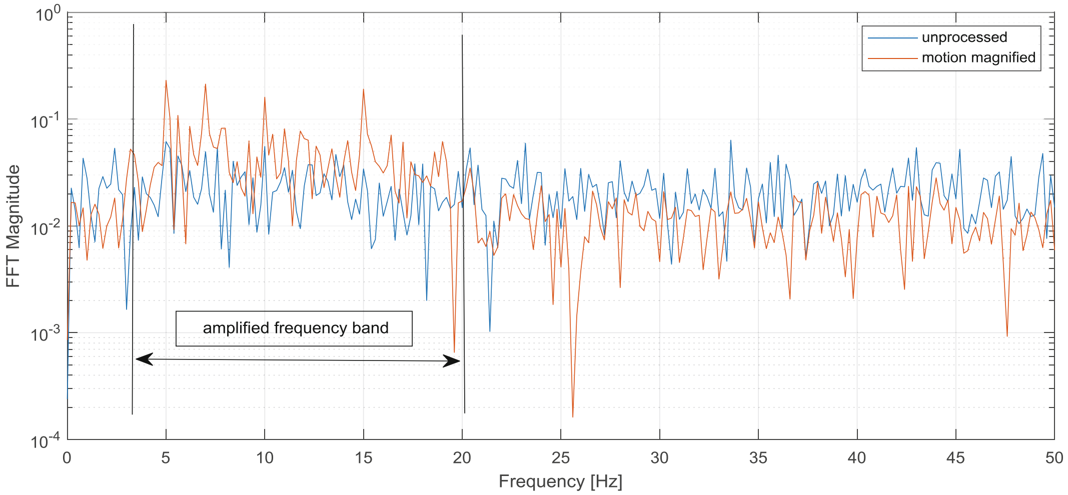

Fig. 3.5 Frequency spectrum of single marker from numerical study. All four peaks corresponding to eigenfrequencies become clearly visible if PMA is used

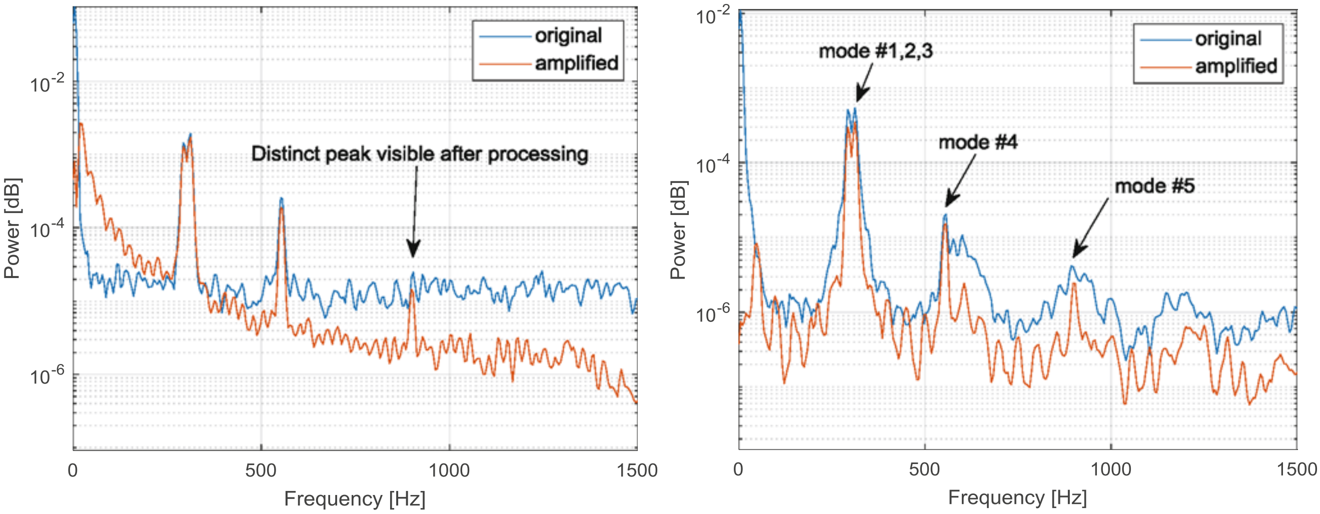

Fig. 3.6 Power spectrum of single marker; (left) first test with close-up camera position; (right) second test with distant camera position. In the first test the frequency band 0–1400 Hz was amplified in the second the amplified frequency band was 250–1400 Hz

lowest errors for the modal parameters (note that the actual eigenfrequencies were in the range of 5–15 Hz). This includes the eigenfrequencies of interest plus an additional buffer of 30% relative to the highest and lowest eigenfrequency.

A plot of the frequency spectrum for a single marker before and after motion amplification is shown in Fig. 3.5.

The four distinct peaks visible in the processed data correspond to the eigenfrequencies. The appearance of the four peaks in the plot indicates an improvement of the SNR in the amplified frequency band, resulting in less erroneous modal parameters

3.4.2 *Results of the Nozzle Experiment*

The high-speed video images from both experiments (close camera position in test #1 and distant camera position in test #2) were analyzed. For each set of images the modal parameters were computed before and after applying motion amplification. Fig. 3.6 shows the power spectra of a single marker before and after PMA for both tests. Differences in camera orientation, pixel resolution as well as in the aerodynamic excitation are reasons for the notable differences in the original power spectra, shown in blue. Low frequency motion of the markers (<20 Hz) is most likely associated with oscillations of the camera

Table 3.4 Modal parameters extracted with Complexity Pursuit algorithm from nozzle test #1 with close-up camera placement

	Frequency [Hz]		Damping ratio [×100]		Goodness of fit R^2 [×100]	
Mode	Original	Amplified	Original	Amplified	Original	Amplified
1	294.3	294.3	0.43	0.40	99.6	99.7
2	311.7	310.9	0.80	0.34	83.6	99.0
3	316.4	315.8	0.45	0.20	84.9	98.9
4	553.5	553.6	0.26	0.15	91.2	98.6
5	901.2	901.4	0.18	0.19	93.5	94.6
6	1314	1314	0.17	0.13	24.9	75.9

Modal parameters extracted before and after motion magnification ($\alpha = 3$, band-pass filter 0–1400 Hz)

induced by the nozzle exhaust and therefore left out of the following analysis. The orange curves show the power spectra extracted from the motion amplified images with $\alpha = 3$. In both tests motion amplification seems to induce a significant change in the frequency band around the fifth mode (around 900 Hz). The peak, indicating an eigenfrequency is much more distinct in the processed (motion amplified) data. There seems to be little change in the peaks of the lower modes.

The modal parameters extracted from the original and motion amplified images taken during the first test, where the camera was close to the nozzle, are shown in Table 3.4. The extracted eigenfrequencies vary less than 0.3% before and after motion amplification. The differences in the extracted damping ratios is larger, with a maximum difference of 58%. In the final step of the modal parameter identification process the separated source signals (corresponding to the modal coordinates) were fit to an impulse response function. For ideal operating conditions (white noise excitation, very long measurement time) this curve fit should be exact for correctly separated source signals. The goodness of fit value R^2 is used as an indicator of how well the extracted source signals (modal coordinates) fit the theoretical impulse response function. For a perfect fit the value becomes $R^2 = 1$. Comparison of the R^2 values before and after motion amplification shows a clear improvement of the curve fits when using the motion magnified images. The average value for the original data set is $R^2_{average} = 0.80$ while the average value for the motion magnified images is$R^2_{average} = 0.94$. This clearly indicates that the source separation procedure of the CP algorithm is improved when using the motion magnified image set. Test with different amplified frequency bands revealed no additional modes beyond the sixth mode.

The estimated modal parameters from the second test, where the camera was placed further away from the nozzle exhibit similar trends. As in the previous test, application of the motion amplification process leads to an overall improvement of the R^2 values. The average increases from $R^2_{average} = 0.85$ for the original data to $R^2_{average} = 0.96$ for the motion amplified data. Relative changes in estimated eigenfrequencies were below 0.5% and the damping ratios changed by less than 55%.

A Finite Element (FE) model of the nozzle was constructed in ANSYS. It was used to calculate eigenfrequencies and mode shapes which were used to evaluate the quality of the experimental results. Using the original and motion amplified images from the experiments, mode shapes were estimated as part of the modal parameter estimation process (see Fig. 3.2). The three sets of mode shapes (from original images, motion amplified images, FE model) were compared visually. It was found that for the first three modes, all sets of mode shapes matched each other and no differences were noticeable. For the fourth and fifth mode, considerable differences appeared. In Fig. 3.7 the mode shapes for those two modes are displayed, as computed from the images (original and motion amplified) of the second nozzle test and the FE model. For the fourth mode, the mode shapes of the amplified images matches the FE results better than the mode shape estimated from the original images. This improvement coincides with improvement in the curve fitting process of the modal coordinates, where the R^2 value was increased from 90.3 to 97.8. For the fifth mode the improvement in the mode shape is less prominent, yet noticeable. The quality of the mode shapes of the fifth mode seems lower than that of the fourth mode, which is due to a decrease in SNR with increasing frequency.

3.5 Conclusion

Broad-band Phase-based Motion Amplification was used to increase the SNR of images capturing oscillating structures. Two sets of experiments were performed including simulation and laboratory test. In a numerical study, noisy images were simulated showing four oscillating markers. Using 2DPT, the displacement history of the markers could be extracted. Modal parameters were estimated with the Complexity Pursuit algorithm using the displacement data only. Then the images were processed using PMA and the displacement history was computed again. Analysis of the power spectra clearly showed an improvement in SNR in the frequencies near the natural modes. This resulted in the peaks becoming more prominent

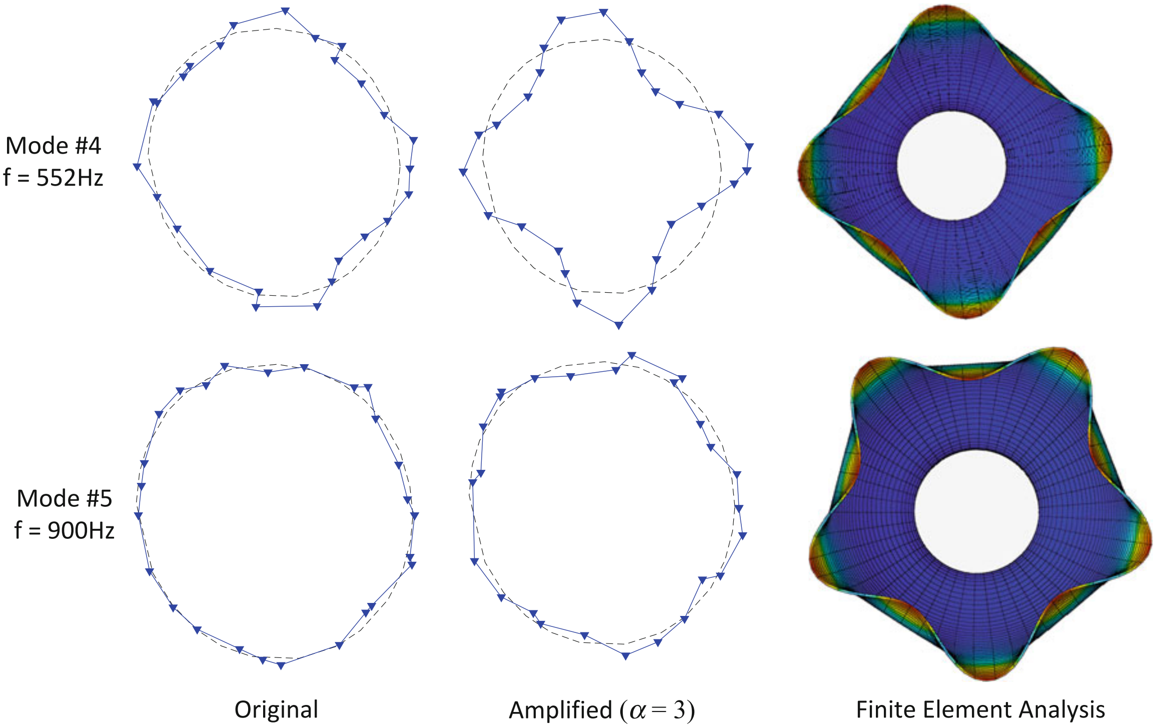

Fig. 3.7 Comparison of mode shapes estimated from original images (left), motion amplified images (center) and FE model (right). Mode shapes are shown from the top (downstream) looking into the nozzle

in the power spectrum plot. The value of magnification used in the PMA algorithm seems to have little influence on the extracted modal parameters. Comparison of bandwidths for motion amplification showed that optimal modal parameters were estimated when the frequency band included only the eigenfrequencies under investigation and no additional lower or upper 'buffer'. In two sets of tests performed on a reduced scale large area-ratio rocket nozzle, the method was applied to a real structure. Modal parameters were computed from high-speed video images with and without motion amplification. A goodness of fit value from the modal parameter estimation process was used as an indication of the quality of the modal parameters. A clear improvement was demonstrated when using the high-speed images processed with PMA. Small changes in the eigenfrequencies were noticeable but were limited to below 0.5%. Relative changes in the estimated damping ratios were larger, limited to 58%. As in the numerical simulation, the peaks in the frequency spectrum became more prominent when using PMA, especially those corresponding to higher modes. A comparison of the mode shapes to those obtained from an FE simulation showed that the motion amplification process increases the quality of the estimated mode shapes for higher modes.

The method of using broad-band PMA as a preprocessing step for noisy images of vibrating structures has been validated in this paper. By using a broad frequency band containing all eigenfrequencies of interest in the PMA algorithm, all modal parameters can be extracted from the same motion amplified set of images.

Acknowledgements The authors would like to thank Mr. John Valdez of the Applied Research Laboratories of The University of Texas at Austin for assisting with the experimental measurements.

References

1. Baars, W.J., Tinney, C.E., Ruf, J.H., Brown, A.M., McDaniels, D.M.: Wall pressure unsteadiness and side loads in overexpanded rocket nozzles. AIAA J. **50**(1), 61–73 (2012)
2. Baars, W.J., Tinney, C.E., Ruf, J.H.: Non-stationary shock motion unsteadiness in an axisymmetric geometry with pressure gradient. Exp. Fluids. **56**(92), 1–18 (2015)
3. Blades, E.L., Luke, E.A., Ruf, J.: Fully coupled fluid-structure interaction simulation of rocket engine side loads. 48th AIAA/ASME/SAE/ASEE Joint Propulsion Conference & Exhibit, AIAA Paper 2012–3969, Atlanta, Georgia, 30July–1 Aug 2012

4. Tinney, C.E., Scott, K., Routen, M., Sirohi, J., Ruf, J.: Effect of aeroelasticity on vibroacoustic loads during startup of large area ratio nozzles. 23rd AIAA/CEAS Aeroacoustics Conference, AIAA Paper 2017-3361, Denver, Colorado, 5–9 June 2017
5. Stone, J.V.: Blind source separation using temporal predictability. Neural Comput. **13**(7), 1559–1574 (2001)
6. Wadhwa, N., Rubenstein, M., Fredo, D., Freeman, W.T.: Phase-based video motion processing. ACM Trans. Graph. **32**(4), 80:1–80:10 (2013)
7. Poozesh, P., Sarrafi, A., Mao, Z., Avitabile, P., Niezrecki, C.: Feasibility of extracting operating shapes using phase-based motion magnification technique and stereo-photogrammetry. J. Sound Vib. **407**, 350–366 (2017)
8. Yang, Y., Dorn, C., Mancini, T., Talken, Z., Kenyon, G., Farrar, C., Mascarenas, D.: Blind identification of full-field vibration modes from video measurements with phase-based video motion magnification. Mech. Syst. Signal Process. **85**, 567–590 (2017)
9. Simoncelli, E.P., Freeman, W.T.: The steerable pyramid: a flexible architecture for multi-scale derivative computation. In: Proceedings of the 1995 International Conference on Image Processing, Washington, DC, 23–26 Oct 1995
10. Simoncelli, E.P., Freeman, W.T., Adelson, E.H., Heeger, D.J.: Shiftable multi-scale transforms. IEEE Trans. Inf. Theory. **38**(2), 587–607 (1992)
11. Meirovitch, L.: Fundamentals of Vibration. McGraw-Hill, New York (2001)
12. Valdez, J.A., Tinney, C.E.: Measurements of a Mach 3 jet using high-speed optical flow techniques. AIAA/CEAS Aeroacoustics Conference, AIAA Paper 2018-3148, Atlanta, Georgia, 25–29 June 2018

Chapter 4
Full-Field Strain Shape Estimation from 3D SLDV

Bryan Witt, Dan Rohe, and Tyler Schoenherr

Abstract The ability to measure full-field strains is desirable for analytical model validation or characterization of test articles for which there is no model. Of further interest is the ability to determine if a given environmental test's boundary conditions are suitable to replicate the strain fields the test article undergoes in service. In this work, full-field strain shapes are estimated using a 3D scanning laser Doppler vibrometer and several post-processing methods. The processing methods are categorized in two groups: direct or transformation. Direct methods compute strain fields with only spatial filtering applied to the measurements. Transformation methods utilize SEREP shape expansion/smoothing of the measurements in conjunction with a finite element model. Both methods are used with mode shapes as well as operational deflection shapes. A comparison of each method is presented. It was found that performing a SEREP expansion of the mode shapes and post-processing to estimate strain fields was very effective, while directly measuring strains from ODS or modes was highly subject to noise and filtering effects.

Keywords Laser · Vibrometer · Strain · Full-field · Expansion

4.1 Introduction

The capability to experimentally derive full-field strain response is of interest for several application areas such as model validation, fatigue life estimation, test object characterization, and determining the effectiveness of a test fixture to reproduce the damage potential seen in actual service. Full-field measurements are only now practically achievable thanks to advances in optical methods such as digital image correlation (DIC) and 3D scanning laser Doppler vibrometry (SLDV). DIC is a well-established method for full-field strain measurements but is not always the method of choice for a given test object. Cazzolato et al. [1] demonstrated in 2008 that the state of 3D SLDV was such that strain measurements were feasible, but very sensitive to noise and issues such as quantization errors and laser head/specimen alignment. Weisbecker et al. [2] further studied the sensitivities of using 3D LDV for strain measurements, including issues of laser head alignment, measurement mesh size, and the selection of spatial filter parameters (Savitzky-Golay differentiation filter). Reyes and Avitabile [3] among others have since applied 3D SLDV strain measurements on more complicated objects such as wind turbine blades, also demonstrating that results are highly subject to noise and related measurement issues.

Where previous works have focused on direct strain comparisons between 3D SLDV and finite element (FE) results or strain gage measurements, this work looks to develop a mode-based model of full-field strain shapes. This approach was taken for several reasons, the most poignant being the ability to determine which modes are the most damaging to an object and at which physical location. With this information and an applied environment, the total strain response can be determined as a superposition of the modal strains. Further, this allows for the direct comparison, on a mode-by-mode basis, of an object's strain field in actual service versus in a test fixture. This provides a means to determine if a test fixture provides the correct

---

Sandia National Laboratories is a multimission laboratory managed and operated by National Technology and Engineering Solutions of Sandia, LLC., a wholly owned subsidiary of Honeywell International, Inc., for the U.S. Department of Energy's National Nuclear Security Administration under contract DE-NA-0003525.

B. Witt (✉) · D. Rohe · T. Schoenherr
Sandia National Laboratories, Albuquerque, NM, USA
e-mail: blwitt@sandia.gov; dprohe@sandia.gov; tfschoe@sandia.gov

C. Niezrecki et al. (eds.), *Rotating Machinery, Optical Methods & Scanning LDV Methods, Volume 6*, Conference Proceedings of the Society for Experimental Mechanics Series, https://doi.org/10.1007/978-3-030-12935-4_4

boundary conditions/structural dynamic characteristics for an appropriate environmental test; often a test fixture does not provide the correct dynamics to generate the same damage potentials encountered in actual service.

Multiple methods for establishing full-field modal strains using 3D SLDV are evaluated for a moderately complicated test structure. The methods fall into two categories: direct or transformation. The direct methods employ spatial filtering prior to taking derivatives of measured shape displacements to arrive at strain shapes. The transformation methods use mode shapes or operational deflection shapes (ODS) as basis functions to expand and/or smooth the measured data prior to taking derivatives of measured shape data to arrive at strain shapes. The use of some type of basis functions to reduce noise in measured data was proposed in [1]. Expansion and smoothing are both done using the System Equivalent Reduction/Expansion Process (SEREP) [4]. Expansion of limited measured points to an augmented set of points requires the availability of a finite element model (FEM), whereas smoothing alone can be achieved with only measured shapes.

4.2 Test Structure and Setup

The test article is a jointed aluminum assembly, taken from the "Box Assembly with Removable Component," or BARC test structure, that is currently used in many boundary condition assessment studies [5]. In this work, the "Removable Component," comprising two C-channel legs and a flat top member (see Fig. 4.1b), is taken as the object of interest. To simulate a typical environmental test setup, the "bench" is bolted to a fixture plate which is in turn affixed to a 7″ vibration cube that would mount to a shaker table. The object was to identify full-field modal strain shapes of the bench when rigidly affixed to its test fixturing.

Measurements were taken with a Polytec PSV-500 Xtra (Infrared laser heads) 3D SLDV system. As shown in Fig. 4.2, the LDV heads are supported by a frame made from optical railing and the test object is supported on soft foam to approximate

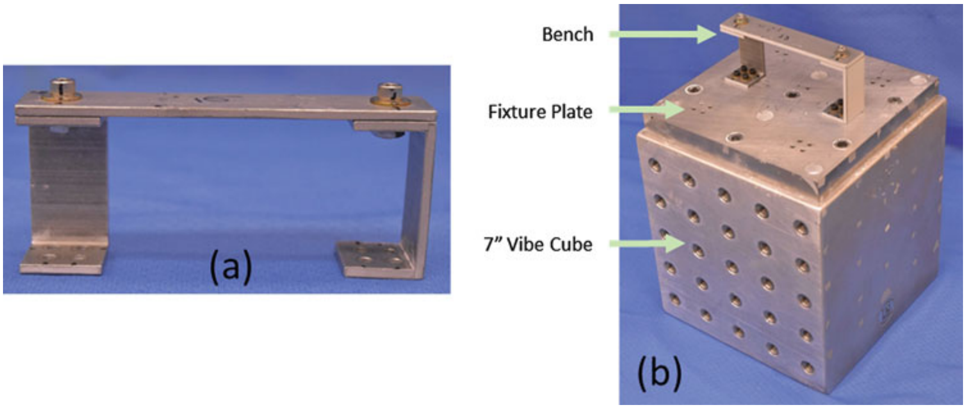

Fig. 4.1 Test article (**a**) and test configuration (**b**)

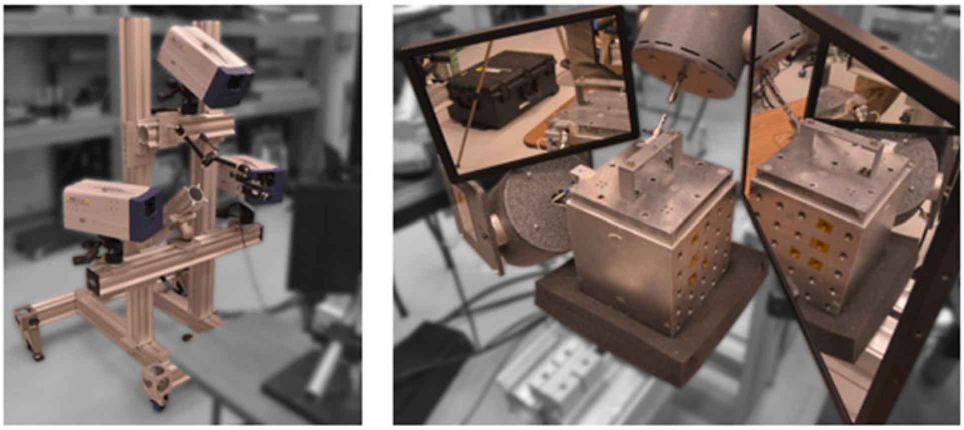

Fig. 4.2 Physical setup for modal testing

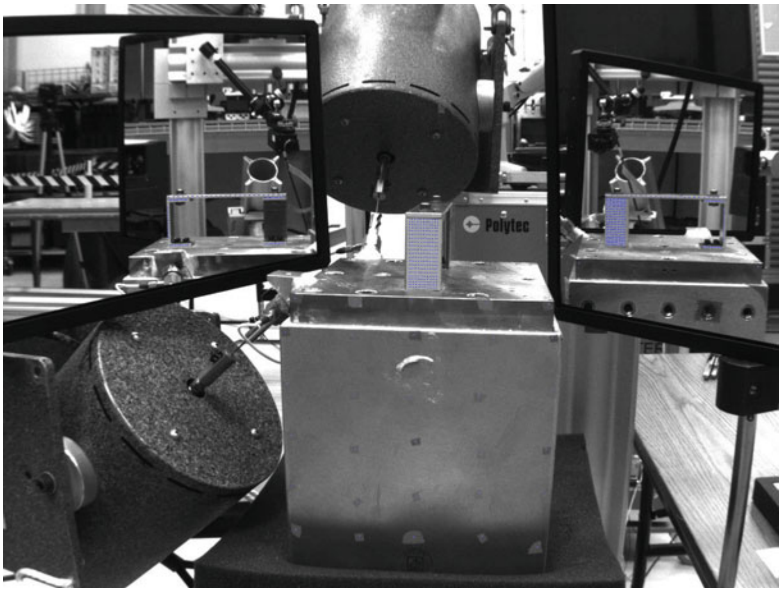

Fig. 4.3 Scan points (blue markers)

a free-free boundary condition for modal parameter estimations. Two electromagnetic shakers were placed at oblique angles on perpendicular sides of the vibration cube to provide excitation in multiple directions. Two front surface mirrors were placed at angles on either side of the test object to allow LDV measurements on three sides (front, left, right) without having to move the test article or laser heads between scans. The scan points are shown as blue markers in Fig. 4.3, which is a view from the LDV system's camera. Retroreflective tape was applied at all scan point locations to increase signal return to the LDV heads. A moderately dense 13 × 21 measurement grid was placed on the C-channel leg faces, while a single row of points was measured along the top beam and C-channel edges. Placement of the shakers and mirrors to have a view of three faces simultaneously drove the camera field of view to be wide relative to the areas of interest, meaning that the pixels per inch in the camera view were not optimized in any sense.

Two types of excitation methods were used: random and sine-dwell. Random excitation tests were used to obtain the displacement mode shapes and natural frequencies, $(\boldsymbol{E}, \boldsymbol{\omega})$. The random signal had a bandwidth of 10–6400 Hz and Hann windowing was used with 50 averages. Sine-dwell tests were used to obtain ODS at the $\boldsymbol{\omega}$ frequencies identified from the random data, $(\boldsymbol{O}, \boldsymbol{f})$. The sine-dwells used 100 averages and produced ODS that were overall less noisy than those obtained from the random testing. For both tests, the vibrometer was set for a measurement bandwidth of 1–6400 Hz, a sample frequency of 16,000 and a 1 Hz resolution. Signal Enhancement set to Standard and Speckle Tracking enabled.

4.3 Overview of Methods and Tools

An overview of the methods used in this work to derive full-field strain shapes is shown in Fig. 4.4. This flowchart will be discussed at length in the following sections. Within these methods there are three general tools (blue boxes in Fig. 4.4) that will be discussed in this section: Gaussian spatial filters, a strain post-processor, and SEREP.

4.3.1 Gaussian Filter

The raw measured displacements from LDV systems can be noisy relative to accelerometer data, which is exacerbated when differentiating to obtain strain. Previous works, including [1–4], have emphasized the importance of applying spatial filtering to address the noise in measured displacements. In this work, the displacements are shape functions, either ODS or modal

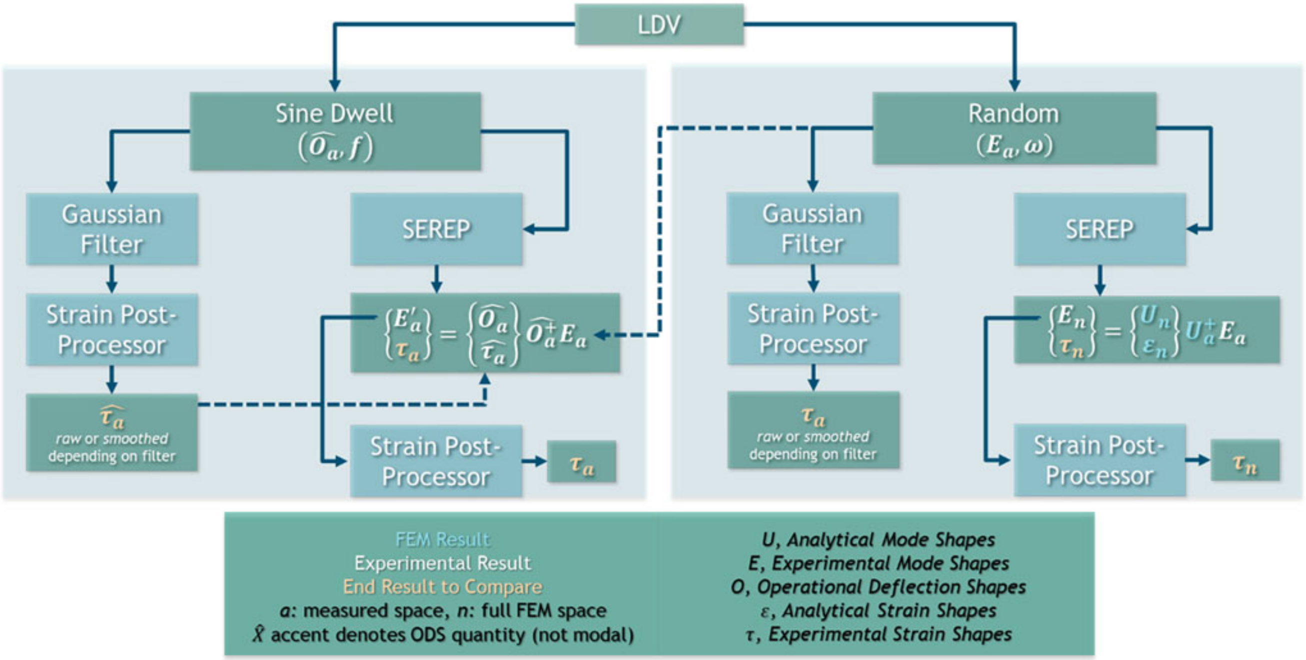

Fig. 4.4 Overview of full-field strain derivation methods studied

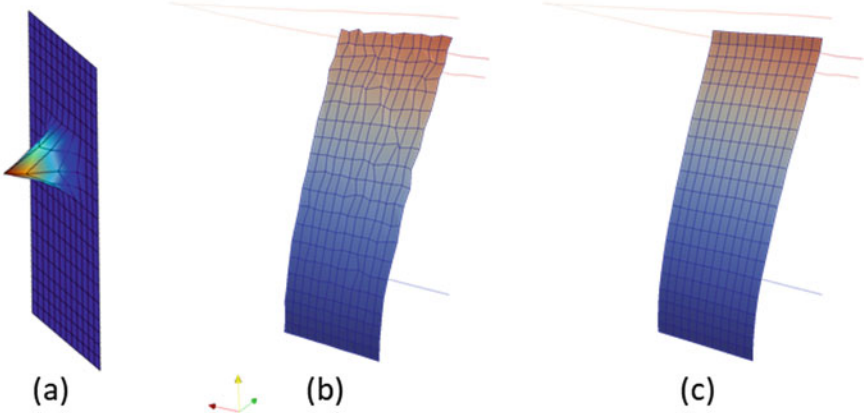

Fig. 4.5 Gaussian spatial filtering: (**a**) weighting coefficients, (**b**) raw shape, (**c**) filtered shape

displacement shapes. In the direct methods used in this work, a 2D Gaussian spatial filter is applied as a low-pass smoothing function prior to calculating strains. The *i*th filter weight for the *j*th point is given by:

$$w_{ij} = \frac{1}{\sigma\sqrt{2\pi}} \left(\frac{\left\| \mathbf{r}_i - \mathbf{r}_j \right\|}{\sigma} \right)^2 \tag{4.1}$$

where the σ parameter is the size (e.g. 2.5 mm) and **r** are the coordinates of the measured points. The filtered displacement for the *j*th point can then be calculated as:

$$\overline{d_j} = \frac{\sum_i w_{ij} d_i}{\sum_i w_{ij}} \tag{4.2}$$

An example 3D representation of filter weights on one of the bench's c-channel faces is shown in Fig. 4.5a, along with a raw ODS (Fig. 4.5b) and the same ODS after the spatial filter was applied (Fig. 4.5c).

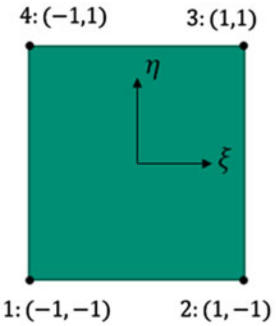

Fig. 4.6 Element nodes and coordinate system

4.3.2 *Strain Post-processor*

In this work, the displacements are arbitrary shapes (mode shapes or ODS) rather than directly measured displacements. This posed an issue for using the Polytec strain post-processor, which operates on Band Data within their proprietary scan file format. Rather than creating a tool to write arbitrary shapes to a Band Data scan file, a standalone 2D strain post-processing script was written in MATLAB (note, 3D implementations will work equally well). Measured data from the SLDV system were exported in Universal File Format, which included the test geometry. The geometry node coordinates were in 3D (*x*,*y*,*z*) but were reduced to 2D surface coordinates (*x*,*y*) for each surface of interest. Node coordinates (*x*,*y*) and connectivity information were extracted from these files to create elements. Elemental deformations were either the experimental mode shapes ($\boldsymbol{E}$) estimated from the SLDV data using Synthesize Modes and Correlate (SMAC) [6] or ODS ($\widehat{\boldsymbol{O}}$) that were extracted directly from Polytec "Fastscan" data. With geometry and displacement data, strains were then calculated using a bilinear quadrilateral element formulation as detailed in [7] and summarized below. Strains were computed at the center of the element, $(\xi, \eta) = (0, 0)$, and interpolated to a common set of points with the FEM so the measured results could be directly compared to analytical results. The elemental coordinate system is shown in Fig. 4.6 and the element shape functions are given in Eq. 4.3:

$$\begin{aligned} N_1 &= \tfrac{1}{4}(1-\xi)(1-\eta) \\ N_2 &= \tfrac{1}{4}(1+\xi)(1-\eta) \\ N_3 &= \tfrac{1}{4}(1+\xi)(1+\eta) \\ N_4 &= \tfrac{1}{4}(1-\xi)(1+\eta) \end{aligned} \tag{4.3}$$

The Jacobian matrix of (*x*,*y*) with respect to (ξ, η), denoted as $\boldsymbol{J}$, is used to establish the relationship between the derivatives of physical and elemental displacement:

$$\begin{bmatrix} \frac{\partial N_i}{\partial x} \\ \frac{\partial N_i}{\partial y} \end{bmatrix} = \boldsymbol{J}^{-1} \begin{bmatrix} \frac{\partial N_i}{\partial \xi} \\ \frac{\partial N_i}{\partial \eta} \end{bmatrix}; \boldsymbol{J} = \begin{bmatrix} \frac{\partial x}{\partial \xi} & \frac{\partial y}{\partial \xi} \\ \frac{\partial x}{\partial \eta} & \frac{\partial y}{\partial \eta} \end{bmatrix} \tag{4.4}$$

where the differential entries of $\boldsymbol{J}$ are obtained through Eq. (4.5) below.

$$\frac{\partial x}{\partial \xi} = \sum_i x_i \frac{\partial N_i}{\partial \xi}, \frac{\partial y}{\partial \xi} = \sum_i y_i \frac{\partial N_i}{\partial \xi}, \frac{\partial x}{\partial \eta} = \sum_i x_i \frac{\partial N_i}{\partial \eta}, \frac{\partial y}{\partial \eta} = \sum_i y_i \frac{\partial N_i}{\partial \eta} \tag{4.5}$$

Finally, strains are calculated using the strain-displacement matrix, $\boldsymbol{B}$, composed of the differentials calculated above and measured displacements, denoted here as (*u*,*v*) representing either ODS or mode shape coefficients.

$$\boldsymbol{\tau} = \begin{bmatrix} \tau_{xx} \\ \tau_{yy} \\ 2\tau_{xy} \end{bmatrix} = \begin{bmatrix} \frac{\partial N_1}{\partial x} & 0 & \frac{\partial N_2}{\partial x} & 0 & \ldots & \frac{\partial N_m}{\partial x} & 0 \\ 0 & \frac{\partial N_1}{\partial y} & 0 & \frac{\partial N_2}{\partial y} & \ldots & 0 & \frac{\partial N_m}{\partial y} \\ \frac{\partial N_1}{\partial y} & \frac{\partial N_1}{\partial x} & \frac{\partial N_2}{\partial y} & \frac{\partial N_2}{\partial x} & \ldots & \frac{\partial N_m}{\partial y} & \frac{\partial N_m}{\partial x} \end{bmatrix} \begin{Bmatrix} u_1 \\ v_1 \\ u_2 \\ v_2 \\ u_3 \\ v_3 \\ u_4 \\ v_4 \end{Bmatrix} = \mathbf{Bu} \tag{4.6}$$

4.3.3 SEREP

Model reduction and expansion techniques are based on developing a transformation matrix, $\boldsymbol{T}$, that maps between a reduced space model (a-space) and a full space (n-space) model. Methods such as Guyan and Dynamic Condensation, for example, use system mass and stiffness matrices to form the transformation matrix. SEREP however uses the full space mode shapes as the basis for the transformation matrix which allows for exact preservation of the mode shapes and frequencies, as well as the ability to arbitrarily select which modes and degrees of freedom (DOF) to include in the reduction/expansion [4]. The analytical mode shapes of a FEM in full n-space are denoted by $\boldsymbol{U}_n$, whereas the same shapes at a reduced set of a DOF are denoted by $\boldsymbol{U}_a$. The SEREP transformation between full and reduced space mode shapes is then:

$$\boldsymbol{T} = \boldsymbol{U}_n \boldsymbol{U}_a^{+} \tag{4.7}$$

where $^{+}$ indicates a generalized inverse. Experimental mode shapes, $\boldsymbol{E}$, measured at a DOF can be expanded to the full FEM n-space DOF by:

$$\boldsymbol{E}_n = \boldsymbol{T}\boldsymbol{E}_a = \boldsymbol{U}_n \boldsymbol{U}_a^{+} \boldsymbol{E}_a \tag{4.8}$$

This method is of course not without limitations and caveats in usage. While the FEM used does not need to be exactly correlated to the test data, it is imperative that the FEM shapes span the space of the experimental shapes for an accurate expansion. For this reason, analytical rigid body mode shapes must be retained. Also, to prevent $\boldsymbol{E}_n$ from being rank deficient, the number of DOF kept needs to be greater than the number of preserved modes ($a > m$). It is also intuitive that including analytical mode shapes dominated by components which were not measured or captured experimentally will cause issues in the expansion process.

An example of an experimentally measured mode shape is shown in Fig. 4.7a. Using the FEM to create $\boldsymbol{T}$, the same shape expanded to full-space is shown in (Fig. 4.7b). This method was applied to all ten experimentally identified mode shapes, as shown in Fig. 4.8.

The FEM used in this work was generally very well correlated to the test data, as shown by the modal assurance criterion (MAC) in Fig. 4.9. One of the experimental shapes did not have a match in the FEM (mode 8, large contribution from vibration cube), and experimental mode 9 was highly correlated to FEM shapes 14 and 15. Otherwise, the MAC values are quite good. Even so, the analytical FEM shapes still did not quite span the space of some of the experimental shapes, resulting in slightly imperfect expansions; two examples are shown in Fig. 4.10, where the experimental (mesh grid) and expanded shapes (solid) do not perfectly align.

Modal displacement vectors are used as the basis for the transformation in Eq. (4.8). However, the data can be expanded using other modal quantities as well. For example, if modal strain shapes from the FEM ($\boldsymbol{\epsilon}_n$) are available, they can be used in the expansion to arrive at full n-space strain shapes directly as:

$$\boldsymbol{\tau}_n = \boldsymbol{\varepsilon}_n \boldsymbol{U}_a^{+} \boldsymbol{E}_a \tag{4.9}$$

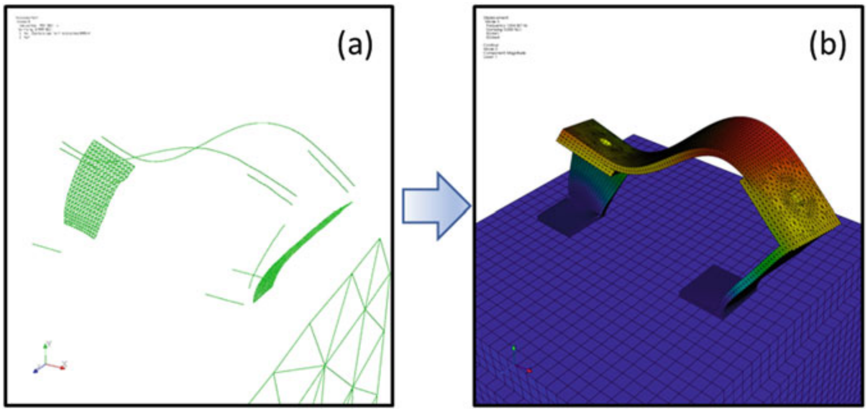

Fig. 4.7 Example of an original measured shape (**a**) expanded to full-space using SEREP (**b**)

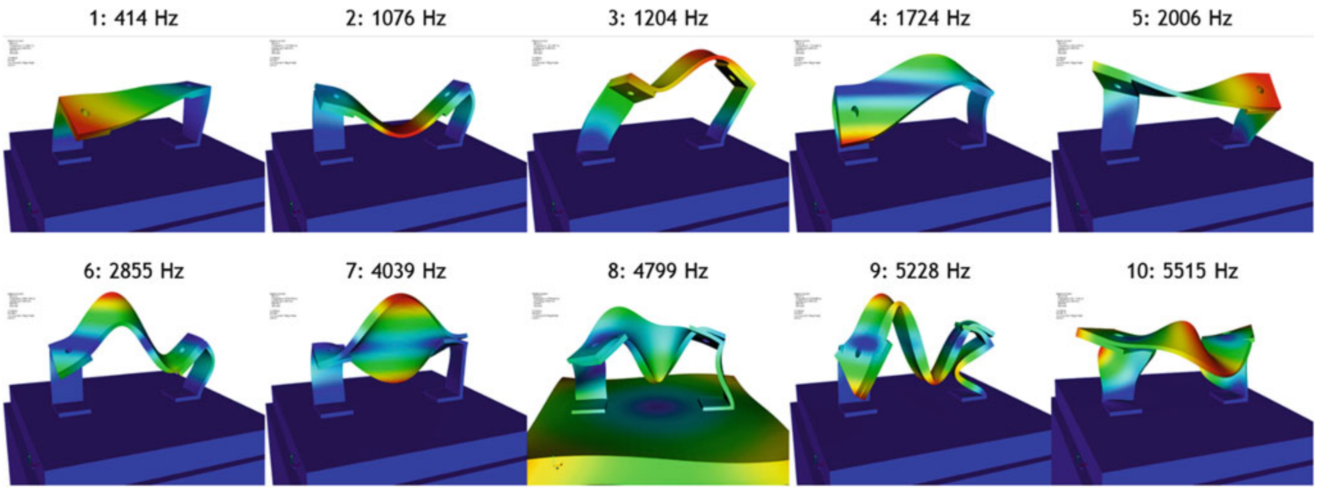

Fig. 4.8 Expansion of all experimentally derived mode shapes

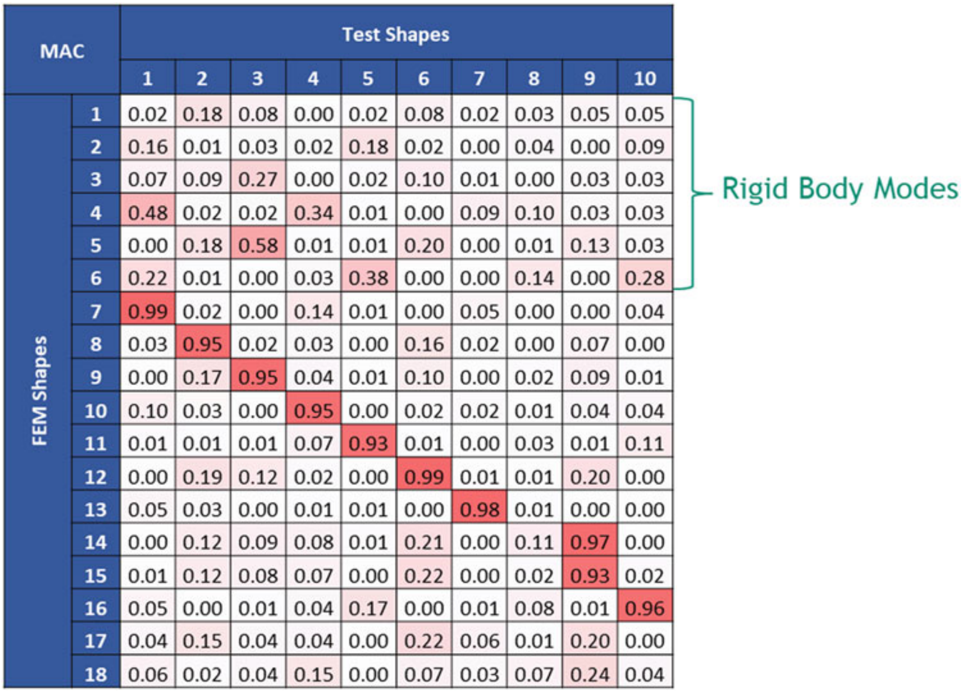

MAC		Test Shapes									
		1	2	3	4	5	6	7	8	9	10
FEM Shapes	1	0.02	0.18	0.08	0.00	0.02	0.08	0.02	0.03	0.05	0.05
	2	0.16	0.01	0.03	0.02	0.18	0.02	0.00	0.04	0.00	0.09
	3	0.07	0.09	0.27	0.00	0.02	0.10	0.01	0.00	0.03	0.03
	4	0.48	0.02	0.02	0.34	0.01	0.00	0.09	0.10	0.03	0.03
	5	0.00	0.18	0.58	0.01	0.01	0.20	0.00	0.01	0.13	0.03
	6	0.22	0.01	0.00	0.03	0.38	0.00	0.00	0.14	0.00	0.28
	7	0.99	0.02	0.00	0.14	0.01	0.00	0.05	0.00	0.00	0.04
	8	0.03	0.95	0.02	0.03	0.00	0.16	0.02	0.00	0.07	0.00
	9	0.00	0.17	0.95	0.04	0.01	0.10	0.00	0.02	0.09	0.01
	10	0.10	0.03	0.00	0.95	0.00	0.02	0.02	0.01	0.04	0.04
	11	0.01	0.01	0.01	0.07	0.93	0.01	0.00	0.03	0.01	0.11
	12	0.00	0.19	0.12	0.02	0.00	0.99	0.01	0.01	0.20	0.00
	13	0.05	0.03	0.00	0.01	0.01	0.00	0.98	0.01	0.00	0.00
	14	0.00	0.12	0.09	0.08	0.01	0.21	0.00	0.11	0.97	0.00
	15	0.01	0.12	0.08	0.07	0.00	0.22	0.00	0.02	0.93	0.02
	16	0.05	0.00	0.01	0.04	0.17	0.00	0.01	0.08	0.01	0.96
	17	0.04	0.15	0.04	0.04	0.00	0.22	0.06	0.01	0.20	0.00
	18	0.06	0.02	0.04	0.15	0.00	0.07	0.03	0.07	0.24	0.04

Rigid Body Modes

Fig. 4.9 MAC between FEM and experimental mode shapes

SEREP can also be used as a least squares error minimization using shape vectors as the basis, removing variance from measured data. We can exploit this as a method to smooth noisy measured mode shapes ($\boldsymbol{E}_a$) using ODS (which potentially have a higher signal-to-noise ratio) in addition to using Gaussian spatial filters:

$$\boldsymbol{E}'_a = \widehat{\boldsymbol{O}_a}\widehat{\boldsymbol{O}_a}^{+}\boldsymbol{E}_a \tag{4.10}$$

Similar to Eq. (4.9), we can alternatively choose to use ODS derived strain shapes ($\widehat{\boldsymbol{\tau}_a}$, discussed in the next section, can be extracted from $\widehat{\boldsymbol{O}_a}$ using Polytec's strain post-processor) as part of the basis for the smoothing, and directly arrive at smoothed modal strain shapes in the measured a-space:

$$\boldsymbol{\tau}_a = \widehat{\boldsymbol{\tau}_a}\widehat{\boldsymbol{O}_a}^{+}\boldsymbol{E}_a \tag{4.11}$$

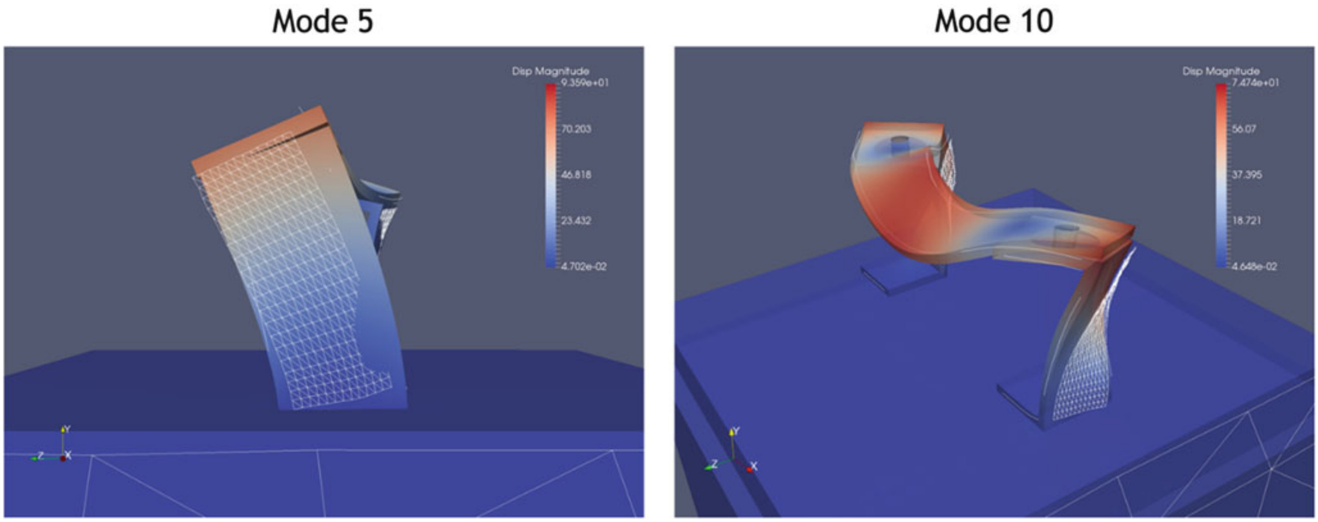

Fig. 4.10 Examples of imperfect shape expansions

4.4 LDV Direct Methods

As mentioned in the previous section, several methods for generating full-field modal strain shapes were utilized. All methods can be grouped into two categories: direct or transformation methods. This section focuses on the direct methods, which can be generated either on an ODS or modal quantity basis. Figure 4.11 shows the two direct methods; the "Direct ODS Method" is the workflow on the left and the "Direct Modal Method" is the workflow on the right.

In some cases, it is expected that ODS extracted from sine dwell data near natural resonance frequencies ($\widehat{\boldsymbol{O}}_a$, $\boldsymbol{f}$) at *a*-space measurement locations would be less noisy than traditionally fit mode shapes from LDV data ($\boldsymbol{E}_a$). For example, if a sine-dwell test had a better signal-to-noise ratio than a random vibration test from which modes would be extracted, the Direct ODS Method could be used. The measured $\widehat{\boldsymbol{O}}_a$ should then be smoothed with a Gaussian filter. Note that a Gaussian filter of size σ less than approximately one third of the scan point spacing effectively provides no smoothing and leaves shapes in an unfiltered or raw state. Once any desired filtering is applied, the shapes can be run through the strain post-processor to arrive at an ODS-quantity estimation of the strain shapes in *a*-space, $\widehat{\boldsymbol{\tau}}_a$. For structures where the ODS well approximate the mode shapes (i.e. resonances well separated), $\widehat{\boldsymbol{\tau}}_a$ will, to the same degree, approximate the $\boldsymbol{\tau}_a$ modal strain shapes we are seeking, although they will be scaled differently. This method most closely aligns with the Polytec Strain Post-Processor that is integrated into the LDV software, which operates on Band Data within a scan file.

For applications where a modal test can be conducted and relatively clean mode shapes and natural frequencies ($\boldsymbol{E}_a$, $\boldsymbol{\omega}$) extracted, the Direct Modal Method can be utilized. The same process of smoothing shapes with a Gaussian spatial filter and post-processing the results for strain are used. In this case, the resulting $\boldsymbol{\tau}_a$ strain shapes are actual modal quantities.

Both Direct methods have the benefits of not requiring a FEM of the test object nor needing an expansion process for sufficiently dense measurement grids. However, both are subject to any noise in the measurements and are also highly dependent on the spatial filter parameters used. To demonstrate these effects, Gaussian filters with $\sigma = 0.5$–3.5 mm were evaluated. The scan grid on the c-channel faces of interest had a horizontal and vertical spacing of approximately 1.6 × 2.6 mm, respectively. This means that filter sizes of approximately 0.5 mm or less are providing almost no smoothing. Surface strains ($\boldsymbol{\tau}_{xx}$, $\boldsymbol{\tau}_{yy}$, $\boldsymbol{\tau}_{xy}$) in *a*-space were calculated for the two c-channel faces (X-surface and Z-surface, see Fig. 4.12), although only $\boldsymbol{\tau}_{yy}$ results on the X-face are shown here for brevity. Figures 4.13 and 4.14 show the $\boldsymbol{\tau}_{yy}$ results of the Direct ODS Method and Direct Modal Methods, respectively, for multiple filter sizes. Black indicates noise values that are out of range.

Both figures show that filter sizes greater than the nominal spacing of measurement points is necessary to remove spurious noise in the shapes, which is approximately 2.0 mm here. However, it is noted that the Direct ODS Method results for the 1.5 mm filter are noticeably noisier than their Modal counterparts, indicating the ODS for this test structure were not cleaner than the mode shapes, as had been postulated. The test article exhibited nonlinear behavior which is believed to be the reason for this observation. Filter effects near the edges are clearly observed in several shapes, for example ODS 5 and Mode 4; as filter weight increases, the maximum strains at the edges are artificially reduced due to the distribution of the weighting coefficients of the filter. There is a tradeoff between noise reduction and maximum strain accuracy, particularly near edges.

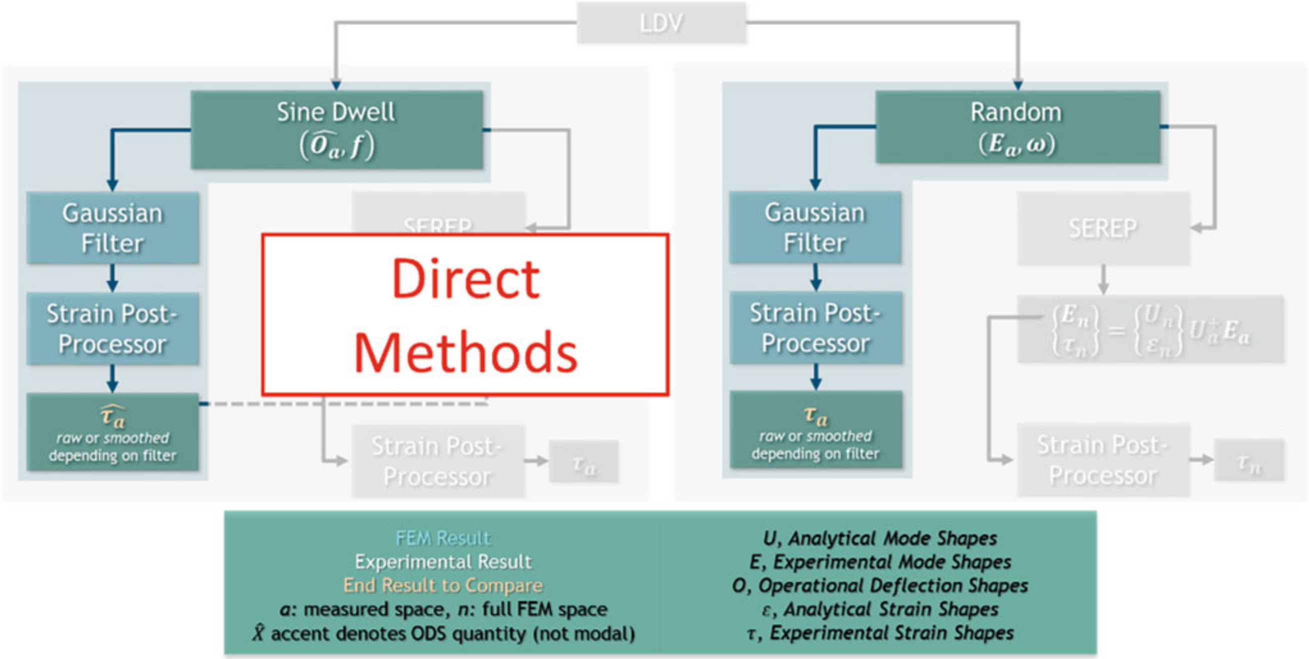

Fig. 4.11 Direct methods for strain shape estimation

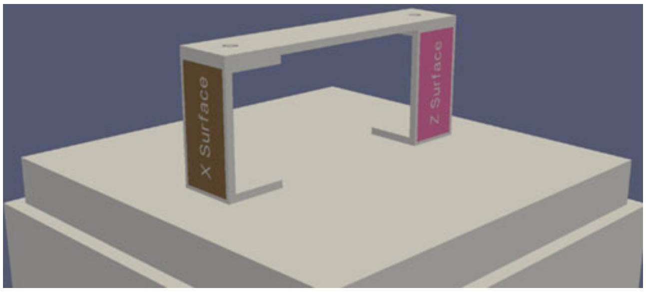

Fig. 4.12 Area patches where surface strains were calculated

Figures 4.13 and 4.14 also illustrate the differences between ODS and modal strain shapes, even for a structure whose modes are well spaced and the ODS are very similar to the mode shapes, as illustrated by the MAC between the two in Fig. 4.15.

4.5 LDV Transformation Methods

The second category of methods utilize transformations to derive full-field modal strain shapes, as shown in Fig. 4.16.

The workflow on the right side of the figure will be referred to as the "Transformation Modal Method". In this method, the displacement mode shapes extracted from a measurement points ($\boldsymbol{E}_a$) are expanded to the full FEM n-space using SEREP, as shown in Eq. (4.8). These $\boldsymbol{E}_n$ shapes are then post-processed to obtain full n-space modal strain shapes $\boldsymbol{\tau}_n$. Alternatively, if the FEM includes analytical strain shapes ($\boldsymbol{\varepsilon}_n$), the expansion in Eq. (4.9) can be used to directly arrive at the same $\boldsymbol{\tau}_n$ without the need to use a standalone strain post-processor. Provided that strains are calculated the same in the FEM as the standalone strain post-processor, these two variations will be identical and only circumstance would dictate which should be used. In this work, $\boldsymbol{\varepsilon}_n$ were available from the FEM, so Eq. (4.9) is used for the Transformation Modal Method results herein, but the alternative path was also computed to verify they produce equivalent results.

On the left side of Fig. 4.16 is the so-called "Transformation ODS Method", although it is noted that both ODS $\widehat{\boldsymbol{O}}_a$ and mode shapes $\boldsymbol{E}_a$ are required. It should be noted that while this method required both shape sets, it does not need a FEM of the test object. The first variation would be to use the ODS to smooth the measured mode shapes per Eq. (4.10) and then

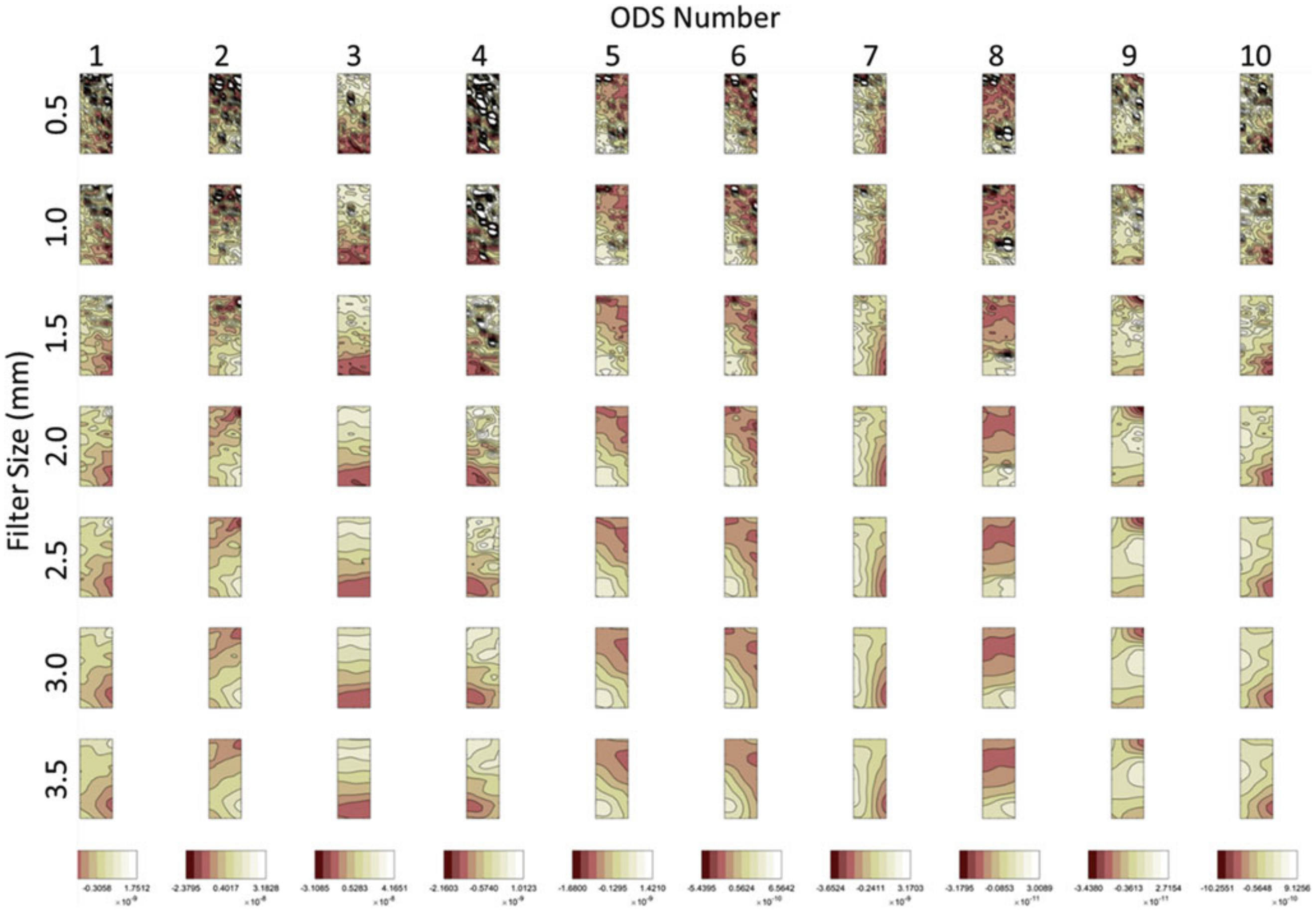

Fig. 4.13 Direct ODS method: X-Face $\boldsymbol{\tau}_{yy}$ for multiple filter sizes

post-process to obtain modal strain shapes $\boldsymbol{\tau}_a$. It was observed in our application that the smoothed $\boldsymbol{E}'_a$ was still too noisy to calculate strains and required the additional application of a Gaussian filter prior to being post-processed for strains. Note that the results are in the measured *a*-space, as the SEREP implementation here is for smoothing only and does not involve an expansion to *n*-space. The second variation of this method is to first calculate an ODS based set of strain shapes $\widehat{\boldsymbol{\tau}_a}$ using either the Direct ODS Method or the Polytec Strain Post-Processor, which then feeds into Eq. (4.11) to directly arrive at *modal* strain shapes in *a*-space, $\boldsymbol{\tau}_a$. These two variations are mathematically identical, as can be shown by combining Eq. (4.6) and Eqs. (4.10 and 4.11):

$$\begin{aligned}\text{variation 1} : \boldsymbol{\tau}_a &= \boldsymbol{B}\boldsymbol{E}'_a = \boldsymbol{B}\boldsymbol{W}\widehat{\boldsymbol{O}_a}\widehat{\boldsymbol{O}_a}^{+}\boldsymbol{E}_a \\ \text{variation 2} : \boldsymbol{\tau}_a &= \widehat{\boldsymbol{\tau}_a}\widehat{\boldsymbol{O}_a}^{+}\boldsymbol{E}_a = \boldsymbol{B}\boldsymbol{W}\widehat{\boldsymbol{O}_a}\widehat{\boldsymbol{O}_a}^{+}\boldsymbol{E}_a\end{aligned} \tag{4.12}$$

where $\boldsymbol{W}$ is the applied Gaussian filter weights matrix. Although these variations produce identical results, we choose to leave them as different workflows to point out the two usage cases: (1) a modal test is performed, $\boldsymbol{E}_a$, $\widehat{\boldsymbol{O}_a}$ are both obtained and a standalone strain post-processing is performed to generate modal strain shapes, versus (2) a modal test is performed in conjunction with Fastscan testing via the Polytec LDV system and the results are combined to generate modal strain shapes.

The FEM was delivered with 300 modes and 127,155 DOF. Ten modes were experimentally extracted from the modal test in which 2202 DOF were measured (*a*-space set) with the 3D SLDV system. Using SEREP, the FEM was reduced to 20 DOF and the first 18 analytical shapes were retained, which includes the rigid body modes and excludes modes dominated by the vibration cube, since these were not well measured in the modal test. These were used in the Transformation Modal Method calculations.

Twelve ODS were extracted from the sine dwell data (first 10 shown in figures below). A total of 2202 DOF were measured with the 3D SLDV system, corresponding to the same set as the modal test. All DOF (*a*-space set) and all extracted ODS were retained in the SEREP smoothing step of the Transformation ODS Method. Example results from the Transformation

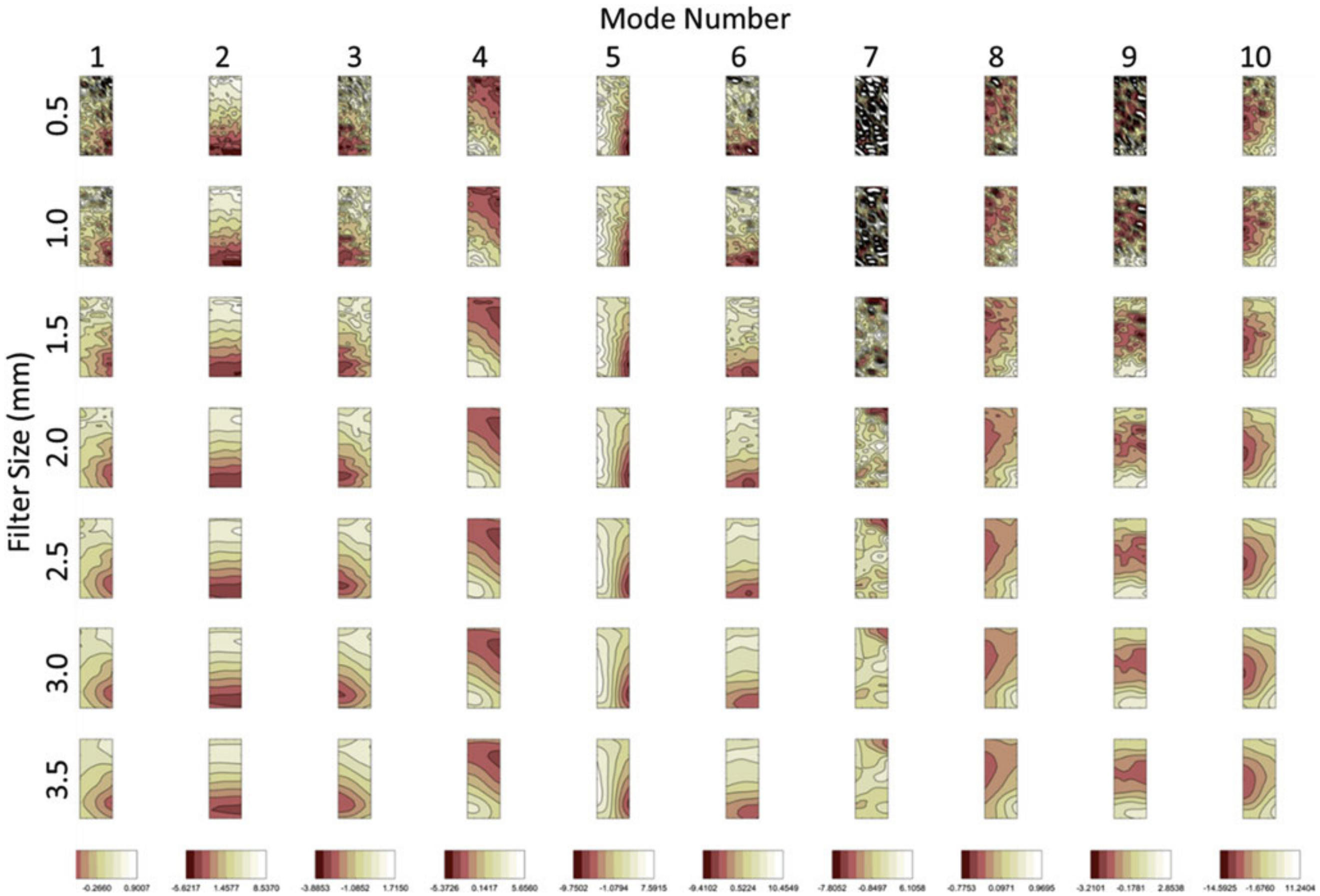

Fig. 4.14 Direct modal method: X-Face τ_{yy} for multiple filter sizes

MAC		Mode Shapes									
		1	2	3	4	5	6	7	8	9	10
ODS	2	0.99	0.03	0.00	0.15	0.01	0.00	0.06	0.00	0.00	0.05
	3	0.02	0.99	0.11	0.02	0.01	0.17	0.03	0.00	0.08	0.00
	4	0.00	0.09	0.95	0.01	0.03	0.09	0.00	0.00	0.04	0.01
	5	0.11	0.02	0.01	0.99	0.02	0.01	0.02	0.02	0.06	0.02
	7	0.00	0.00	0.00	0.01	0.95	0.00	0.00	0.04	0.01	0.17
	8	0.01	0.15	0.10	0.03	0.01	0.88	0.00	0.00	0.13	0.01
	9	0.05	0.04	0.00	0.01	0.00	0.00	0.99	0.02	0.00	0.00
	10	0.00	0.01	0.02	0.02	0.05	0.01	0.01	1.00	0.14	0.11
	11	0.00	0.10	0.06	0.07	0.01	0.19	0.00	0.08	0.98	0.01
	12	0.05	0.01	0.02	0.02	0.17	0.00	0.00	0.12	0.00	0.98

Fig. 4.15 MAC between ODS and mode shapes

ODS and Transformation Modal Methods are shown in Figs. 4.17 and 4.18, respectively, for the τ_{yy} component of strain on the X-Face of the c-channel support (see Fig. 4.12). As mentioned above, the smoothed E'_a shapes in the Transformation ODS Method were still too noisy to use directly for strain calculations, so Gaussian filters were applied, ranging in size from 0.5 to 3.5 mm as can be seen in Fig. 4.17.

The results shown in Fig. 4.18 are practically identical to each other because the standalone strain post-processor and the FEM calculated strains in the same manner. Overall, these results are very clean, are obtained in full n-space, and do not exhibit filter edge effects that the methods which utilize the spatial filters suffer from. Further, the Transformation Modal Method measurement a-space does not actually need to approach full-field; only enough measurement DOF to adequately describe the shapes for the expansion process are required to then obtain full-field modal strain shapes.

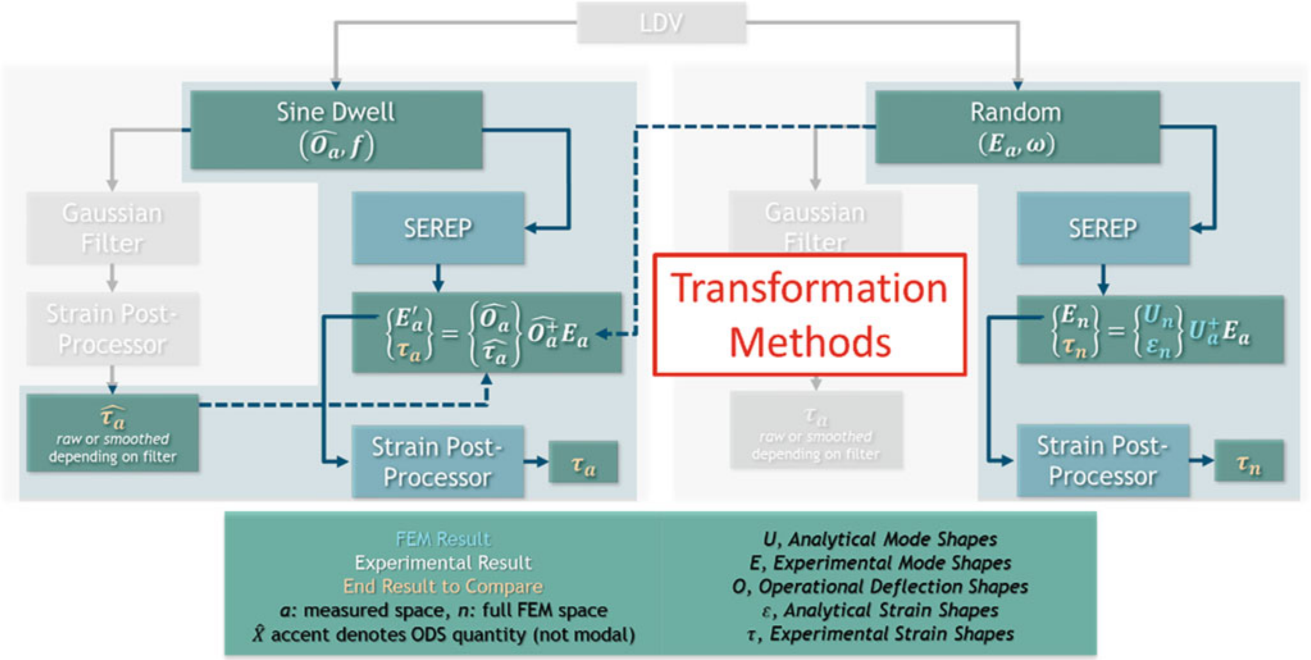

Fig. 4.16 Transformation methods for strain shape estimation

Fig. 4.17 Transformation ODS method: X-Face τ_{yy} (both variations identical)

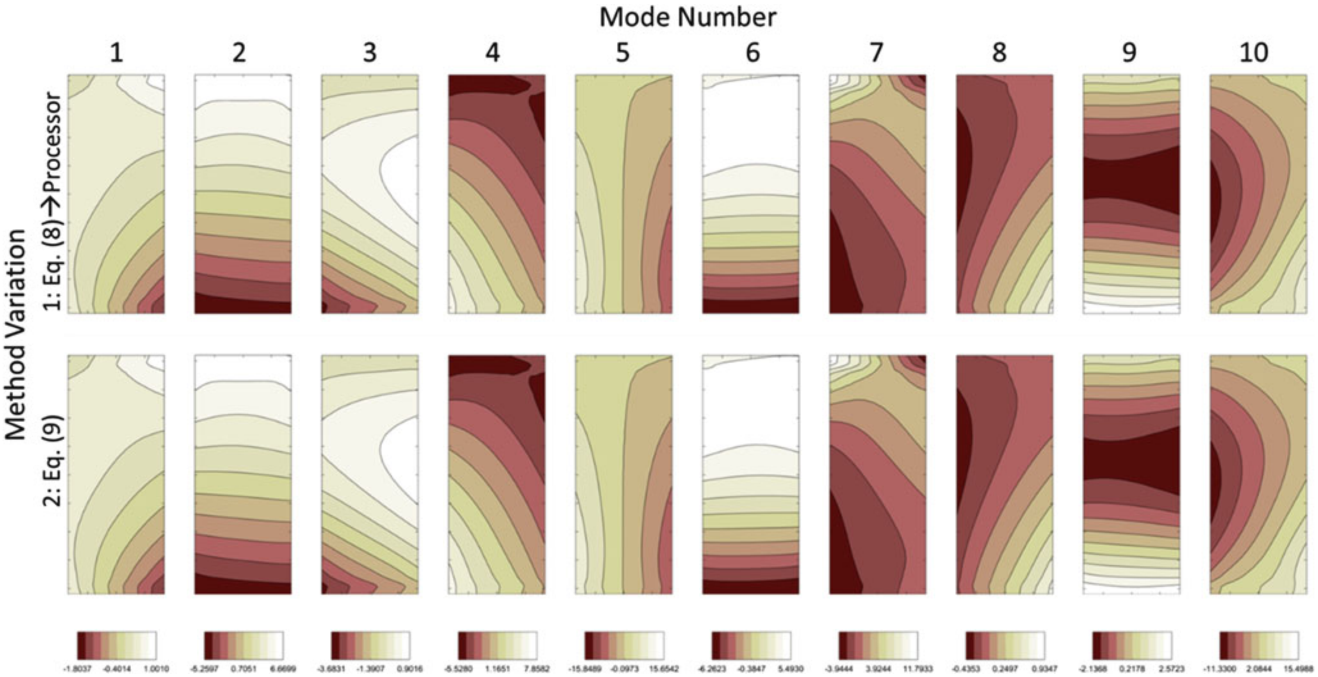

Fig. 4.18 Transformation modal method: X-Face $\boldsymbol{\tau}_{yy}$ for both method variations

4.6 Comparison of Methods

Comparing all four methods is not trivial due to the differences in scaling between ODS strain shapes and modal strain shapes. The MAC between the ODS and mode shapes was used to match ODS to shapes for comparison of the first six mode shapes. The scaling is different between ODS and modal shapes as well. For comparison of the methods which utilize a Gaussian filter, results from the 3.0 mm filter size were selected based on the overall tradeoff between edge effects and noise reduction. Fig. 4.19 shows this final comparison between each of the methods and the FEM for the $\boldsymbol{\tau}_{yy}$ component of strain on the c-channel X-face. The remaining components of strain were calculated for this and the Z-face as well but are omitted for brevity as the results are typical in each case.

The traditional Direct ODS method produces very usable results, which are comparable to the Transformation ODS in terms of noise. However, the results have the disadvantage of not being actual modal quantities. Although ODS data may be obtained with the 3D SLDV much more rapidly than a modal test with the same number of measured DOF, there is an advantage to extracting the modal parameters to use in the strain estimation, as evidenced by the difference between Direct ODS and Direct Modal methods. While Direct Modal is still in *a*-space, it is obviously a smoothed modal quantity which was a desired attribute of this work, and the results are good considering no FEM was required.

The Transformation ODS Method admittedly does not appear to be much of an improvement over the Direct ODS results, but does render modal quantity results. The comparison to Direct Modal is comparable; both are in *a*-space, have similar sensitivity to measurement noise, and suffer from filter edge effects. Given the amount of work that the Transformation ODS Method takes compared to the Direct Modal method, the latter would likely be an easier choice between the two. However, if Polytec Fastscan data and Strain Post-Processor are to be used, the Transformation ODS Method can be used to obtain modal strain shapes from that data.

Finally, the Transformation Modal Method is found to perform very well. The method is very robust against measurement noise, does not suffer from filter edge effects and provides results in full *n*-space. The obvious downside is the requirement to have a FEM of your test object. The FEM does not have to be perfectly correlated to test data, however the analytical shapes must span the space of the experimental shapes. The comparison of the experimental full-field modal strain shapes from the Transformation Modal Method to the FEM is expectedly very good, since they are a superposition of FEM shapes. The results may be a better indication of the actual strain fields than the FEM as they are experimentally derived and the model is not fully correlated. While surface strains were of interest in this work due to use of the 3D SLDV measurements, we note that this method can provide experimentally derived full-field *n*-space *volume* strains as well by substituting their analytical FEM counterparts into Eq. (4.9) in place of $\boldsymbol{\varepsilon}_n$ surface strains.

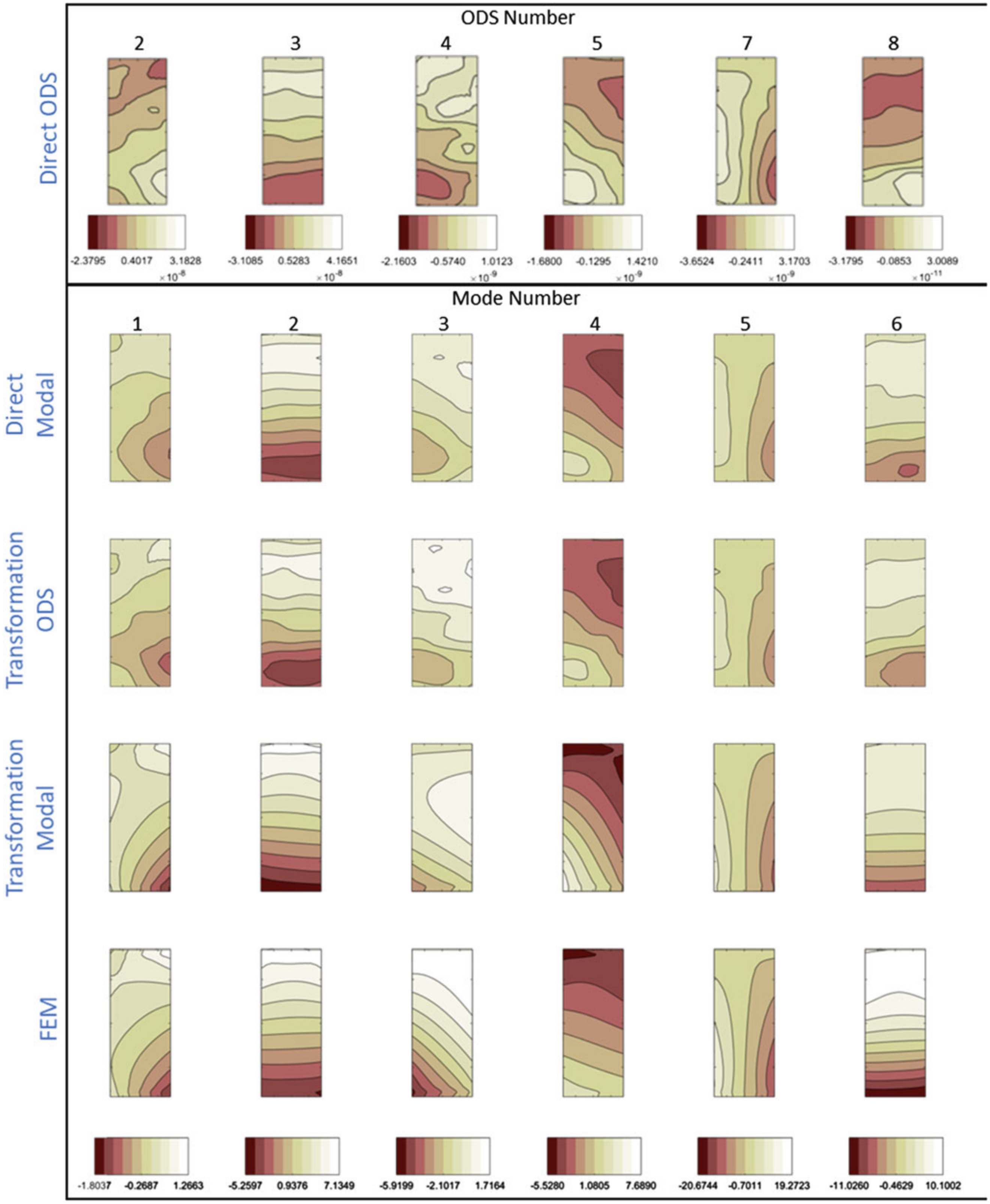

Fig. 4.19 Comparison of methods for X-face τ_{yy}

4.7 Conclusions

Several methods for determining full-field modal strain shapes from 3D SLDV data were evaluated. The Direct Modal method was found to work reasonably well, does not require a FEM, and provides improvements over the Direct ODS Method, which is considered as the current standard ODS strain shape measurement method. The use of direct measurements (ODS or modal) without some manner of filtering to smooth the displacements is not recommended due to the sensitivity to measurement noise in the strain estimation process. The Transformation ODS Method provides a means to convert ODS strain shapes to modal quantities, also without use of a FEM. However, if starting from nothing, the Direct Modal Method provided similar, if not better, results with less processing effort but potentially longer test times. Further, the SEREP smoothing using (noisy) ODS may not provide enough smoothing by itself, driving the need to use a spatial filter in addition. The test article used in this work was observed to exhibit nonlinear behavior, which is believed to have caused a reduction in the ODS methods' effectiveness. Finally, the Transformation Modal Method was shown to work very well; it is robust against measurement noise, avoids spatial filter edge effects, results are obtained in full n-space, and either surface or volume strains can be estimated. The primary drawback is that a FEM is required.

Acknowledgements This manuscript has been authored by National Technology and Engineering Solutions of Sandia, LLC. under Contract No. DE-NA0003525 with the U.S. Department of Energy/National Nuclear Security Administration. The United States Government retains and the publisher, by accepting the article for publication, acknowledges that the United States Government retains a non-exclusive, paid-up, irrevocable, world-wide license to publish or reproduce the published form of this manuscript, or allow others to do so, for United States Government purposes.

References

1. Cazzolato, B., Wildy, S., Codrington, J., et al.: Scanning laser vibrometer for non-contact three-dimensional displacement and strain measurements. In: Proceedings of ACOUSTICS, Geelong, 24–26 Nov 2008
2. Weisbecker, H., Cazzolato, B., Wildy, S., et al.: Surface strain measurements using a 3D scanning laser vibrometer. Exp. Mech. **52**(7), 805–815 (2012)
3. Reyes, J., Avitabile, P.: Use of 3D scanning laser vibrometer for full field strain measurements. In: De Clerck, J. (ed.) Experimental Techniques, Rotating Machinery, and Acoustics, Volume 8 Conference Proceedings of the Society for Experimental Mechanics Series. Orlando, Springer (2015)
4. O'Callahan, J., Avitabile, P., Riemer, R.: System Equivalent Reduction Expansion Process (SEREP). In: Proceedings of the 7th International Modal Analysis Conference, Las Vegas, 1989
5. Rohe, D., Schoenherr, T., Skousen, T., et al.: Testing summary for the box and removable component structure. In: Proceedings of the 37th International Modal Analysis Conference, Orlando, Jan 2019
6. Hensley, D., Mayes, R.: Extending SMAC to multiple references. In: Proceedings of the 24th International Modal Analysis Conference, St. Louis, pp. 220–230, Feb 2006
7. Felippa, C.: Introduction to Finite Element Methods (2004), Chapter 17. Department of Aerospace Engineering Sciences, University of Colorado at Boulder. https://www.colorado.edu/engineering/CAS/courses.d/IFEM.d/. Accessed online 2018

Chapter 5
Characterization of a Small Electro-Mechanical Contact Using LDV Measurement Techniques

Kelsey M. Johnson

Abstract Numerically modeling chatter behavior of small electrical components embedded within larger components is challenging. Reduced order models (ROMs) have been developed to assess these components' chatter behavior in vibration and shock environments. These ROMs require experimental validation to instill confidence that these components meet their performance requirements. While achieving conservative results, experimental validation is required, especially considering that the ROMs neglect the viscous damping effects of the fluid that surrounds these particular components within their system. Dynamic ring-down data of the electrical receptacles in air will be explored and will be assessed as to whether that data provides a validation data set for this ROM. Additional data will be examined in which dynamic ring-down data was taken on the receptacle while submerged in an oil, resulting in a unique experimental setup that should prove as a proof of concept for this type of testing on small components in unique environments.

Keywords LDV · Experimental methods · Modal testing

5.1 Introduction

This report will explore the setup and results of an experiment conducted by Johnson [1] that aimed to provide a model validation data set for a chatter predicting ROM developed by Lacayo and Brake [2]. This particular model is of a small electrical assembly made up of a cylindrical pin and a bifurcated receptacle. The ROM models the receptacle as two pre-loaded leaf-springs in the shape of a tuning fork. There is added complexity to this assembly, as there is a viscous fluid filling the entire enclosure. The ROM currently neglects those effects of fluid damping on the system.

This experiment focused solely on the modal characteristics of the receptacle. This allowed for a simplified test that could still provide useful data for the modelers as well as proof of concept for the experimental setup. First, dynamic ring-down data of the bifurcated receptacle was measured in air to validate and instill confidence in the current state of modeling for the system. Then, the same test was performed in a relatively large volume of fluid to observe the damping effects on the receptacle.

The conditions of this particular sub-assembly lead to a unique experimental setup. First, the size of the electrical receptacle had to be taken into account. It is important to validate models of such small components as small-scale effects, such as friction and effective mass, can be large contributors and are challenging to model correctly. This small size leads to unconventional actuation and measurement techniques so as to not mass-load the test article. Second, the experimental setup had to accommodate the fluid found around the system, as viscous damping will affect the modal characteristics of the receptacle. The fluid also creates a challenge with the actuation and measurement of the test article. The methods employed for this experiment needed to be able to survive in a fluid environment. The techniques used during this test as well as the challenges associated with them will be explored further.

Sandia National Laboratories is a multimission laboratory managed and operated by National Technology and Engineering Solutions of Sandia LLC, a wholly owned subsidiary of Honeywell International Inc., for the U.S. Department of Energy?s National Nuclear Security Administration under contract DE-NA0003525.

K. M. Johnson (✉)
Vibration and Acoustic Simulation – Org 1521, Sandia National Laboratories, Albuquerque, NM, USA
e-mail: kmjohn@sandia.gov

C. Niezrecki et al. (eds.), *Rotating Machinery, Optical Methods & Scanning LDV Methods, Volume 6*, Conference Proceedings of the Society for Experimental Mechanics Series, https://doi.org/10.1007/978-3-030-12935-4_5

Fig. 5.1 Test fixture with fluid [1]

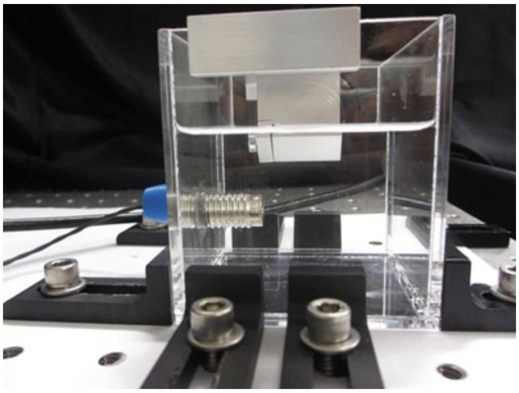

Fig. 5.2 Voltage signal for actuator [1]

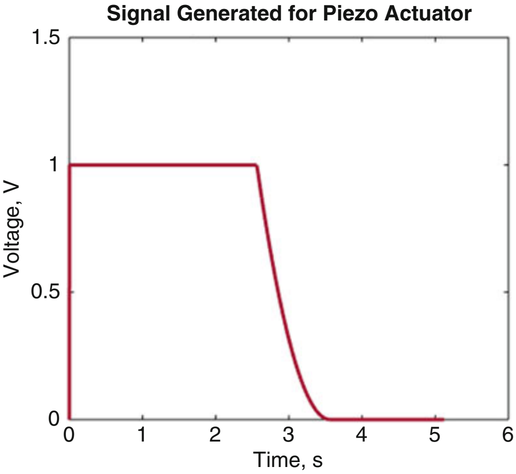

5.2 Experimental Setup

With the unique test boundary conditions, the setup pictured below was developed. This fixture creates a clamped boundary condition for the receptacle while suspending it in a tank made of plexiglass (Fig. 5.1).

The actuation of the test article was provided by an Encapsulated PICMA® Stack Piezo Actuator made by Physik Instrumente [3], which is tolerant of fluid environments. This method was chosen over other non-contact actuation methods, such as ultrasonic, as the least invasive way to excite the test article without exciting the surrounding fluid excessively. The actuator had a custom voltage signal applied to excite the part while pulling away slowly after actuation so as to not affect the measurement of the test article. This signal is depicted in Fig. 5.2.

A laser doppler vibrometer is a common method for measuring the responses of test articles that cannot be mass-loaded by accelerometers. For this experiment, a Polytec PSV-400 one dimensional system was used. A close-up module was added to aid in focusing on the small receptacle. Plexiglass was chosen as the container so that the alpha angle to the normal part surface wouldn't be dramatically affected. The different test setups between air and added fluid changed the position of the laser heads slightly, but it was simple to attain a good focus on the points regardless. Using Polytec's proprietary software, the voltage signal was supplied to the actuator and was timed with the measurement scans of each point.

The fluid used in the test setup is a XIAMETER® PMX-200 silicon oil with two different viscosities of 10cs and 20cs [4, 5]. Varying the viscosity of the oil was intended to give insight as to the effects of that viscosity on the part dynamics. This also gives more data for modelers as to the differences between the part being surrounded by varying oils as well as air.

5.3 Testing and Results

As mentioned above, the Polytec software would supply the actuation signal to the piezoelectric actuator. Fifteen measurement points were created on one tine of the bifurcated receptacle. This was done to maximize the measurement surface area, but sacrificed measurement data from the second tine. The Polytec software produced fast Fourier transform

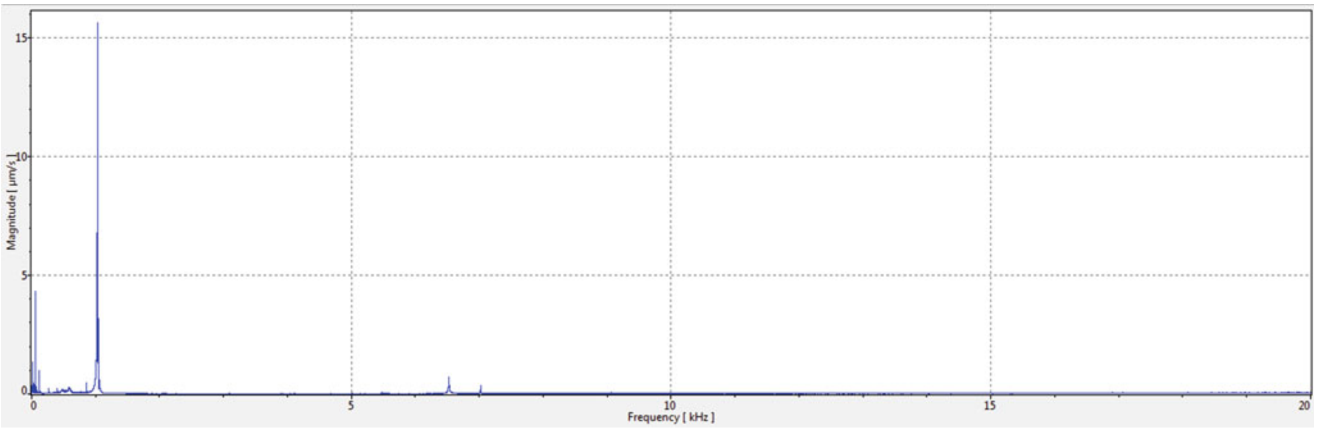

Fig. 5.3 Frequency contact of electrical contact in air [1]

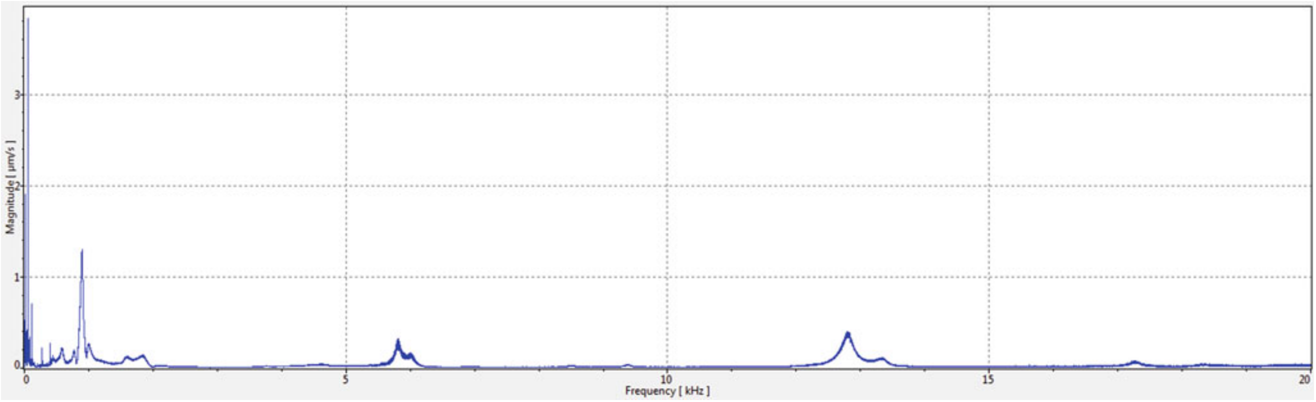

Fig. 5.4 Frequency contact of electrical contact in 10cs oil [1]

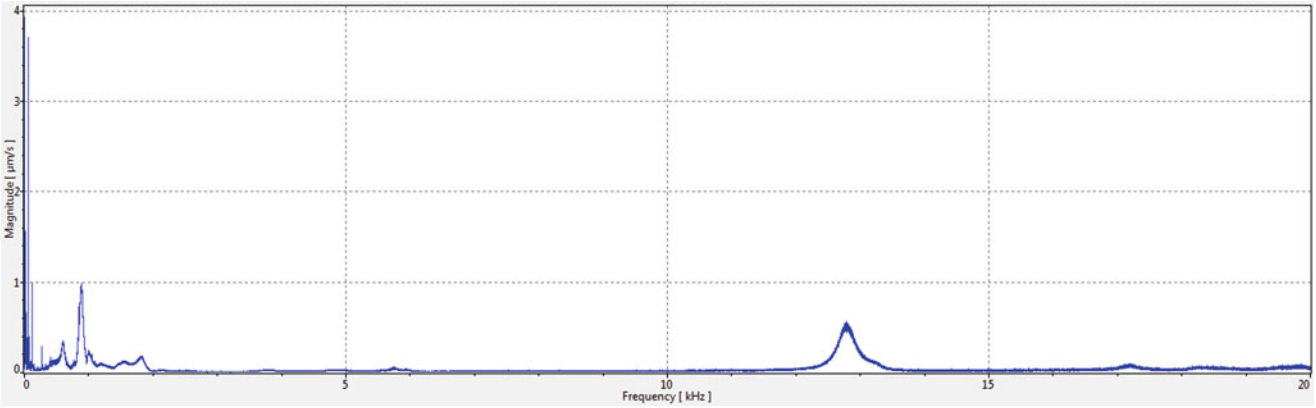

Fig. 5.5 Frequency contact of electrical contact in 20cs oil [1]

(FFT) data for each of the setups— one in air, one in 10cs oil, and the last in 20cs oil, as seen in Figs. 5.3, 5.4, and 5.5, respectively. These FFTs aren't quite right, as an input force measurement is required to get a proper transfer function. This is due to a challenge with the actuation method used. The displacement of the actuator is 14 µm ± 10%. Without a more complex test fixture, it is nearly impossible to get the actuator positioned to the part within that displacement value. The actuation provided is technically the fluid, including the air, being displaced by the actuator. This fluid movement is what excited the part enough for measurements to be taken by the LDV. Figures 5.6 and 5.7 display the measurement results from the LDV of the first and second bending modes in air. All figures are referenced from Johnson's results [1].

Fig. 5.6 First bending mode in air [1]

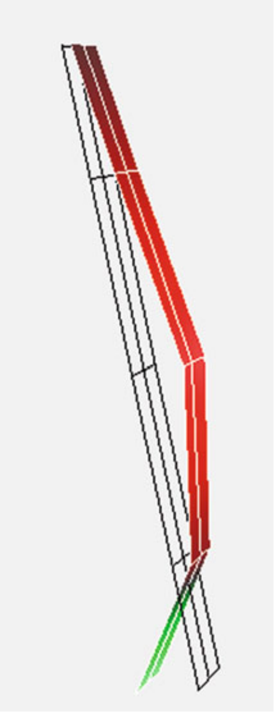

Fig. 5.7 Second bending mode in air [1]

To process the time history data, Johnson used the Short Time Fourier Transform (STFT) method developed by Kuether at Sandia National Laboratories. In short, this method takes the instantaneous frequency and damping as well as the amplitude of the time history signal in short windows around the frequencies of interest. Using the estimated FFT from Polytec's measurements, Johnson was able to estimate the frequency locations of the modes of interest. Then, modal data was processed using the STFT method, which was more mathematically exact than Polytec's estimation. The settings used by Johnson for the STFT method can be found in [1].

First, we'll examine the results of the first bending modes of the system in the three different test configurations. Figures 5.8 and 5.9 show the Polytec measured FFT of the first bending mode in air and the STFT results. As mentioned before, the receptacle is bifurcated. This means that there will be an in-phase and an out-of-phase mode for every mode of interest. Theoretically, these modes should have the same frequency, but once losses are taken into account, it is expected that these in-phase and out-of-phase modes will be slightly separated. The first mode data for 10cs and 20cs oil is shown in Figs. 5.10 or 5.11 and 5.12 or 5.13, respectively.

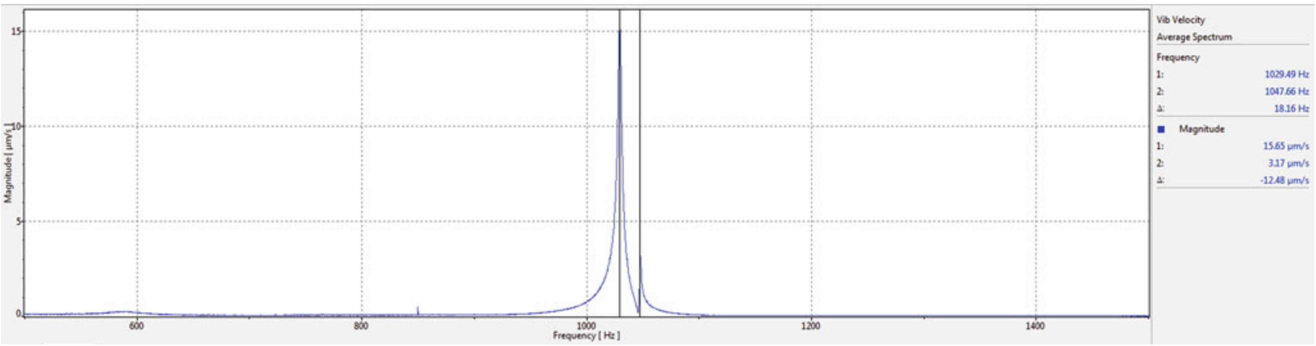

Fig. 5.8 Test in air – first bending mode [1]

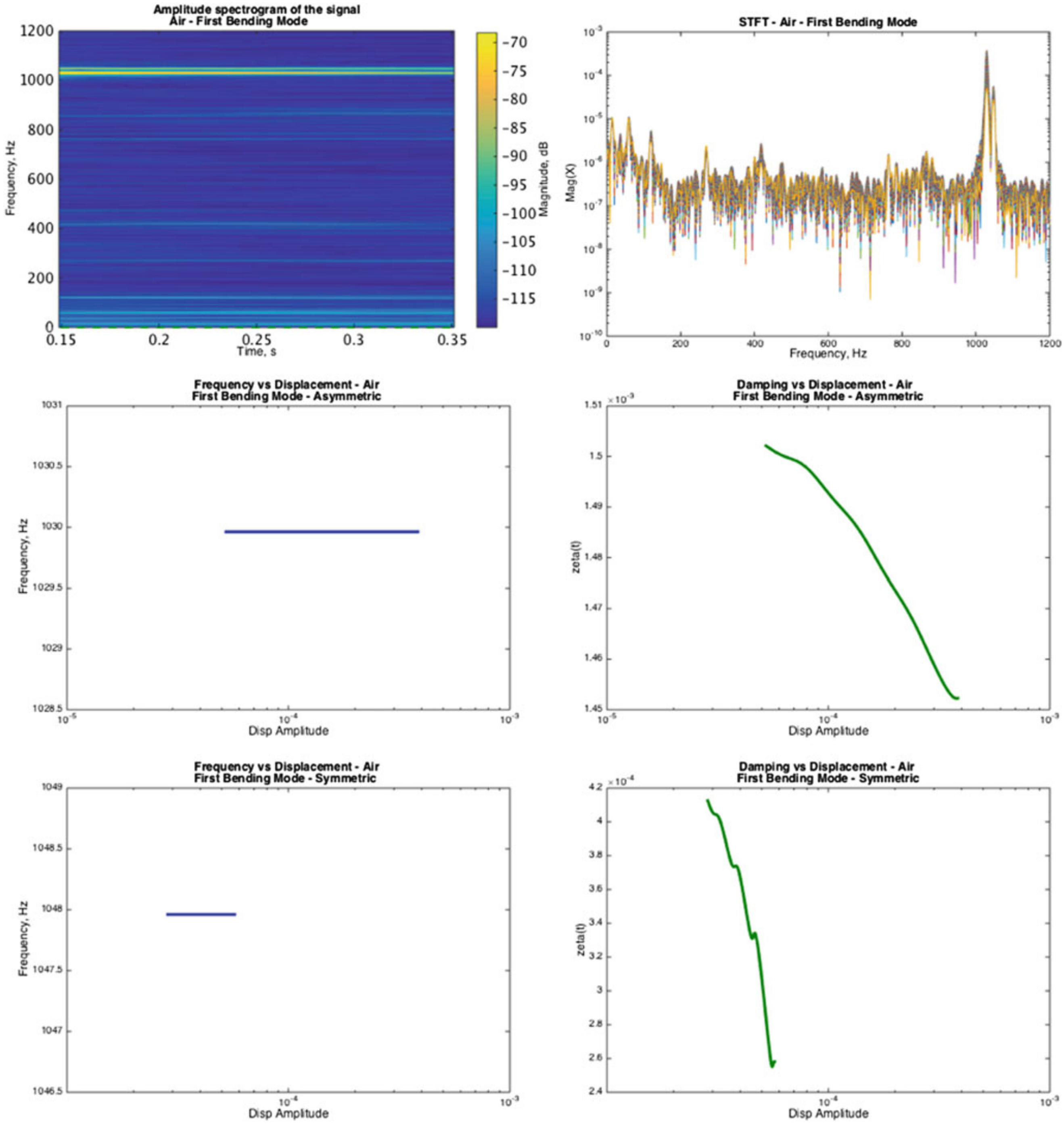

Fig. 5.9 Test in air – first bending mode STFT data [1]

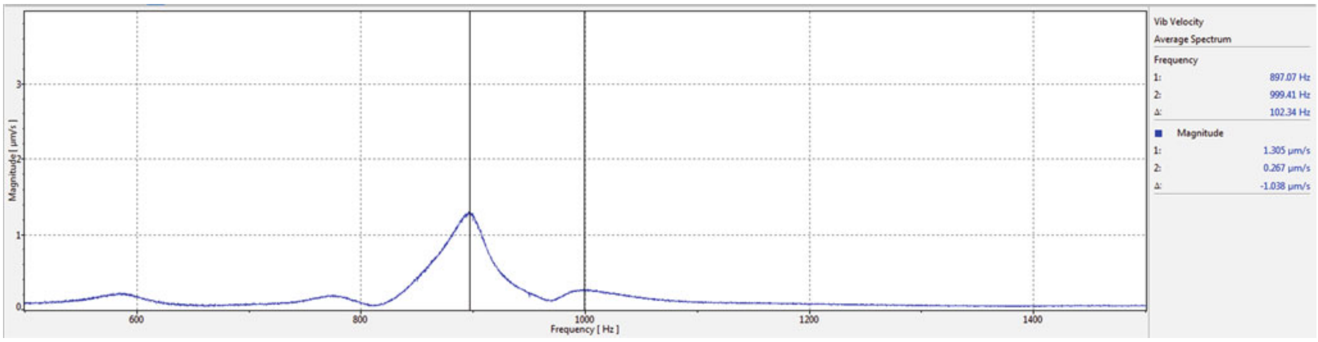

Fig. 5.10 Test in 10cs Oil – first bending mode [1]

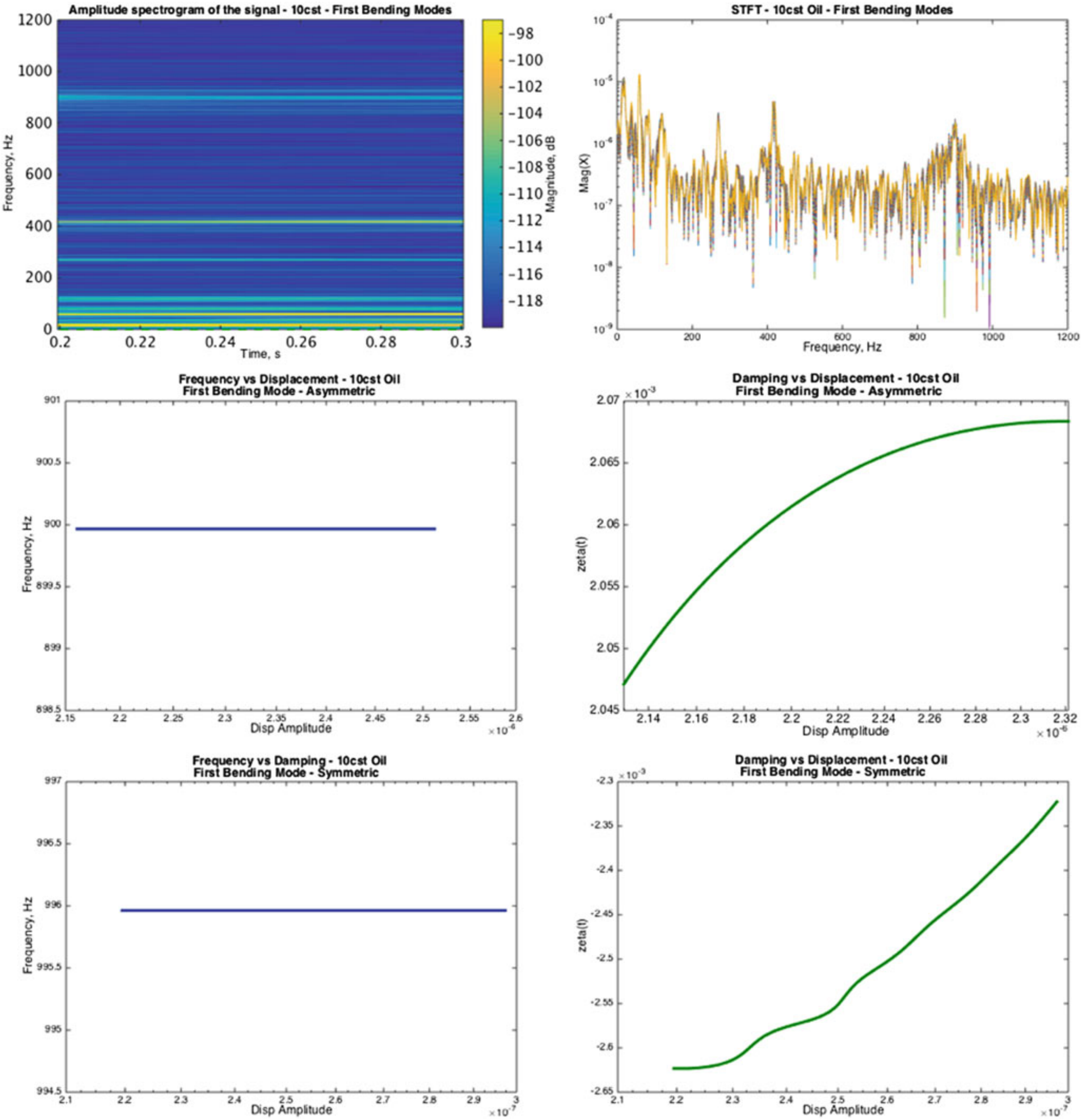

Fig. 5.11 Test in 10cs oil – first bending mode STFT data [1]

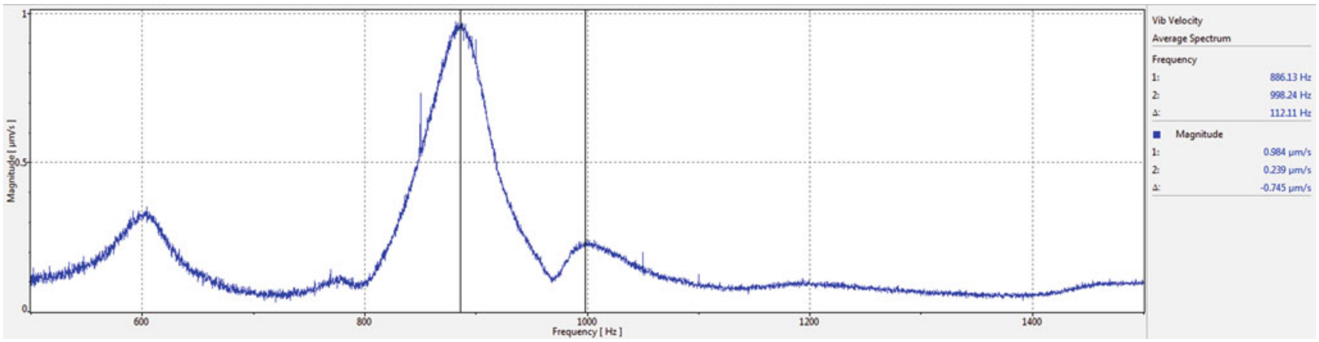

Fig. 5.12 Test in 20cs Oil – first bending mode [1]

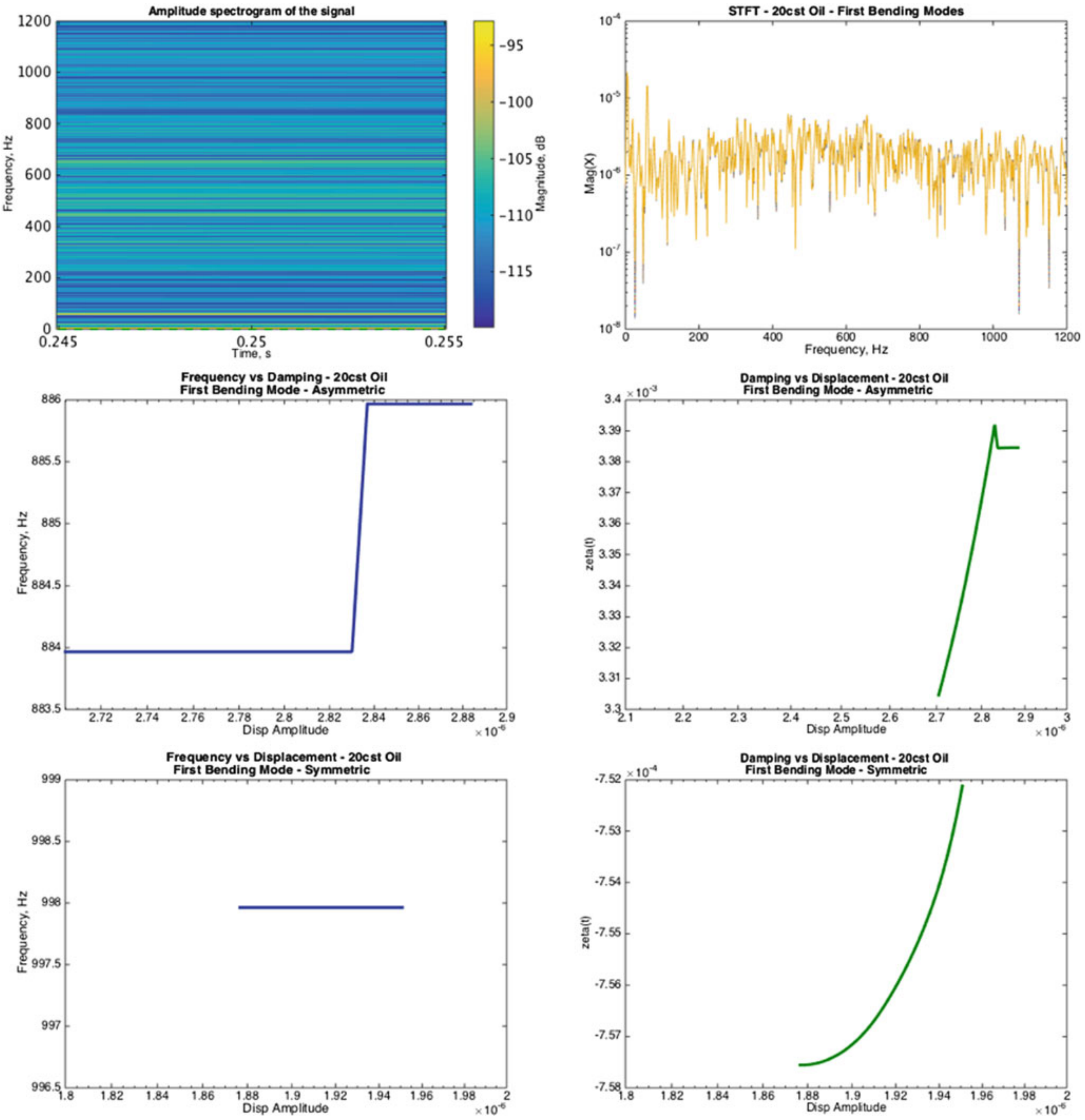

Fig. 5.13 Test in 20cs oil – first bending mode STFT data [1]

Table 5.1 STFT extracted frequency and damping for first bending modes [1]

	Air (in-phase)	Air (out-of-phase)	10cst (in-phase)	10cst (out-of-phase)	20cst (in-phase)	20cst (out-of-phase)
Frequency	1030.00 Hz	1048.00 Hz	899.97 Hz	995.96 Hz	884.17 Hz	997.96 Hz
Damping ( )	0.0015	0.0003477	0.0021	0.0019	0.0034	0.0007557

To summarize the above data, Table 5.1 shows the frequency and damping data extracted from each first bending mode in the above tests. This comparison shows that with increasing viscosity, the frequency separation between the in-phase and out-of-phase complimentary modes also increases as well as an overall frequency softening of the first modes. There were challenges with the STFT code processing the data with the added oil, described by Johnson. *"With increasing oil viscosity, there is an increase in the measurement noise, which is most obvious in the spectrogram and STFT of the 20cst data. The code is also having difficulty finding the first in-phase bending mode frequency peak. This is likely due to the displacements being damped by the oil as well as the oil movement continuing past the actuation signal, causing more actuation in various directions. There are also more fixture modes measured in oil than in air. Again, this is likely due to fluid movement during the measurements."* [1]

As mentioned in the experimental setup section, a one-dimensional LDV was used for this testing. This limited Johnson's ability to measure the responses of both tines of the receptacle together. The simultaneous response of both tines together was important to confirming the in-phase and out-of-phase modes. Two methods were used to confirm these complementary modes. Both tests were completed without the added fluid. First, the one dimensional LDV was angled to the part so as to maintain measuring the surface of the front tine of the receptacle, and also catch the inside edge of the back tine. The data was measured with Polytec software, then processed in MATLAB®. The 2D coordinates measured by the Polytec 400 were transformed to 3D coordinates manually. This transformed data was then processed through Randy Mayes Synthesize Modes and Correlate algorithm (SMAC) [6]. This algorithm is ideal for closely spaced modes, which was perfect for this particular situation of close complementary modes. The measurement point selection and processing is described more in [1]. The results from SMAC are shown in Figs. 5.14 and 5.15. SMAC was able to confirm for Johnson that the in-phase mode was located at the lower frequency and the out-of-phase mode was located at the higher frequency. This makes sense, as a base deformation mode would be expected to be at a lower frequency.

The second method used to confirm the order of the first bending modes was the use of a 3D LDV. A Polytec PSV-500 was used. With this updated technology, measurements were able to be taken along the thin side profile of the tines. This allowed for Johnson to see the measured response of both tines at once. The measured FFT can be seen in Fig. 5.16 and the measured first bending mode FFTs can be seen in Fig. 5.17. Figures 5.18 and 5.19 show the real-time mode shape data measured by the Polytec PSV-500. This data agrees with Mayes' SMAC method and the STFT data processed by Johnson.

5.4 Model Validation

Lacayo and Brake employed the efforts of Blecke to create a modal model of the electrical system [7]. She used Sandia's Salinas Structural Dyanamics code for this model. Table 5.2 shows a comparison between the first bending modes extracted by Johnson's experiments and the first bending modes calculated by Blecke's high-fidelity model. There is error of about 20 Hz (∼2%) between the measured and calculated modes. Johnson states that this is likely due to fixturing within the experiment not exactly matching the fixed boundary condition of the model. There is added inherent error in the material damping model. Examining the extent that this material model variation has on the data would require a statistical study.

5.5 Conclusion

Experiments on small-scale components are inherently difficult. In this particular case, there was added complexity due to the viscous fluid environment. A unique test set up was developed, using the combination of LDV measurements and piezoelectric excitation to extract modal data from a small bifurcated receptacle, while also accounting for that fluid. This

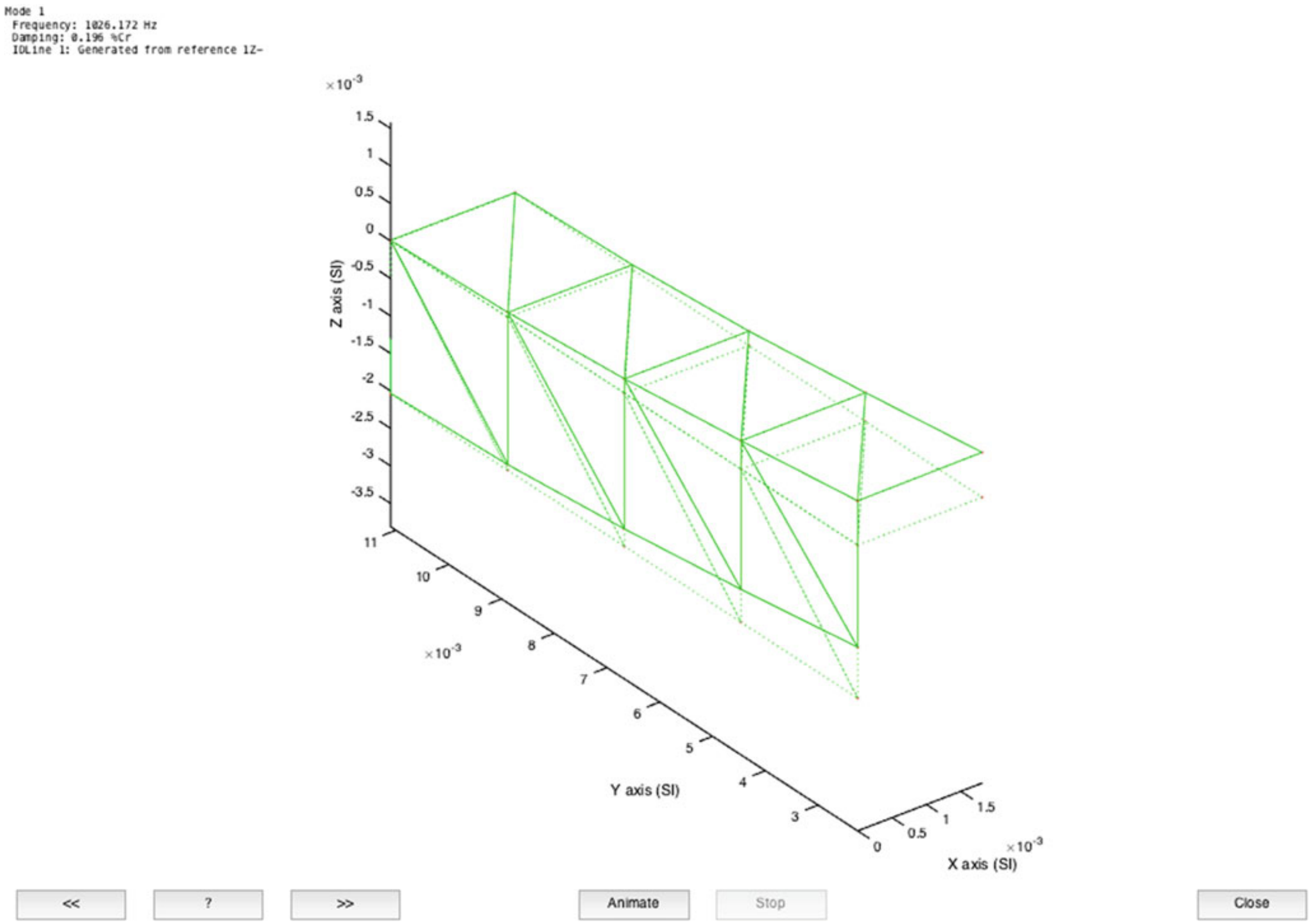

```
Mode 1
 Frequency: 1026.172 Hz
 Damping: 0.196 %Cr
 IDLine 1: Generated from reference 1Z-
```

Fig. 5.14 SMAC in-phase first bending mode [1]

experiment was able to validate current modeling efforts for the receptacle in an air environment, with minimal error, as well as provide additional data for modelers to account for fluid damping effects.

Challenges with this experiment can be examined further for improvement in the test setup. A more precise fixture could aid in aligning the actuator properly so as to accurately measure the input force to the test article. In regard to the test and model comparison, the model could be changed to reflect the test setup boundary conditions as well as an improvement in the experimental clamping of the test article. The test setup could also be expanded upon to better match the entire system. Future work will include testing the full component with a clear container on a shaker, allowing for real-time chatter monitoring. This work will provide the most realistic testing environment while also being able to excite the system with the actual vibration and shock profiles that cause the chatter events. This will lead to matching recorded chatter during testing to mode shape data during those events.

Model validation is key to providing low-cost confidence in the design phase of component development. Experimental data that can point to mode shapes of interest that could possibly cause functionality issues can help designers avoid these pitfalls in the future. Once there is sufficient data to support a model and its behaviors, these models will speed up the design to manufacturing process and lead to more reliable components.

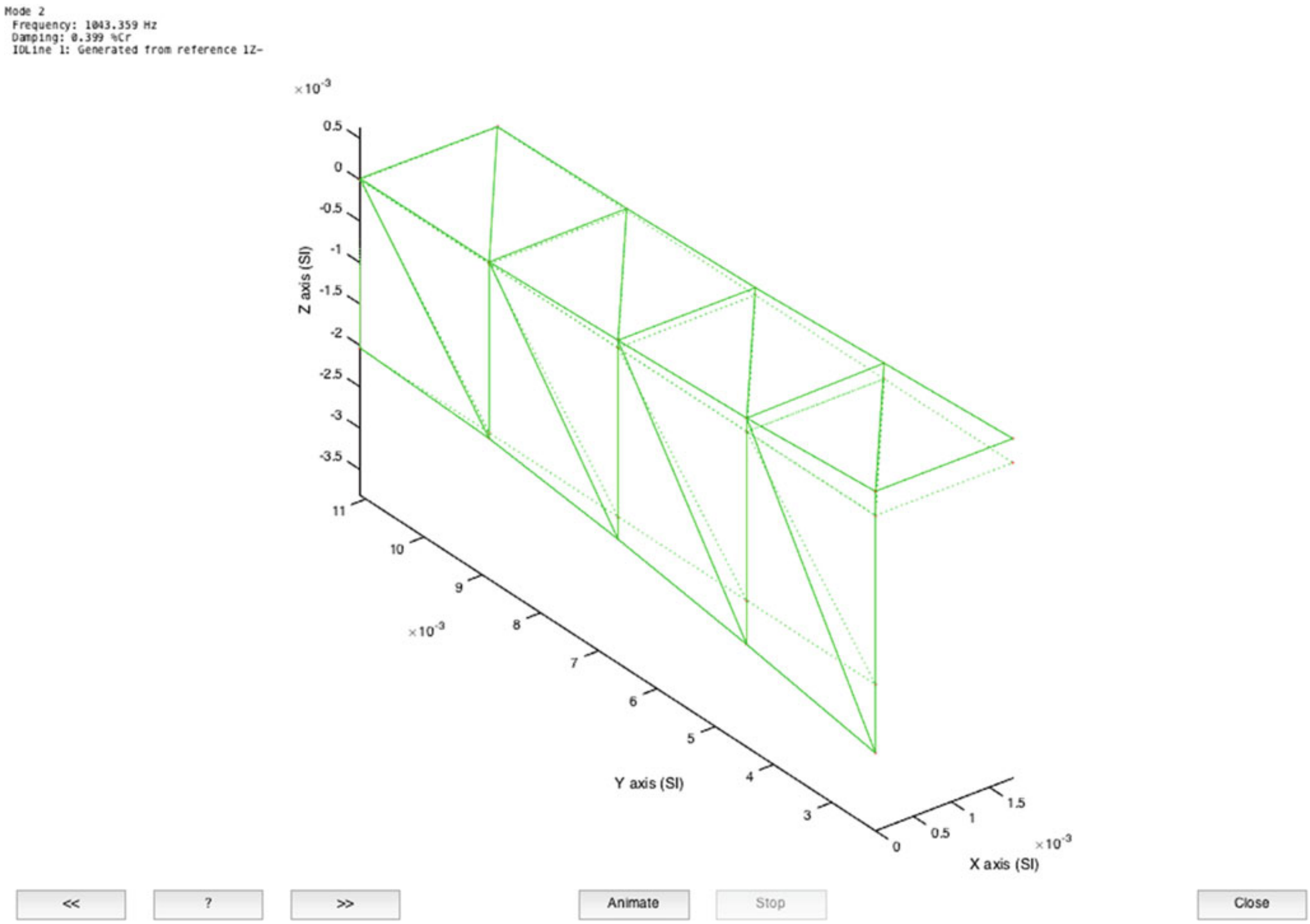

```
Mode 2
 Frequency: 1043.359 Hz
 Damping: 0.399 %Cr
 IDLine 1: Generated from reference 1Z-
```

Fig. 5.15 SMAC out-of-phase first bending mode

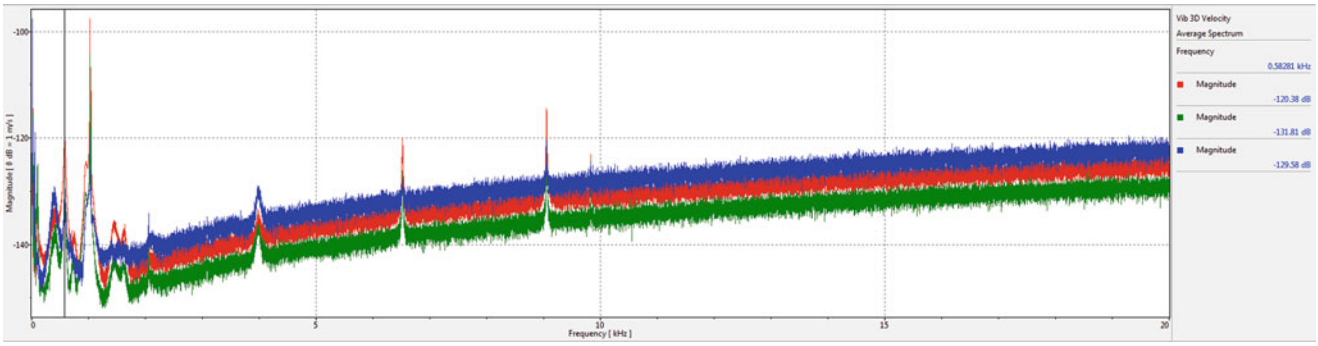

Vib 3D Velocity
Average Spectrum
Frequency
0.58281 kHz
🟥 Magnitude
-120.38 dB
🟩 Magnitude
-131.81 dB
🟦 Magnitude
-129.58 dB

Fig. 5.16 3D LDV FFT measurement [1]

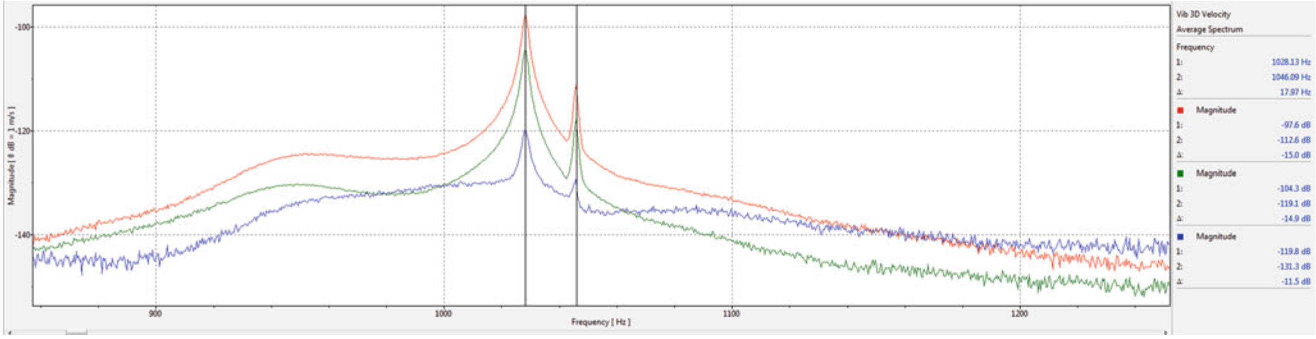

Fig. 5.17 3D LDV FFT first bending mode [1]

Fig. 5.18 3D LDV in-phase first bending mode [1]

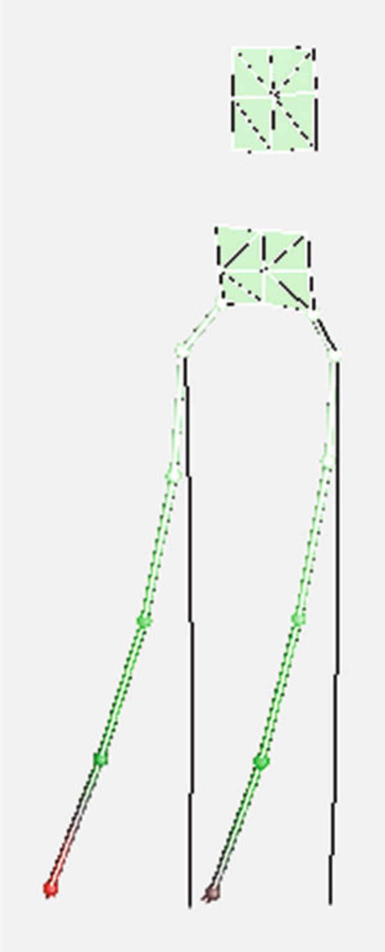

Fig. 5.19 3D LDV out-of-phase first bending mode [1]

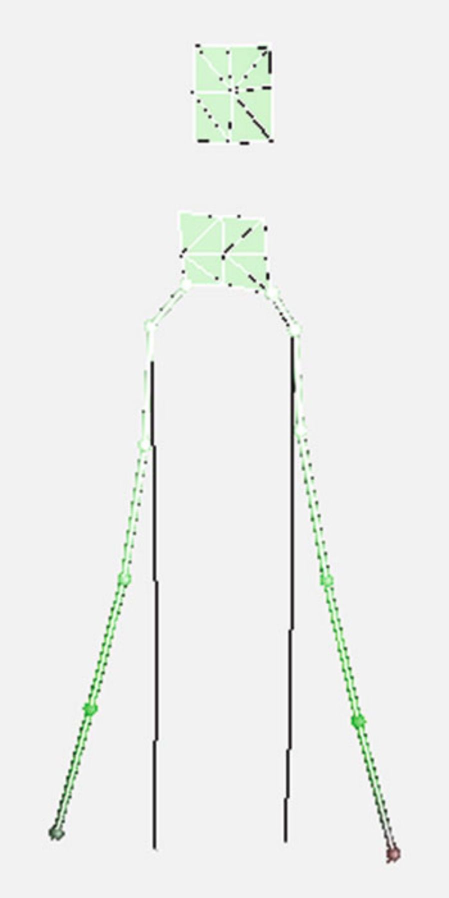

Table 5.2 Model vs experiment – first bending mode [1]

	Air – first bending mode (in-phase)	Air – first bending mode (out-of-phase)
High fidelity model frequency	1046.20 Hz	1053.70 Hz
Measured frequency data	1030.00 Hz	1048.00 Hz
% error	1.74%	0.54%

References

1. Johnson, K.M.: Characterization of a Small Electro-Mechanical Contact Using Non-conventional Measurement Techniques. University of New Mexico (2017)
2. Lacayo, R.M.: Title Omitted, SAND2015-1647 (OUO). Sandia National Laboratories, Albuquerque (2015)
3. *Encapsulated PICMA(R) Stack Piezo Actuators*, p. 9. PI Ceramic, Lederhose (2016)
4. Corning, D.: XIAMETER(R) PMX-200 Silicone Fluid 10 CS Safety Data Sheet (2017)
5. Corning, D.: XIAMETER(R) PMX-200 Silicone Fluid 20 CS Safety Data Sheet (2017)
6. Mayes, R.L.J.D.D.: A Modal Parameter Extraction Algorithm Using Best-Fit Reciprocal Vectors. Sandia National Laboratories, Albuquerque (1998)
7. Blecke, J.C.W.M.C.: Title Omitted, SAND2015-2032. Sandia National Laboratories, Albuqerque (2015)

Chapter 6
Remote Detection of Abnormal Behavior in Mechanical Systems

Greta Colford, Erica Jacobson, Kaden Plewe, Eric Flynn, and Adam Wachtor

Abstract Machinery can undergo many different types of operational faults during use. Mitigating these faults through scheduled maintenance programs or upon failure is costly, inefficient, and can introduce safety hazards. An alternative approach to identifying abnormal behavior in mechanical systems is through condition based monitoring, which is applied by taking measurements of machinery and using spectral analysis to diagnose faults. The signals produced by machines contain characteristic frequencies describing the operating state. The application of local sensors to monitor the health of mechanical systems is often expensive or not feasible; it is of interest to find methods of remote sensing to allow for detection of abnormalities in mechanical systems without the need for sensors at the local point of operation. This work intends to utilize the method of remote detection to study the diminishment of fault feature observability as a function of sensor location relative to operating equipment. In this study, the procedure used for fault detection consists of the following: (1) collect signals for rotating machinery operating in a healthy, faulty, and off state (2) identify features that are unique to a faulty operating state (3) use those features to identify faulty behavior. This procedure is performed at three locations. For each location, the observable feature for a healthy, faulty and motor off state is calculated and compared using the statistical mean, standard deviation, p-value and Bhattacharyya distance. The relationship between fault observability and distance is presented as a function of Bhattacharyya distance and classified based on a one-way ANOVA test. Machine fault diagnosis becomes more difficult as the measurement location increases. At greater distances, there is no statistical significance between healthy and faulty machine operation. Using a predictable frequency response, machine faults can be correctly identified up to a certain threshold determined by environment noise.

Keywords Condition Monitoring · Remote Sensing · Rotating Machinery · Signal Processing · Spectral Analysis

6.1 Introduction and Motivation

Condition Based Monitoring (CBM) is used to identify developing faults in mechanical systems and is desired by many industries because of the significant economic and safety benefits that result from using this technology [1]. Specifically, CBM can be used as an effective damage detection method for machinery or mechanical systems. A key part of CBM is to acquire measurements of the system of interest and use the signals collected to diagnose the extent of damage experienced by the machine. Local measurements on the system of interest are not always possible due to limited access or excessive instrumentation costs. In this case, remote sensing can be used to collect signals for CBM and machine fault diagnosis. When considering a Remote Condition Based Monitoring (RCBM) system, the distance between the equipment of interest and the sensing system is a highly influential variable. As the sensing distance from the point of interest increases, the environmental dependence of the signal being collected increases and, as a consequence, the signals of interest are less distinguishable. In this study, the effect of distance in the process of RCBM is investigated experimentally.

G. Colford · E. Jacobson
Michigan Technological University, Houghton, MI, USA

K. Plewe
University of Utah, Salt Lake City, UT, USA

E. Flynn · A. Wachtor (✉)
Los Alamos National Laboratory, Los Alamos, NM, USA
e-mail: ajw@lanl.gov

C. Niezrecki et al. (eds.), *Rotating Machinery, Optical Methods & Scanning LDV Methods, Volume 6*, Conference Proceedings of the Society for Experimental Mechanics Series, https://doi.org/10.1007/978-3-030-12935-4_6

6.2 Background

Machine fault diagnosis and monitoring is not a new task, but recent developments in sensor technology, data processing, and online monitoring open the possibility of improvements. Multiple methods of machine fault diagnosis exist, with the most basic being operating the machine to failure. Most failures are the cause of inadequate training and misdiagnosis by the machine analyst [2]. Another method of machine fault monitoring includes implementing a time-based maintenance schedule where the machinery would cease operation and be analyzed for damage at periodic time intervals. Even time-based maintenance systems have shortfalls which include the cost and hazards associated with pausing machine operation, misdiagnosis on behalf of the human analyst, and delayed identification of machine damages. By outfitting machines of interest with localized sensors, continuous machine monitoring can take place and damages can be detected before failure. However, implementing localized CBM can come at a high capital cost and potential issues with machine accessibility could exist. With new developments in remote sensing and machine learning, the practicality of implementing machine fault diagnosis methods in systems that don't facilitate local data collection is increasing.

With the availability of vibration signals (or another frequency characteristic measurements such as electrical signatures) associated with rotating machinery, common fault types can be diagnosed. Faults that occur in machinery include unbalance, misalignment, shaft cracks, rotor rub, looseness and bearing faults; all of which produce frequencies that can be characterized and detected with available equipment and signal processing techniques [3]. Observations in operating behavior and digital signals from AC motors such as characteristic frequencies, signal amplitudes, or ramp-up/ramp-down behavior can be attributed to common AC induction motor abnormalities. The fault case for this study is a combination of bearing faults, which included inner and outer race defects, as well as ball bearing defects. The frequencies of each fault can be calculated based on the physical properties of the bearing.

CMB is typically implemented by collecting dynamic measurements of the mechanical system over time, extracting features that indicate damage from the measurements, and performing a statistical analysis of the extracted features to determine the state of the mechanical system [1]. Two common methods for performing fault detection of induction motors are current analysis and vibration analysis. The superiority of each method is dependent on the type of fault being detected. For example, Oakridge National Laboratory has been successful with remote damage detection on their nuclear power plants using motor current signature analysis (MCSA) on the motor control power lines, successfully monitoring and detecting faults from hundreds of feet away [4], and vibration analysis has been used to detect and diagnose electrical faults in induction motors [5].

6.2.1 Modeling

Certain faults can be predicted if some basic properties of the operating system are known. Some abnormalities in the current and vibration spectrums of AC induction motors can determine what type of fault is present in the motor. For example, the SQI Machinery Fault Simulator instruction manual has a list of key frequencies and their associated faults that come with the kit. An experiment performed on the SQI Rotating Machinery Fault Simulator detected bearing faults through vibration spectral analysis. The harmonics of the running frequency were significantly increased in amplitude during faulty operation. Characteristic frequencies of the bearing can also be spotted on the spectrum, but identification requires extensive knowledge of the bearing geometry. These frequencies appear as sidebands on either side of the fundamental supply frequency [6].

6.2.2 Data Acquisition

Some literature states that vibration measurements alone are insufficient to indicate electrical induction motor issues [7]. Others studies use accelerometers to detect most electrical faults [5]. Others have used thermal imaging, microphones, and acoustic emissions sensors for fault detection. It was determined that the microphone was not able to read far-field measurements without serious attenuation. The thermal imaging camera can only detect serious faults as they are happening, and is slow to respond. Both methods have high risk associated with environment noise and conditions [8].

6.2.3 Signal Processing

Common signal processing techniques used for modal analysis of rotating machinery include the Frequency Response Function (FRF), Fast Fourier Transform (FFT), Short Time Fourier Transform (STFT) and Wavelet Transforms. Frequency Response Functions (FRF) are used to identify characteristic frequencies and to define the relationship between an input and output in the frequency domain. The FFT is useful for identifying natural frequencies but doesn't retain temporal information, making its application limited in time-varying signals [3, 9]. All these techniques have been used to process machine fault signals. For this study, the Fourier transform is used to bring the time domain signal into the frequency domain for specific frequency content identification and analysis.

Damage detection in mechanical systems is typically based on the comparison of real-time signals to a baseline that represents the healthy state of the system. A coherence function is typically used to achieve this task in signal processing; as it is a measure that can quantify the correlation between two frequency signals. Transmissibility —a quantity used to compare a signal response to the system input— has also been implemented in mechanical fault detection procedures [10]. Wavelet transforms are also utilized as a mathematical tool for analyzing signals both in the time and frequency domain, and can provide a solution to the limitations to the traditional Fourier Transform [11]. Wavelet transformation is beneficial for data with wide frequency ranges, as the scale factors change how well the signal is represented in the frequency domain [11].

Rotating machinery, when operated at a constant speed, produces a periodic transient response in the vibrational signal measured. A pseudo wavelet system was developed by [12] based on a fusion of multiple quasi-analytic wavelet tight frames, and then the wavelet packets were evaluated using kurtosis and spectral kurtosis [12]. Measuring the RMS value of a signal reveals that different faults increase the RMS value in different frequency bands. One method of CBM is to monitor the RMS values real-time in different frequency bands. A fault is indicated when an RMS value exceeds a determined threshold [8].

Using a basic vibration signal, operational conditions can be monitored through calculations of RMS, kurtosis, and crest factor [8]. These factors are to be monitored in frequency bands and compared to the healthy signal baseline threshold. Another study recommends the use of a Hilbert Transform to increase accuracy of detecting electrical faults with vibration data [5]. Another method, called the Spectral Distribution Function (SDF) is a finite integration of the power spectral density (PSD) function. Through this integration, the data is compressed (good for storage issues), can be normalized (good for comparison), and is simple to model [13]. Marmugi et al. found that remote sensing of rotating machinery can been accomplished using radio-frequency optical atomic magnetometers (RF AM) to detect the magnetic signature of the rotating machine at a distance of up to 2 m [14].

6.2.4 Machine Learning and Data Fusion

Data fusion and machine learning in the application of condition-based monitoring can increase the accuracy of fault detection in mechanical systems. Fault frequency indicators can be derived from characteristic vibration signals, oftentimes correlating with the rotating speed of the motor and by extracting the amplitude of the frequency domain signal. By adding machine learning and data fusion, the process of fault detection becomes more accurate [11, 12]. Data can be combined at the raw level, state vector level, or the decision level. Only commensurate data can be combined at the raw level. Features are extracted from the data, then combined at the state vector level. Fusion at the decision level requires some sort of weighted decision method to combine all features [15].

One study successfully demonstrated combining current and vibration data (using Waterfall Fusion Process Model) after feature extraction and classification to enhance detection of a faulty bearing [16]. Another study used data fusion in combination with a mathematical dynamics model to detect faults faster and more confidently than with sensors alone [17]. However, this method requires extensive knowledge of the healthy structure and a substantial amount of training data.

Intelligent solutions for machine based condition monitoring include common machine learning algorithms such as artificial neural networks (ANN) and support vector machines (SVMs) [12, 18]. Konar et al. used a continuous wavelet transform and a feature extraction algorithm to feed three different parameters into an ANN and SVM in order to identify bearing faults. The ANN and SVM approaches were then compared using the same set of data and it was found that the SVM outperformed the ANN [11, 18] has demonstrated the use of a sophisticated three-level neural network in order to detect and classify faults by detecting the changes in fault frequency of rotating machines. There have been machine learning approaches that have been applied using total power over small frequency ranges as features in order to decide what state a fan system is in [19]. Data fusion over multiple sensors has also been utilized to make decisions regarding the state of a system [19].

6.3 Experimental Setup

An experiment investigating the effect of distance of RCBM on rotating machinery was performed using the SpectraQuest Inc. Machinery Fault Simulator (MFS). This device is capable of operating in a healthy condition and faulty condition, by installing components which reconstruct common machine faults. A combination fault bearing was installed to simulate a common bearing fault, which produced signatures related to inner race, outer race, and ball defects.

6.3.1 Data Acquisition Hardware and Testing Parameters

National Instrument's LabVIEW software and USB-4431 DAQ hardware (G in Fig. 6.1) were used to acquire the data. A local sensing station was created using multiple DAQ hardware, a desktop computer, and local sensing channels. A similar setup was created for remote sensing on a cart using one USB-4431 DAQ, a laptop computer, and remote sensing channels.

All data was collected simultaneously, where local and remote sensing systems were synced with an internal clock. A sampling frequency of 50 kHz and a block size of 3 minutes was used for each set. Ten sets of data were collected during a single test for a total of 30 minutes per test. This was repeated for healthy operation, faulty operation, and motor off.

Data was recorded by alternating healthy, faulty, and motor off tests to ensure statistical separation in the data was due to the machine operating conditions and not by time. The healthy and faulty bearing conditions were altered using the MFS kits on the right bearing pedestal (C, in Fig. 6.1). The machine alteration procedure was closely documented to make the switch between healthy and faulty as consistent as possible. The testing environment for each test was quantified and anomalies were recorded in a testing data sheet. The machine was turned on and left running for a minimum of 1 minute before recording data to eliminate any motor start-up transients in the recorded data. Time domain data was collected and saved from all sensors, with local and remote sensor groups saved as separate files.

6.3.2 Local Sensing Channels

The MFS came stock with a 3-phase 1 HP variable speed AC induction motor, speed controller, tachometer, and a digital speed readout. Figures 6.1 and 6.2 show the local sensing set up around the MFS. The variable speed controller (E) was used to control the motor speed. Testing was performed with a speed of 3400 RPM, which was shown to be near resonance during a ramp-up test of the motor. Motor speed of each test was recorded using the stock tachometer (D). A Pearson Electric Wide Band Current Monitor current probe (H) was used to monitor current going through the fault simulator's main power cord.

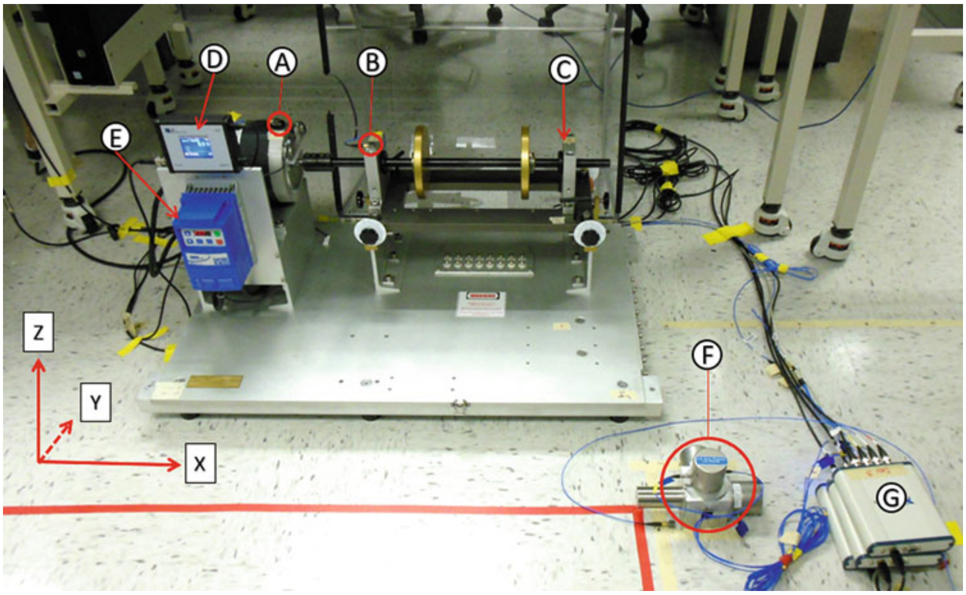

Fig. 6.1 Local measurement setup

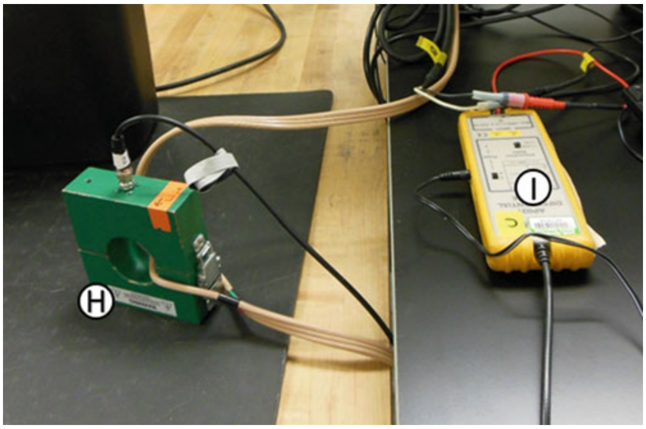

Fig. 6.2 Local current and voltage measurement setup

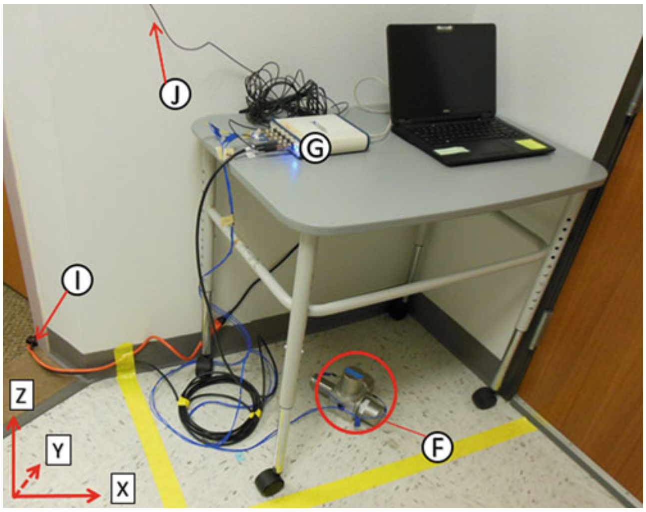

Fig. 6.3 Remote sensing setup

Local vibration data was recorded using accelerometers from MTS System's PCB Piezotronics. Two tri-axial accelerometers (356A43) with 10 mV/g sensitivity were adhered to the fault simulator on the motor (A) and left rotor deck bearing pedestal (B). These accelerometers did not move over the testing period.

6.3.3 *Remote Sensing Channels*

One seismic tri-axial accelerometer (F) (three uniaxial seismic accelerometers with 1200 mV/g sensitivity, 393 C) was used for remote vibration sensing. The seismic accelerometer was moved away from the zero point of the MFS to straight-line distances of 7 and 16 m.

A LaCroy AP031 differential probe (I in Fig. 6.3) was used to monitor the voltage used by the fault simulator. An LF Engineering Co. L-400 VLF/LF E-Probe antenna (J, not pictured) was placed near the fault simulator 5 feet in the Z direction and 4 feet in the negative Y direction, with respect to the zero distance location. The antenna was mounted to a wall close to the seismic accelerometer location. The voltage probe was plugged in to an outlet near the seismic accelerometer (I in Fig. 6.3). All voltage probe locations were on the same circuit, shown by building electrical schematics. Figure 6.3 shows the remote sensing set up, and Fig. 6.4 shows a schematic of the remote sensing locations with respect to the MFS origin.

The current, tachometer, local accelerometer, and voltage data were all recorded but not analyzed, and therefore omitted from this report of the study.

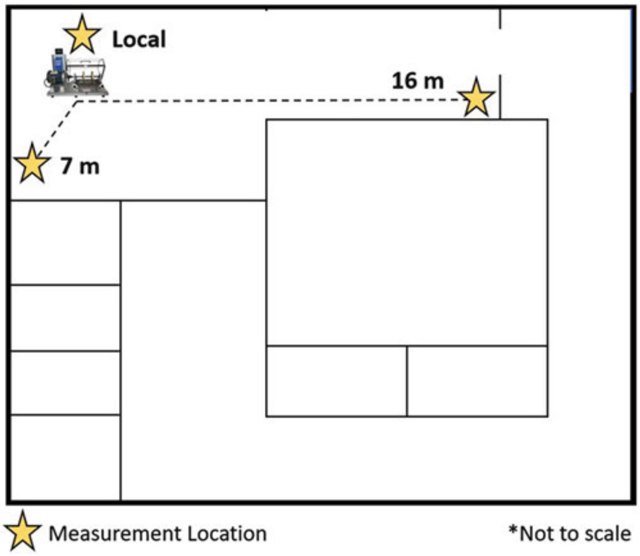

Fig. 6.4 Remote sensing schematic

6.4 Data Collection and Signal Processing

Key frequencies that would show separation of features between machine operating conditions are dependent on the type of fault. In the case of the combination bearing fault as provided in the fault simulator kit, new peaks appear at the inner and outer ball pass frequencies. The geometry of the provided combination fault bearing was used to calculate possible fault frequencies (Eq. 6.1). In this investigation, the ball pass inner frequency (BPIF) of 279.7 Hz showed the most significant difference between the healthy and faulty operating conditions. A frequency range of 278–282 Hz was selected to calculate features.

$$Ball\ Pass\ Inner\ Frequecy = \frac{n}{2} * \left(1 - \frac{BD}{PD}\cos(\theta)\right) * f \tag{6.1}$$

Where n is the number of balls, BD and PD are the ball and pitch diameter, respectively, theta is the contact angle, and f is the mechanical fundamental frequency – in our case the motor speed of 3400 RPM (or 56.6 Hz).

Once the frequency range of interest for separation was identified in the initial data sets, the recorded time data was down-sampled by a factor of 20. A Fourier transform was performed on the down-sampled data, preserving a frequency resolution of 0.0056 Hz but reducing the Nyquist frequency down to 1250 Hz. Autopower spectra were calculated for each 3-minute set within a test. The ten sets of autopower spectra were averaged together to produce one column of data for each sensor in a single test. This was repeated for all healthy, faulty, and motor off tests at local, 7 m, and 16 m from the MFS. Even though tests were recorded in a healthy/faulty/motor off order, some variation was noticeable between each 30-minute test. Averaging of the autopower spectra was used to attenuate background noise and transients that may have appeared within a set of data, but nowhere else in the test.

6.5 Data Analysis

6.5.1 Feature Selection

An investigation into features that exhibited high variation between the healthy and faulty operating state of the induction motor was important for (1) maximizing the observability of fault features and (2) reducing the feature space required for classification. In this work, 70–80 data points were collected at three different locations for each operating state: healthy, faulty, and motor off. Here, a single high-performing feature is selected to demonstrate the diminishment of the observability

Table 6.1 Bhattacharyya distance and p-value for all seismic accelerometer features calculated for 278–282 Hz

		SAX-RMS (g^2/Hz)	SeisX-Power (g^2)	SeisX-Kurtosis	SeisY-RMS (g^2/Hz)	SeisY-Power (g^2)	SeisY-Kurtosis	SeisZ-RMS (g^2/Hz)	SeisZ-Power (g^2)	SeisZ-Kurtosis
0 m	Bhattacharya Dist.	0.816	0.589	0.484	0.673	0.450	0.429	1.67	1.37	1.15
	P-Value	0.122	0.126	0.00370	0.0577	0.0474	0.00487	0.115	0.109	0.000105
7 m	Bhattacharya Dist.	0.610	0.449	0.206	1.09	0.835	0.277	0.864	0.648	0.544
	P-Value	0.0940	0.153	0.0375	0.0267	0.0421	0.0146	0.0525	0.0609	0.00951
16 m	Bhattacharya Dist.	0.260	0.0495	1.34	0.0416	0.0317	0.267	0.915	0.796	0.218
	P-Value	0.0778	0.301	0.0153	0.913	0.959	0.0732	0.313	0.326	0.297

From this set of features, SeisZ-Kurtosis is selected as the optimal feature because it has the largest Bhattacharyya distance in the group of features with p-value >0.05

of a fault feature as the distance between the sensor and the motor is increased. For this application, "high-performing" is defined using the Bhattacharyya distance and the p-value from a one-way ANOVA test.

The parameters that define the feature space that features are selected from include sensor type, frequency range and spectral variables (RMS, power and kurtosis). The p-value from a one-way ANOVA test is used as a preliminary metric for identifying features that show a statistically significant difference between healthy and faulty data sets. A p-value greater than 0.05 indicates that, for the selected feature, there is no evidence for variation between healthy and faulty measurements (null hypothesis validation) and the opposite validation is true for p-values less than 0.05. The Bhattacharyya distance, which has been shown to be a good metric for feature selection in classification problems [17, 20, 21], is used as a secondary measure for ranking features with a null hypothesis rejection. The Bhattacharyya distance, BD(x, y), between two distributions x and y is given by:

$$BD\left(x,y\right)=\frac{1}{4}\ln\left(\frac{1}{4}\left(\left(\sigma_x^2\right)/\left(\sigma_y^2\right)+\left(\sigma_y^2\right)/\left(\sigma_x^2\right)+2\right)\right)+\frac{1}{4}\left(\left(\mu_x-\mu_y\right)^2/\left(\sigma_x^2+\sigma_y^2\right)\right) \tag{6.2}$$

The Bhattacharyya distance represents the separation between two distributions, based on the mean (μ) and standard deviation (σ) of each. Hence, in this application, features with the highest Bhattacharyya distance between healthy and faulty data sets are used for relating fault feature observability to distance.

Table 6.1 includes the Bhattacharyya distance and p-value for each feature calculated for the seismic accelerometer over the frequency range of 278–282 Hz. Using the procedure described above and outlined in Fig. 6.5, the seismic Z-Axis kurtosis feature was selected as the optimal feature within this set. This feature (SeisZ-Kurtosis) will be used to explain the results from this work.

6.6 Results

The results from this study are drawn from comparing healthy, faulty and motor off distributions for the SeisZ-Kurtosis feature over the frequency range of 278–282 Hz. The power spectrum for Z direction at the various test locations can be seen in Fig. 6.6. At the local measurement location, the spectral magnitude of healthy and faulty response is separated from environment noise, with an increase at the inner ball pass frequency in the faulty data. This peak is still detectable at 7 m, but the amplitude falls closer to the environment noise. At 16 m, the faulty operating case is barely distinguishable from the background noise. A tight frequency range around a predictable frequency for feature detection is critical to separate out background noise from healthy and faulty operating cases.

While the SeisZ-Kurtosis feature outperformed a subset of the feature space that was studied in this work, it is likely that there are other features outside of the feature set shown in Table 6.1 that have equal or better performance metrics. Beyond the procedure that is outlined for the feature selection process, consideration was also given to the expected versus observed behavior to avoid anomalies. For example, referencing Table 6.1, the SeisX-Kurtosis feature is considered an anomaly because it does not show a consistent feature trend as the sensors are moved from 0 m to 16 m.

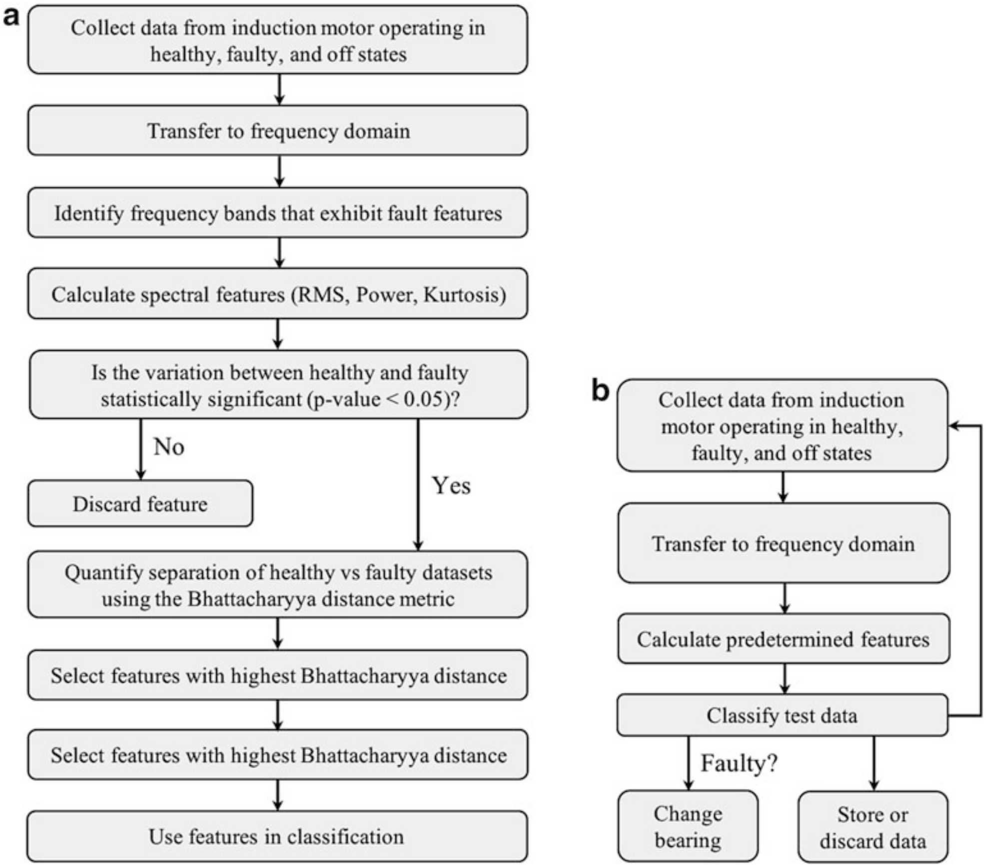

Fig. 6.5 (**a**) Process flow diagram for feature selection in classification procedure. (**b**) Process flow diagram for application phase of classification procedure

In Fig. 6.7, box-plots for local, healthy and motor off measurements are shown for each location. Within these boxes, the 25th and 75th percentiles are represented by the lower and upper boundaries of the boxes, the line inside of the boxes represents the median and the length of the whiskers on both ends of the box are the outlier thresholds. The motor off data is plotted alongside the healthy and faulty data to ensure that the information contained in the signals is independent of the noise floor. Taking this into consideration, it is evident that the combination of measurement, processing and analysis techniques that were used in this study was able to capture information at 0 m and 7 m, but not at 16 m. This is because the motor off features for 0 m and 7 m both behave as expected based on Table 6.1 and don't resemble the calculated noise distribution. In Figs. 6.6 and 6.7, it is evident that at 16 m, the healthy and faulty signals are strongly correlated to the noise distribution.

Kurtosis is a useful feature for identifying bearing faults because it successfully quantifies power impulses that are caused by cyclic impacts. These impulses appear in the frequency domain as sharp peaks occurring at the respective impulse frequency. Here, the ball pass frequency for the inner race is identified within the range of 278–282 Hz and it is shown in Fig. 6.7 that calculating the kurtosis over this range for the z-axis signals is successful in separating healthy versus faulty operating conditions at 0 m and 7 m. It is important to note that kurtosis is dependent on the shape of a distribution, and doesn't necessarily represent the magnitude of a detected fault. Hence, the increase in magnitude in the healthy and faulty distributions going from 0 m to 7 m is representative of the wave propagation path from the point of initiation to the sensor, not the fault observability at each location. The fault observability can be recognized by the separation of distributions in Fig. 6.7 or by the Bhattacharyya distance in Fig. 6.8.

The classification threshold shown in Fig. 6.8 represents the fault observability limit, with p-values less than and greater than 0.05 indicating that the fault is and is not observable, respectively. For p-values less than 0.05, the Bhattacharyya distance acts as a metric for relative observability. On this basis, the expected decrease in observability with sensing distance is depicted in Fig. 6.8. This decrease in observability can be attributed to the signatures of the machine attenuating to the level of measured environment noise. Therefore, the average signals of healthy and faulty are dominated by noise and not the mechanical signatures. To increase positive detection at further distances, greater separation is needed between the environment noise and machine signatures.

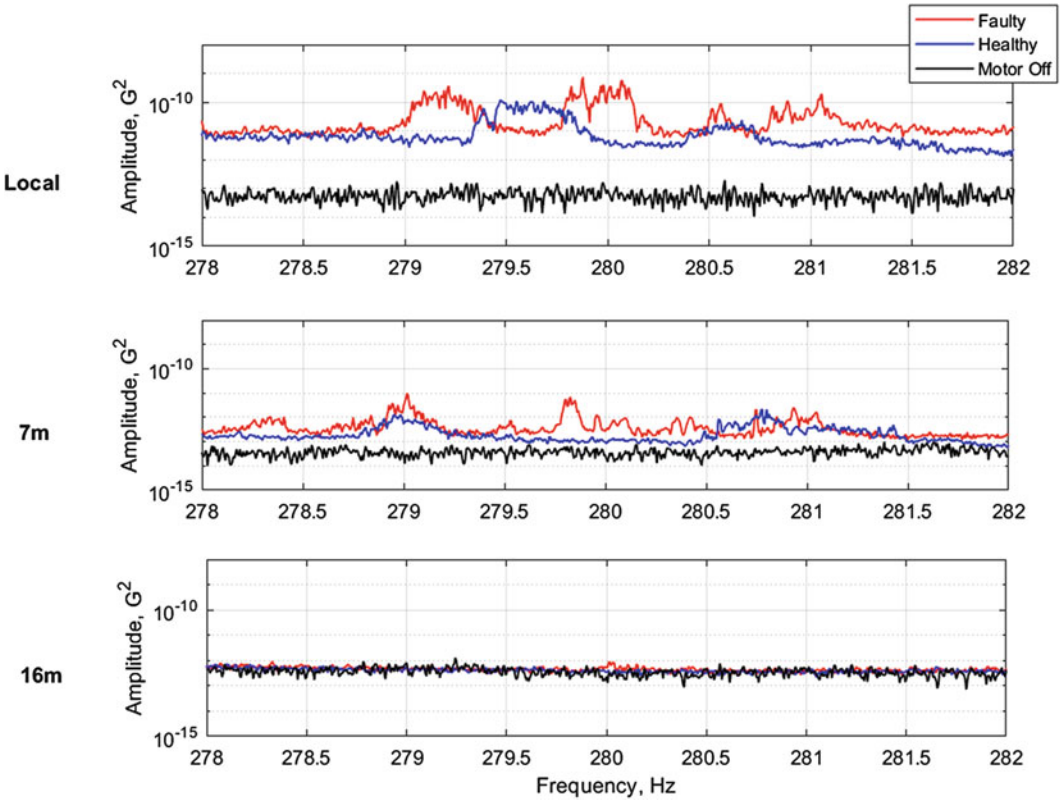

Fig. 6.6 Power spectrum of healthy, faulty, and motor off at all test locations

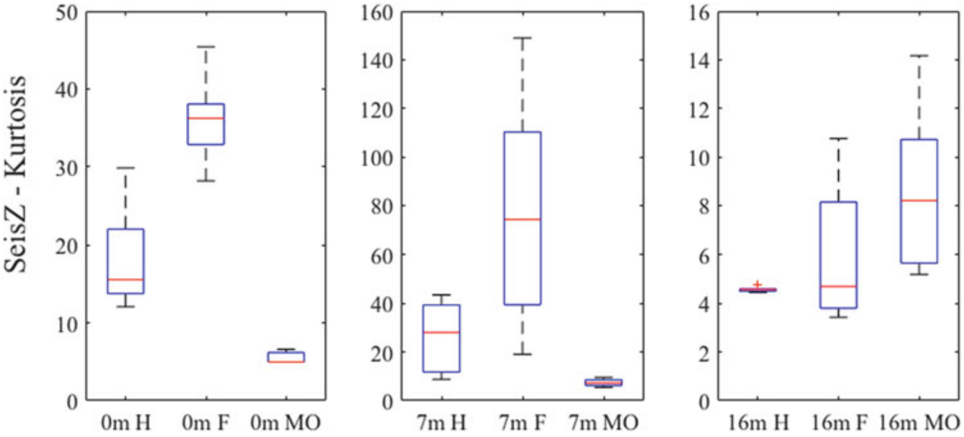

Fig. 6.7 Comparison of healthy (H), faulty (F) and motor off (MO) states for each location with the Seismic Z-Axis Kurtosis feature

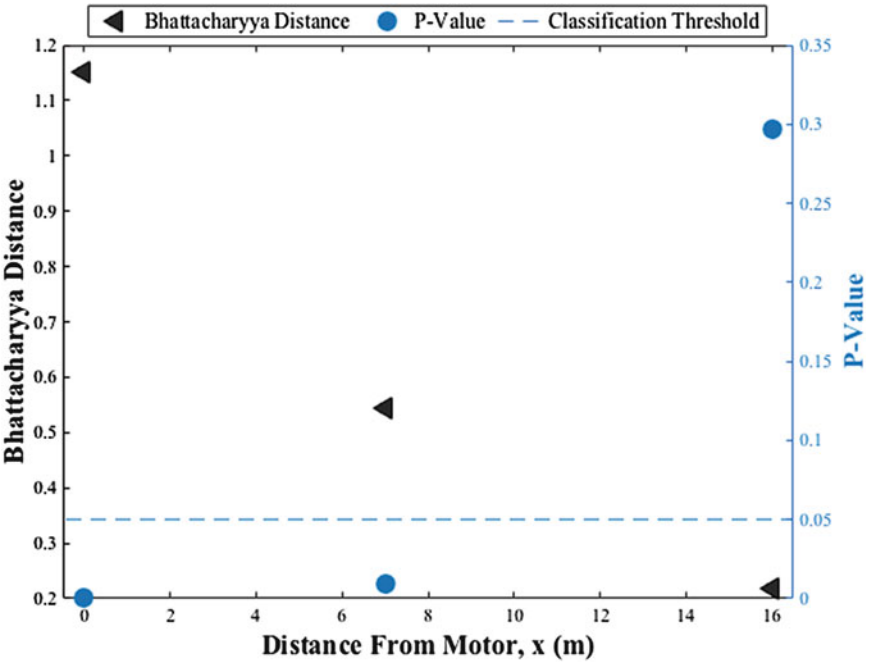

Fig. 6.8 Bhattacharyya distance and p-values comparing healthy and faulty data sets for measurements taken locally, 7 m and 16 m away from the motor. The classification threshold represents the null hypothesis limit (point at which healthy and faulty distribution

6.7 Conclusions

This research focused on the ability to detect mechanical signatures at several distances in a laboratory setting. With adequate lengths of data, proper signal processing techniques, and indicated frequencies of interest, healthy and faulty operation signatures can be separated using various features. In this case, long-duration time signals were averaged and brought in to the frequency domain. One distinct feature to separate the healthy and faulty data was to calculate kurtosis over a frequency band specific to the fault being tested. Statistically, the p-values and Bhattacharyya distances were used to calculate separation and provide a threshold for detection. Of the three locations tested, the furthest exceeded this threshold, resulting in no statistical separation between healthy and faulty signatures. However, these metrics were able to successfully detect healthy and faulty signatures locally and at a distance of seven meters.

Remote sensing is a challenging problem that can be addressed using results found in this study. However, tests performed in a laboratory setting produce consistent and predictable results, in contrast to field tests. While these results can be applied to field and industry CBM, more research is required to determine the measurability of faults of industrial machinery. As distance from the machine increases, there is a greater risk of environment noise interfering with the detection process, therefore additional measures to attenuate environment noise and amplify fault signatures should be investigated and implemented. Remote CBM could be enhanced through the implementation of data fusion on an array of sensors and machine learning for automatic feature selection and fault detection.

References

1. Farrar, C.R., Worden, K.: Structural Health Monitoring: A Machine Learning Perspective. Wiley, Hoboken (2013)
2. SpectraQuest Inc, Applied Vibration Analysis Training Manual & Laboratory Exercises, Richmond, VA
3. Mogal, S., Lalwani, D.: A brief review on fault diagnosis of rotating machinery. Appl. Mech. Mater. **541–542**, 635–640 (2014)
4. Kryer, R., Haynes, H.: Condition monitoring of machinery using motor current signaure analysis. In: Power Plant Dynamics, Control and Testing Symposium, vol. 7 (1989)
5. Filho, P.C., Brito, J.N., Silva, V.A., Pederiva, R.: Detection of electrical faults in induction motors using vibration analysis. J. Qual. Maint. Eng. **19**(4), 364–380 (2013)
6. Singh, S., Kumar, A., Kumar, N.: Motor current signature analysis for bearing fault detection in mechanical systems. Procedia Mater. Sci. **6**, 171–177 (2014)

7. Thomson, W.T., Orpin, P.: Current and vibration monitoring for fault diagnosis and root cause analysis of induction motor drives. In: Proceedings of the Thirty-First Turbomachinery Symposium, pp. 61–67 (2002)
8. Dykas, B., Becker, A.: Comparison of measurement techniques for remote diagnosis of damage in non-HUMS-equipped bearings. IEEE Aerospace Conference, pp. 1–16 (2016)
9. Siemens. What is a Frequency Response Function (FRF)? Siemens PLM Community (2016)
10. Zhou, Y.-L., Figueiredo, E., Maia, N., Perera, R.: Damage detection and quantification using transmissibility coherence analysis. Shock. Vib. **2015**, 290714, 16 pp. (2015)
11. Konar, P., Chattopadhyay, P.: Bearing fault detection of induction motor using wavelet and Support Vector Machines (SVMs). Appl. Soft Comput. **11**, 4203–4211 (2011)
12. Chen, F., Tang, B., Chen, R.: A novel fault diagnosis model for gearbox based on wavelet support vector machine with immune genetic algorithm. Measurement. **46**, 220–232 (2013)
13. Yan, R., Gao, R.X., Chen, X.: Wavelets for fault diagnosis of rotary machines: a review with applications. Signal Process. **96**, 1–15 (2014)
14. Marmugi, L., Gori, L., Hussain, S., Deans, C., Renzoni, F.: Remote detection of rotating machinery with a portable atomic magnetometer. Appl. Opt. **57**(3), 743 (2017)
15. Hall, D.L., LLinas, J.: An introduction to multisensor data fusion. Proc. IEEE. **85**(1), 6–23 (1997)
16. Safizadeh, M., Latifi, S.: Using multi-sensor data fusion for vibration fault diagnosis of rolling element bearings by accelerometer and load cell. Inform. Fusion. **18**, 1–8 (2014)
17. Dash, M., Lui, H.: Feature selection for classification. IDA Elsevier Intelligent Data Analysis. **1**(97), 131–156 (1997)
18. Ngolah, C.F., Morden, Ed, Wang, Y.: An intelligent fault recognizer for rotating machinery via remote characteristic vibration signal detection. In: IEEE 10th International Conference for Cognitive Computing (2011)
19. Danforth, S.M., Martz, J.T., Root, A.H., Flynn, E.B., Harvey, D.Y.: Multi-source sensing and analysis for machine-array conditioning monitoring. In: Structural Health Monitoring & Damange Detection, vol. 7, pp. 9–21 (2017)
20. Choi, E., Lee, C.: Feature extraction based on the Bhattacharyya distance. Pattern Recogn. **36**(8), 1703–1709 (2003)
21. Lee, C., Choi, E.: Bayes error evaluation of the Gaussian ML classifier. IEEE Trans. Geosci. Remote Sens. **38**(3), 1471–1475 (2000)

Chapter 7

Modal Analysis of a High-Speed Turbomachinery for Reliable Prediction of RD Properties Throughout Operating Speed Range

Yuhei Shindo, Kazuhiko Adachi, Satoshi Kawasaki, and Mitsuru Shimagaki

Abstract In this study, a novel one-dimensional beam finite element rotor-bearing model considering rotor dynamic (RD) fluid and gyroscopic forces is proposed, and modal analysis of a single shaft turbopump (TP) in the whole operating speed range is performed to predict the rotor dynamic properties of the TP. The effects of both RD fluid and gyroscopic forces on the RD properties of the TP were clearly shown on the Campbell diagram, and the damped natural circular frequencies of the TP within the operating speed range were also successfully identified.

Keywords Rotordynamics · Fuel turbopump · Oxidizer turbopump · Rotor dynamic fluid force · Gyroscopic force

7.1 Introduction

A severe vibration of the high-speed turbomachinery might have happened during the normal operation, and it causes the functional failure of the machinery and/or the whole system. In the case of the turbopump of the liquid rocket engine, such functional failure leads to the rocket launch mission failure. A typical fuel or oxidizer turbopump (TP) consists of several components such as an inducer, centrifugal impellers, a turbine, bearings, seal, and so on. These components are mounted on the TP shaft, and their stiffness and damping characteristics strongly depend on the rotating speed of the TP due to the effect of both rotor dynamic (RD) fluid and gyroscopic forces. As a result, throughout the operating speed range, mode crossing/veering phenomena appeared on a Campbell diagram, and then the RD properties of the TP are dramatically changed under the effect of both RD fluid and gyroscopic forces.

This study aims at proposing a novel one-dimensional beam finite element rotor-bearing model considering RD fluid and gyroscopic forces and performing modal analysis of a high-speed TP in the whole operating speed range.

7.2 Method

The equation of motion of a rotor-bearing model considering RD fluid and gyroscopic forces is given by Eq. (7.1).

$$M\ddot{q} + (C + \omega G)\,\dot{q} + Kq = f_{RD}(\omega) \tag{7.1}$$

where q is the nodal displacement vector of the rotor. In this study, the rotor is modeled by one-dimensional two-node beam element [1] in which each node has four degrees of freedom. The matrices M, C, and K are the mass, damping, and stiffness matrices of the rotor, respectively. The matrix G is corresponding to the gyroscopic force. Support stiffness and damping

Y. Shindo
Department of Mechanical Engineering, Graduate School of Engineering, Chubu University, Kasugai, Japan

K. Adachi (✉)
Department of Mechanical Engineering, College of Engineering, Chubu University, Kasugai, Japan
e-mail: kazuhiko@isc.chubu.ac.jp

S. Kawasaki · M. Shimagaki
Japan Aerospace Exploration Agency, Kimigaya, Kakuda, Japan

C. Niezrecki et al. (eds.), *Rotating Machinery, Optical Methods & Scanning LDV Methods, Volume 6*, Conference Proceedings
of the Society for Experimental Mechanics Series, https://doi.org/10.1007/978-3-030-12935-4_7

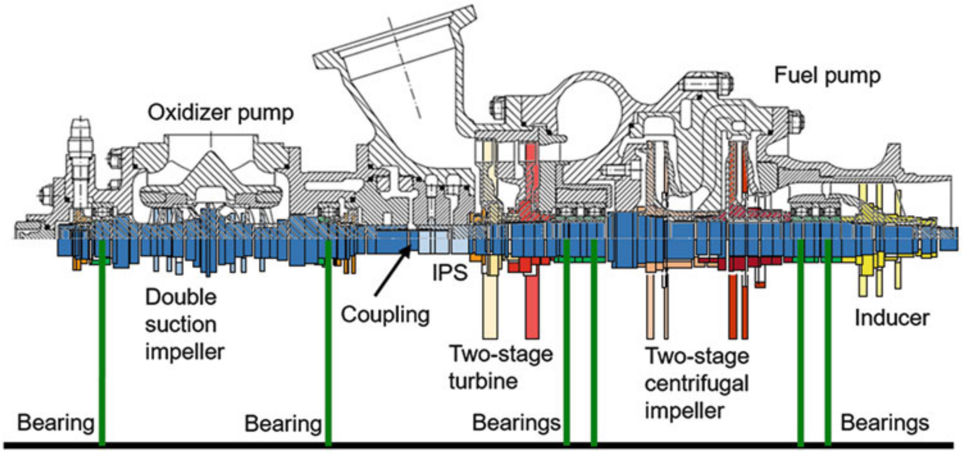

Fig. 7.1 Rotor-bearing finite element model of single shaft turbopump

of the bearings are including both K and C matrices. In the right hand of the equation, $f_{RD}(\omega)$ indicates the RD fluid forces at the operating speed ω rpm. In the proposed model, RD fluid forces acting on the inducer, centrifugal impeller, and seal are modeled by using nondimensional normalized direct and cross-coupled RD coefficients and introduced as matrices into the node corresponding to the locations acting on the RD fluid forces as the following form:

$$f_{RDi}(\omega) = -\begin{bmatrix} M_{RDi} & m_{RDi} \\ m_{RDi} & M_{RDi} \end{bmatrix} \begin{Bmatrix} \ddot{q}_{xi} \\ \ddot{q}_{yi} \end{Bmatrix} - \begin{bmatrix} C_{RDi} & c_{RDi} \\ c_{RDi} & C_{RDi} \end{bmatrix} \begin{Bmatrix} \dot{q}_{xi} \\ \dot{q}_{yi} \end{Bmatrix} - \begin{bmatrix} K_{RDi} & k_{RDi} \\ k_{RDi} & K_{RDi} \end{bmatrix} \begin{Bmatrix} q_{xi} \\ q_{yi} \end{Bmatrix} \quad (7.2)$$

Thomas force is adopted as the RD fluid force acting on the turbine [2]. In the numerical simulation of this study, RD properties of a single shaft turbopump rotor system was analyzed by using the proposed modeling. The configuration of the turbopump was adopted from reference [3]; however only an axial cross-sectional view was available. Therefore, in this study, each component size of both fuel turbopump and oxidizer pump is evaluated based on the performance analysis of the fuel pump. Figure 7.1 shows the rotor-bearing finite element model of the single shaft TP.

7.3 Results

Lower three damped natural circular frequencies and their vibration mode shapes were successfully obtained by the proposed modeling. Due to the effect of both RD fluid and gyroscopic forces, each vibration mode was separated into backward and forward modes. In the Campbell diagram, mode crossing/veering phenomena appeared from 0 rpm to the normal operating speed 46,000 rpm. Lower three forward natural circular frequencies at 46,000 rpm are 1702 Hz, 882 Hz, and 1052 Hz, respectively. First forward natural circular frequency is quite higher than the second and third forward natural circular frequencies due to both RD fluid force and gyroscopic effect. Figures 7.2, 7.3, and 7.4 show these three forward mode shapes.

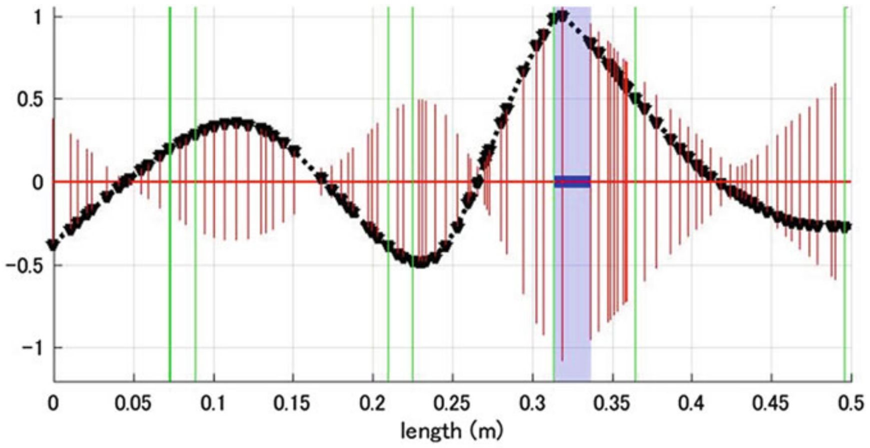

Fig. 7.2 First forward vibration mode shape at the normal operating speed 46,000 rpm

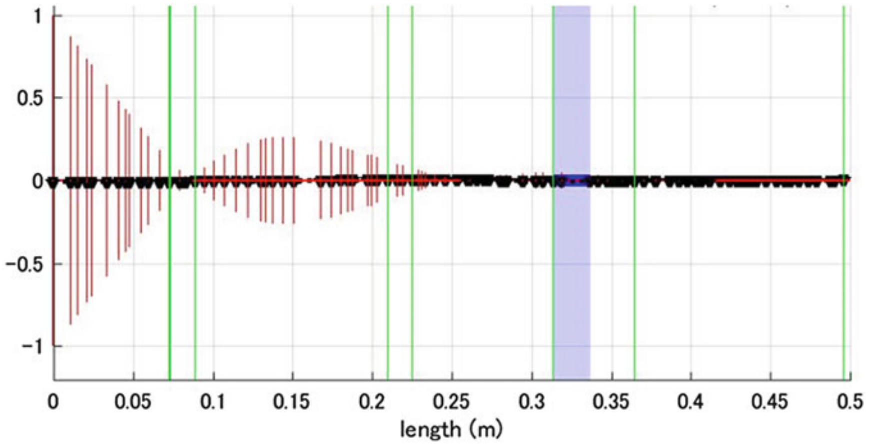

Fig. 7.3 Second forward vibration mode shape at the normal operating speed 46,000 rpm

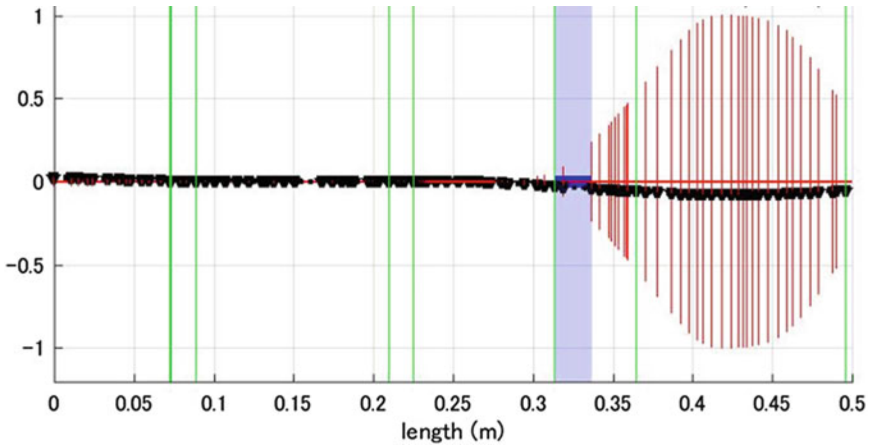

Fig. 7.4 Third forward vibration mode shape at the normal operating speed 46,000 rpm

7.4 Conclusion

A rotor-bearing finite element model for single shaft TP considering both RD fluid and gyroscopic forces was developed. According to the modal analysis, the effect of both RD fluid and gyroscopic forces on the RD properties of the single shaft TP was clearly shown on the Campbell diagram, and the damped natural circular frequencies of the TP within the operating speed range were also successfully identified.

References

1. Meirovitch, L.: Elements of Vibration Analysis, 2nd edn, pp. 300–328, p. 284. McGraw-Hill Co., New York (1986)
2. Motoi, H., Kitamura, A., Sakazume, N., Uchiumi, M., Uchida, M., Saiki, K., Nozaki, O., Iwatsubo, T.: Sub-synchronous whirl in The LE-7A rocket engine fuel turbo-pump. Second International Symposium on Stability Control of Rotating Machinery ISCORMA-2, 2003
3. Rachuk, V., Dmitrenko, A., Buser, M., Minick, A.: Single shaft turbopump expands capabilities of upper stage liquid propulsion. Proceedings of the 44th AIAA/ASME/SAE/ASEE Joint Propulsion Conference & Exhibit, AIAA-2008-4946, July 2008

Chapter 8
Mapping Motion-Magnified Videos to Operating Deflection Shape Vectors Using Particle Filters

Aral Sarrafi and Zhu Mao

Abstract Phase-based motion estimation and magnification are targetless methods that have been used recently to perform experimental modal analysis (EMA) and operational modal analysis (OMA) on a variety of structures. Mapping the motion-magnified sequence of images into quantified operating deflection shape (ODS) vectors is currently being conducted via edge detection methods that require intensive human supervision and interference. Within this study, a new hybrid computer vision approach is introduced to extract the quantified ODS vectors from the motion-magnified sequence of images with minimal human supervision. The particle filter point tracking method is utilized to follow the desired feature points in the motion-magnified sequence of images. Moreover, the k-means clustering algorithm is employed as an unsupervised learning approach to performing the segmentation of the particles and assigning them to specific feature points in the in the motion-magnified sequence of images. This study shows that the cluster centers can be employed to estimate the ODS vectors, and the performance of the proposed methodology is evaluated experimentally on a lab-scale cantilever beam and validated via a finite element model.

Keywords Phase-based motion estimation · Video magnification · Particle filter · Computer vision · Clustering · Unsupervised learning

8.1 Introduction

In recent years using digital cameras for structural dynamics identification and structural health monitoring (SHM) has been gaining much attention [1, 2]. As a non-contact measurement method, digital cameras have several advantages over other traditional approaches for structural dynamics identification. In general, instrumentation of structures with accelerometers is labor-intensive, time-consuming and costly, but for digital cameras, the instrumentation is normally much easier and attaching a couple of optical targets is sufficient in most of the cases. Another major advantage of camera-based measurement over traditional structural response measurement methods such as accelerometers or laser vibrometers is that the cameras can provide full-field measurements in the field of view of the camera simultaneously [3]. Laser vibrometers can provide high spatial resolutions [4], but normally scanning the surface of the measurement will take a long time that may increase the testing time dramatically.

Although cameras-based measurements have several advantages compared to other techniques, the post-processing of the sequence of images captured by the camera is generally an elaborate and complex task which involves advanced signal processing [5, 6], computer vision, and computational photogrammetry algorithms. Computer vision is one of the fastest growing branches in computer science that aims to extract useful information from the images captured from a scene. 3-dimensional digital images correlation (3D-DIC), and 3-dimensional point tracking (3DPT) are among the computer vision algorithms that have been implemented successfully for measuring structural responses including displacements and strains [7, 8]. These techniques are well developed and are being used extensively both in academic research and industrial applications [9, 10]. Optical flow motion estimation algorithms are another set of approaches that have been showing promising outcomes for structural dynamics identification from recorded videos. There have been several studies on using Lucas-Kanade [11] and Horn-Schunck motion estimation algorithms in the context of structural dynamics identification that can be found in the references [12–16].

A. Sarrafi · Z. Mao (✉)
Structural Dynamics and Acoustic Systems Laboratory, Department of Mechanical Engineering, University of Massachusetts Lowell, Lowell, MA, USA
e-mail: zhu_mao@uml.edu

C. Niezrecki et al. (eds.), *Rotating Machinery, Optical Methods & Scanning LDV Methods, Volume 6*, Conference Proceedings of the Society for Experimental Mechanics Series, https://doi.org/10.1007/978-3-030-12935-4_8

As discussed earlier, several computer vision algorithms have been studied in the literature to extract reliable modes from a sequence of images for describing the dynamics of the structures. Phase-based motion estimation [17, 18], and phase-based video magnification(VM) [19, 20] algorithms are among the most recent approaches that have been used for structural dynamics identification. The phase-based motion estimation is based on the fact that the spatial motion can be retrieved from the phase variations in the frequency domain. Phase-based video magnification is a more recent algorithm primarily related to computational photogrammetry rather than computer vision, that can magnify the subtle motions in a video to generate a new video in which the small motions are visible to the human vision system. Structural vibrations are normally very small (less than 2 pixels) in the scope of video cameras, and phase-based motion magnification has been successfully used by researchers in structural dynamics identification and structural health monitoring in both lab-scale structures such as cantilever-beam [21, 22], three-story building model [23, 24], pipe-line cross-section [25], and large-scale structures [26] such as wind turbine blades [27, 28], and bridges [29].

In previous studies on the applications of phase-based video magnification, very accurate visual perceptions of the ODSs of the structures were obtained which can provide intuitive insight for the engineers about the ODSs and mode shapes of the subjected structure. However, for engineering applications such as model-updating and model-validation visual perceptions are not compatible with the available methodologies. Therefore, mapping the motion-magnified videos to quantified ODS vectors is necessary. So far, the Canny edge detection was used in previous studies for mapping the motion-magnified videos to quantified ODS vectors. However, almost all the previous publications have reported that to obtain reasonable ODS vectors using the Canny edge detection, thresholding, trial, and error, and also intensive human supervision and interference were needed [21, 23, 27]. The problem originates from the fact that the edges are low-level features of an image and the edge detection algorithms often detect the edges that are associated with the background and some of the artifacts that are induced to the motion-magnified video during the magnification procedure.

Within this paper, we have introduced a new approach for converting the motion-magnified sequence of images to quantified ODS vectors that requires considerably less human-supervision that can make the ODS vector estimation procedure much faster and more reliable due to eliminating the human factor. The proposed methodology requires basic surface preparation such as painting high-contrast key-points on the structure. Then the particle filter point tracking method is utilized to track the key-points through all the frames of the motion-magnified video. As the final step, the k-means clustering method is used to group and assign the particles to specific key-points to represent the ODS vector. Also, the performance of the methodology has been evaluated on a cantilever beam. It has been shown the proposed procedure can convert the outcome of phase-based video magnification to quantified ODS vectors with higher precision and less human supervision.

The paper starts with a brief theoretical background on the particle filters, and then the details on the experimental test-setup will be presented. Afterward, the performance of the proposed methodology is evaluated on a lab-scale cantilever beam. In the last section, the conclusions are available.

8.2 Particle Filter for Point Tracking

The particle filter is one of the most general and practical tools in estimation theory and has numerous applications in all aspect of engineering especially in estimating the states of the dynamic systems such as navigation systems, robotic systems, and smart structures [30]. In computer vision, particle filters can be utilized for point tracking applications [31]. Compared to Kalman filters, particle filters can estimate the states of a non-linear system with non-Gaussian noise, while the conventional Kalman filter is derived based on the linear system dynamics and Gaussian process and measurement noise distribution assumptions. Alternative versions of Kalman filter such as Unscented Kalman Filter (UKF) and Extended Kalman Filter (EKF) can estimate the states of a non-linear system, but the Gaussian distribution of measurement and process noise assumptions should be satisfied to achieve an optimal estimation.

Within this paper, only the critical subjects on implementing the particle filter for point tracking is presented, and the detailed explanations on the derivation of the general particle filter framework are avoided.

For point tracking, M particles will be initiated. By definition, each particle is a sample of the posterior distribution. Within this study, it is assumed that each particle is a vector consisting of x and y coordinate of the targets and the velocity of the targets in x and y-direction. Therefore particle number j at time step i can be represented as $\mathbf{p}_i^j = \left[x_i^j, y_i^j, \dot{x}_i^j, \dot{y}_i^j\right]$. Therefore, the initial set of M particles will be $\mathbf{P}_i = \left\{p_i^1, p_i^2, \dots, p_i^j, \dots, p_i^M\right\}$.

For implementing one step of particle filter first, the states in the next time step needs to be predicted. This step is mainly implemented by only plugging in the particles in the current time step in the system dynamics. In this study, a constant velocity system dynamics is as described below:

$$\begin{Bmatrix} x_{i+1} \\ y_{i+1} \\ \dot{x}_{i+1} \\ \dot{y}_{i+1} \end{Bmatrix} = \begin{pmatrix} 1\,0\,1\,0 \\ 0\,1\,0\,1 \\ 0\,0\,1\,0 \\ 0\,0\,0\,1 \end{pmatrix} \begin{Bmatrix} x_i \\ y_i \\ \dot{x}_i \\ \dot{y}_i \end{Bmatrix} + \begin{Bmatrix} n_x \\ n_y \\ \dot{n}_x \\ \dot{n}_y \end{Bmatrix}. \tag{8.1}$$

x_i, y_i are the location of the targets and $\dot{x}_i$, $\dot{y}_i$ are the speed of the target at the frame i. In Eq. (8.1) n_x, $n_y\dot{n}_x\dot{n}_y$ are process noise that can have an arbitrary distribution. After predicting the new states for all the particles, a new set of particles will be obtained $\overline{\mathbf{P}}_{i+1} = \left\{\overline{p}_{i+1}^1, \overline{p}_{i+1}^2, \dots, \overline{p}_{i+1}^j, \dots, \overline{p}_{i+1}^M\right\}$ we are using the notation $\overline{\mathbf{P}}_{i+1}$ to show that this is not the final estimation for the time step $i+1$. Each particle in $\overline{\mathbf{P}}_{i+1}$ is obtained by substituting a particle from $\mathbf{P}_i$ in Eq. (8.1).

The next step in the particle filter algorithm for tracking is to compute the likelihood function for each of the particles in $\overline{\mathbf{P}}_{i+1}$.

The likelihood distribution function is selected based on the Euclidian distance between the RGB values of the target and the RGB vector associated with each particle in $\overline{\mathbf{P}}_{i+1}$ as indicated below.

$$d = \sqrt{(r - r_t)^2 + (g - g_t)^2 + (b - b_t)^2}. \tag{8.2}$$

d is the Euclidian distance between the pixel RGB (from the particle) values and target RGB in which r, g, b are the RGB values of the pixel associated with a particle in the scene and r_t, g_t, b_t are the RGB values of the specific targets that are desired to be tracked in the scene. The likelihood function can be expressed as below:

$$P\left(T|p_{i+1}^j\right) = \frac{1}{\sqrt{2\pi}\sigma} \exp\left(-\frac{d^2}{2\sigma^2}\right). \tag{8.3}$$

In Eq. (8.3) T stands for the target. This likelihood function evaluates the probability of a particle being the target based on its RGB value. Therefore, for each of the particles in $\overline{\mathbf{P}}_{i+1}$, a weight can be assigned to determine the similarity of a specific particle to the desired target $w_{i+1}^j = P\left(T\left|p_{i+1}^j\right.\right)$. It is also worth mentioning that we are assuming that the target is not changing in different frames; therefore, the target does not have an index to keep track of the time step. The final stage of the particle filter algorithm for tracking is to resample the particles form $\overline{\mathbf{P}}_{i+1}$ with replacement, proportional to the weight of each particle w_{i+1}^j to populate the final estimation at time $i+1$, i.e. $\mathbf{P}_{i+1}$. In other words, the particles with higher weight in $\overline{\mathbf{P}}_{i+1}$ will be resampled more often compared to the particles with smaller weights. Therefore, the final particles will represent a posterior distribution of the desired states.

At this stage, the particle filter will be tracking the targets in the motion-magnified videos. However, the particles are not registered to specific targets. In other words, the computer perceives all the particles as a 2D point cloud. Therefore, a clustering algorithm will be applied on top of the particle filter to assign the particles to specific targets [32]. Within this study, we will be using the k-means clustering algorithm to group the particles and assign them to specific targets. In the next section, first, the experimental test-setup for the evaluation of the algorithm will be presented, and then the results for mapping the motion-magnified videos to quantified ODS vectors will be discussed in more detail.

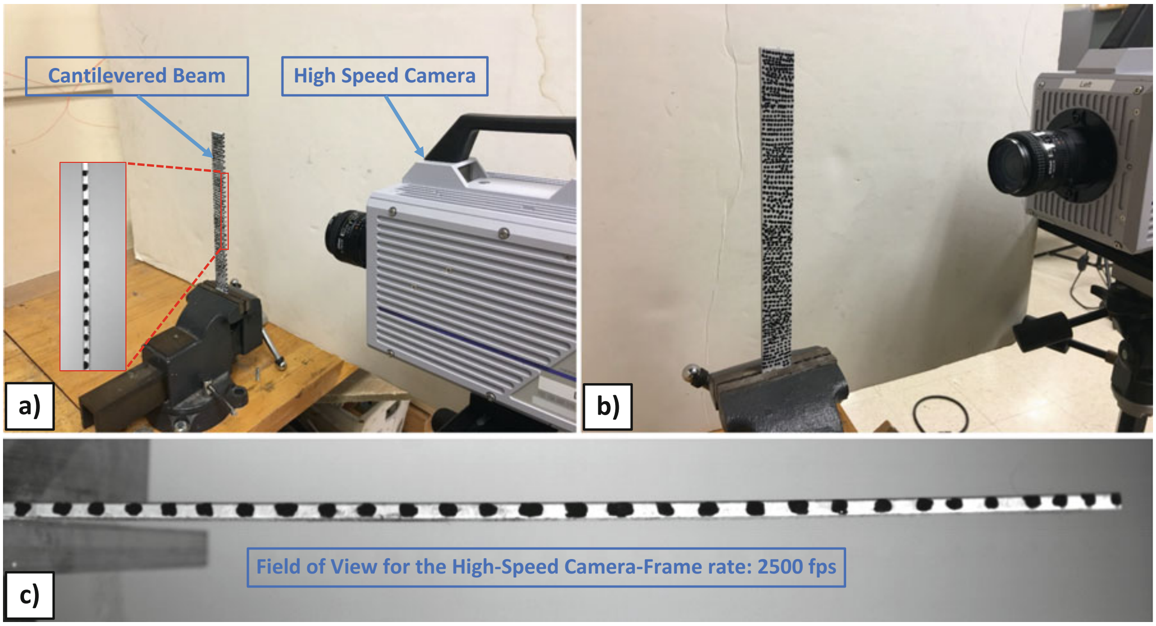

Fig. 8.1 (**a**, **b**) The CMOS high-speed camera and the cantilever beam, (**c**) field of view for the camera capturing the sequence of images of the vibrating beam

8.3 Experimental Test-Setup

In order to evaluate the performance of the proposed algorithm, a lab-scale test setup has been prepared. A contrived cantilever beam is selected as the case study. A CMOS high-speed camera shown in Fig. 8.1 captures the sequence of images from the vibrating cantilever-beam. The sequence of images was recorded with a sampling rate of 2500 frames per second, and based on the Nyquist theorem the resonant frequencies and operating deflection shapes can be extracted up to 1250 Hz without facing aliasing. Because there is no anti-aliasing filtering available for optical measurements the aliased higher order frequencies can be detected often, and the post-processing of the data should be handled more carefully. High contrast black dots are also painted on the edge of the cantilever-beam, which are going to be used as the key-points form tracking.

8.4 Quantifying the ODS Vectors

Within this section, the performance of the proposed methodology will be evaluated on the cantilever-beam experimental test-setup. Figure 8.2 shows the two snapshots of the motion-magnified videos for the first four ODSs of the cantilever-beam when the beam is at its maximum deflection. The snapshots are overlaid by an image fusion method for visualization purposes. The first four resonant frequencies of the cantilever-beam are 34.18 Hz, 212.4 Hz, 595.7 Hz, and 1167 Hz. The resonant frequencies are obtained by applying the phase-based motion estimation on the original video captured by the high-speed camera while the beam was vibrating. Applying the phase-based video magnification in frequency bands that are containing only one of the resonant frequencies of the beam will generate motion-magnified videos that will reveal the operating deflection shape of the cantilever-beam at the selected resonant frequency.

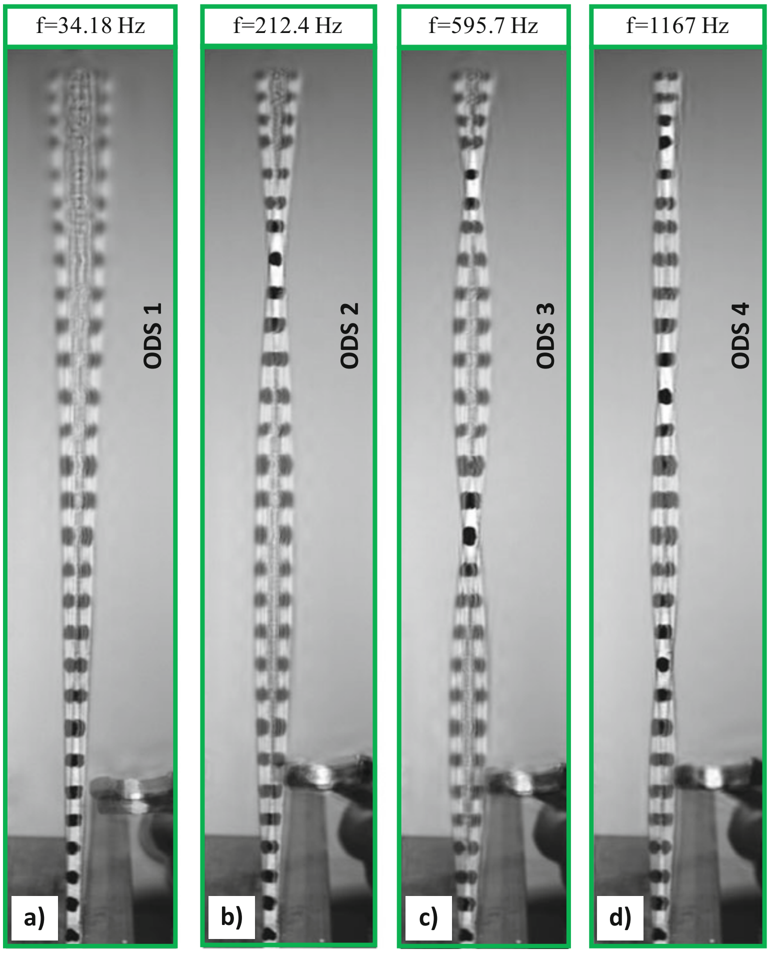

Fig. 8.2 Frames of motion magnified videos representing the visual perception of the first four operating deflection shapes of the cantilever beam

Figure 8.2 is demonstrating a visual perception of the ODSs of the cantilever-beam that is obtained by applying the phase-based motion magnification on the original video of the vibrating cantilever-beam. However, for engineering applications such as model updating, model validation or structural health monitoring decision-makings recovering the quantified ODS vectors is necessary. In order to obtain the ODS vectors from motion magnified-video the particle filter tracker is used to track the key-points throughout the frames as discussed earlier in the introduction. In this study the targets are black; therefore we have selected a target RGB vector will small values ([15], and $\sigma = 20$). Figure 8.3 shows the snapshots of the motion-magnified video while the particle filter estimator is being used to track the key-points on the cantilever-beam. All the orange dots converge to the key-points in the motion-magnified videos and track them frame by frame. Within this study, we are using 220,000 particles to achieve a robust tracking performance in all the frames, while maintaining a fast execution time for the particle filter algorithm.

Once the tracking is performed, the particles should be grouped and assigned to specific targets (key-points). This procedure is completed via the k-means clustering algorithm. Figure 8.4 demonstrates the particles after applying the k-means clustering. The number of cluster centers should be larger than the number of key-points. Within this case study, we have 29 targets; therefore, we have selected 30 cluster centers. As it is clear the nearby particles will be grouped and assigned to a cluster center which will be used later as the estimation of the ODS vector.

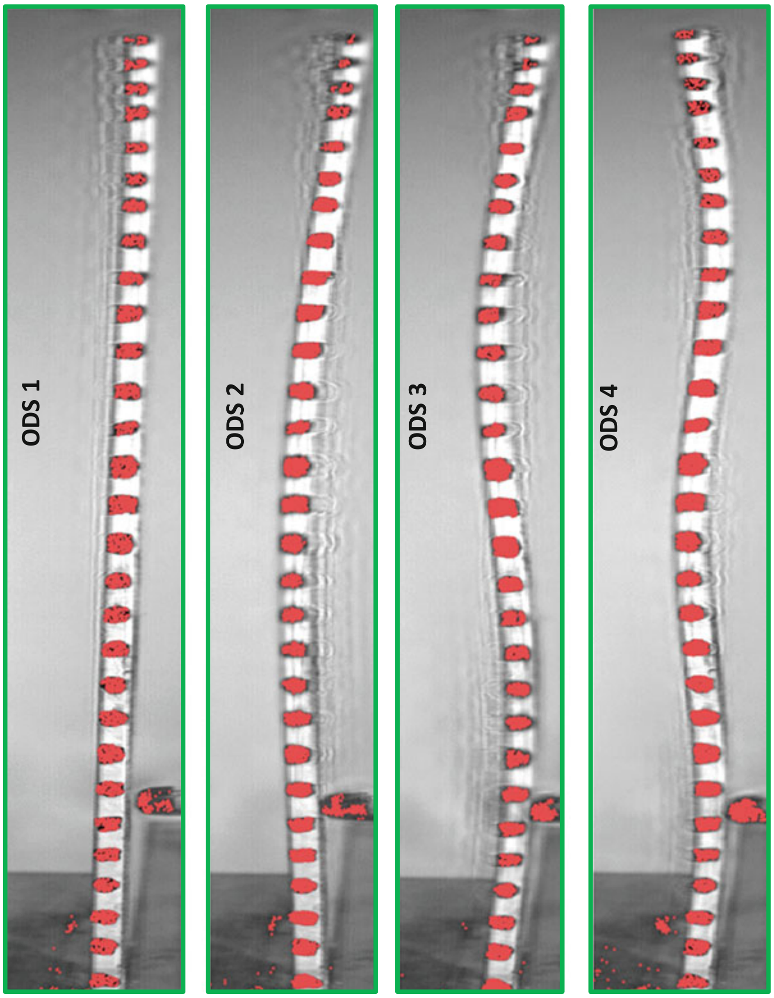

Fig. 8.3 Tracking the targets in motion-magnified videos using the particle filter algorithm

After clustering the particles, the quantified ODS vectors are estimated. The center of the clusters is the average of the grouped particles. Because the averaging is taking place among a swarm of particles, the cluster centers can be a reliable estimation of the ODS vectors. Each of the clusters is represented with a different color, and the center of the cluster is a circle with the black edge around it. Moreover, some of the outliers of the estimation that are detected from the background can be eliminated by applying a median filter. The median filter can detect the points that are not following the general trend of the ODS vector and excludes them from the estimated ODS vector as shown in Fig. 8.5a–d.

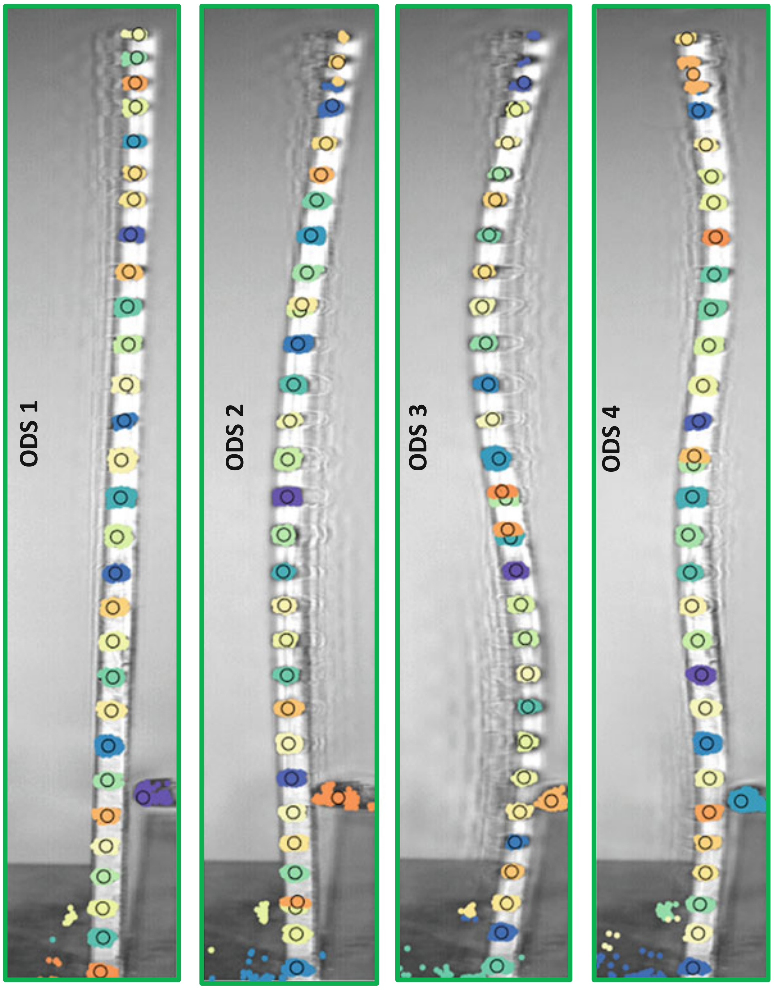

Fig. 8.4 Applying k-means clustering algorithm for assigning particles to a specific target (segmentation step)

For quantitative evaluation, the MAC values between the estimated ODS vectors using the proposed methodology and the ODSs obtained from the finite element model (FEM) in ABAQUS are computed and presented in Table 8.1. The MAC values on the main diagonal are relatively close to one, which indicates the high correlation between the ODSs from the video processing method introduced in this paper and FEM model implemented in ABAQUS. Moreover, the off-diagonal terms in the MAC matrix are close to zeros that implies the orthogonality across different modes. The cantilever-beam is a simple structure and obtaining a reliable FEM model is feasible in this case. The high correlation between the estimated ODS vectors and the ODS vectors from the FEM model validates that the correctness of extracted ODS vectors

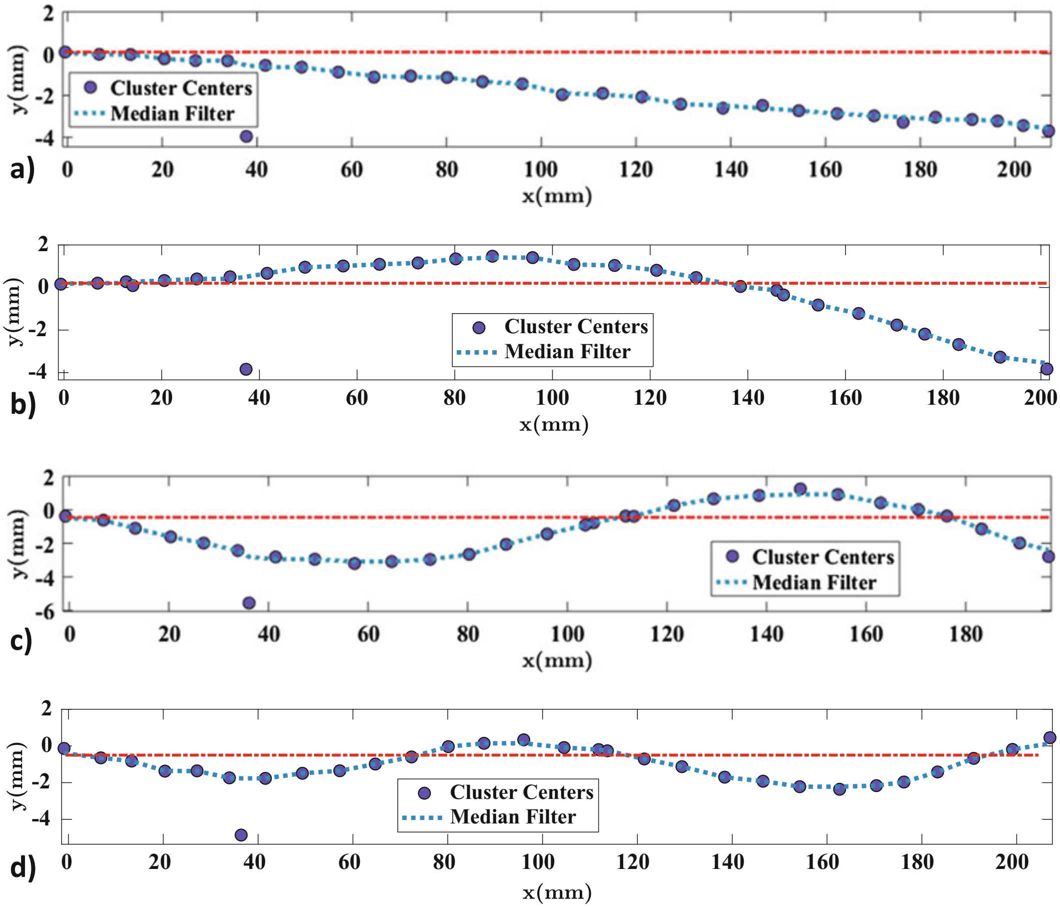

Fig. 8.5 Quantified ODS vectors obtained from motion-magnified videos by applying particle filters for tracking and the k-means clustering for segmentation. (**a**) ODS 1, (**b**) ODS 2, (**c**) ODS 3, (**d**) ODS 4

Table 8.1 MAC values between the ODS vectors obtained from VM and mode shapes obtained from FEM

	ODS vectors from the motion-magnified video			
Frequency extraction	34.18 Hz	212.4 Hz	594.5 Hz	1167 Hz
33.69 Hz	**0.972**	0.062	0.018	0.004
211.0 Hz	0.031	**0.957**	0.010	0.017
590.3 Hz	0.021	0.017	**0.953**	0.002
1155 Hz	0.020	0.021	0.014	**0.920**

8.5 Conclusions

The paper proposes a new computer vision approach for mapping motion-magnified videos to quantified ODS vectors, which can be used to enhance structure model validation, model updating, and structural health monitoring. The main contribution in the proposed framework is that the human supervision for estimating the ODS vectors is decreased dramatically and the ODS vector estimation procedure can be considered (semi)-automatic. Our workflow uses the particle filter algorithm to track the key points in the motion-magnified videos, which are visual perceptions of the ODSs of the structure. Once the tracking is performed a segmentation step is applied to the particles via a k-means clustering algorithm. The segmentation stage groups and assigns the particles to specific targets to recover the operating deflection shape of the structure. The cluster centers are providing good estimations for the ODSs of the case study of this paper (cantilevered-beam). Therefore, evaluating the performance of this framework on more complex structures with elaborate geometry is also necessary. For future studies, further investigations on the hyper-parameters of the proposed methodology such as the optimal number of particles or the number of cluster-centers can be pursued to enhance the reliability and accuracy of the approach.

References

1. Baqersad, J., Poozesh, P., Niezrecki, C., Avitabile, P.: Photogrammetry and optical methods in structural dynamics–a review. Mech. Syst. Signal Process. **86**(Part B), 17 (2017)
2. Feng, D., Feng, M.Q.: Computer vision for SHM of civil infrastructure: from dynamic response measurement to damage detection–a review. Eng. Struct. **156**, 105–117 (2018)
3. Sarrafi, A., Poozesh, P., Mao, Z.: A comparison of computer-vision-based structural dynamics characterizations. In: Model Validation and Uncertainty Quantification, Volume 3, pp. 295–301. Springer, Cham (2017)
4. Castellini, P., Martarelli, M., Tomasini, E.P.: Laser Doppler Vibrometry: development of advanced solutions answering to technology's needs. Mech. Syst. Signal Process. **20**, 1265–1285 (2006)
5. Cigada, A., Mazzoleni, P., Zappa, E.: Vibration monitoring of multiple bridge points by means of a unique vision-based measuring system. Exp. Mech. **54**, 255–271 (2014)
6. Mazzoleni, P., Zappa, E.: Vision-based estimation of vertical dynamic loading induced by jumping and bobbing crowds on civil structures. Mech. Syst. Signal Process. **33**, 1–12 (2012)
7. Li, J., Xie, X., Yang, G., Zhang, B., Siebert, T., Yang, L.: Whole-field thickness strain measurement using multiple camera digital image correlation system. Opt. Lasers Eng. **90**, 19–25 (2017)
8. Xie, X., Zeng, D., Li, J., Dahl, J., Zhao, Q., Yang, L.: Tensile test for polymer plastics with extreme large elongation using quad-camera digital image correlation. SAE Technical Paper 0148-7191 (2016)
9. Baqersad, J., Niezrecki, C., Avitabile, P.: Full-field dynamic strain prediction on a wind turbine using displacements of optical targets measured by stereophotogrammetry. Mech. Syst. Signal Process. **62**, 284–295 (2015)
10. Baqersad, J., Niezrecki, C., Avitabile, P.: Extracting full-field dynamic strain on a wind turbine rotor subjected to arbitrary excitations using 3D point tracking and a modal expansion technique. J. Sound Vib. **352**, 16–29 (2015)
11. Baker, S., Matthews, I.: Lucas-kanade 20 years on: a unifying framework. Int. J. Comput. Vis. **56**, 221–255 (2004)
12. Javh, J., Slavič, J., Boltežar, M.: The subpixel resolution of optical-flow-based modal analysis. Mech. Syst. Signal Process. **88**, 89–99 (2017)
13. Javh, J., Slavič, J., Boltežar, M.: High frequency modal identification on noisy high-speed camera data. Mech. Syst. Signal Process. **98**, 344–351 (2018)
14. Feng, D., Feng, M.Q.: Identification of structural stiffness and excitation forces in time domain using noncontact vision-based displacement measurement. J. Sound Vib. **406**, 15–28 (2017)
15. Feng, D., Feng, M.Q., Ozer, E., Fukuda, Y.: A vision-based sensor for noncontact structural displacement measurement. Sensors. **15**, 16557–16575 (2015)
16. Celik, O., Dong, C.-Z., Catbas, F.N.: A computer vision approach for the load time history estimation of lively individuals and crowds. Comput. Struct. **200**, 32–52 (2018)
17. Fleet, D., Weiss, Y.: Optical flow estimation. In: Handbook of Mathematical Models in Computer Vision, pp. 237–257. Springer, New York (2006)
18. Fleet, D.J., Jepson, A.D.: Computation of component image velocity from local phase information. Int. J. Comput. Vis. **5**, 77–104 (1990)
19. Wadhwa, N., Rubinstein, M., Durand, F., Freeman, W.T.: Phase-based video motion processing. ACM Transactions on Graphics (TOG). **32**, 80 (2013)
20. Wadhwa, N., Rubinstein, M., Durand, F., Freeman, W.T.: Riesz pyramids for fast phase-based video magnification. US Patent 9,338,331, 2016
21. Chen, J.G., Wadhwa, N., Cha, Y.-J., Durand, F., Freeman, W.T., Buyukozturk, O.: Modal identification of simple structures with high-speed video using motion magnification. J. Sound Vib. **345**, 58–71 (2015)
22. Yang, Y., Dorn, C., Mancini, T., Talken, Z., Theiler, J., Kenyon, G., et al.: Reference-free detection of minute, non-visible, damage using full-field, high-resolution mode shapes output-only identified from digital videos of structures. Struct. Health Monit. **17**(3), 1475921717704385 (2017)
23. Yang, Y., Dorn, C., Mancini, T., Talken, Z., Kenyon, G., Farrar, C., et al.: Blind identification of full-field vibration modes from video measurements with phase-based video motion magnification. Mech. Syst. Signal Process. **85**, 567–590 (2017)
24. Yang, Y., Dorn, C., Mancini, T., Talken, Z., Nagarajaiah, S., Kenyon, G., et al.: Blind identification of full-field vibration modes of output-only structures from uniformly-sampled, possibly temporally-aliased (sub-Nyquist), video measurements. J. Sound Vib. **390**, 232–256 (2017)
25. Chen, J.G., Wadhwa, N., Cha, Y.-J., Durand, F., Freeman, W.T., Buyukozturk, O.: Structural modal identification through high speed camera video: Motion magnification. In: Topics in Modal Analysis I, vol. 7, pp. 191–197. Springer International Publishing (2014)
26. Sarrafi, A., Poozesh, P., Niezrecki, C., Mao, Z.: Detection of natural frequency and mode shape correspondence using phase-based video magnification in large-scale structures. In: Niezrecki, C., Baqersad, J. (eds.) Structural Health Monitoring, Photogrammetry & DIC, vol. 6. Conference Proceedings of the Society for Experimental Mechanics Series. Springer, Cham (2019)
27. Sarrafi, A., Mao, Z., Niezrecki, C., Poozesh, P.: Vibration-based damage detection in wind turbine blades using Phase-based Motion Estimation and motion magnification. J. Sound Vib. **421**, 300–318 (2018)
28. Sarrafi, A., Poozesh, P., Niezrecki, C., Mao, Z.: Mode extraction on wind turbine blades via phase-based video motion estimation. In: SPIE Smart Structures and Materials+ Nondestructive Evaluation and Health Monitoring, pp. 101710E–101710E-12 (2017)
29. Shang, Z., Shen, Z.: Multi-point vibration measurement and mode magnification of civil structures using video-based motion processing. Autom. Constr. **93**, 231–240 (2018)
30. Arulampalam, M.S., Maskell, S., Gordon, N., Clapp, T.: A tutorial on particle filters for online nonlinear/non-Gaussian Bayesian tracking. IEEE Trans. Signal Process. **50**, 174–188 (2002)
31. Schulz, D., Burgard, W., Fox, D., Cremers, A.B.: Tracking multiple moving targets with a mobile robot using particle filters and statistical data association. In: Robotics and Automation, 2001. Proceedings 2001 ICRA. IEEE International Conference on, 2001, pp. 1665–1670
32. Jain, A.K.: Data clustering: 50 years beyond K-means. Pattern Recogn. Lett. **31**, 651–666 (2010)

Chapter 9
Structural Health Monitoring of Wind Turbines Using a Digital Image Correlation System on a UAV

Ashim Khadka, Yaomin Dong, and Javad Baqersad

Abstract Unmanned aerial vehicles (UAVs) have recently emerged as a robust tool for remote inspection and data acquisition at places that are either inaccessible or riskier to perform measurements. To quantify the level of strain/stress and loading conditions that the rotating structures such as wind turbine experience during operation, an approach is proposed that can perform a nondestructive evaluation of these rotating structures using non-contact, three-dimensional (3D) digital image correlation (DIC). This technique addresses the benefit of non-interference with structure functionality and can be used for rotating or non-rotating structures. In this project, a synchronized set of a stereo camera system is used to acquire the images of a rotating turbine. These images are processed to obtain displacement, geometry, and strain over the wind turbine blades during deformation.

Keywords Modal analysis · DIC · Wind turbine · Drone · Structural health monitoring

9.1 Introduction

Recently, wind turbines with large rotor blades are frequently used in the wind industry. These blades are critical components that their failure may lead to fatal physical and financial loss. Thus, there is an increasing need for periodic damage prognosis and condition-based monitoring of these structures to ensure the reliability of such critical systems [1–2]. Present practices usually allow monitoring the gearbox, shaft, and bearings with the sensors mounted near the nacelle while many turbines fail due to the damages at turbine blades. Numerical models can be used to analyze the dynamics of wind turbines [3]. However, these models need to be validated. Thus, developing a measurement technique that can quantify the level of strain/stress and the loading conditions that the rotating structures experience during operation is of interest to the wind and rotorcraft industry.

Contact-based sensors such as accelerometers and strain gages are conventionally used for health monitoring of structures. Many researchers have used these sensors for performing measurements in laboratory conditions or test facilities [4–6]. However, it is very challenging to use these sensors for measurements on rotating structures.

Non-contact techniques such as laser Doppler vibrometer [7–9] and photogrammetry [10–12] have been recently used to measure vibrations of rotating structures. These techniques do not need wiring and can be readily integrated for rotating structures measurements. Photogrammetry and DIC have been used for measurements on wind turbines [13–19], helicopter rotors [20, 21], automotive components [22–25], and bridges [26, 27]. Recently, there have also been some efforts to integrate the numerical methods and experimental techniques to obtain full-field strain data [28–35]. However, wind farms are in remote areas such as ocean offshore. Thus, it is very desirable to perform measurements using a mobile platform. Researchers have installed DIC cameras on drones to measure defects on bridges [36]. However, most of these measurements were performed on static test structures.

The current paper proposes using a drone to perform dynamic measurements. The paper shows the methodology for the measurements. It also presents a laboratory test case for validating the results. A field test on a small scale wind turbine was also performed to ensure the system can capture the dynamics of rotating turbines. This technique can be easily scaled up to be used for utility-scale wind turbines.

A. Khadka · Y. Dong · J. Baqersad (✉)
NVH & Experimental Mechanics Laboratory (NVHEM Lab), Kettering University, Flint, MI, USA
e-mail: jbaqersad@kettering.edu

C. Niezrecki et al. (eds.), *Rotating Machinery, Optical Methods & Scanning LDV Methods, Volume 6*, Conference Proceedings of the Society for Experimental Mechanics Series, https://doi.org/10.1007/978-3-030-12935-4_9

9.2 Methodology

In this paper, a non-destructive technique is proposed to monitor rotating wind turbines using digital image correlation. The proposed approach uses a drone with eight motors and propellers. An experiment was performed on a small-scale wind turbine (see Fig. 9.1) to show the merit of the approach.

Figure 9.1 shows the wind turbine that is used for this measurement. The test structure is a six-bladed wind turbine with 113 cm blade diameter and 154 cm hub height.

For measurement using DIC, the area of the test structure must be prepared before the measurement by applying a high contrast speckle pattern on the structure. This system is also capable of point tracking, in which the 3D coordinates of optical targets mounted to the structure are extracted during deformation.

The principal aim of the project was remote structural health monitoring. A pair of high-speed cameras was desired to be mounted in an unmanned aerial vehicle. For this project, a UAV was used with eight propellers and eight motors that is controlled by 9-channel remote. Figure 9.2 depicts the drone with the stereo camera installed on it for DIC measurements of wind turbine blades. Moreover, for better flight and stability, this drone is equipped with a GPS.

Fig. 9.1 A six-bladed wind turbine that was used for measurement

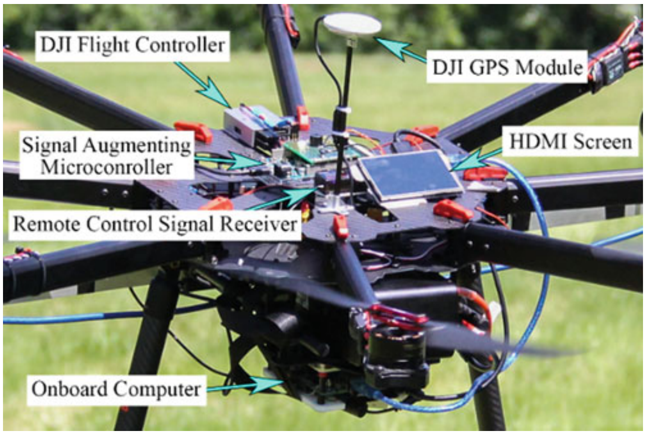

Fig. 9.2 Flight control electronics and view screen

Fig. 9.3 Point Grey GS3-U3-32S4M-C camera with Fujinon 1:1.4/12.5 mm CF12.5HA-1 lens

Fig. 9.4 Diagram of camera configuration and focal length

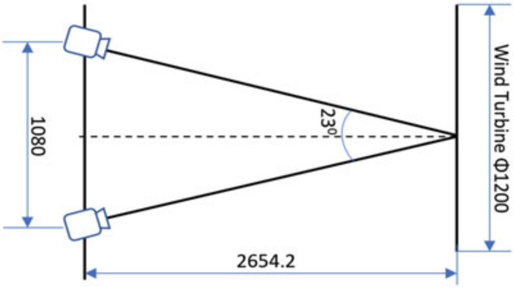

To perform 3-dimensional DIC measurements, a pair of cameras are required. The drone used two Point Grey GS3-U3-32S4M-C cameras with Fujinon 1:1.4/12.5 mm CF12.5HA-1 lenses. These lenses allow for a wide depth of field to maintain image clarity and compensate for any movement of the drone while taking images.

The camera mounting beam consists of a single 1″ × 1″, 1/16″ thick square aluminum tube. The camera configuration for the test measurements is shown in Figs. 9.3 and 9.4. The cameras are 1.08 m (∼39.4″) apart with a focal length of 2.65 m (∼104.5 in). At this focal length, the cameras form a 23° with the target. The cameras were synchronized in slave-slave configuration, and the triggering was performed remotely.

9.3 Laboratory Results/Validation

The first experiment was conducted before the actual test flight. For this case, the turbine blades were non-rotating with the fixed drone.

The experiment was conducted in controlled conditions inside the laboratory where the light intensity and camera position could be set according to the need. This indoor experiment was conducted with the non-rotating turbine blades. Figure 9.5 shows the laboratory setup for the measurement of non-rotating turbine blades. To excite the turbine for DIC measurements, the tip of one of the blades were displaced and allowed to vibrate freely.

Figures 9.6 and 9.7 are respectively the deformation contour and a mode shape of the non-rotating turbine blades obtained using images captured from standing stereo camera on the fixed drone.

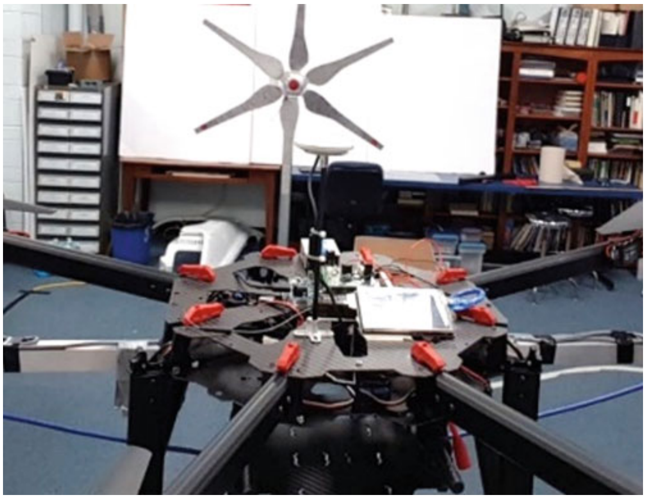

Fig. 9.5 Indoor laboratory test setup to measure vibrations of wind turbine

Fig. 9.6 Full field – analysis for non-rotating blades

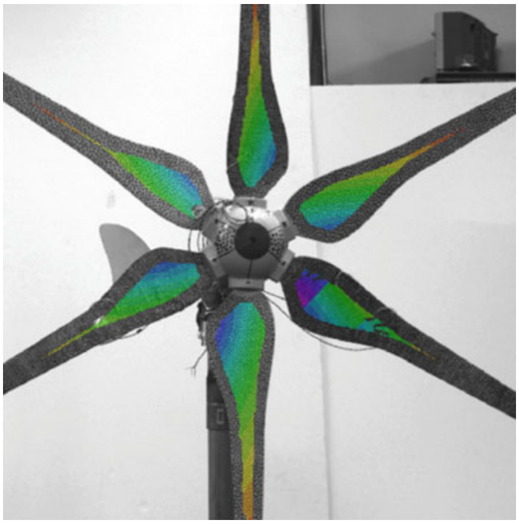

Fig. 9.7 Mode shape at 13.67 Hz for non-rotating turbine blades and fixed drone condition

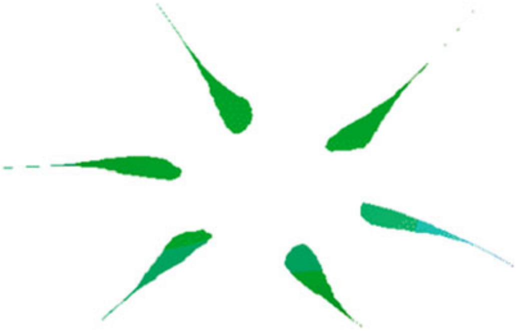

9.4 Outdoor Measurement

For this measurement, the drone was hovering in front of the wind turbine as shown in Fig. 9.8. Three cameras were installed on the drone; two designated for photogrammetry and the other one for live video output to the remote screen and computer vision. The onboard computer was operated using remote desktop. The distance and location for the drone from where

Fig. 9.8 Flying drone for capturing images of the wind turbine blades

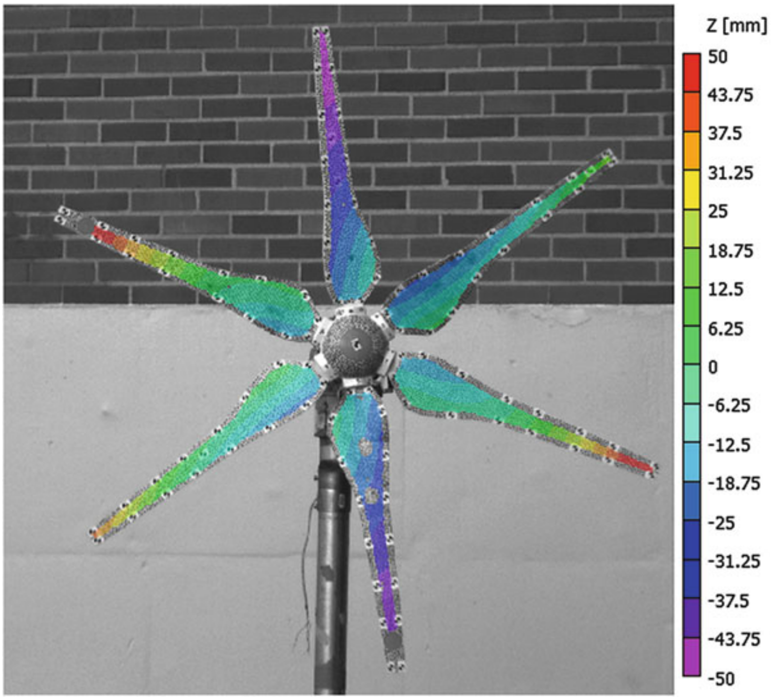

Fig. 9.9 Full field analysis of rotating blades

it would capture the images of the turbine blades was set according to the live feed from the camera. After locating the position, cameras were triggered to capture the images. These images were processed using digital image correlation to obtain the dynamic characteristics of the wind turbine.

The full field analysis of the turbine blades requires analyzing the speckle pattern on the turbine blades. The processing of the images includes selecting the area of interest (AOI) and placing reference points. The post-processing step requires defining the global cylindrical coordinates into the turbine blades. The out of plane deformation of the wind turbine at a sample time is shown in Fig. 9.9. Then the time domain displacement was post-processed in the frequency domain. FRF plot shows that the natural frequency of this turbine blade is 13.83 Hz. This frequency compares well with the laboratory measurement.

9.5 Conclusion

This paper aims to obtain the dynamic characteristics of the structure, here wind turbine, using non-contact full field digital image correlation. The experiments were conducted for both indoor and outdoor conditions. The full field method is based on analyzing the speckle pattern on the structure while point tracking tracks the optical targets to obtain the mode shape and natural frequency of the turbine blades. Both the indoor and outdoor experiments validate the use of the stereo camera for DIC in a mobile platform. The technique allows for health monitoring of prototype wind turbines by obtaining its full field displacement in operating conditions without affecting the functionality of the wind turbine.

References

1. Ciang, C.C., Lee, J.-R., Bang, H.-J.: Structural health monitoring for a wind turbine system: a review of damage detection methods. Meas. Sci. Technol. **19**, 122001 (2008)
2. Larsen, F.M., Sorensen, T.: New lightning qualification test procedure for large wind turbine blades. In: Proceedings of International Conference on Lightning and Static Electricity, Blackpool, UK, 2003
3. Baqersad, J., Niezrecki, C., Avitabile, P.: Numerical and experimental analysis of the boundary conditions effects on the dynamics of wind turbines. Wind Eng. **39**, 437–452 (2015)
4. Baqersad, J., Niezrecki, C., Avitabile, P., Slattery, M.: Dynamic characterization of a free-free wind turbine blade assembly. In: Special Topics in Structural Dynamics, vol. 6, pp. 303–312. Springer (2013)
5. Baqersad, J., Poozesh, P., Niezrecki, C., Avitabile, P.: Comparison of modal parameters extracted using MIMO, SIMO, and impact hammer tests on a three-bladed wind Turbine. In: Topics in Modal Analysis II, vol. 8, pp. 185–197. Springer (2014)
6. Obando, S.E., Baqersad, J., Avitabile, P.: Improved modal characterization using hybrid data. Sound Vib. **48**, 8–12 (2014)
7. Yang, S., Allen, M.S.: Output-only modal analysis using continuous-scan laser Doppler Vibrometry and application to a 20 kW wind turbine. Mech. Syst. Signal Process. **31**, 228–245 (2012). https://doi.org/10.1016/j.ymssp.2012.04.012
8. Ozbek, M., Rixen, D.J., Erne, O., Sanow, G.: Feasibility of monitoring large wind turbines using photogrammetry. Energy. **35**, 4802–4811 (2010). https://doi.org/10.1016/j.energy.2010.09.008
9. Ehrhardt, D.A., Allen, M.S., Yang, S., Beberniss, T.J.: Full-field linear and nonlinear measurements using continuous-scan laser Doppler Vibrometry and high speed three-dimensional digital image correlation. Mech. Syst. Signal Process. **86**, 82–97. https://doi.org/10.1016/j.ymssp.2015.12.003
10. Baqersad, J., Poozesh, P., Niezrecki, C., Avitabile, P.: Photogrammetry and optical methods in structural dynamics – a review. Mech. Syst. Signal Process. **86**, 17–34. https://doi.org/10.1016/j.ymssp.2016.02.011
11. Sarrafi, A., Poozesh, P., Mao, Z.: A comparison of computer-vision-based structural dynamics characterizations. In: Barthorpe, R., Platz, R., Lopez, I., Moaveni, B., Papadimitriou, C. (eds.) Model Validation and Uncertainty Quantification, Volume 3: Proceedings of the 35th IMAC, A Conference and Exposition on Structural Dynamics 2017, pp. 295–301. Springer International Publishing, Cham (2017). https://doi.org/10.1007/978-3-319-54858-6_29
12. Niezrecki, C., Baqersad, J., Sabato, A.: Digital image correlation techniques for NDE and SHM. In: Handbook of Advanced Non-Destructive Evaluation, pp. 1–46 (2018). https://doi.org/10.1007/978-3-319-30050-4_47-1
13. Baqersad, J., Carr, J., Lundstrom, T., Niezrecki, C., Avitabile, P., Slattery, M.: Dynamic characteristics of a wind turbine blade using 3D digital image correlation. In: SPIE Smart Structures and Materials+ Nondestructive Evaluation and Health Monitoring, International Society for Optics and Photonics, pp. 83482I-83482I-83489 (2012)
14. Carr, J., Baqersad, J., Niezrecki, C., Avitabile, P., Slattery, M.: Dynamic stress–strain on turbine blades using digital image correlation techniques part 2: dynamic measurements. In: Topics in Experimental Dynamics Substructuring and Wind Turbine Dynamics, vol. 2, pp. 221–226. Springer, New York, NY (2012)
15. Lundstrom, T., Baqersad, J., Niezrecki, C., Avitabile, P.: Using high-speed stereophotogrammetry techniques to extract shape information from wind turbine/rotor operating data. In: 30th IMAC, A Conference on Structural Dynamics, 2012, January 30, 2012–February 2, 2012, Springer New York, Jacksonville, 2012, pp. 269–275. https://doi.org/10.1007/978-1-4614-2419-2_26
16. Poozesh, P., Sarrafi, A., Mao, Z., Avitabile, P., Niezrecki, C.: Feasibility of extracting operating shapes using phase-based motion magnification technique and stereo-photogrammetry. J. Sound Vib. **407**, 350–366 (2017). https://doi.org/10.1016/j.jsv.2017.06.003
17. Poozesh, P., Sarrafi, A., Mao, Z., Niezrecki, C.: Modal parameter estimation from optically-measured data using a hybrid output-only system identification method. Measurement. **110**, 134–145 (2017)
18. Sarrafi, A., Mao, Z.: Wind turbine blade damage detection via 3-dimensional phase-based motion estimation. In: Proceedings of the 11th International Workshop on Structural Heath Monitoring 2017, (2017). https://doi.org/10.12783/shm2017/14154
19. Sarrafi, A., Poozesh, P., Niezrecki, C., Mao, Z.: Mode extraction on wind turbine blades via phase-based video motion estimation. In: SPIE Smart Structures and Materials+ Nondestructive Evaluation and Health Monitoring, International Society for Optics and Photonics, pp. 101710E-101710E-101712, 2017
20. Lundstrom, T., Baqersad, J., Niezrecki, C.: Monitoring the dynamics of a helicopter Main rotor with high-speed Stereophotogrammetry. Exp. Tech. (2015). https://doi.org/10.1111/ext.12127
21. Schneider, O.: Analysis of SPR measurements from HART II. Aerosp. Sci. Technol. **9**, 409–420 (2005). https://doi.org/10.1016/j.ast.2005.01.013
22. Patil, K., Baqersad, J., Sheidaei, A.: A multi-view digital image correlation for extracting mode shapes of a tire. In: Shock & Vibration, Aircraft/Aerospace, Energy Harvesting, Acoustics & Optics, vol. 9, pp. 211–217. Springer, Cham (2017)

23. Mange, A., Srivastava, V., More, J., Baqersad, J.: Using digital image correlation to measure dynamics of rolling tires. In: SAE World Congress, SAE Technical Paper, Detroit (2018). https://doi.org/10.4271/2018-01-1217
24. Patil, K., Srivastava, V., Baqersad, J.: A Multi-view optical technique to obtain mode shapes of structures. Measurement. **122**, 358–367 (2018). https://doi.org/10.1016/j.measurement.2018.02.059
25. Srivastava, V., Patil, K., Baqersad, J., Zhang, J.: A multi-view DIC approach to extract operating mode shapes of structures. In: Structural Health Monitoring, Photogrammetry & DIC, vol. 6, pp. 43–48. Springer (2019)
26. Kim, S.-W., Kim, N.-S.: Dynamic characteristics of suspension bridge hanger cables using digital image processing. NDT & E Int. **59**, 25–33 (2013). https://doi.org/10.1016/j.ndteint.2013.05.002
27. Busca, G., Cigada, A., Mazzoleni, P., Zappa, E.: Vibration monitoring of multiple bridge points by means of a unique vision-based measuring system. Exp. Mech. **54**, 255–271 (2014). https://doi.org/10.1007/s11340-013-9784-8
28. Baqersad, J., Niezrecki, C., Avitabile, P.: Extracting full-field dynamic strain on a wind turbine rotor subjected to arbitrary excitations using 3D point tracking and a modal expansion technique. J. Sound Vib. **352**, 16–29 (2015). https://doi.org/10.1016/j.jsv.2015.04.026
29. Baqersad, J., Niezrecki, C., Avitabile, P.: Full-field dynamic strain prediction on a wind turbine using displacements of optical targets measured by stereophotogrammetry. Mech. Syst. Signal Process. **62**, 284–295 (2015). https://doi.org/10.1016/j.ymssp.2015.03.021
30. Carr, J., Baqersad, J., Niezrecki, C., Avitabile, P.: Full-field dynamic strain on wind turbine blade using digital image correlation techniques and limited sets of measured data from photogrammetric targets. Exp. Tech. (2015). https://doi.org/10.1111/ext.12129
31. Baqersad, J., Poozesh, P., Niezrecki, C., Avitabile, P.: A noncontacting approach for full-field strain monitoring of rotating structures. J. Vib. Acoust. **138**, 031008–031008 (2016). https://doi.org/10.1115/1.4032721
32. Baqersad, J., Bharadwaj, K., Poozesh, P.: Modal expansion using strain mode shapes. In: Shock & Vibration, Aircraft/Aerospace, Energy Harvesting, Acoustics & Optics, vol. 9, pp. 219–226. Springer (2017)
33. Bharadwaj, K., Baqersad, J.: Strain Expansion Using Mode Shapes Obtained with Digital Image Correlation, Composite Structures (2018, in press)
34. Chen, Y., Joffre, D., Avitabile, P.: Underwater dynamic response at limited points expanded to full-field strain response. J. Vib. Acoust. **140**, 051016 (2018)
35. Rahneshin, V., Chierichetti, M.: An integrated approach for non-periodic dynamic response prediction of complex structures: numerical and experimental analysis. J. Sound Vib. **378**, 38–55 (2016). https://doi.org/10.1016/j.jsv.2016.05.017
36. Reagan, D., Sabato, A., Niezrecki, C.: Feasibility of using digital image correlation for unmanned aerial vehicle structural health monitoring of bridges. Struct. Health Monit. **17**(5), 1056–1072 (2018). https://doi.org/10.1177/1475921717735326

Chapter 10
Full-Field Mode Shape Identification of Vibrating Structures from Compressively Sampled Video

Bridget Martinez, Yongchao Yang, Ashlee Liao, Charles Farrar, Harshini Mukundan, Pulak Nath, and David Mascareñas

Abstract Video-based techniques for structural dynamics have shown great potential for identifying full-field, high-resolution modal properties. One significant advantage of these techniques is that they lend themselves to being applied to structures at very small length scales such as MEMS devices and living cells. These small structures typically will have resonant frequencies greater than 1 Khz, thus requiring the use of high-speed photography to capture their dynamics without aliasing. High speed photography generally requires the structure-under-test (*e.g.* living cell) to be exposed to high levels of illumination. It is well-known that exposing delicate structures such as living cells to these high levels of light energy can result in damage to their structural integrity. It is therefore desirable to develop techniques to minimize the amount of illumination that is required to capture the modal properties of interest. This is particularly important given that the mechanical properties of living cells have recently been found to be of interest to the biomedical community. For example, it is known that changes in cell stiffness are correlated with grade of metastasis in cancer cells. Compressive sensing techniques could help mitigate this problem, particularly in fluorescence microscopy applications where cells are illuminated using a laser light source. Compressive sampling would allow for the cells to be exposed to the laser light with a significantly lower duty cycle, thus resulting in less damage to the cells. As a result the structural dynamics of the cells can be measured at increasingly high frequencies yielding new information about cellular material properties that can be coupled with biochemical cues to yield new therapeutic strategies. Furthermore, video-based techniques would benefit from the reductions in memory, bandwidth and computational requirements normally associated with compressive sampling. In this work we present a technique that intimately combines solutions to the blind-source separation problem for video-based, high-resolution operational modal analysis with compressive sampling.

Keywords Compressive sensing · Operational modal analysis · Imager · Microscopy · Cancer

10.1 Introduction

Since its introduction to the field of signal processing in 2004, compressed sensing (CS) has enabled many applications which allow for the recovery of sparse or compressible signaling. Following the famous Shanon sampling theorem, CS has proven a great triumph in the field of signal processing [1–4]. As abovementioned, CS is useful in the acquisition of signals which are either spare or compressible; both compressibility and sparsity are properties that can be assigned to information which can be represented in its entirety, or completeness with only a few, key components of data. Furthermore, these characteristics are not limited to being represented in the original domain but can also exist in transform domains. Traditionally, acquisition of sparse signals must meet Nyquist criterion, wherein the ratio of signal to data is increased, as well as requires compressing the signal, transforming coefficients and retaining only some of the coefficients. CS was

---

B. Martinez (✉) · A. Liao · C. Farrar · D. Mascareñas
Los Alamos National Lab, Engineering Institute, Los Alamos National Lab, Los Alamos, NM, USA
e-mail: bmartinez26@ucmerced.edu

Y. Yang
Energy and Global Security, Argonne National Laboratory, Lemont, IL, USA

H. Mukundan
Los Alamos National Lab, Physical Chemistry and Applied Spectroscopy, Chemistry Division, Los Alamos National Lab, Los Alamos, NM, USA

P. Nath
Los Alamos National Lab, Applied Modern Physics, Los Alamos National Lab, Los Alamos, NM, USA

C. Niezrecki et al. (eds.), *Rotating Machinery, Optical Methods & Scanning LDV Methods, Volume 6*, Conference Proceedings of the Society for Experimental Mechanics Series, https://doi.org/10.1007/978-3-030-12935-4_10

inspired by efforts to decrease sampling amounts when most would eventually be discarded anyway. Since its introduction to the field, this signal processing technique has become particularly attractive in the fields of microscopy and medical imaging, where taking measurements poses great expense and sensing is time consuming and more prone to error [5–9].

CS appeal as a successful technique for imaging recovery comes from its utility in being able to reconstruct signals perfectly with the use of non-linear reconstruction algorithms. As abovementioned, it has become particularly attractive in the field of medicine. Its uses are evident in the reconstruction of x-ray cone-beam computed tomography (CBCT). In CBCT, subsampling due to slow rotation and low frame rate of x-ray detectors is circumvented through content-driven hierarchical reconstruction based on compressed sensing [10]. In addition, CS is also used in multichannel EEG signals. The study by Lui et al., for example, shows how the simultaneous co-sparsity and low-rank optimization enables successful compressed sensing of EEG signals. The study further highlights that this is true even during poor sparse representation. In this wireless EEG system, the authors show that their proposed model with L0 norm with Schatten-O norm reduces the power consumption of the system [11].

Compressed sensing has also been found useful in magnetic resonance imaging (MRI). This type of imaging is critical in clinical settings where its sensitivity enables crucial diagnostic and research efforts. Patient comfort and compliance is often hindered given the high cost and lengthy acquisition times of the imaging modality. For these reasons, compressed sensing has been identified as a fruitful technique useful for lowering scan acquisition times. Normally, the minimum scan acquisition time is set via the invariable amount of data that is necessitated to meet Nyquist criteria. Applying compressed sensing theory, a MR image that is sparse, or which can be mathematically transformed into a sparse image, can be exploited to recover high definition images [12]. The concept of random under sampling/data acquisition followed by a constrained reconstruction has existed in the field of signal processing for some time, but the idea to apply the theory in the field of medicine, especially in imaging modalities and its practicality in the field, are still being sorted [2]. Variation sparsity is also exploited in other imaging modalities, including ultrasound computed tomography (UCT). For example, Van Sloun et al. demonstrated that acquisition time is reduced by a complete order of magnitude while still maintaining high spatial resolution using compressed acquisitions with concurrent randomized transmission in circular array configurations. UCT is invaluable in medicine, enabling the reconstruction of tissue characteristics which provide the field of oncology with crucial information. Moreover, while it is beneficial to reduce the slice acquisition time, it will be interesting to contemplate future applications in 3-D UCT [13].

Given its utility in many imaging modalities, it seems possible that CS would also find utility in structural dynamics at the cellular level. Current research aims are to develop and use sensitive image analysis techniques for quantitatively characterizing cells undergoing cancer metastasis. There still exists significant gaps in quantitatively analyzing the data from current techniques, and in using them to verify and validate finite element models describing the mechanics of cells. This is primarily because of the lack of comprehensive techniques to measure the full-field structural stiffness of cells. There is a need for novel and unique imaging techniques develop that provide verification and validation of finite element models of cellular structure. Understanding how cellular structure drives resulting function can facilitate formulation of unique anti-cancer treatments by directly affecting ECM structure, bypassing its drug-inhibitory effect in cancer cells altogether. Compressive sensing techniques could help mitigate this problem, particularly in fluorescence microscopy applications where cells are illuminated using a laser light source. Compressive sampling would allow for the cells to be exposed to the laser light with a significantly lower duty cycle, thus resulting in less damage to the cells. As a result, the structural dynamics of the cells can be measured at increasingly high frequencies yielding new information about cellular material properties that can be coupled with biochemical cues to yield new therapeutic strategies. An additional benefit in using video-based techniques would be the reductions in memory, bandwidth and computational requirements normally associated with compressive sampling. In this work we present a technique that intimately combines solutions to the blind-source separation problem for operational modal analysis with compressive sampling.

Recently, a significant useful technique has been identified as a potential tool to measure and characterize the mode shapes of cells at very high spatial resolution. By combining the theory of structural dynamics with computer vision and unsupervised machine learning algorithms, researchers have recently developed a technique that that is able to autonomously and efficiently measure and characterize structural dynamics at very high spatial density using only an imager [21–23]. It will be exciting to exploit this novel technique in hopes that it will provide a new, efficient tool for significantly better characterization of how stiffness and mass distribution changes in a cell and in identifying its associated EMC biochemical cues, highlighting potential therapeutic targets. This knowledge could be used to provide verification and validation of finite element models of cellular structure. This highly interdisciplinary work combines knowledge and data from experimental structural dynamics and molecular cellular biology in efforts to characterize the structural dynamics of cells at high spatial resolution.

10.2 Background

The algorithm for extracting full-field, high resolution structural dynamics information from video of vibrating structures can be summarized as follows [14]:

1. Convert the intensity measurements at each pixel into a quantity that represents the displacement at each pixel. This transformation can potentially be accomplished in a variety of ways. For in-plane motion phase-based optical flow [15–17], provides a useful means to perform the conversion from pixel intensity to displacement and is used in this work. Ultimately this procedure is applied across the time-span of the video and the result is a time series of displacement for every pixel.
2. Perform principle components analysis (PCA) across all of the displacement time series in order to reduce the dimensionality of the data. It is expected that the number of non-trivial eigenvalues calculated from the displacement time series for each pixel generated from a video of a vibrating structure will be of the same order as the number of mode shapes that are observable from the displacement time series. For this reason, it is only necessary to retain about the number of top eigenvectors that correspond to the number of non-trivial singular values.
3. We now take advantage of the observation that the canonical form of the blind source separation problem has exactly the same form as the linear, multi-degree-of-freedom, structural dynamics equations when written in the modal form [18, 19]. If the blind source separation problem is solved using the time series extracted from the principle components analysis above as input, the columns of the mixing matrix provided by a blind source separation solution technique will yield the mode shapes at high-spatial resolution, and the resulting individual signal sources correspond to the modal coordinates for each mode. Thus far complexity pursuit [20] has been found to be an attractive algorithm for solving the blind-source separation problem for structural dynamics applications.

After applying these steps to the video, the result is high-resolution mode shapes and modal coordinates that can be used to estimate resonant frequencies and damping ratios. This approach to structural dynamics identification is attractive because it is conceptually easy to understand and the mode shapes provided have spatial resolution on the order of the pixel size. Furthermore, the algorithm lends itself to being automated, which makes it attractive for long-term monitoring of structures. However, if one is particularly perceptive it is possible to see that this algorithm also inherently possess properties of compressive sampling similar to those found in [21]. In fact, the algorithm in its current form allows for the automatic estimation of the mode shapes when only a randomly selected subset of the frames are used for analysis.

Amazingly, it is not even necessary to know what the random measurement matrix is. In contrast, traditional applications of compressive sampling to structural dynamics data requires the measurement matrix be known in order to perform an L1 minimization step to recover the original signal from the compressively sampled signal [22]. The reason that mode shapes can be recovered automatically from randomly measured samples is related to the phenomena that allows this algorithm to operate even when the video is captured at a framerate below the Nyquist frequency of the structural vibrations [23]. To clarify, the canonical blind source separation problem can be written as:

$$x(t) = As(t) \tag{10.1}$$

Where $x(t)$ is a column vector of the time series for each measurement available for analysis, $s(t)$ is a column vector of time series associated with the sources generating the measured data, and A is the mixing matrix that indicates how the source time series are combined to form the measured time series. For comparison, the linear, multi-degree-of-freedom structural dynamics equations are written as:

$$x(t) = \Phi q(t) \tag{10.2}$$

Where $x(t)$ is once again a column vector of the time series for each measurement available for analysis. In this case presumably displacement measurements from a vibrating structure. Φ is a matrix whose columns are the structural mode shapes, and q(t) is a column vector of the modal coordinates. An examination of Eqs. (10.1) and (10.2) reveals that the mixing matrix A, and by extension the mode shape matrix Φ do not depend on the temporal nature of the measurements or the temporal nature of the generating sources/modal coordinates. As a result, if all that is needed is the high-resolution mode shapes, the blind source separation step will theoretically extract the mode shapes regardless of whether all the frames are present, or only a subset of the frames are present. In either case, the mixing relationship between the source signals is preserved and therefore the algorithm will theoretically return the correct mode shapes.

Furthermore, unlike in conventional compressive sampling procedures there is no need to perform any kind of L1 minimization-based reconstruction step, there is no need to know the form of the mixing matrix, and there is no need to know the basis in which the signal is sparse. Solving the blind source separation problem automatically estimates the mode shapes without any of this information or extra steps. It is interesting to note that theoretically it is possible to extract the mode shapes even if the order of the random subset of frames were randomly shuffled**.** It is important to note that the modal coordinates are not recovered by solving the blind source separation problem for the case of only a random subset of the frames being used for the analysis. However, it is hypothesized that the modal coordinates could be recovered in the case of a random subset of frames by using an L1 reconstruction step with knowledge of the measurement matrix and assuming the modal coordinates are sparsely represented in a Fourier basis as is expected for a linear dynamical system. This hypothesis will be explored in future work.

10.3 Experimental Setup

In order to demonstrate the performance of the blind source separation techniques for extracting high-resolution, full-field mode shapes from a random subset of frames from the original video we consider the case of a vertical, aluminum cantilever beam that has been subject to an impact excitation at its base. A video of the vibrating beam was captured at 480 frames per second (FPS). A total of 600 frames were captured and the dimensions of the frames are 216 pixels × 384 pixels. Figure 10.1 shows a representative frame captured by the video camera.

For the sake of completeness, the original video was run through the algorithm described in the background section. The algorithm was directed to search for 3 modes. Figure 10.2 provides the resulting modal coordinates shown in both the time and frequency domain. An examination of the modal coordinates reveals that 3 modes can be observed from the video. These modes occur at 7.2 Hz, 47.2 Hz, and 133.6 Hz. The three modes are highly separated in the frequency domain.

10.4 Analysis

Next, we demonstrate the ability of the algorithm described in the background section to extract high resolution mode shapes from random subsets of the frames that make up the original video. Figure 10.3 shows the mode shapes extracted by the algorithm for different numbers of frames in the subset of random frames used to perform the analysis. Row a shows the mode shapes extracted from the original video as a benchmark. These mode shapes have the characteristics that would be expected for a cantilever beam. The mode shapes shown for rows a through c were extracted with the algorithm directed to find 3 mode shapes. The mode shapes extracted when only a random subset of 48.8% of the original frames were used (row b) are visually identical to the case where 100% of the frames were used (row a). In the case where a random subset of only 16.83% of the frames were used (row c) the first mode is essentially visually identical to the 100% frames case, however the second and third modes appear to have experienced some degradation in comparison to the 100% frames case.

Fig. 10.1 Example frame captured from the camera of the vibrating beam. 600 frames were captured at 480 frames per second. Video pixel dimension is 216 × 384

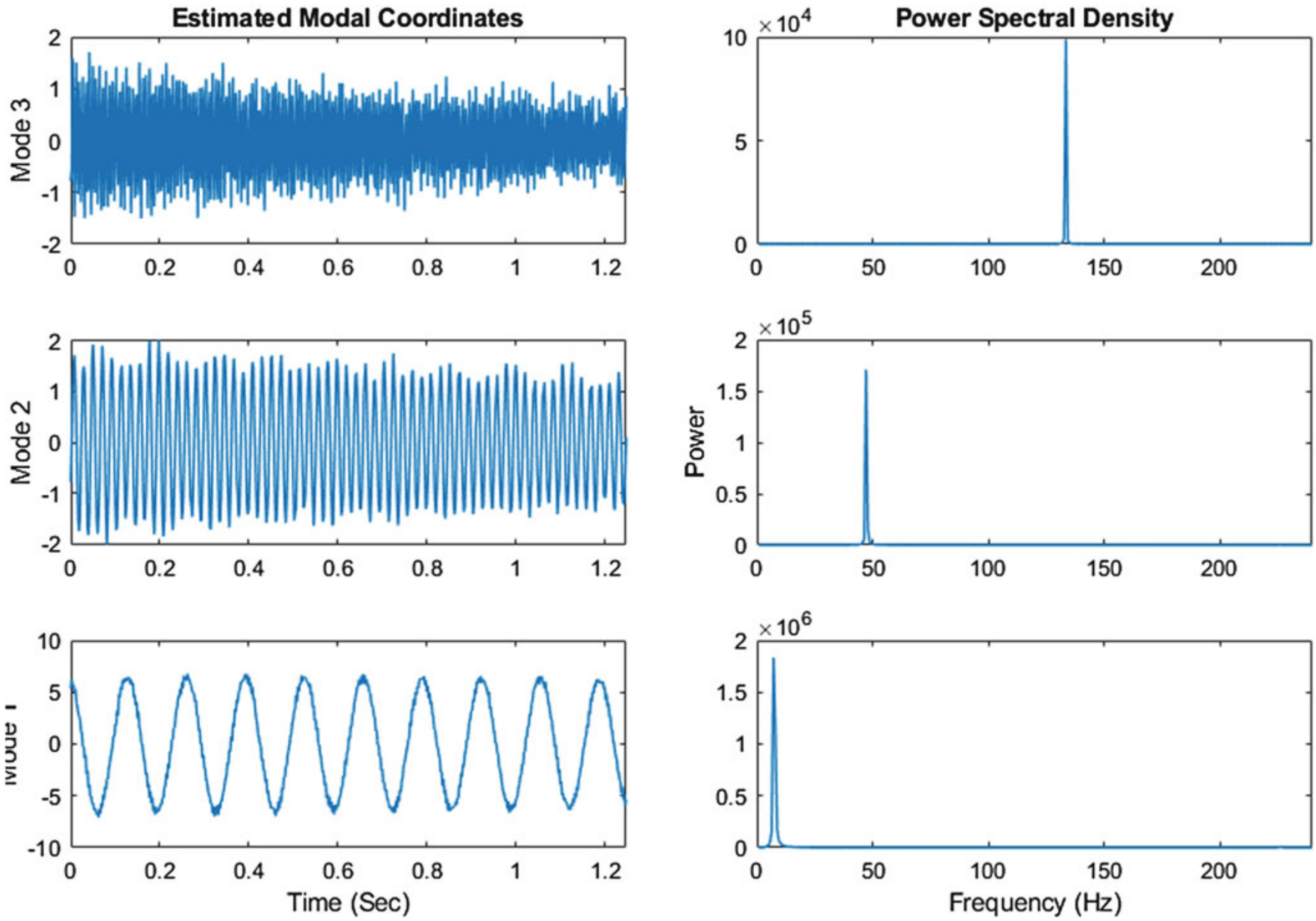

Fig. 10.2 The modal coordinates extracted from the video of the vibrating cantilever beam with no compressive downsampling. Mode 1 occurs at 7.2 Hz, mode 2 is at 47.2 Hz and Mode 3 occurs at 133.6 Hz. The original video is captured at 480 FPS

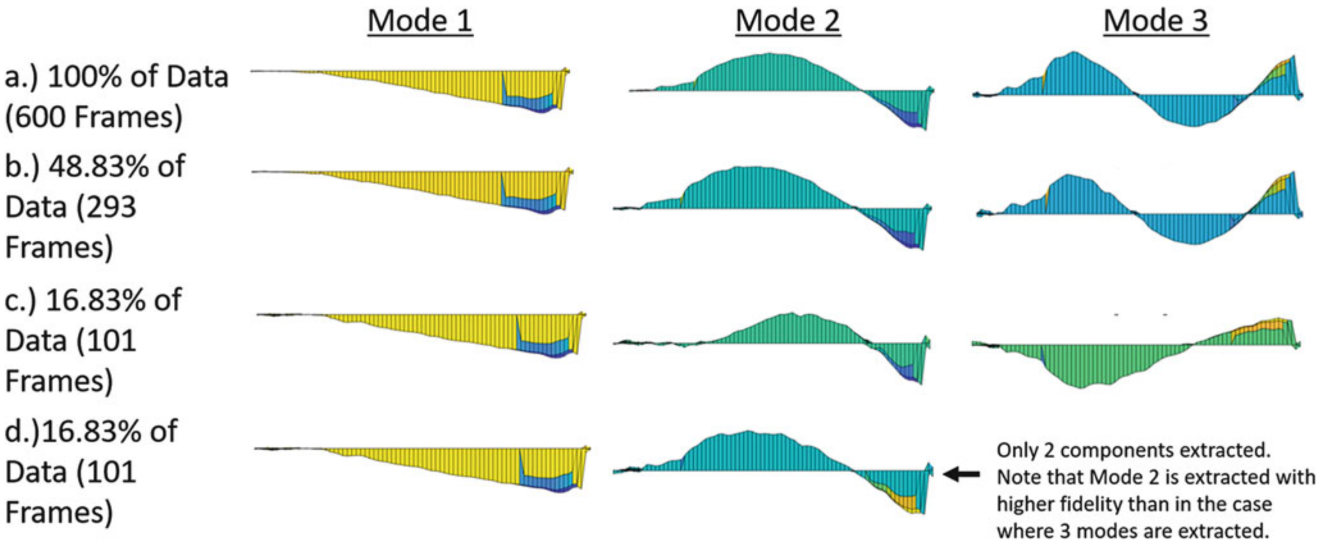

Only 2 components extracted. Note that Mode 2 is extracted with higher fidelity than in the case where 3 modes are extracted.

Fig. 10.3 Modes extracted from the randomly selected frames. The original video is captured at 480 FPS. The mode shapes have been rotated 90° from the vertical position in order to facilitate their display and visual comparison

It appeared that the algorithm was not able to observe the third mode in this case, and instead tried to split the second mode into two separate independent shapes. This observation was based on the fact that the 2nd and 3rd mode shape extracted by the algorithm both only have 1 inflection point which is consistent with what would be expected for the 2nd mode shape of a cantilever beam. Based on this observation, it was determined that in the case of using only a random subset of 16.83% of the original frames it made sense to direct the algorithm to only search for 2 modes. The resulting modes are shown in row d. An inspection of the mode shapes shown in row d show that the 1st and 2nd mode shape are visually identical to the mode shapes captured in the case of 100% of the frames.

The results shown in Fig. 10.3 provide strong evidence that compressive sampling techniques can be effectively be used when trying to estimate the mode shapes of structures. It is found that as the number of frames is decreased, the higher 3rd mode is no longer observed. This result suggests that the technique gracefully degrades in performance as the number of frames used in the analysis decreases. A quantifiable degradation in the performance of compressive sampling techniques for structural dynamics applications was also observed in [22] and is arguably a desirable property of compressive sampling techniques. Future research should focus on the development of improved techniques to automatically decide the number of independent components that the algorithm should retain. The number of components that should be searched for will be dependent on the number of frames used in the analysis and the number of modes that are excited during the structural vibration.

10.5 Conclusions

In this work we demonstrate that full-field, high-resolution blind-source separation-based techniques for structural mode shape identification are immediately suited for compressive sensing analysis. These techniques do not require knowledge of the random measurement matrix, the basis in which the mode shapes are sparse, or an additional L1 reconstruction step. These techniques are readily amenable to both field applications as well as to applications such as fluorescence microscopy where it is desirable to reduce the duty cycle of active laser illumination on cells which might otherwise cause damage. Furthermore, the application of compressive sampling techniques to high-resolution structural identification is particularly attractive for structural monitoring applications in bandwidth-limited environments such as monitoring underwater structures and monitoring from spacecraft. In addition, the use of compressive sampling techniques reduces the energy resources needed to perform analysis in wireless multimedia sensor networks.

Acknowledgements Bridget Martinez is supported by a Director's Funded Postdoctoral fellowship from the Laboratory Directed Research and Development program at Los Alamos National Laboratory. Los Alamos National Laboratory is operated by Los Alamos National Security LLC, for the National Nuclear Security Administration of the U.S. Department of Energy, under DOE Contract DE-AC52-06NA25396.

References

1. Candes, E.J., Romberg, J., Tao, T.: Robust uncertainty principles: exact signal reconstruction from highly incomplete frequency information. IEEE Trans. Inf. Theory. **52**(2), 489–509 (2006)
2. Donoho, D.L.: Compressed sensing. IEEE Trans. Inf. Theory. **52**(4), 1289–1306 (2006)
3. Candes, E.J., Tao, T.: Near-optimal signal recovery from random projections: universal encoding strategies? IEEE Trans. Inf. Theory. **52**(12), 5406–5425 (2006)
4. Candes, E.J., Wakin, M.B.: An introduction to compressive sampling. IEEE Signal Process. Mag. **25**(2), 21–30 (2008)
5. Stern, A.S., Hoch, J.C.: A new approach to compressed sensing for NMR. Magn. Reson. Chem. **53**(11), 908–912 (2015)
6. Ho, C.M., Hsu, S.D.H.: Determination of nonlinear genetic architecture using compressed sensing. Gigascience. **4**(1), 44 (2015). s13742-015-0081-6-s13742-015-0081-6
7. Wiens, C.N., et al.: R2*-corrected water-fat imaging using compressed sensing and parallel imaging. Magn Reson Med. **71**(2), 608–616 (2014)
8. Liu, J., He, Q., Luo, J.: Compressed sensing for high frame rate, high resolution and high contrast ultrasound imaging. In: 2015 37th Annual International Conference of the IEEE Engineering in Medicine and Biology Society (EMBC) (2015)
9. Park, S., Park, J.: Compressed sensing MRI exploiting complementary dual decomposition. Med. Image Anal. **18**(3), 472–486 (2014)
10. Langet, H., et al.: Compressed-sensing-based content-driven hierarchical reconstruction: Theory and application to C-arm cone-beam tomography. Med. Phys. **42**(9), 5222–5237 (2015)
11. Liu, Y., Vos, M.D., Huffel, S.V.: Compressed sensing of multichannel EEG signals: the simultaneous cosparsity and low-rank optimization. IEEE Trans. Biomed. Eng. **62**(8), 2055–2061 (2015)
12. Kieren Grant, H.: Reducing acquisition time in clinical MRI by data undersampling and compressed sensing reconstruction. Phys. Med. Biol. **60**(21), R297 (2015)
13. van RJG, S., et al.: Compressed sensing for ultrasound computed tomography. IEEE Trans. Biomed. Eng. **62**(6), 1660–1664 (2015)
14. Yang, Y., et al.: Blind identification of full-field vibration modes from video measurements with phase-based video motion magnification. Mech. Syst. Signal Process. **85**, 567–590 (2016)

15. Fleet, D.J., Jepson, A.D.: Computation of component image velocity from local phase information. Int. J. Comput. Vis. **5**(1), 77–104 (1990)
16. Wadhwa, N., et al.: Phase-based video motion processing. In: ACM Trans. Graph. (Proceedings SIGGRAPH 2013) (32). Anaheim, CA (2013)
17. Simoncelli, E.P. matlabPyrTools. 2009
18. Kerschen, G., Poncelet, F., Golinval, J.-C.: Physical interpretation of independent component analysis in structural dynamics. Mech. Syst. Signal Process. **21**, 1561–1575 (2007)
19. Poncelet, F., Kershen, G., Verhelstb, D., Golinval, J.-C.: Output-only modal analysis using blind source separation techniques. Mech. Syst. Signal Process. **21**, 2335–2358 (2007)
20. Stone, J.V.: Blind source separation using temporal predictability. Neural Comput. **13**(7), 1559–1574 (2001)
21. Yang, Y., Nagarajaiah, S.: Output-only modal identification by compressed sensing: non-uniform low-rate random sampling. Mech. Syst. Signal Process. **56-57**, 15–34 (2015)
22. Mascareñas, D., et al.: Compressed sensing techniques for detecting damage in structures. Struct. Health Monit. **12**(4), 325–338 (2013)
23. Yang, Y., et al.: Output-only modal identification with uniformly-sampled, possibly temporally-aliased, full field video measurements. J. Sound Vib. **390**, 232–256 (2017)

Chapter 11
Experimental Modal Analysis of Tumorigenesis and Cancer Metastasis

Bridget Martinez, Yongchao Yang, Charles Farrar, Harshini Mukundan, Pulak Nath, and David Mascareñas

Abstract Traditionally, performing an experimental modal analysis of a building/structure required instrumenting the structure with a spatially distributed array of accelerometers or strain gages. Alternatively, a laser doppler vibrometer would have to be scanned across the structure of interest in a sequential manner to measure structural response. Recently, researchers at LANL developed a technology that combines the theory of structural dynamics with computer vision that provides the capability to characterize structural dynamics at very high spatial density using only an imager. With this newfound success at the macro-scale, we have exploited this novel technology to a whole new scale- to studying the basic structure of life itself, the human cell. We hypothesize that this new technology and novel application will provide a significantly better understanding of how stiffness and mass distribution changes in a cell as it undergoes epithelial-mesenchymal transition, and in identifying its associated EMC biochemical cues, highlight potential therapeutic targets. For the first time it should be possible to measure the high-resolution mode shapes of cells; given that all cells undergoing cancer metastasis experience a breakdown in the cytoskeleton, this work will enable groundbreaking advances in various fields including medicine and structural dynamics. It is imperative to highlight, that we are only beginning to understand the relationship between biophysical properties of cells and their potential to regulate tumorigenesis and motility, which is commonly known as metastasis. This knowledge could be used to provide verification and validation of finite element models of cellular structure. This work will represent the first time that expertise in experimental structural dynamics will be brought to bear on the problem of characterizing the structural dynamics of cells at high spatial resolution, which is novel and unique on its own. When successful, this new technology could be used to couple the biophysical cues associated with other detrimental human pathologies.

Keywords Cancer · Mode shapes · Microscopy · Finite element models · Tumorigenesis

11.1 Introduction

Mechanoreciprocity refers to a cell's ability to maintain tensional homeostasis in response to various types of forces. Physical forces are continually being exerted upon cells of various tissue types, even those considered static tissues, such as the brain. Through mechanoreceptors, cells sense and subsequently respond to these stimuli. These forces and their respective cellular responses are prevalent in regulating everything from embryogenic tissue-specific differentiation, programmed cell death, and in what has garnered the most attention, disease progression. Abnormal mechanical remodeling of cells can provide clues as to the pathological status of many tissues. This becomes particularly important in cancer cells, where cellular stiffness has been recently accepted as a novel biomarker for cancer metastasis. Several studies have elucidated the importance of cell stiffness in cancer metastasis, with data highlighting that a reversal of tumor stiffness has the capacity to revert the metastatic properties of cancer. Thus, our research endeavors to exploit this knowledge and, in using new strategies such as recently developed video-based techniques for structural dynamics, venture to further our understanding of the mechanisms

---

B. Martinez (✉) · C. Farrar · D. Mascareñas
Los Alamos National Lab, Engineering Institute, Los Alamos National Lab, Los Alamos, NM, USA
e-mail: bmartinez26@ucmerced.edu

Y. Yang
Energy and Global Security, Argonne National Laboratory, Lemont, IL, USA

H. Mukundan
Los Alamos National Lab, Physical Chemistry and Applied Spectroscopy, Chemistry Division, Los Alamos National Lab, Los Alamos, NM, USA

P. Nath
Los Alamos National Lab, Applied Modern Physics, Los Alamos National Lab, Los Alamos, NM, USA

C. Niezrecki et al. (eds.), *Rotating Machinery, Optical Methods & Scanning LDV Methods, Volume 6*, Conference Proceedings of the Society for Experimental Mechanics Series, https://doi.org/10.1007/978-3-030-12935-4_11

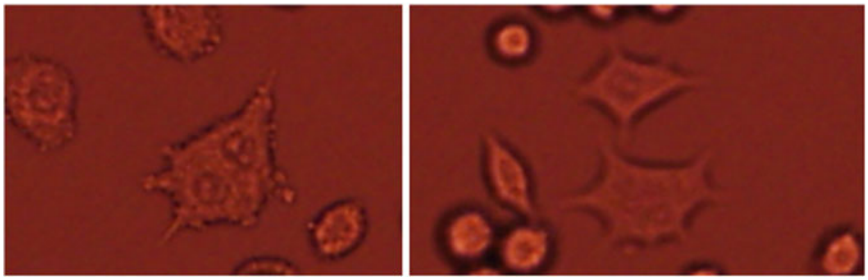

Fig. 11.1 Confocal light microscopy image; CCL1 mouse fibroblast cell line (10 × 10) (**a**) cells undergoing cell division (**b**) cell line displaying normal dimorphism

which generate pathogenic cell stiffness. Our research strives to highlight potential new strategies which have the capacity to advance our understanding of one of human-kind's most detrimental medical pathologies, and in so doing, outline potential new therapeutic targets against it.

The importance of maintenance of extracellular matrix (ECM) biophysical properties can be extrapolated from studies showing that inappropriate alterations are associated with fibrotic, or tissue scarring conditions and metastatic cancer. Indeed, it is well recognized that the ECM of a tumor is largely distinct from its physiologic counterpart [1–4]. Additionally, studies which outline how post-translational cross-linking of the ECM in premalignant breast cancer is a necessary step for transformation into a malignant cancer further enables us to appreciate how an ECM's biochemical composition plays such paramount importance in cancer progression [5, 6]. Similar results have been published for other various types of cancer, including colorectal [7, 8]. This highly impactful data underscores the significance of ECM homeostasis and highlights the necessity to better understand the mechanism(s) that drive ECM remodeling in the context of oncology.

Our current work seeks to succeed in the following two aims. The first aim of our study is to be able to extract full-field, high resolution, modal properties from various types of cancer cells using technology that combines the theory of structural dynamics with computer vision that provides the capability to characterize structural dynamics at very high spatial density using only an imager. The image acquisition will be facilitated with the use of fluorescence microcopy, using GFP-alpha tubulin to express cell structure and microtubule network. Our current work is focused on using the CCL1 mouse fibroblast cell line (Fig. 11.1).

By combining the theory of structural dynamics with computer vision and unsupervised machine learning algorithms, researchers have recently developed a technique that that is able to autonomously and efficiently measure and characterize structural dynamics at very high spatial density using only an imager. It will be exciting to exploit this novel technique in hopes that it will provide a new, efficient tool for significantly better characterization of how stiffness and mass distribution changes in a cell and in identifying its associated EMC biochemical cues, highlighting potential therapeutic targets. With the success of these studies, we will be well on our way to understanding the intricate relationship between the biophysical properties of cells and their potential to regulate tumorigenesis and motility. This knowledge could be used to provide verification and validation of finite element models of cellular structure. Our current research demonstrates the first time that knowledge in experimental structural dynamics will be brought to bear on the problem of characterizing the structural dynamics of cells at high spatial resolution.

The second aim of our study seeks to excite varying types of cancer cells using cavitation bubble techniques combined with microfluidic capabilities. Sonoporation, or micro-bubble mediated cell lysis, facilitates gene-drug delivery to cells, here we attempt to use the technique to excite cells to specific frequencies by controlling the distance from which cavitation bubbles are induced, roughly around 40 um. We are currently working to develop a unique microfluidic device which allows for the capacity to control "shooting distance" from cavitation bubble generation to cancer cell. The design will aim to enable pre- as well as post-device applications, such as the ability to carry out genomic and proteomic capabilities. For example, it would be ideal to be able to control the cell distance from the cavitation bubbles, as well as have the potential to remove single cells from microfluidic devices and proceed straight to real-time polymerase chain reaction applications. Given that distance from cavitation bubble to cell defines function, i.e. whether we are generating localized displacement of cellular membrane, or simply exciting the cell to its natural frequency, it is imperative to able to develop a device that has the capacity to both simply excite as well as lyse the cell. Cell lysis through this microbubble-medicated biophysical process will enable quick throughput applications of specific cells, as well as remove the need to induce sonoporation through chemical interactions. Here we provide a simple schematic of the proposed device (Fig. 11.2).

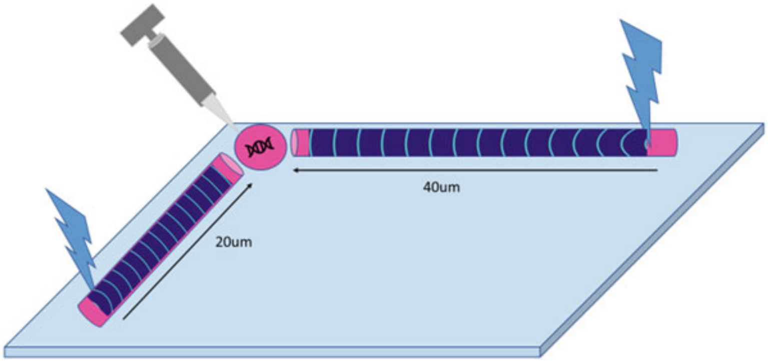

Fig. 11.2 Proposed microfluid device configuration; controlling the distance from which cavitation bubbles are induced, roughly around 40 um

11.2 Conclusion

Currently, interesting non-contact/non-intrusive imaging methods are being used for diagnostic purposes is interferometric phase microscopy (IPM), which provides several advantages over AFM [9]. The appeal of IPM is that it captures the entire amplitude and phase data from the optical illumination of the sample, generating an optical thickness fluctuation map, which indicates rigidity strength for every cell in the field of view [9], with the added benefit of cell to cell comparison. Even as we circumvent existing limitations and find novel techniques that increase imaging sensitivity, it is imperative to note that we are only beginning to understand the relationship between biophysical properties of cells, and their potential to regulate tumorigenesis and motility [10]. There is a need for novel and unique imaging techniques develop that provide verification and validation of finite element models of cellular structure. Understanding how cellular structure drives resulting function can facilitate formulation of unique anti-cancer treatments by directly affecting ECM structure, bypassing its drug-inhibitory effect in cancer cells altogether. As we circumvent more and more limitations and find novel techniques that increase imaging sensitivity, it is imperative to note that we are only beginning to understand the relationship between biophysical properties of cells and their potential to regulate tumorigenesis and motility. As more novel and unique imaging techniques develop which can be used to provide verification and validation of finite element models of cellular structure, the knowledge obtained of how cellular structure drives function could be used to formulate unique anti-cancer treatments by directly affecting ECM structure, bypassing its drug-inhibitory effect in cancer cells altogether.

References

1. Cox, T.R., Erler, J.T.: Remodeling and homeostasis of the extracellular matrix: implications for fibrotic diseases and cancer. Dis. Model. Mech. **4**(2), 165 (2011)
2. Aszódi, A., et al.: What mouse mutants teach us about extracellular matrix function. Annu. Rev. Cell Dev. Biol. **22**(1), 591–621 (2006)
3. Leight, J.L., Drain, A.P., Weaver, V.M.: Extracellular matrix remodeling and stiffening modulate tumor phenotype and treatment response. Ann. Rev. Cancer Biol. **1**(1), 313–334 (2017)
4. Sotgia, F., et al.: Caveolin-1 and cancer metabolism in the tumor microenvironment: markers, models, and mechanisms. Annu Rev Pathol. **7**(1), 423–467 (2012)
5. Levental, K.R., et al.: Matrix crosslinking forces tumor progression by enhancing integrin signaling. Cell. **139**(5), 891–906 (2009)
6. Paszek, M.J., et al.: Tensional homeostasis and the malignant phenotype. Cancer Cell. **8**(3), 241–254 (2005)
7. Erler, J.T., et al.: Lysyl oxidase is essential for hypoxia-induced metastasis. Nature. **440**, 1222–1226 (2006)
8. Baker, A.M., et al.: Lysyl oxidase enzymatic function increases stiffness to drive colorectal cancer progression through FAK. Oncogene. **32**, 1863 (2012)
9. Bishitz, Y., et al.: Optical-mechanical signatures of cancer cells based on fluctuation profiles measured by interferometry. J. Biophotonics. **7**(8), 624–630 (2014)
10. Paszek, M.J., Weaver, V.M.: The tension mounts: mechanics meets morphogenesis and malignancy. J. Mammary Gland Biol. Neoplasia. **9**(4), 325–342 (2004)

Chapter 12
Full Field Strain Measurements Using 3D Laser Vibrometry

Samuel Tilmann

Abstract Obtaining accurate strain measurements is a critical component of testing when it comes to validating aerospace structures designed for extreme environments. Using a 3D laser vibrometry system it is possible to measure the velocity at a point and from that calculate displacement. From that displacement strain can be calculated across an array of points. With a fine enough grid it is possible to obtain accurate full field dynamic strain measurements of an article under load. One advantage this method has over traditional strain measuring techniques is that there is no need to install additional instrumentation on the test article. This is critical to eliminate mass loading on lightly damped structures. Using 3D laser vibrometry, it is also possible to obtain dynamic strain measurements in extreme thermal environments. In order for this method to be verified it needs to be compared against more traditional, reliable strain measurement techniques. This paper will be comparing the results of the 3D laser vibrometry system's strain measurements using several different surface treatments at several different temperatures to measurements obtained from traditional foil strain gages.

Keywords Laser vibrometry · Dynamic strain · Full field strain · Non-contact measurements

12.1 Introduction

Through the use of three laser vibrometers it is possible to obtain 3D velocity measurements of an article at multiple points and from those measurements calculate full field displacement and strain of that article. This paper discusses the viability of using this strain calculation method on thin skinned articles with high out of plane displacement. There is also concern with the viability of the system at elevated temperatures due to interference from radiant heat sources or damage to the surface treatment of the article. In the experiment a PSV-500 3D laser vibrometry system is used along with a 12,000 lbf electrodynamic shaker to excite and take measurements from test articles at room temperature.

12.2 Background

12.2.1 3D Laser Vibrometry

Laser Doppler vibrometers make use of the Doppler Effect in order to measure instantaneous velocity of a single point. By using three laser heads at different angles to measure the same point, a 3D velocity vector can be triangulated. From these velocity measurements displacement can be calculated. Using the displacement measurements and a grid of points with either a rectangular or triangular pattern full field strain measurements can be calculated. Three Polytec PSV500 laser vibrometers along with a single high definition camera were mounted on a single stand in this experiment shown in Fig. 12.1. The assembly was placed so that the front end of the top sensor had a standoff distance of 700 mm away from the article. The laser heads were given a 2D alignment using an automatic 2D alignment tool available in Polytec's PSV 9.2 Acquisition Software. 3D alignment was done manually using an alignment plate. The target quality goal for a good 3D alignment is

---

Distribution A: Cleared For Public Release. Distribution is unlimited. Case Number 88ABW-2010-5200

S. Tilmann (✉)
Aerospace Systems Directorate, Aerospace Vehicles Division, Air Force Research Laboratory, WPAFB, OH, USA
e-mail: samuel.tilmann@us.af.mil

C. Niezrecki et al. (eds.), *Rotating Machinery, Optical Methods & Scanning LDV Methods, Volume 6*, Conference Proceedings of the Society for Experimental Mechanics Series, https://doi.org/10.1007/978-3-030-12935-4_12

Fig. 12.1 Polytec PSV500 Assembly and high definition video camera

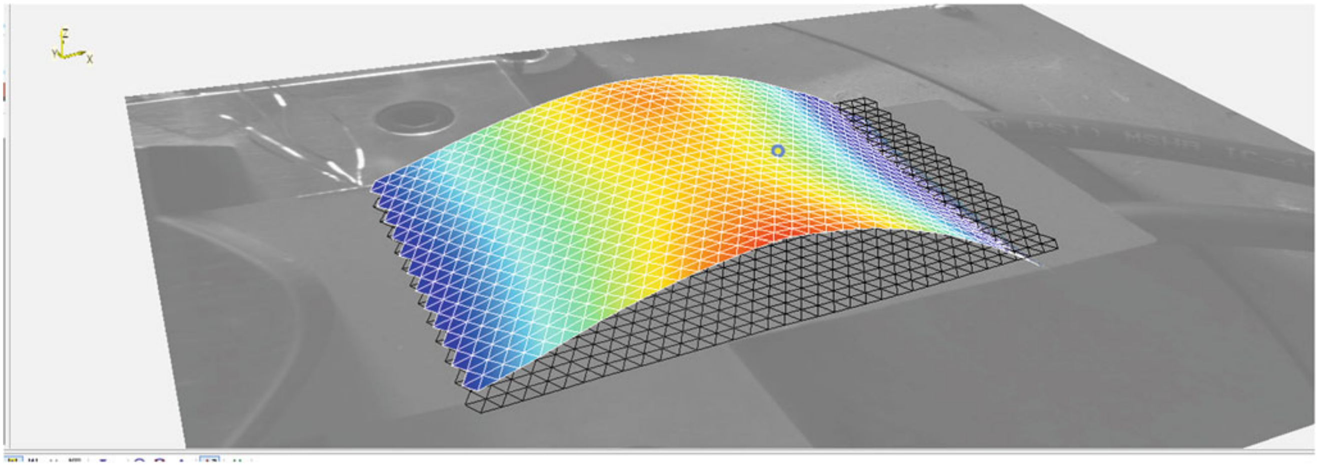

Fig. 12.2 Rectangular coupon second bending mode at 239.9 Hz

less than 0.3 mm error. The final error on the 3D alignment for the top, left, and right laser heads were 0.2 mm, 0.2 mm, and 0.1 mm respectively. Fast video triangulation was performed using the high definition camera during the scan in order to further reduce error. Video triangulation ensures that all three lasers are aimed at the same point by comparing the assigned location of the lasers with the video feed and making small adjustments to ensure they match.

12.3 Experimental Setup

12.3.1 Rectangular Coupon

A rectangular aluminum coupon was chosen for this experiment because of its simple geometry and relatively uniform lines of stress present in its bending modes. The second bending mode of the rectangular coupon was chosen due to its high stress concentration near the middle of the coupon. The second bending mode of the coupon is at approximately 239.9 Hz with a mode shape shown in Fig. 12.2. Five strain gages oriented in the X-axis were placed on the article near the center of the article due to the high strain concentration as shown in Fig. 12.3.

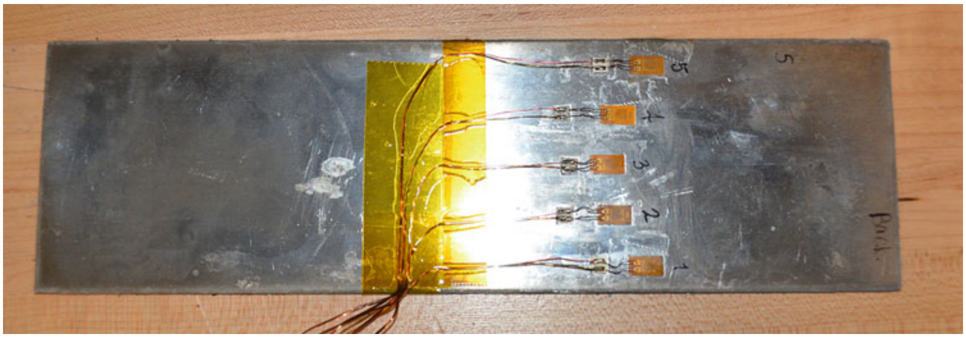

Fig. 12.3 Rectangular coupon strain gage locations

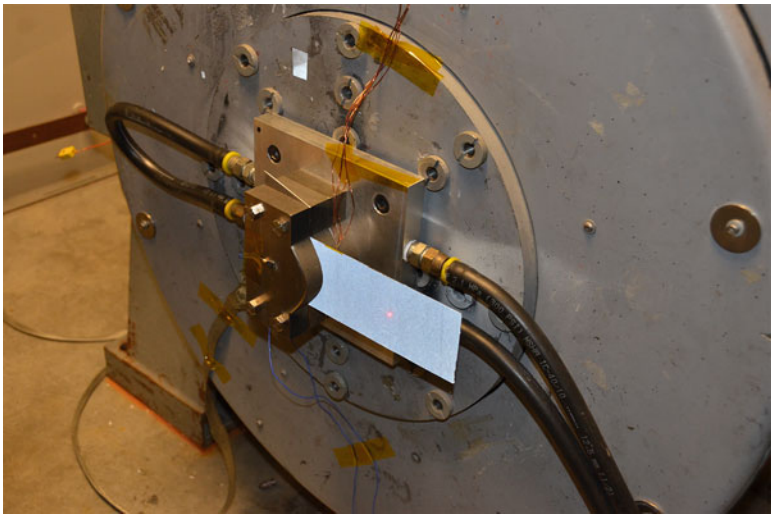

Fig. 12.4 12K Shaker Assembly, sine clamp holding test article

Table 12.1 Strain data acquisition settings

Bandwidth	500 Hz
Bandwidth from	220 Hz
Bandwidth to	260 Hz
Number of lines	6400
Frequency resolution	78.125 mHz
Sampling frequency	1.25 kHz
Sample time	12.8 sec
# of averages	16

12.3.2 *Excitation Method*

The rectangular coupon was mounted to a 12,000 lbf electrodynamic shaker with a sine clamp as seen in Fig. 12.4. Broadband random excitation (20–20,000 Hz) was used to determine mode shapes and frequencies from which a mode of interest was chosen. The shaker then excited the article at a chosen mode in order to collect data for strain calculations using the data acquisition settings shown in Table 12.1.

12.3.3 *Coffin Coupon*

A previously tested titanium coffin shaped coupon was also used in this experiment. Due to the nature of the aluminum coupon it would not be able to be tested at elevated temperatures. The coffin coupon, shown in Fig. 12.5, was chosen because

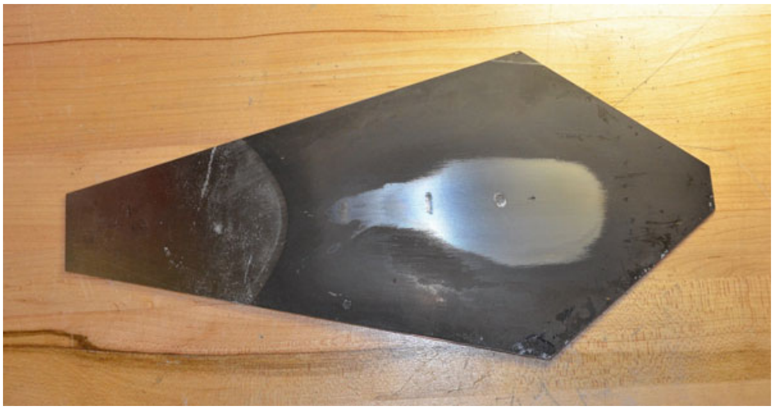

Fig. 12.5 Coffin coupon

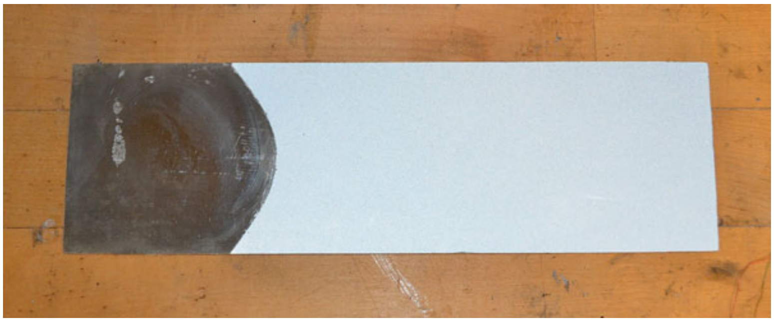

Fig. 12.6 Rectangular coupon with retroreflective tape

of the more stable properties of titanium at elevated temperatures. The same method used to determine the natural frequencies of the rectangular coupon was used to determine the natural frequencies and mode shapes of the coffin coupon. Due to the nonlinearities present in the coupon around the mode that would be of interest, it was not a good candidate for this initial testing of the systems strain measurement capabilities. This coupon is planned to be used in the future in order to test the system on more complex structures with nonlinearities.

12.3.4 Surface Treatment

The rectangular coupon was covered with retroreflective tape which as shown in Fig. 12.6. This is done in order to improve the speckle pattern of the reflected light from the laser which will in turn give a better return signal on the laser heads. The adhesive on the retroreflective tape has a relatively low temperature limit so another coating method was devised for use at elevated temperatures. For high temperature coating the front surface of the coffin coupon was coated with Cotronics Corporation’s 1529FS Duraseal+ Compound and then evenly coated with a layer of 3Ms retroreflective glass beads. The adhesive coating was then cured for 2 hours at room temperature and two additional hours at 425 °F. The resulting surface finish can be seen in Fig. 12.7.

12.3.5 Elevated Temperature

The purpose of this elevated temperature testing is to assess the survivability of the surface treatment under dynamic load at elevated temperature as well as determine if there is any degradation in the return signal or interference from the radiant heat sources. For this test the coffin coupon was used since the titanium has more stable material properties at elevated temperatures. Quartz lamps were used to radiantly heat the article while it was being excited at its fifth mode of 540.7 Hz by

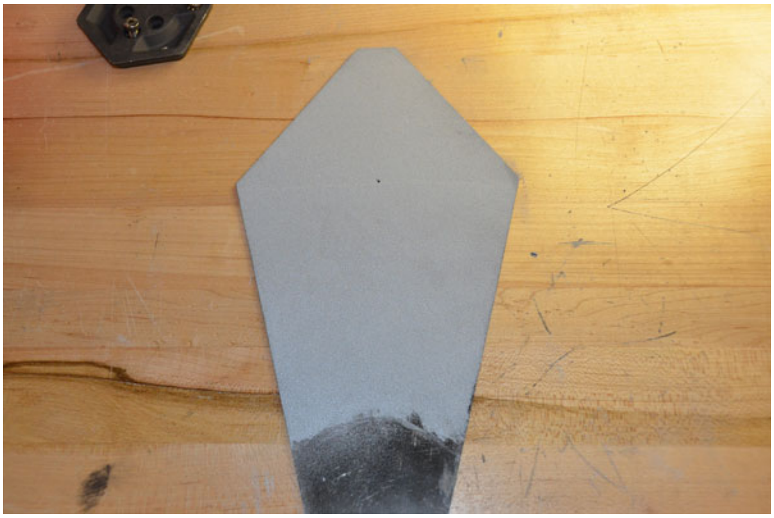

Fig. 12.7 Coffin coupon with high temperature surface treatment – glass bead coating

the 12K shaker. Since the lamps obstructed the view of a majority of the article it was not possible to obtain full field strain measurements, instead a single point measurement was taken and the quality of the signal at temperature was evaluated along with any visible degradation of the coating.

12.4 Results and Discussion

12.4.1 Temperature Drift

During the initial runs of this test there was difficulty controlling the ambient temperature of the room which lead to large 10–15 °F fluctuations in temperature after the shaker had started. Not only did this affect the material properties and boundary conditions at the clamp enough to significantly change strains, it also occasionally caused the coffin coupon to change modes entirely due to the nonlinearities around the fifth mode. While these effects could be reduced by attempting to wait until the room had reached a steady temperature they could not be entirely eliminated. This led to unacceptable results and postponing the experiment until the climate could be better controlled.

12.4.2 Data Processing

The raw velocity data was post-processed using Polytec's strain processing software in order to obtain displacement and strain measurements. The software first calculated displacement measurements for each point and then calculated strain from those displacement calculations. In order to determine strain from displacement measurements, a finite element approach is used as described in the Polytec PSV Strain document [1]. After strain in each element is calculated, strain for each point is determined by taking the average strain of all elements adjacent to that point. In this software the vibration data filter setting has the most significant effect on the final calculated strain values. The vibration filter setting was increased enough so that the data did not contain noise, but not so much that the actual signal started appearing in the FilterDiff results [2]. A comparison of two FilterDiff results based on different filter settings can be seen in Fig. 12.8 below. The top image is of a 15 mm vibration filter while the bottom is of a 50 mm filter. With the larger filter the second mode is clearly visible which indicates too large of a filter. While in this case it is clear which of these two is an appropriate filter due to the extremely large filter on the second image, generally it is not so clear and comes down to a judgement call by the engineer. While simply matching measured strain values in and of itself is not a sufficient method for choosing filters, it can be a good indicator of an appropriate filter. Table 12.2 shows the strain results compared to the strain gage-measured value for several different filter settings. In this table the top numbers of the magnitude columns represents the value for the signal filter with outliers

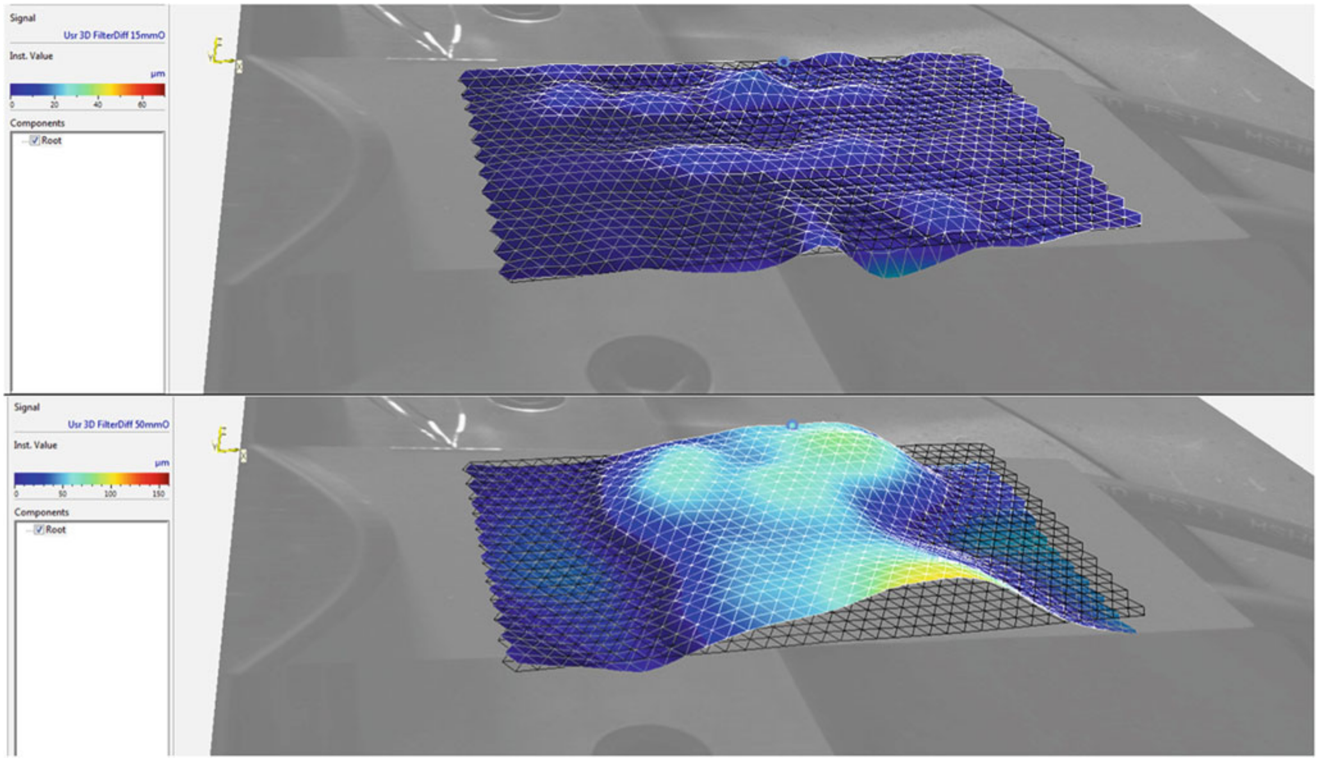

Signal: Usr 3D FilterDiff 15mmO

Signal: Usr 3D FilterDiff 50mmO

Fig. 12.8 FilterDiff comparison of rectangular coupons second bending mode

Table 12.2 Filter comparisons

Point	Strain gage	Measured strain peak-peak (με)	7 mmO, 7 mm geo magnitude (με)	7 mmO, 15 mm geo magnitude (με)	10 mmO, 7 mm geo magnitude (με)	10 mmO, 15 mm geo magnitude (με)	15 mmO, 7 mm geo magnitude (με)	15 mmO, 15 mm geo magnitude (με)
86	1	235.2	295.8	278.6	285.9	270.9	272.0	260.4
267	2	229.5	263.1	255.8	253.7	243.8	245.8	234.6
445	3	225.3	231.1	231.4	229.4	227.7	228.6	225.6
622	4	229.5	235.7	231.2	234.7	229.2	235.6	231.1
796	5	234.0	275.1	262.6	268.4	258.3	259.1	252.2

removed while the bottom number represents the geometry filter used to process the data. The filter appeared to have a much greater effect on the outer points while the inner points values only varied by a couple percent depending on the filter. The final filter settings chosen were based on deviation from measured strain and qualitative assessment of the FilterDiff and GeoDiff outputs from the strain processing software. The settings that obtained the best measurements were a vibration filter of 15 mm with a geometry filter of 15 mm.

12.4.3 Displacement

A triangular grid pattern was used to collect data for the strain calculations. The velocity data was banded from 239 to 240.5 Hz around the second bending mode frequency of 239.9 and the strain processing software was applied using the filters specified in the previous section. The displacement results for the coupon can be seen in Fig. 12.9. These displacement results were used by the strain calculator to determine strain at each point.

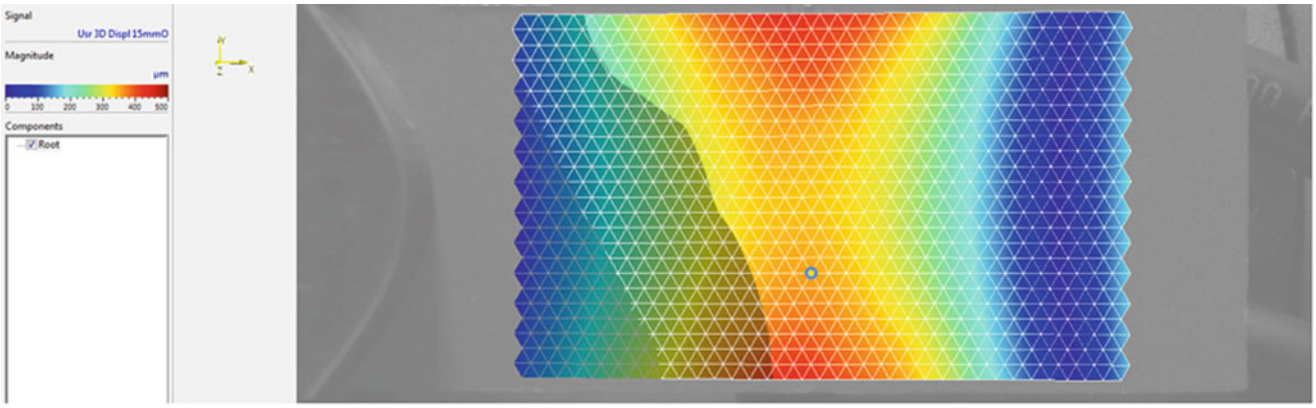

Fig. 12.9 Rectangular coupon displacement triangular grid

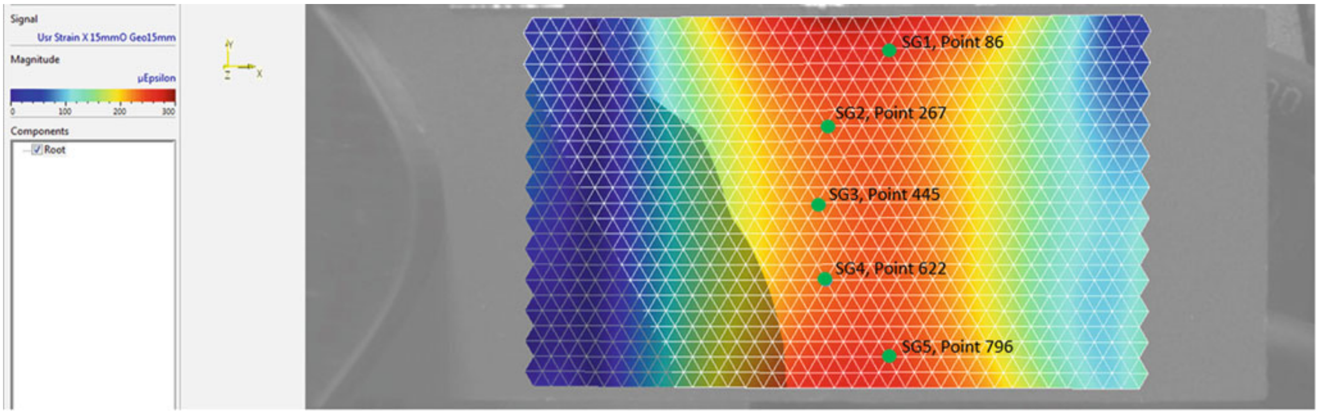

Fig. 12.10 Rectangular coupon X-strain triangular grid

Table 12.3 Triangular grid results and comparison

Strain gage	Point	RMS ($\mu\varepsilon$)	Peak-peak ($\mu\varepsilon$)	Calculated magnitude ($\mu\varepsilon$)	Error
1	86	166.3	235.2	260.4	10.72%
2	267	162.3	229.5	234.6	2.21%
3	445	159.3	225.3	225.6	0.14%
4	622	162.3	229.5	231.1	0.69%
5	796	165.4	234.0	252.2	7.82%

12.4.4 Strain

The calculated strain results for the rectangular coupon can be seen in Fig. 12.10 below. The rectangular coupon was given five strain gages oriented in the X-axis to compare calculated strain against. Measurement points were placed directly opposite of the strain gages in order to have as direct of a comparison as possible, a summary of which can be seen in Table 12.3. Measurement points 86, 267, 445, 622, and 796 correlate with the strain gages 1–5 as shown in Fig. 12.10. The measured and calculated values and deviation from the strain gage-measured values can be seen below in Table 12.3. The peak to peak value was assumed to be the RMS multiplied by the square root of two due to the sinusoidal excitation of the specimen. The central three strain gages, 2–4, had very close values to the measured strain varying from 0.1% to 2.2% deviation from the strain gage, while the outermost gages, 1 and 5, had a significantly higher deviation from the measured strain of up to 10.7%. This difference in the outer measurements could be explained by the measurement points on the front side being slightly offset from the strain gage on the back. The outer strain gages were placed in an area with a very high strain gradient and any variance in position could drastically change the measured strain. It is also possible that these strain calculations suffered from edge effects since the points were close to the top and bottom edges of the measured area.

12.4.5 Elevated Temperature Signal

The temperature was raised to 850 °F with the coffin coupon being shaken at its fifth natural frequency of 540.7 Hz. The signal remained acceptable throughout the entirety of the run with minimal damage to the surface treatment. While the actual heat and vibration did not visibly damage the surface treatment, it was exceptionally susceptible to abrasion and scratching. Any articles using this surface treatment must be handled with much more care than would otherwise be necessary.

12.5 Future Work

The ultimate goal for the use of this system is to be able to measure strains of a system under broadband random excitation with multiple modes contributing to the overall strain levels. In order to reach this goal several steps must be taken to validate this strain measurement method. The first step towards this goal is to ensure the strain measurements are reliable and trustworthy for which more testing must be performed on multiple articles until a consistent process is established. It must also be proven that this method can work with more than just simple articles like the rectangular coupon. In order to do this the coffin coupon will be used as a slightly more complex structure with the complication of the nonlinear mode at the frequency of interest. It must also be proven that the measurements taken at elevated temperature are accurate enough to obtain accurate strain measurements. In order to do this an article must be excited at temperature without obstructing the laser heads' lines of sight. The results must then be compared to proven strain measurement techniques such as DIC or platinum strain gages. Once this is done the system can be used in the structural validation branch's acoustic chambers to take dynamic strain measurements of test articles. The laser heads have often been used to take single point measurements during testing but have not been used to take strain measurements during a test run. There is also an interest in newer infrared laser heads. These infrared laser heads reportedly do not require any surface treatment of the test article which, if they work properly, would make the need for surface treatments irrelevant and solve the issue with the high temperature surface treatment's low durability.

12.6 Conclusions

The use of 3D laser vibrometry to provide full field dynamic strain measurement is promising, however future work must be done to ensure the reliability and consistency of strain measurements using this method. While the system is able to obtain accurate central strain measurements it has difficulty dealing with measurement taken at the edge of an article. Filters had a major effect on calculated strain and while there is some method to picking appropriate filters that selection process is largely subjective at this point in time. The system takes an exceptionally long time to take enough high quality data for high fidelity strain measurements. The time taken to complete the measurements presented in this paper was 72 hours. This can be reduced in actual tests by either coarsening the grid or shrinking the area of interest, but any compromise lowers the fidelity of the strain measurements. Special consideration must be given to maintaining steady state throughout the test whether that is maintaining a constant temperature or avoiding nonlinearities.

Acknowledgements I would like to acknowledge my colleagues from the Air Force Research Laboratory's Structural Validation Branch (AFRL/RQVV) for providing technical assistance with the laser vibrometry system as well as reviewing and providing input for this report.

References

1. Polytec, "PSV-S-Strain", 2009
2. Polytec, "Strain Measurements with PSV-3D: Background Information on Settings for Strain Measurements", 2010

Chapter 13
Output-Only Modal Parameter Estimation Using a Continuously Scanning Laser Doppler Vibrometer System with Application to Structural Damage Detection

Y. F. Xu, Da-Ming Chen, and W. D. Zhu

Abstract Spatially dense vibration measurement can be obtained by use of a continuously scanning laser Doppler vibrometer (CSLDV) system that sweeps its laser spot along a scan path. For a linear, time-invariant, viscously damped structure undergoing free vibration, a new type of vibration shapes called free response shapes was defined and obtained by the authors using a CSLDV system with the demodulation method. To date, application of free response shapes is limited to structural damage identification, and they cannot be directly used for model validation while mode shapes can be. This paper extends the concept of free response shapes by proposing a new output-only modal parameter estimation (OMPE) method using a CSLDV system to estimate modal parameters of the structure undergoing free vibration, including natural frequencies, modal damping ratios, and mode shapes. Advantages of the proposed method are: (1) modal damping ratios and mode shapes can be accurately estimated from obtained free response shapes, (2) the scanning frequency of the CSLDV system can be relatively low, and (3) estimated mode shapes can be used for structural damage identification as if they were measured by stepped scanning of a scanning laser Doppler vibrometer. A baseline-free method is applied to identify structural damage using mode shapes estimated by the proposed OMPE method. The analytical expression of free response shapes of the structure is derived, based on which the OMPE method is proposed and presented as a step-by-step procedure. In the proposed OMPE method, natural frequencies of the structure are identified from free response of certain fixed points on the structure; its modal damping ratios and mode shapes are simultaneously estimated using free response shapes measured by a CSLDV system. A numerical investigation is conducted to study the OMPE method and its application to baseline-free damage identification with mode shapes estimated by the OMPE method.

Keywords Continuously scanning laser Doppler vibrometer system · Modal parameter estimation · Output-only method · Baseline-free structural damage identification · Demodulation method

13.1 Introduction

Vibration-based damage identification has been a major research topic of structural dynamics in the past few decades [1, 2]. More than often, occurrence of damage in a structure undermines its capability of supporting design loads and can result in its excessive deformation, which is attributed to changes in its structural properties, such as its stiffness. One assumption of a vibration-based damage identification method is that occurrence of damage changes modal parameters of a structure, including natural frequencies, modal damping ratios, and mode shapes, which can be accurately estimated by modal analysis [3]. Accurately estimated modal parameters can also assist model validation and updating. A continuously scanning laser Doppler vibrometer (CSLDV) system is an ideal instrument for modal parameter estimation as it is capable of accurate, non-contact and temporally dense vibration measurement and also capable of spatially dense mode shape measurement [4]. A CSLDV system consists of three key components: a laser Doppler vibrometer, a scanner and a controller [5]. The vibrometer measures the velocity of a point on a test structure where its laser spot is located. The laser beam of the vibrometer is directly shined onto first-surface mirrors of the scanner and the spot is continuously swept along a prescribed scan path

---

Y. F. Xu
Department of Mechanical and Materials Engineering, University of Cincinnati, Cincinnati, OH, USA
e-mail: xu2yf@uc.edu

D.-M. Chen · W. D. Zhu (✉)
Department of Mechanical Engineering, University of Maryland, Baltimore, MD, USA
e-mail: damingc1@umbc.edu; wzhu@umbc.edu

C. Niezrecki et al. (eds.), *Rotating Machinery, Optical Methods & Scanning LDV Methods, Volume 6*, Conference Proceedings of the Society for Experimental Mechanics Series, https://doi.org/10.1007/978-3-030-12935-4_13

on the structure by rotating the mirrors that are controlled by the controller. While the spot is continuously swept, velocity at each discrete measurement point on the scan path is measured, and the number of the measurement points can be tens and even hundreds of thousands, depending on the sampling and scan frequencies of the vibrometer. A CSLDV system has been successfully used for modal analysis and measurements of vibration shapes, such as mode shapes [6–8] and operating deflection shapes [9–11], which can be achieved with high accuracy and in a relatively short time, e.g., in a few seconds. Specifically, two operational modal analysis methods [12, 13] have been developed based on harmonic power spectra [14], where only one CSLDV system is used to measure response of a structure under environmental excitation without any additional sensors, and modal parameters of a wind turbine blade were measured [12, 13].

A CSLDV system has been used to measure high-fidelity vibration shapes of structures undergoing steady-state vibrations for damage identification [5, 15], and the vibration shapes measured by a CSLDV system can be used to identify structural damage as small as notch-size ones [16]. A new type of vibration shapes called free response shapes was defined and measured by a CSLDV system when a linear underdamped beam underwent free vibration [17]. Free response shapes were used to identify structural damage, where damage indices associated with multiple elastic modes of a beam could be obtained. The free response shapes can be considered to be obtained in an output-only manner, since initial conditions of and excitation given to the beam do not need to be measured. A free response shape is different from a mode shape, since the former is time-varying with decaying amplitudes and the latter is not. So far, application of free response shapes is limited to structural damage identification and they cannot be directly used for model validation and updating due to two reasons. One is that a free response shape has an amplitude that is determined by excitation. Unless one can accurately measure the excitation, a free response shape cannot be used for model validation and updating. Another reason is that damping ratios cannot be estimated from free response shapes that are obtained in the method in Ref. [17]. An experimental modal analysis method was proposed [8], where excitation to a test structure and its free response measured by a CSLDV system yielded pseudo-frequency response functions of the structure, which were used to estimate modal parameters of the structure. In this method, the measured response is lifted to each measurement point as if the response were measured in a pointwise manner. A limitation of the method is that measured mode shapes of modes with relatively high natural frequencies can have low qualities due to speckle noise caused by a relatively high scanning frequency, which is needed since the scanning frequency of the CSLDV system is equal to the sampling frequency of the lifted response at each measurement point. While operational modal analysis methods using a CSLDV system have been proposed and their capabilities of modal parameter estimation have been experimentally validated, their resulting mode shapes and associated curvature mode shapes cannot be used for structural damage identification. The reason is that the resulting mode shapes are represented by smooth sinusoidal functions [12, 13] and local anomalies caused by existing local structural damage cannot be reflected in the mode shapes and associated curvature mode shapes.

In this work, derivation of free response shapes of a linear, time-invariant, viscously damped structure undergoing free vibration is shown. A new output-only modal parameter estimation (OMPE) method using free response measured by a CSLDV system is proposed to accurately estimate modal parameters of the structure with a step-by-step procedure. The proposed OMPE method extends the concept of free response shapes of the structure as they are directly related to its modal damping ratios and mode shapes, which can be simultaneously obtained in the proposed method. A baseline-free non-model-based damage identification method is applied to identify structural damage in a structure. In the identification method, a curvature damage index (CDI) is obtained by comparing a curvature mode shape corresponding to a mode shape estimated by the OMPE method with that from a polynomial that fits the estimated mode shape with a properly determined order. Structural damage can be identified in neighborhoods with consistently large CDIs corresponding to multiple modes. A numerical investigation is conducted to study the OMPE method and application of the damage identification method.

The remaining part of this paper is outlined as follows. Derivation of free response shapes is presented in Sects. 13.2.1 and 13.2.2, the new OMPE method using a CSLDV system is proposed in Sect. 13.2.3, and the structural damage identification method is presented in Sect. 13.2.4. A numerical investigation of the OMPE method and baseline-free method are presented in Sect. 13.3. Finally, conclusions of this study is presented in Sect. 13.4.

13.2 Methodology

13.2.1 Free Response of a Damped Structure

Free response in the form of the displacement of a linear, time-invariant, viscously damped structure can be obtained by solving its governing partial differential equation:

$$B\left[\frac{\partial^2 z(\mathbf{x},t)}{\partial^2 t}\right]+C\left[\frac{\partial z(\mathbf{x},t)}{\partial t}\right]+L\left[z(\mathbf{x},t)\right]=0,\qquad \mathbf{x}\in D,\qquad t\geq 0 \tag{13.1}$$

where $B(\cdot)$, $C(\cdot)$ and $L(\cdot)$ are a mass operator, a damping operator and a stiffness operator, respectively, z is the displacement of the structure at the spatial position $\mathbf{x}$ at time t, and D is its spatial domain. Boundary and initial conditions of the structure are known. Note that the initial conditions can be induced by an external force that the structure is subject to when $t<0$. A solution to Eq. (13.1) can be obtained using the expansion theorem [18]:

$$z(\mathbf{x},t)=\sum_{i=1}^{\infty}\boldsymbol{\phi}_i(\mathbf{x})\,u_i(t) \tag{13.2}$$

where $\boldsymbol{\phi}_i$ is the i-th mass-normalized eigenfunction of the associated undamped structure, which is assumed to be self-adjoint, and u_i is the corresponding unknown time function. Orthonormality between $\boldsymbol{\phi}_i$ and $\boldsymbol{\phi}_j$ $(j=1,\ 2,\ \ldots,\ \infty)$ with respect to B is expressed by

$$\int_D \boldsymbol{\phi}_j(\mathbf{p})\,B\left[\boldsymbol{\phi}_i(\mathbf{p})\right]\mathrm{d}\mathbf{p}=\delta_{ij} \tag{13.3}$$

where δ_{ij} denotes Kronecker delta function, which satisfies $\delta_{ij}=1$ if $i=j$ and $\delta_{ij}=0$ if $i\neq j$. Assuming that damping of the structure can be modeled by Kelvin-Voigt viscoelastic model, which leads to a classically damped system [18, 19], one can obtain u_i in Eq. (13.2) by solving an ordinary differential equation:

$$\ddot{u}_i(t)+2\zeta_i\omega_i\dot{u}_i(t)+\omega_i^2u_i(t)=0 \tag{13.4}$$

where ω_i is the corresponding i-th undamped natural frequency of the structure, ζ_i is the i-th modal damping ratio, which is smaller than 1 for an underdamped structure, and an overdot denotes differentiation with respect to t. The initial conditions $u_i(0)$ and $\dot{u}_i(0)$ can be determined from the initial conditions of Eq. (13.1). The solution to Eq. (13.4) can be expressed by [20]

$$\begin{aligned} u_i(t) &= \mathrm{e}^{-\omega_i\zeta_i t}\left[u_i(0)\cos\left(\omega_{i,d}t\right)+\tfrac{\dot{u}_i(0)+\omega_i\zeta_i u_i(0)}{\omega_{i,d}}\sin\left(\omega_{i,d}t\right)\right] \\ &= A_i\mathrm{e}^{-\omega_i\zeta_i t}\cos\left(\omega_{i,d}t-\gamma_i\right) \end{aligned} \tag{13.5}$$

where

$$\omega_{i,d}=\omega_i\sqrt{1-\zeta_i^2} \tag{13.6}$$

is the i-th damped natural frequency of the structure,

$$A_i=\sqrt{\left[u_i(0)\right]^2+\left[\frac{\dot{u}_i(0)+\omega_i\zeta_i u_i(0)}{\omega_{i,d}}\right]^2} \tag{13.7}$$

is an amplitude constant, and

$$\gamma_i=\operatorname{arctan2}\left(\frac{\dot{u}_i(0)+\omega_i\zeta_i u_i(0)}{\omega_{i,d}},u_i(0)\right) \tag{13.8}$$

is a phase angle; $\omega_i\zeta_i$ in Eq. (13.5) is referred to as the decaying rate of u_i. Based on Eqs. (13.2) and (13.5), Eq. (13.2) becomes

$$z(\mathbf{x},t)=\sum_{i=1}^{\infty}A_i\phi_i(\mathbf{x})\,\mathrm{e}^{-\omega_i\zeta_i t}\cos\left(\omega_{i,d}t-\gamma_i\right) \tag{13.9}$$

13.2.2 Free Response Shapes

A free response shape associated with the i-th mode of the structure can be defined by

$$y_i\left(\mathbf{x},t\right)=A_i\phi_i\left(\mathbf{x}\right)\mathrm{e}^{-\omega_i\zeta_i t} \tag{13.10}$$

and Eq. (13.9) becomes

$$z\left(\mathbf{x},t\right)=\sum_{i=1}^{\infty}y_i\left(\mathbf{x},t\right)\cos\left(\omega_{i,d}t-\gamma_i\right) \tag{13.11}$$

The i-th eigenfunction ϕ_i that is the i-th undamped mode shape of the structure exists in the definition of y_i in Eq. (13.10). A similarity between ϕ_i and y_i is that they both correspond to the i-th mode of the structure; however, the former is time-invariant while the latter is time-varying due to the term $\mathrm{e}^{-\omega_i\zeta_i t}$ in Eq. (13.10).

A CSLDV system continuously sweeps its laser spot over a surface of a structure with a specific scan path. The system measures response of a measurement point on the structure with a certain sampling frequency, where its laser spot is located during a scan, and a finite number of modes of the structure are included in free response measured by the system. Let $\tilde{\mathbf{x}}\left(t\right)$ be the position of a laser spot on the surface of the structure at time t, which describes the scan path on the structure as a function of t. Free response of the structure measured by the CSLDV system along $\tilde{\mathbf{x}}\left(t\right)$ can be expressed by

$$\tilde{z}\left(t\right)=\sum_{i=1}^{N}\tilde{y}_i\left[\tilde{\mathbf{x}}\left(t\right),t\right]\tilde{u}_i\left(t\right) \tag{13.12}$$

where N is the number of modes included in $\tilde{z}$, and $\tilde{y}_i$ and $\tilde{u}_i$ are the free response shape and time function associated with the i-th mode measured by the system, respectively. The free response shape $\tilde{y}_i$ in Eq. (13.12) can be written as

$$\tilde{y}_i\left[\tilde{\mathbf{x}}\left(t\right),t\right]=A_i\phi_i\left[\tilde{\mathbf{x}}\left(t\right),t\right]\mathrm{e}^{-\omega_i\zeta_i t} \tag{13.13}$$

The time function $\tilde{u}_i$ can be expressed by

$$\tilde{u}_i\left(t\right)=\cos\left(\omega_{i,d}t-\alpha_i-\theta_i\right) \tag{13.14}$$

where α_i is the difference between the phase determined by the initial conditions and force associated with the i-th mode and that by a mirror feedback signal, and θ_i is a phase variable that controls amplitudes of in-phase and quadrature components of $\tilde{y}_i$, which can be expressed by

$$\tilde{y}_{I,i}=\tilde{y}_i\left[\tilde{\mathbf{x}}\left(t\right),t\right]\cos\left(\alpha_i+\theta_i\right) \tag{13.15}$$

and

$$\tilde{y}_{Q,i}=\tilde{y}_i\left[\tilde{\mathbf{x}}\left(t\right),t\right]\sin\left(\alpha_i+\theta_i\right) \tag{13.16}$$

respectively [5]. The demodulation method has been used to obtain $\tilde{y}_i$ corresponding to each half-scan period by the system [17]. A half-scan period starts when the laser spot of the system arrives at one end of a scan path and ends when the laser spot arrives at the other end of the scan path. Multiple $\tilde{y}_i$ can be obtained from free response of the structure measured by the system in one scan. To identify the start and end of a half-scan period, one can refer to mirror feedback signals of the system and determine instants when its laser spot arrives at ends of a scan path.

13.2.3 OMPE Method

The amplitude of $\tilde{y}_i$ in Eq. (13.13) is time-varying and exponentially decays to zero with t at the decaying rate $\omega_i \zeta_i$. In order to obtain a non-zero amplitude of $\tilde{y}_i$ from the demodulation method, one needs to determine natural frequencies of the structure and instants when the amplitude of $\tilde{y}_i$ decays to zero. The natural frequencies can be determined from the auto-power spectrum of z at a point that is measured by the system, and the instants can be determined using the short-time Fourier transform of $\tilde{z}$ [21], which is denoted by $\tilde{V_w}$. Some details of the short-time Fourier transform can be found in "Appendix: Short-Time Fourier Transform". Multiple non-zero $\tilde{y}_i$ can be obtained by using $\tilde{z}$ of the first $N_{i,0}$ half-scan periods, where $N_{i,0}$ is an integer that is defined by

$$\arg \max_{N_{i,0}} \frac{N_{i,0} T}{2} \leq t_{i,0} - t_1 \tag{13.17}$$

in which T is the length of a scan period, $t_{i,0}$ is the instant when $\tilde{V_w}$ at the i-th natural frequency of the structure becomes almost zero, and t_1 is the instant when the first half-scan period starts.

Let

$$Q_i = A_i \mathrm{e}^{-\omega_i \zeta_i t_1} \tag{13.18}$$

which is a complex constant, and $Q_i \phi_i$ can also represent the i-th mode shape of the structure. One has $Q_i = A_i$ when $t_1 = 0$, and Eq. (13.13) with $t \geq t_1$ can be expressed by

$$\tilde{y}_i \left[\tilde{\mathbf{x}}(t), t \right] = Q_i \phi_i \left[\tilde{\mathbf{x}}(t), t \right] \mathrm{e}^{-\omega_i \zeta_i (t - t_1)} \tag{13.19}$$

One can estimate $Q_i \phi_i$ in Eq. (13.19) if ζ_i is known. Let t_k be the instant when the k-th half-scan period starts and $\tilde{y}_{i,k}$ be the free response shape associated with the i-th mode in the k-th half-scan period. The term $Q_i \phi_i$ in Eq. (13.19) associated with $\tilde{y}_{i,k}$ is independent of t and can be estimated by eliminating $\mathrm{e}^{-\omega_i \zeta_i (t - t_1)}$ in $\tilde{y}_{i,k}$; it can be expressed by

$$Q_{i,k} \phi_{i,k} \left[\tilde{\mathbf{x}}(t), t \right] = \tilde{y}_{i,k} \left[\tilde{\mathbf{x}}(t), t \right] \mathrm{e}^{\omega_i \zeta_i (t - t_1)} \tag{13.20}$$

where $0 \leq t - t_k \leq T$. The mean of $Q_{i,k} \phi_{i,k}$ with $k \in [1, N_i]$, where $N_i \leq N_{i,0}$, can be defined by

$$\mu_i (\tilde{\mathbf{x}}) = \frac{\sum_{k=1}^{N_i} Q_{i,k} \phi_{i,k} (\tilde{\mathbf{x}})}{N_i} \tag{13.21}$$

Though $\omega_i \zeta_i$ in Eqs. (13.19) and (13.20) is unknown, it can be estimated by solving an optimization problem:

$$\overline{\omega_i \zeta_i} = \arg \min_{\omega_i \zeta_i} \sum_{k=1}^{N_i} \left| \mu (\tilde{\mathbf{x}}) - Q_{i,k} \phi_{i,k} (\tilde{\mathbf{x}}) \right| \tag{13.22}$$

where $|\cdot|$ denotes the L^2-norm of a function in a half-scan period. Note that N_i must be greater than two; otherwise $\omega_i \zeta_i$ cannot be estimated since the problem in Eq. (13.22) becomes trivial. With estimated $\omega_{i,d}$ and $\overline{\omega_i \zeta_i}$, ζ_i can be estimated by

$$\zeta_i = \frac{\overline{\omega_i \zeta_i}}{\sqrt{\omega_{i,d}^2 + \left(\overline{\omega_i \zeta_i} \right)^2}} \tag{13.23}$$

This completes theoretical derivation of the OMPE method using free response of the structure measured by the CSLDV system. The procedure of the method is summarized below:

Step 1. Measure $z(t)$ of the structure using the system with its laser spot staying at least one fixed point of the structure.
Step 2. Estimate $\omega_{i,d}$ of the structure using the auto-power spectrum of z measured in Step 1.
Step 3. Measure $\tilde{z}(t)$ using the system along a scan path with certain scan and sampling frequencies.

Step 4. Estimate $\tilde{y}_i\left(\tilde{\mathbf{x}}\right)$ associated with measured modes in N_i half-scan periods using the demodulation method.
Step 5. Estimate ζ_i based on Eq. (13.23) using $\overline{\omega_i\zeta_i}$ obtained by solving the optimization problem in Eq. (13.22).
Step 6. Express $Q_i\phi_i\left(\tilde{\mathbf{x}}\right)$ as $\tilde{y}_{i,1}\left(\tilde{\mathbf{x}}\right)\mathrm{e}^{\overline{\omega_i\zeta_i}(t-t_1)}$ with $0 \le t - t_1 \le T$ and $\overline{\omega_i\zeta_i}$ obtained in Step 5.

13.2.4 *Baseline-Free Structural Damage Identification*

Local damage of a structure can cause prominent anomalies in its curvature mode shapes in neighborhoods of the damage, and the damage can be identified by comparing the curvature mode shapes with those of the associated undamaged structure [22]. However, the curvature mode shapes of the undamaged structure that can be considered as baselines are usually unavailable in practice. When the undamaged structure is geometrically smooth and made of materials without mass and/or stiffness discontinuities, the curvatures of the undamaged structure can be well approximated by those from polynomials that fit mode shapes of the damaged structure with properly determined orders. In previous works [15, 16, 23], a curvature damage index (CDI) was proposed, which consists of the difference between a curvature mode shape of a damaged structure and that from a polynomial fit:

$$\delta_i\left(\mathbf{x}\right) = \left[\boldsymbol{\phi}_i''\left(\mathbf{x}\right) - \boldsymbol{\phi}_i^{p''}\left(\mathbf{x}\right)\right]^2 \tag{13.24}$$

where a prime denotes spatial differentiation with respect to the arc length s of a scan path at $\mathbf{x}$, and $\boldsymbol{\phi}_i^p$ is the corresponding mode shape from the polynomial that fits ϕ_i. Since mode shapes corresponding to multiple modes can be measured in one scan, CDIs corresponding to multiple modes can be obtained in the scan, and damage regions can be identified in neighborhoods with consistently large CDI values associated with the measured modes. Note that use of δ_i corresponding to rigid-body modes of a structure should be excluded in damage identification as their curvature mode shapes are zero, and one should use δ_i corresponding to elastic modes of the structure in damage identification. An auxiliary CDI associated with δ_i corresponding to various measured modes can be defined to assist identification of the neighborhoods; it can be expressed by

$$\tilde{\delta}\left(\mathbf{x}\right) = \sum \hat{\delta}_i\left(\tilde{x}\right) \tag{13.25}$$

where $\hat{\delta}_i$ is a normalized CDI associated with the i-th mode of the structure with the maximum unit amplitude and $\sum$ denotes summation of $\hat{\delta}_i$ over all measured modes. Since boundary distortions would occur in curvature free response shapes of a structure associated with its free response shapes obtained from the demodulation method [17], similar distortions would occur in curvature mode shapes here. Hence, boundary regions are excluded in normalization of δ_i in $\tilde{\delta}$ and presenting them. Neighborhoods with consistently large values of δ_i associated with measured modes can be identified in those with large values of $\tilde{\delta}$.

By nondimensionalizing s so that it ranges between -1 and 1, a polynomial that fits ϕ_i with an order r can be expressed by

$$\phi_i^p\left(\tilde{s}\right) = \sum_{q=0}^{r} a_q \tilde{s}^q \tag{13.26}$$

where $\tilde{s}$ denotes the nondimensionalized s, a_q are coefficients of the polynomial. As pointed out in Ref. [17], an increase of r in the polynomial in Eq. (13.26) can improve the level of approximation of ϕ_i^p to ϕ_i. To determine a proper order of the polynomial fit, the modal assurance criterion (MAC) value between a mode shape of the damaged structure and that from a polynomial that fits the mode shape, which is defined by

$$\mathrm{MAC}\left(\phi_i, \phi_i^p\right) = \frac{\left(\phi_i^{\mathrm{H}}\phi_i^p\right)^2}{\left(\phi_i^{\mathrm{H}}\phi_i\right)\left(\phi_i^{p\mathrm{H}}\phi_i^p\right)} \times 100\% \tag{13.27}$$

where the superscript H denotes matrix Hermitization, is used. A proper order for the polynomial fit is two plus the minimum order with which $\mathrm{MAC}\left(\phi_i, \phi_i^p\right)$ is greater than 90% [23]. Two is added here in order to preserve smoothness of a curvature mode shape from the polynomial fit, since calculation of a curvature incurs second-order differentiation that reduces the order of a polynomial by two.

13.3 Numerical Investigation

A finite element model of a damaged aluminum cantilever beam with a length $L = 0.8$ m, Young's modulus of 68.9 GPa, a mass density of 2700 kg/m^3 and a damping coefficient of Kelvin-Voigt damping model of 8×10^{-7} s is constructed using ABAQUS. The beam has a uniform square cross-section with a side length of 0.01 m. The damage is in the form of thickness reduction, which is located between $x = \frac{6}{16}L$ and $x = \frac{7}{16}L$, where x is the position of a point on the beam. The damaged portion of the beam has a height of 0.008 m and a length of 0.05 m. The beam has fixed and free ends at $x = 0$ and $x = L$, respectively. The first five natural frequencies and modal damping ratios of the beam are listed in Table 13.1a, b, respectively. The first five mass-normalized mode shapes of the beam from its finite element model are shown in Fig. 13.1.

In this section, a single impulse is applied to the damaged cantilever beam. Assume that the beam has zero initial conditions; responses of the beam are calculated using the expansion theorem, where the number of included modes is five. A simulated CSLDV system is used to measure responses of the beam caused by the forces with a scan period $T = 2$ s and a sampling frequency of 16384 Hz. The simulated CSLDV system is capable of measuring response in the form of displacement. Positions of the laser spot of the system on the beam in the first eight seconds of a scan is shown in Fig. 13.2.

A single impulse with an intensity of 0.01 Ns is applied to the free end of the damaged beam $x = L$ at $t = 0$ s. Response of the beam at $x = 0.7$ m is measured in the form of displacement for eight seconds, as shown in Fig. 13.3a, and its auto-power spectrum is shown in Fig. 13.3b. Natural frequencies of the beam can be identified in the spectrum as frequencies where prominent peaks are found, and identified natural frequencies are listed in Table 13.1a. The largest error between the identified natural frequencies and those from the finite element model is 0.16%. Response of the beam is then measured using the simulated CSLDV system, and the measured response in the first eight seconds are shown in Fig. 13.4a; the associated

Table 13.1 First five (a) natural frequencies in Hz and (b) modal damping ratios in percentage of the damaged beam from its finite element model and the OMPE method using its response caused by a single impulse

(a)

Mode	Finite element	OMPE method
1	12.64	12.62
2	79.04	79.00
3	222.0	222.0
4	434.8	434.7
5	711.2	711.2

(b)

Mode	Finite element	OMPE method
1	0.0032	0.0032
2	0.0199	0.0199
3	0.0558	0.0558
4	0.1093	–
5	0.1787	–

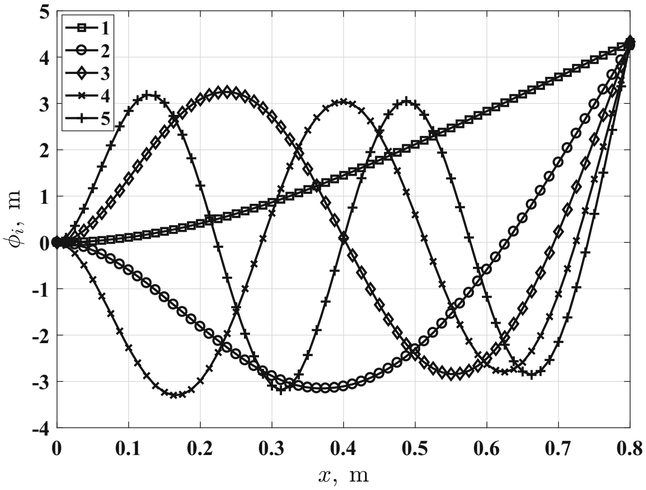

Fig. 13.1 Mass-normalized mode shapes of the damaged cantilever beam associated with its first five modes from its finite element model

Fig. 13.2 Position of the laser spot of the simulated CSLDV system on the damaged beam

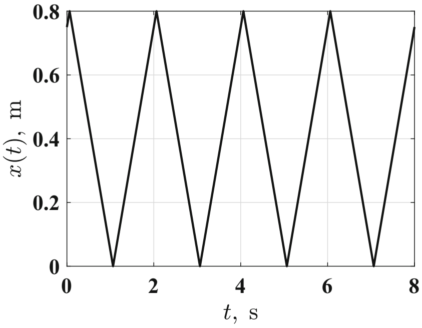

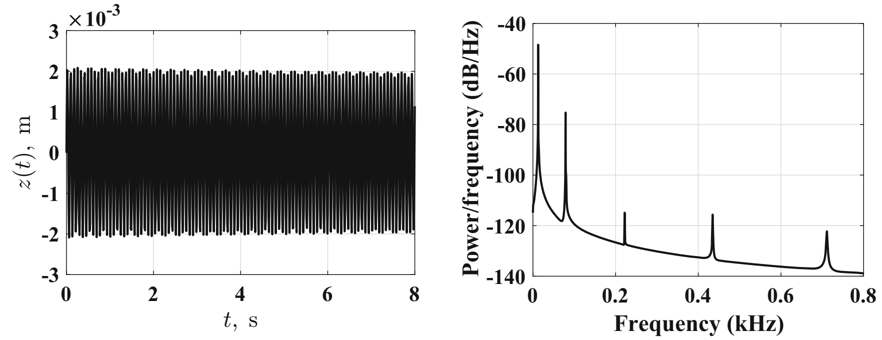

(a) (b)

Fig. 13.3 (**a**) Response of the damaged cantilever beam at $x = 0.7$ due to the single impact at its free end and (**b**) the auto-power spectrum of the response in (**a**)

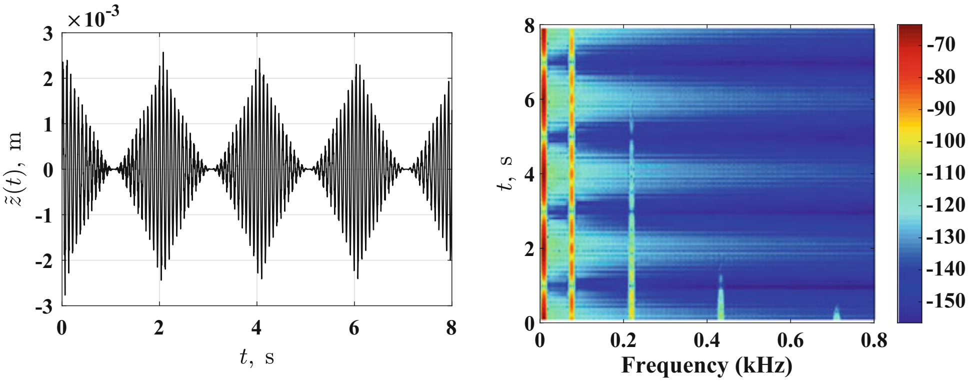

(a) (b)

Fig. 13.4 (**a**) Response measured by the simulated CSLDV system in the first eight seconds and (**b**) a spectrogram of the response in (**a**)

spectrogram is shown in Fig. 13.4b. It can be observed that amplitudes of frequency components associated with the third through fifth modes decay faster than those with the first and second modes. Specifically, the frequency component associated with the fourth mode decays to almost zero before the second half-scan period ends and that associated with the fifth mode fast decays within the first half-scan period. Since the duration of a half-scan period is $\frac{T}{2} = 1$ s, non-zero-amplitude free response shapes of at least one half-scan period associated with the first through fourth modes can be obtained from the free response measured by the CSLDV system and that associated with the fifth mode cannot. Free response shapes obtained from the free response are shown in Fig. 13.5a–e, which correspond to the first through fifth modes, respectively. It can be seen that amplitudes of the free response shapes associated with the fourth and fifth modes of the structure decay to almost zero faster than those associated with the first three modes, which verifies the observations on the spectrogram in Fig. 13.4b.

Since there is only one non-zero-amplitude free response shape associated with the fourth mode and the free response shape associated with the fifth mode has decayed almost to zero before the end of the first half-scan period of the CSLDV system, modal damping ratios and mode shapes associated with the two modes cannot be estimated here. However, they can

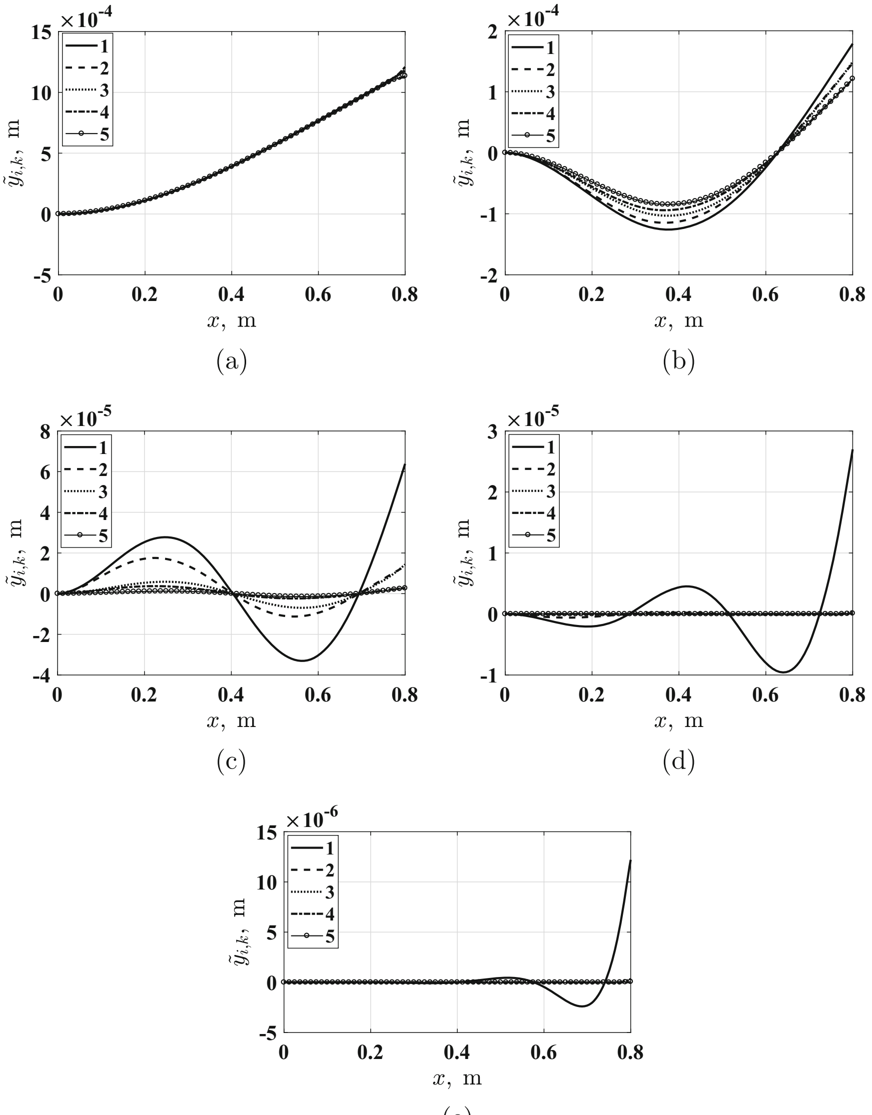

(a) (b) (c) (d) (e)

Fig. 13.5 Free response shapes of the damaged cantilever beam associated with its (**a**) first, (**b**) second, (**c**) third, (**d**) fourth and (**e**) fifth modes obtained from the response measured by the CSLDV system

be estimated if a higher scan frequency is applied so that at least two non-zero-amplitude free response shapes associated with each of the two modes can be obtained from the response measured by the CSLDV system. By applying the OMPE method in Sect. 13.2.3, modal damping ratios and mode shapes associated with the first three modes can be estimated with the obtained free response shapes here. Estimated damping ratios associated with the first three modes are listed in Table 13.1b, which compare well with those from the finite element model. Estimated mode shapes are shown in Fig. 13.6, and modal assurance criterion (MAC) values between mode shapes from the OMPE method and finite element model are above 99.99%, which indicates that the mode shapes compare well with each other. Note that the mode shapes are normalized so that they have a maximum unit amplitude.

The estimated mode shapes are then used for structural damage identification. The three mode shapes of the damaged cantilever beam are fitted by polynomials with properly determined orders. The orders of the polynomial fits are 7, 8 and 11 for the first through third mode shapes, respectively. Curvature mode shapes corresponding to the first three mode shapes and those from the polynomial fits are shown in Fig. 13.7. It can be seen that local anomaly due to the damage can be well observed by comparing the curvature mode shapes of the beam with those from the polynomial fits. CDIs corresponding to the three mode shapes are shown in Fig. 13.8a–c, and the auxiliary CDI corresponding to the three

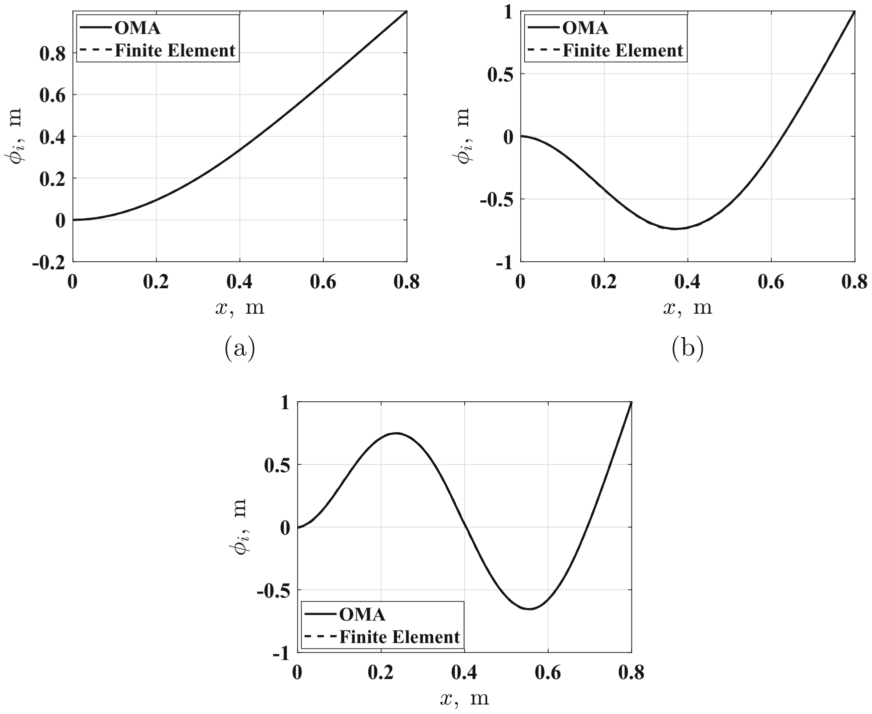

(a)

(b)

(c)

Fig. 13.6 Comparison between mode shapes of the damaged cantilever beam from the OMPE method using the free response shapes and its finite element model associated with its (**a**) first, (**b**) second and (**c**) third modes

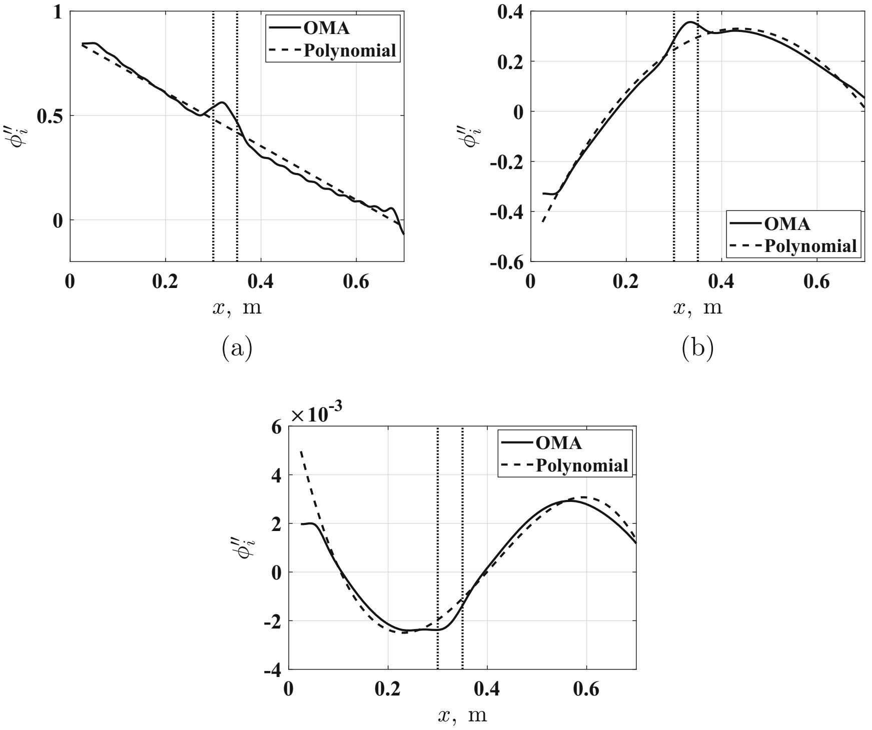

(a)

(b)

(c)

Fig. 13.7 Comparison between curvature mode shapes of the damaged cantilever beam from the OMPE method and polynomial fits associated with its (**a**) first, (**b**) second and (**c**) third modes

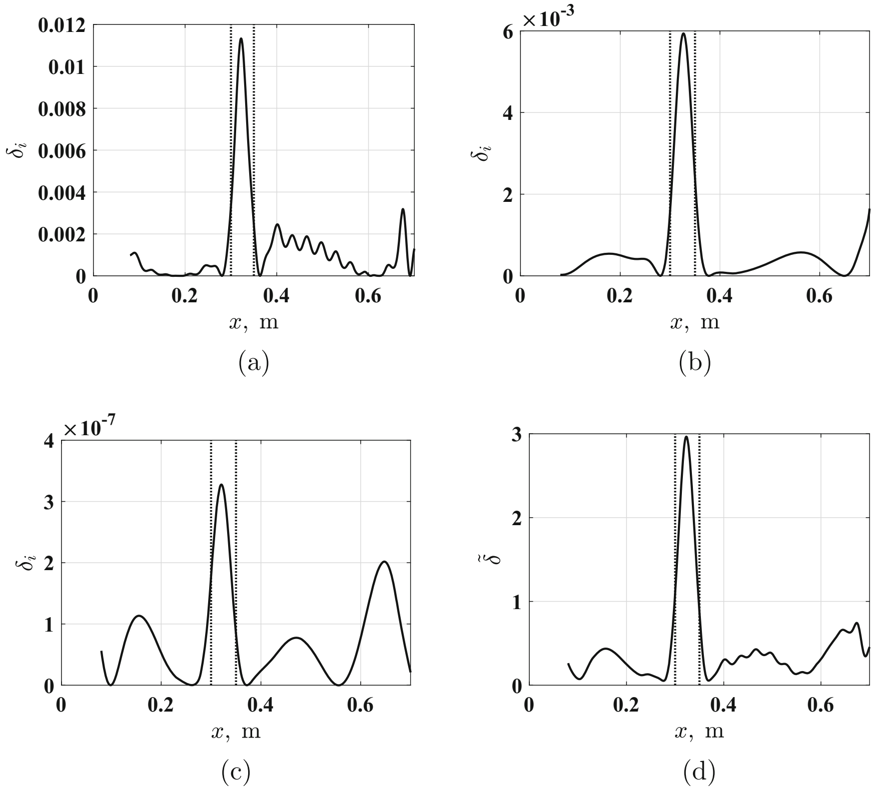

Fig. 13.8 CDIs of the damaged cantilever beam associated with its (**a**) first, (**b**) second and (**c**) third modes; (**d**) the auxiliary CDI associated with the curvature damage indices in (**a**) through (**c**). Ends of the damage are indicated by two dotted lines

damage indices is shown in Fig. 13.8d. The structural damage can be clearly and accurately identified in neighborhoods with consistently large values of the CDIs in Fig. 13.8a–c and the auxiliary CDI in Fig. 13.8d can well assist identification of the neighborhood.

13.4 Conclusions

Derivation of free response shapes of a linear, time-invariant, viscously damped structure is shown. The only current application of free response shapes is structural damage identification and they cannot be used for model validation and updating. A new OMPE method using free response measured by a CSLDV system is proposed to estimate modal parameters, including natural frequencies, modal damping ratios, and mode shapes based on the concept of free response shapes. Natural frequencies can be estimated by measuring free response of fixed points on the structure. A free response shape associated with an elastic mode corresponds to the mode shape associated with the same mode. The amplitude of the free response shape exponentially decays with a decaying rate that is directly related to the modal damping ratio and natural frequency of the mode. When the decay is compensated with an accurately estimated decaying rate, the mode shape of the mode can be automatically obtained as a result. In the proposed OMPE method, the modal damping ratio and mode shape associated with an elastic mode can be simultaneously estimated by solving an optimization problem. Free response shapes of one elastic mode in at least two half-scan periods are needed to estimate its modal damping ratio and mode shape. Using relatively low scanning frequencies can yield mode shapes of high qualities. A baseline-free method is applied to identify structural damage using mode shapes estimated by the OMPE method. In the numerical investigation, the proposed OMPE method is applied to estimate modal parameters of a viscously damped damaged beam using its free response measured by a simulated CSLDV system. Estimated modal parameters compare well with their theoretical ones and the damage can be accurately identified using the auxiliary CDI.

Acknowledgements The authors are grateful for the financial support from the National Science Foundation through Grant Nos. CMMI-1335024, CMMI-1763024, CMMI-1762917 and the College of Engineering and Information Technology at the University of Maryland, Baltimore County through a Strategic Plan Implementation Grant. The first author is also grateful for the faculty startup support from the Department of Mechanical and Materials Engineering at the University of Cincinnati.

Appendix: Short-Time Fourier Transform

The short-time Fourier transform of $\tilde{z}$, denoted by $\tilde{V}_w\,(t,\,f)$, can be expressed by

$$\tilde{V}_w\,(t,\omega) = \int_{-\infty}^{\infty} \tilde{z}\,(\tau)\, g_s^*\,(\tau - t)\, \mathrm{e}^{-\mathrm{j}\omega\tau} \mathrm{d}\tau \tag{13.28}$$

where g_s is a window function with a scale s, the superscript $*$ denotes complex conjugation, and $\mathrm{j} = \sqrt{-1}$. The scale s determines the width of g_s in the time domain, which should be smaller than that of a half-scan period. When $\tilde{V}_w$ at the i-th natural frequency of the structure becomes almost zero at an instant $t_{i,0}$, the amplitude of $\tilde{y}_i$ is considered to be zero. Note that in Eq. (13.28), $\tilde{V}_w\,(t,\omega)$ is visualized by use of a spectrogram whose intensity denotes the power spectral density associated with $\tilde{V}_w\,(t,\omega)$; g_s is a Hamming function that can be expressed by

$$g_s\,(t) = \begin{cases} 0.54 - 0.46\cos\left(\frac{2\pi t}{s}\right) &, \ 0 \le t \le s \\ 0 &, \ \text{otherwise} \end{cases} \tag{13.29}$$

References

1. Doebling, S.W., Farrar, C.R., Prime, M.B., et al.: A summary review of vibration-based damage identification methods. Shock Vib. Dig. **30**(2), 91–105 (1998)
2. Fan, W., Qiao, P.: Vibration-based damage identification methods: a review and comparative study. Struct. Health Monit. **10**(1), 83–111 (2011)
3. Ewins, D.J.: Modal Testing: Theory and Practice, vol. 15. Research Studies Press, Letchworth (1984)
4. Di Maio, D., Ewins, D.: Continuous scan, a method for performing modal testing using meaningful measurement parameters; Part I. Mech. Syst. Signal Process. **25**(8), 3027–3042 (2011)
5. Chen, D.-M., Xu, Y.F., Zhu, W.D.: Damage identification of beams using a continuously scanning laser doppler vibrometer system. J. Vib. Acoust. **138**(5), 051011 (2016)
6. Stanbridge, A.B., Ewins, D.J.: Modal testing using a scanning laser doppler vibrometer. Mech. Syst. Signal Process. **13**(2), 255–270 (1999)
7. Stanbridge, A.B., Ewins, D., Khan, A.: Modal testing using impact excitation and a scanning LDV. Shock Vib. **7**(2), 91–100 (2000)
8. Allen, M.S., Sracic, M.W.: A new method for processing impact excited continuous-scan laser doppler vibrometer measurements. Mech. Syst. Signal Process. **24**(3), 721–735 (2010)
9. Sriram, P., Craig, J., Hanagud, S.: A scanning laser doppler vibrometer for modal testing. Int. J. Anal. Exp. Modal Anal. **5**, 155–167 (1990)
10. Sriram, P., Hanagud, S., Craig, J.: Mode shape measurement using a scanning laser doppler vibrometer. Int. J. Anal. Exp. Modal Anal. **7**(3), 169–178 (1992)
11. Stanbridge, A.B., Ewins, D.J.: Measurement of translational and angular vibration using a scanning laser doppler vibrometer. Shock Vib. **3**(2), 141–152 (1996)
12. Yang, S., Allen, M.S.: Output-only modal analysis using continuous-scan laser doppler vibrometry and application to a 20 kw wind turbine. Mech. Syst. Signal Process. **31**, 228–245 (2012)
13. Yang, S., Allen, M.S.: Lifting approach to simplify output-only continuous-scan laser vibrometry. Mech. Syst. Signal Process. **45**(2), 267–282 (2014)
14. Wereley, N.M., Hall, S.R.: Linear time periodic systems: transfer function, poles, transmission zeroes and directional properties. In: American Control Conference, pp. 1179–1184. IEEE (1991)
15. Chen, D.-M., Xu, Y.F., Zhu, W.D.: Non-model-based multiple damage identification of beams by a continuously scanning laser doppler vibrometer system. Measurement **115**, 185–196 (2018)
16. Chen, D.-M., Xu, Y.F., Zhu, W.D.: Experimental investigation of notch-type damage identification with a curvature-based method by using a continuously scanning laser doppler vibrometer system. J. Nondestruct. Eval. **36**(2), 38 (2017)
17. Xu, Y.F., Chen, D.-M., Zhu, W.D.: Damage identification of beam structures using free response shapes obtained by use of a continuously scanning laser doppler vibrometer system. Mech. Syst. Signal Process. **92**, 226–247 (2017)
18. Meirovitch, L.: Principles and Techniques of Vibrations, vol. 1. Prentice Hall, New Jersey (1997)
19. Caughey, T., O'Kelly, M.E.: Classical normal modes in damped linear dynamic systems. J. Appl. Mech. **32**(3), 583–588 (1965)
20. Rao, S.S., Yap, F.F.: Mechanical Vibrations, vol. 4. Prentice Hall, Upper Saddle River (2011)
21. Hlawatsch, F., Auger, F.: Time-Frequency Analysis. Wiley-ISTE (2013)
22. Pandey, A., Biswas, M., Samman, M.: Damage detection from changes in curvature mode shapes. J. Sound Vib. **145**(2), 321–332 (1991)
23. Xu, Y.F., Zhu, W.D., Liu, J., Shao, Y.: Identification of embedded horizontal cracks in beams using measured mode shapes. J. Sound Vib. **333**(23), 6273–6294 (2014)